Order Number 9507293

Magnetospheric imaging of EUV emissions at 83.4 and 30.4 nm wavelengths

Garrido, Dante Espino, Ph.D.

University of Alaska Fairbanks, 1994

U·M·I
300 N. Zeeb Rd.
Ann Arbor, MI 48106

MAGNETOSPHERIC IMAGING OF EUV EMISSIONS AT 83.4 AND 30.4 NM WAVELENGTHS

A

THESIS

Presented to the Faculty

of the University of Alaska Fairbanks

in Partial Fulfillment of the Requirements

for the Degree of

DOCTOR OF PHILOSOPHY

By

Dante Espino Garrido, M.A.

Fairbanks, Alaska

May 1994

MAGNETOSPHERIC IMAGING OF EUV EMISSIONS

AT 83.4 AND 30.4 nm WAVELENGTHS

By

Dante Espino Garrido

RECOMMENDED:

R. W. Smith, Thesis Advisor

J. L. Morack, Head, Physics Department

APPROVED:

Dean, College of Natural Sciences

Dean of the Graduate School

April 5, 1994

Date

Abstract

Magnetospheric images are constructed from resonant scattering of emissions by He^+ 30.4-nm and O^+ 83.4-nm ions from different spatial locations to study the structure of the intensities and its relation to the distribution of He^+ and O^+ ions around the Earth. The image intensities at these EUV wavelengths were obtained from a knowledge of ion scattering rates and available data on ion densities. This particular approach is called forward modelling and consists of the calculation of simulated EUV images of the magnetosphere. Different regions in the magnetosphere have been considered in this study to determine the dependence of the image intensities on ion energies and ion drift speeds with respect to the Sun-Earth line. Hot O^+ ions in the energy range from 1 keV to 50 keV are present in the plasma sheet with typical densities of the order of 0.1 ions cm^{-3} arising during disturbed times. Image intensities of the order of a few millirayleighs were obtained in our simulations for these densities. During quiet times the densities are of the order of 0.05 ions cm^{-3}. The reduction of the image intensities as a result of Doppler shifts caused by ion motion relative to the Sun-Earth line is discussed in detail and the effects of ion dynamics (particle acceleration) in the polar cap on the image intensities have also been analyzed for both He^+ and O^+ ions. The possibility of detecting polar outflows may also depend on the location of the imager. Simulated images of the plasmasphere and trough regions in both 30.4-nm and 83.4-nm wavelengths have been obtained to reflect the relative abundance of the ions in these regions.

Photometric intensities of He^+ at 30.4 nm were obtained from a spinning rocket at an altitude of 435 km. The different viewing angles covered a wide range of regions in the magnetosphere, and this particular rocket geometry offered the possibility of obtaining the He^+ ion distribution from the measured intensities. This method (forward inversion) can be applied to 2-D images and it is shown that it is possible to extract 3-D ion distributions from the images.

Table of Contents

List of Figures

Acknowledgements

FATHER in HEAVEN, in the name of YOUR SON, JESUS CHRIST, and by YOUR HOLY SPIRIT, I acknowledge the GRACE, MERCY, POWER of Your Love and I thank You for my SALVATION. Lord Jesus, I confess you publicly as my personal Saviour. In words, in my deeds and in the work of my hands that You have blessed, I shall honor and serve You. Your words says in [Jeremiah 29: 11-13]; 'I know the plans I have for you', declares the Lord, 'plans to prosper you and not to harm you, plans to give you hope and a future. Then you will call upon Me and come and pray to Me, and I will listen to you. You will seek Me and find Me when you seek Me with all your heart.'

Lord Jesus, I thank You through my Dad (Elmo Sr.) and my Mom (Carina) and my brothers Joel, Rocky, Elmo Jr., Raymund, Michael, Roy and Daniel and their families who cared for me, who prayed and encouraged me to fulfill my duties to the Institute when I was broken in spirit and ready to quit. Lord, Bless all my Filipino friends, Drs. Rufino Ibarra and Bayani Ramirez and their families, Janet and Jackie Lansangan, the Vaughan Family, Grandpa and Grandma, David and Rose, Butz and Nena and their families, Angelita Ang and Tom Maher, Frank and Carol Taylor, John and Cecil Evans, Profs. Stephen and Elena Sparrow, Prof. Frank Wooding and wife Josie, who invited me to their festivities to enjoy the delicacies of the Orient and the delights of the West, Praise God!

Lord Jesus, I thank You and Praise You because You have answered my prayers to come to the great country of the United States for my education to learn Your ways and Your wisdom which You have imparted to this nation. O God, Bless America and all the nations that love You. Lord, Bless the Faculty and employees of the Geophysical Institute, University of Alaska, Fairbanks for their help, support and guidance throughout my graduate studies. Lord, Bless the following people whose help and guidance I acknowledge; My Adviser, Prof. R.W. Smith whose encouragement, guidance and words of wisdom has been a great benefit to me, to Prof. Akasofu and Prof. Joe Kan for their grace in financially supporting my studies and the excellence they have achieved in their work is notable and has encouraged me to work diligently, to my official and unofficial advisers Profs. J. Roederer, M. Rees and D. Swift whose valuable advice and critical evaluation of my work has led to published work, to my graduate advisory committee Profs. H. Nielsen, T. Hallinan, Knut Stamnes , J. Craven and J. Hawkins. Special mention goes to Prof. Hawkins for his effort in establishing collaborative research with Lockheed Missiles and Space Company and obtaining research funds from the Alaska Space Grant Program.

Special thanks also goes to Drs. Vondrak, R.M. Robinson, Yam Chiu and J. Cladis for supervising my research while I was an intern at Lockheed Missiles and Space Company, Palo Alto. Lord Jesus, Please bless the following students who shared their talents to me when I needed help; Don Hampton, Joe Minow, Gerard Fasel, Jim Conner, Nettie Labelle-Hamer, Matthew K. Bierer, Yong Xiang Hu and Eric Olson. Special thanks also goes to Evelyn Trabant and

the Photo-graphics staff, Dick Million, Celia Rowher and Dave Covey of the Computer Resource Center.

May the grace of the Lord also go to my brothers and sisters in Christ, Ray Ward, Frank Sheline, Donna Sandberg, Kathy Berry, Carol Gering, Sheila Finch, Jeanne Hume, Sue Hetrick and Joanne Ballew and their respective families. May the Grace, Peace and Blessings of our Father in heaven and the Lord Jesus Christ abound in Pastor Flynn, Tom and Wendy Hogan, Darryl and Ruth Earnshaw, the Praise and Worship team at Lighthouse Christian Center and their respective families. May the Grace and Peace of Our Lord, Jesus Christ abound in The First Assembly of God Church and the Bible Baptist Church of Fairbanks. I share a message from the Lord in [Romans 10:13]; Those who call on the name of the Lord shall be saved and [Acts 16.31]; Believe in the Lord Jesus, and you will be saved, you and your family. Glory to the Most High God, AMEN!

Chapter 1 Introduction

The present picture of the Earth's magnetosphere is based on a large number of satellite and ground based observations made at different times and at different magnetospheric conditions. My goal is to understand the behaviour of the near-Earth environment and also predict how it would respond to changes in solar activity. Many localized observations of the different regions in the magnetosphere have led to the discovery of many important dynamical processes that occur periodically. The auroral regions have been found to be regions of intense ion outflows where particle energization takes place. The ionosphere has also been recognized as a major source of energetic particles for the outer magnetosphere. The plasma sheet is the most difficult to measure because of its great expanse. Also, this region is the site of intensive mixing of solar and ionospheric plasmas. Complex processes of energization occur in the plasma sheet and plasmas which are energized are driven back towards the ionosphere along the Earth's magnetic field lines. How the plasma sheet responds to varying magnetic conditions is also the focus of current research. Magnetic reconnection studies predict the formation of plasmoids and these are phenomena which would be very interesting to observe optically in a global perspective. The plasmasphere is the inner-Earth region defined by closed field lines which are dipolar in character. This region consists of mostly trapped cold plasmas. These plasmas are believed to have diffused from the ionosphere. Also, plasmas that are trapped by field lines that intersect the ionosphere in the low latitude regions (up to about 52 degrees) tend to maintain their flux tube contents even under disturbed magnetic conditions, while plasmas bounded by field lines at higher latitudes are eroded easily. The dynamical process by which the plasmasphere is emptied and refilled by plasma is another exciting event to observe from a global perspective. The ability to make such

observations of these dynamical events occurring in the Earth's magnetosphere depends upon the development of remote sensing techniques such as EUV imaging at suitable ion resonance wavelengths.

The Sun acts as a continous source of both particles and electromagnetic radiation that affect the shape (magnetic field) and the distribution of plasma in the magnetosphere. The discovery by Johnson et al. (1971) of the He^+ 30.4 nm emission line originating in the plasmasphere led to the understanding that this radiation is resonantly scattered by the He^+ ions. He was first to suggest that the magnetosphere would appear to glow if observed at that wavelength. The emission line at 83.4 nm may also be used for the optical detection of O^+ ions. They are both abundant in the ionosphere, and are also found in the outer magnetosphere. The efficiency with which these wavelengths are resonantly scattered is determined by the scattering rate (photons s^{-1} ion^{-1}) of the ions. It will be interesting to estimate the intensity and distribution of the 'magnetoglow' and study how the structure of the glow would respond to different magnetic conditions.

The aim of this thesis is to show that a global picture of the magnetosphere may be seen in an optical image at 30.4 or 83.4 nm wavelengths and that plasma distributions can be derived from them. Naturally occurring He^+ and O^+ ions exist in the Earth's magnetosphere which can resonantly scatter photons coming from the Sun at these wavelengths. The shape or structure of the image intensities reflects the distribution of ions in the Earth's magnetic field and the magnitude of the intensities provides information on the ions' relative abundance in different regions around the Earth, their energies, their response to magnetic disturbances, and Doppler shifts caused by the ion's motion relative to the Sun-Earth line. The magnitude of the intensities also depends on the ions' scattering rate (photons s^{-1} ion^{-1}). Simulated images are constructed based on available density data and known scattering rates for both He^+ and O^+ ions to estimate their image brightness and also determine the shape of the intensity distribution.

Some of the chapters (Chapters 3, 4, 5 and 6) in this thesis have been published or are currently in press. These are self-contained and include conclusions, references and acknowledgements. Chapter 2 describes in detail the density models used in other chapters and also contains some equations that appear in later chapers. This may appear repetitive but at the same time it preserved the style of the published articles from which these chapters are based. A separate chapter on conclusions (Chapter 8) briefly summarizes the conclusions made in other chapters. A review of instrumental considerations pertaining to space-based imaging using 30.4 and 83.4 nm emissions is not included here since it is extensively discussed elsewhere (See the references).

I have adopted ion density models that are simple and convenient to use in my simulations, and the expression for the density distribution has been found to agree reasonably well with observations in the different regions where it has been applied. These are discussed in Chapter 2. The kinetic model due to Huang and Birmingham, (1992) is described briefly and this review provides the necessary background for understanding later chapters. The kinetic description has been found to fit with observations pertaining to the polar regions, and I have used this model to describe the spatial distribution of the outflowing He^+ ions. In the plasmasphere where the ions may be in diffusive equilibrium, the fluid description of Chiu et al. (1979) was used.

I described in Chapter 3 how the magnetospheric images are affected by plasma drift speeds along the Sun-Earth line and variations in plasma temperature in the radiation belt. The focus of this study is on the complicated structure of the O^+ 83.4 nm solar lines that can affect the efficiency at which photons are scattered when the ions have a drift velocity relative to the Sun-Earth line. Energetic O^+ ions occur in the plasma sheet with drift speeds of up to 300 km s^{-1}. Images at different satellite locations were also obtained to determine the global structure of the observed emissions and to evaluate instrumental requirements to possibly detect weak emissions in these regions.

The possibility of detecting optical emissions of He^+ 30.4 nm and O^+ 83.4 nm from the high latitude regions is investigated in Chapter 4. In this chapt er I also examine and contrast the simulated images at two levels of magnetic activity, i.e., during quiet and disturbed conditions using ion outflow data obtained by the Energetic Ion Composition Spectrometer (EICS) on Dynamics Explorer 1 (DE 1). I studied energetic ion outflows in the polar cap which occur as a result of particle energization and investigated the possibility of observing them optically.

In earlier discussions, the regions on which I have focused attention have been the plasmasheet, where ion drifts speeds may be large (Chapter 3), the radiation belt, where the plasma species are hot, and the high latitude regions where polar ion outflows occur (Chapter 4). Although, the intensities in these regions may be weak, the importance of the dynamical processes occurring is unquestionable. In Chapter 5, I simulate images in both 30.4 and 83.4 nm wavelengths for the plasmasphere and trough regions. I have used source densities at 1000 km altitude as inner boundary conditions, and the density models described in Chapter 2 were used to obtain the distribution everywhere inside the flux tubes. I also study how the latitude variation of the source densities would be reflected in the images. The strong intensities obtained in the bright regions of the plasmasphere at 30.4 nm suggest imaging He^+ (30.4 nm) resonant emissions to be favorable.

Aerospace Corporation launched a rocket in March 1982 from Poker Flat, Alaska. The principal investigator for this flight, Dr. A.B. Christensen, gave us emission rate data that covered a wide range of wavelengths, including the He^+ 30.4 nm emission. The rocket was at an altitude of about 435 km and in the night side sector. The spinning motion of the rocket offered the observation of many distinct regions including the ionosphere, the plasmasphere and the polar cap. Successive spins of the rocket provided information on the time variation of the column intensities. An inversion method is introduced in Chapter 6 that allows the extraction of densities from the observed

photometric intensities. The results are significant because they give information on the relative content of each flux tube region in the inner magnetosphere and its time variability.

The extraction of 3-D density distributions from a 2-D image is the study of Chapter 7. Tomographic imaging of the Earth's magnetosphere is highly impractical to implement because it requires that a large number of views be made at many different locations. In this study, I have shown that under certain conditions it is possible to extract density information using only a limited number of views (few columns of pixels in an image) from one location in space.

1.1 References

Chiu, Y.T., J.G. Luhmann, B.K. Ching and D.J. Boucher," An Equilibrium Model of Plasmaspheric Composition and Density", *J. Geophys. Res.*, **84**, pp. 909-916, (1979).

Huang, T.S. and T.J. Birmingham," The Polarization Electric Field and Its Effects in an Anisotropic Rotating Magnetospheric Plasma", *J. Geophys. Res.*, **97**, pp. 1511-1519, (1992).

Johnson, C.Y., J.M. Young, and J.C. Holmes, " Magnetoglow - A New Geophysical Resource", *Science*, **171**, 379, (1971).

Chapter 2 Density Models

2.1 Kinetic Description

In an earlier work by Chiu et al. (1990), magnetospheric images were constructed employing a density profile using a magnetic scaling factor for the outflowing ions. Chiu et al. (1990) also assumed that the magnetosphere is static and that the ion outflow is continuous. However, the effects of the gravitational field and co-rotation of the plasma with the earth's rotation were not accounted for in obtaining the density distribution of the ions along field lines. A detailed analysis of the dynamical motion of charged particles in the guiding center approximation has beer made by Northrop and Birmingham (1982) incorporating rotational effects in the equations of motion and total energy of the particle. A recent study by Huang and Birmingham (1992) applied these results in their calculations of density and temperature along dipole magnetic field lines for a plasma that has a temperature anisotropy in a rotating magnetosphere. Following their description I will show from their results that the magnetic scaling factor in the density profile of the particles arises from the temperature anisotropy. The effects of gravity, rotation and polarization electric field have been accounted for in obtaining the density distribution. Huang and Birmingham (1992) obtained expressions for the density distribution of a plasma composed of electrons and one species of ion. In this section, I extend their analysis to a flux tube where the plasma consists of electrons and three ion species (O^+, He^+, H^+) to obtain the spatial distribution of the ions and electrons

along the magnetic field. The expressions for the density and temperature profiles are simple and thus easy to use in the construction of the magnetospheric images. To keep my discussion self-contained I provide a brief description of their model.

The velocity distribution for each species is assumed to have a bi-Maxwellian form

$$f = f_0 e^{\frac{-v_{\parallel 0}^2}{u_{\parallel 0}^2}} e^{\frac{-v_{\perp 0}^2}{u_{\perp 0}^2}}, \tag{2.1}$$

where the parallel ($T_{\parallel 0}$) and perpendicular ($T_{\perp 0}$) temperatures at a reference point on a field line are defined through the thermal speeds

$$u_{\parallel 0}^2 = \frac{2kT_{\parallel 0}}{m} \tag{2.2a}$$

$$u_{\perp 0}^2 = \frac{2kT_{\perp 0}}{m}, \tag{2.2b}$$

where k is the Boltzmann constant and m is the mass of the particle. In this study I take the reference point to be at the ionospheric boundary defined by R=R_0=1.157 R_e (an altitude of 1000 km). The constant coefficient f_0 can be obtain from the normalization condition

$$n_0 = \int f\, d^3v_0 = 2\pi \int dv_{\parallel 0} dv_{\perp 0} v_{\perp 0} f \tag{2.3}$$

giving

$$f_0 = \frac{2(\frac{\alpha}{\pi})^{3/2} n_0}{(T_{\parallel 0})^{1/2}\, T_{\perp 0}} \tag{2.4a}$$

and

$$\alpha = \frac{m}{2k} \tag{2.4b}$$

Northrop and Birmingham (1982) showed that the expression for the total energy of the particle is

$$E = \frac{1}{2}mv^2 - \frac{1}{2}m\Omega^2 r^2 cos^2\lambda - \frac{GMm}{r} + q\Phi \tag{2.5}$$

where q=Ze is the charge, Φ is the electrostatic potential, Ω=7.29×10^{-5} rad s^{-1} is the angular speed of rotation of the Earth, r is the radial distance measured from the center

of the Earth, λ is latitude and M is the mass of the Earth. The distribution function at any other point on the field line can be obtained by assuming the constancy of the magnetic moment

$$\mu = \frac{\frac{1}{2}mv_{\perp}^2}{B} = \frac{\frac{1}{2}mv_{\perp 0}^2}{B_0} \tag{2.6}$$

and the conservation of energy

$$v_0^2 = v^2 + \frac{q}{m}(\phi - \phi_0) + \Delta v^2, \tag{2.7a}$$

where

$$\Delta v^2 = -\Omega^2(r^2 cos^2\lambda - r_0^2 cos^2\lambda_0) + 2C_0(1 - \frac{r_0}{r}) \tag{2.7b}$$

and

$$C_0 = \frac{GM}{r_0}. \tag{2.8}$$

The application of Liouville's Theorem proceeds by rewriting Eq. (2.1) as

$$f = f_0 e^{\frac{-v_{\parallel 0}^2}{u_{\parallel 0}^2}} e^{\frac{-v_{\perp 0}^2}{u_{\parallel 0}^2}} e^{\frac{v_{\perp 0}^2}{u_{\parallel 0}^2}} e^{\frac{-v_{\perp 0}^2}{u_{\perp 0}^2}} \tag{2.9}$$

or

$$f = f_0 e^{\frac{-v_0^2}{u_{\parallel 0}^2}} e^{-v_{\perp 0}^2(\frac{1}{u_{\perp 0}^2} - \frac{1}{u_{\parallel 0}^2})} \tag{2.10}$$

I can use the results of Eqs. (2.6) and (2.7) to replace v_0^2 and $v_{\perp 0}^2$ in Eq. (2.10) to get

$$f = f_0 e^{\frac{-1}{u_{\parallel 0}^2}[v^2 + \frac{q}{m}(\phi - \phi_0) + \Delta v^2]} e^{-v_{\perp 0}^2 \eta(\frac{1}{u_{\perp 0}^2} - \frac{1}{u_{\parallel 0}^2})} \tag{2.11}$$

where $\eta = \frac{B_0}{B}$. Writing $v^2 = v_{\parallel}^2 + v_{\perp}^2$, I get

$$f = f_0 e^{\frac{-1}{u_{\parallel 0}^2}[v_{\parallel}^2 + \frac{q}{m}(\phi - \phi_0) + \Delta v^2]} e^{\frac{-v_{\perp}^2}{u_{\perp}^2}} \tag{2.12}$$

where

$$\frac{1}{u_{\perp}^2} = \frac{1}{u_{\parallel 0}^2} + \eta(\frac{1}{u_{\perp 0}^2} - \frac{1}{u_{\parallel 0}^2}) \tag{2.13}$$

Defining the perpendicular temperature $T_\perp$ for

$$u_\perp^2 = \frac{2kT_\perp}{m} \tag{2.14}$$

Eq. (2.13) can be rewritten as

$$\frac{1}{T_\perp} = \frac{1}{T_{\|0}} + \eta(\frac{1}{T_{\perp 0}} - \frac{1}{T_{\|0}}) \tag{2.15}$$

I can rearrange Eq. (2.15) as

$$\frac{T_\perp}{T_{\perp 0}} = \frac{B}{B_0}\epsilon_0 \tag{2.16}$$

where

$$\epsilon_0 = \frac{1}{[1 + \frac{1}{\gamma_0}(\frac{1}{\eta} - 1)]} \tag{2.17}$$

and

$$\gamma_0 = \frac{T_{\|0}}{T_{\perp 0}} \tag{2.18}$$

Note that from use of the adiabatic invariants, Eq. (2.12) shows that a bi-Maxwellian distribution at a reference point is mapped to another bi-Maxwellian distribution at another point where the parallel temperature is kept constant while the perpendicular temperature is described by Eq. (2.16). Since η decreases along the field line from the ionosphere to the equator $T_\perp$ also decreases. If the temperature of the particles is isotropic at the reference point, ie., ($\gamma_0 = 1$) then Eq. (2.17) becomes

$$\epsilon_0 = \frac{B_0}{B} \tag{2.19}$$

hence $T_\perp = T_{\perp 0}$ then $\gamma = \frac{T_\|}{T_\perp} = 1$ indicating that the temperature is also isotropic anywhere along the field line.

Density Distribution

The spatial distribution of the density along a field line can be obtain by integrating Eq. (2.12) as

$$n = 2\pi f_0 \int_0^\infty dv_\parallel e^{-\frac{1}{u_{\parallel 0}^2}[v_\parallel^2 + \frac{q}{m}(\phi-\phi_0)+\Delta v^2]} \int_0^\infty dv_\perp v_\perp e^{\frac{-v_\perp^2}{u_\perp}} \tag{2.20}$$

or

$$n = 2\pi f_0 e^{-\frac{q}{2kT_{\parallel 0}}\Delta\psi} e^{\frac{-\Delta v^2}{u_{\parallel 0}^2}} \int_0^\infty dv_\parallel e^{\frac{-v_\parallel^2}{u_\parallel^2}} \int_0^\infty dv_\perp v_\perp e^{\frac{-v_\perp^2}{u_\perp^2}} \tag{2.21}$$

Using Eq. (2.4a) in Eq. (2.21) the result of the integration gives us

$$n_j = n_{0j}\frac{B}{B_0}\epsilon_{0j} e^{-Z\chi_j} e^{\frac{-\Delta v^2}{u_{\parallel 0}^{j2}}} \tag{2.22}$$

where

$$\chi_j = \frac{e\Delta\psi}{2kT_{\parallel 0}^j} \tag{2.23a}$$

$$\Delta\psi = \phi - \phi_0 \tag{2.23b}$$

$$u_\parallel^{j2} = \frac{2kT_{\parallel 0}^j}{m_j} \tag{2.23c}$$

The index j labels the different particle species and Z expresses the sign and the number of electronic charges in the particle. The expression for the density given by Eq. (2.22) is proportional to the magnetic scaling factor and an exponential term that includes the effects of gravity and the earth's rotation contained in the expression for Δv^2 and the electrostatic potential is defined by $\Delta\psi = \phi - \phi_0$. In this paper I extend the model of Huang and Birmingham (1992) to a plasma consisting of electrons and the ions (O^+, He^+, H^+). The polarization potential $\Delta\psi$ can be obtained by requiring charge

neutrality to hold at every point on the field line, ie.

$$n_e = \sum_j n_j$$

or

$$n_e = n(O^+) + n(He^+) + n(H^+), \tag{2.24}$$

where j=1,2,3 refers to (O^+, He^+, H^+), respectively. For electrons, using Z_j=-1 and ions Z_j=1 so that the particle densities are given by

$$n_e = n_{0e}\frac{B}{B_0}\epsilon_{0e}e^{\chi_e}e^{-\frac{m_e\Delta v^2}{2kT^e_{\|0}}} \tag{2.25}$$

$$n_j = n_{0j}\frac{B}{B_0}\epsilon_{0j}e^{-\chi_j}e^{-\frac{m_j\Delta v^2}{2kT^j_{\|0}}}, \tag{2.26}$$

where

$$\epsilon_{0e} = \frac{1}{[1 + \frac{1}{\gamma_{0e}}(\frac{1}{\eta} - 1)]} \tag{2.27a}$$

$$\epsilon_{0j} = \frac{1}{[1 + \frac{1}{\gamma_{0j}}(\frac{1}{\eta} - 1)]} \tag{2.27b}$$

$$\gamma_{0e} = \frac{T^e_{\|0}}{T^e_{\perp 0}} \tag{2.28a}$$

$$\gamma_{0j} = \frac{T^j_{\|0}}{T^j_{\perp 0}}. \tag{2.28b}$$

In general, the parallel and perpendicular temperatures at the reference point will be unequal; in that case, the electrostatic potential along the field line can be obtained by solving a transcendental equation obtained by imposing the neutrality condition given in Eq. (2.24). However, to investigate the major features of the images using resonantly scattered light, the calculation is greatly simplified by assuming $T^e_{\|0} = T^j_{\|0} = T_{\|0}$ so that I get

$$\chi_e = \chi_j = \chi = \frac{e\Delta\psi}{2kT_{\|0}}. \tag{2.29}$$

Deviations from this condition will involve changes in the exponential terms in Eqs. (2.25) and (2.26). Since the exponents are very small, these terms are not the dominating factors

in the variation of particle densities. The quantities n_{0e} and n_{0j} refer to the ionospheric densities. Using Eq. (2.24), I get

$$n_{0e}\epsilon_{0e}e^{\chi}e^{-\frac{m_e\Delta v^2}{2kT_{\|0}}} = e^{-\chi}\sum_j n_{0j}\epsilon_{0j}e^{-\frac{m_j\Delta v^2}{2kT_{\|0}}}.$$

After simplification I get

$$e^{\chi} = (A)^{\frac{1}{2}}, \tag{2.30a}$$

where

$$A = \sum_j N_j e^{-\frac{m_j\Delta v^2}{2kT_{\|0}}} \tag{2.30b}$$

and

$$N_j = \frac{n_{0j}}{n_{0e}}\frac{\epsilon_{0j}}{\epsilon_{0e}}. \tag{2.31}$$

The field aligned potential difference can be obtained from

$$\Delta\psi = \phi - \phi_0 = \frac{2kT_{\|0}}{e}\chi, \tag{2.32}$$

where $\chi = ln(A^{\frac{1}{2}})$.

2.2 Fluid Description

Previous work done by Chiu et al. (1979) and Li et al. (1983) have discussed fluid models describing plasma flow along magnetic field lines pointing out the importance of the magnetic mirror force in describing the spatial distribution of densities along field lines; however, the anisotropy in the fluid properties of the plasma have not been accounted for. Comfort (1988) has shown that when the plasma is isotropic the effects of the mirror force cancel out. However, in a plasma that possesses a temperature anisotropy the effects of the mirror force will be evident in the magnetic scaling factor present in the expression for the density profile of the particles which I will derive shortly. The results of the

analysis by Comfort (1988) showed that the parallel equation of motion for the plasma is given by

$$nm(\frac{\partial \mathbf{v}}{\partial t} + \mathbf{v}\cdot\nabla\mathbf{v})_{\|} = n\mathbf{F}\cdot\hat{s} - \frac{\partial p_{\|}}{\partial s} + \frac{(p_{\|}-p_{\perp})}{B}\frac{\partial B}{\partial s}, \tag{2.33}$$

where n is the number density, m is mass of the species, $p_{\|}$ and $p_{\perp}$ are the parallel and perpendicular pressures, $\hat{s} = \frac{\mathbf{B}}{B}$ is the unit vector along the field line and $\mathbf{F}$=net non-magnetic force. I will consider the case of diffusive equilibrium ($\mathbf{v}$=0) for plasmas in flux tubes from the ionosphere to the equatorial plane. Assuming isotropic plasma where $p_{\|} = p_{\perp}$, then Eq. (2.33) becomes

$$n\mathbf{F}\cdot\hat{s} - \frac{\partial p_{\|}}{\partial s} = 0. \tag{2.34}$$

Thus, the effect of the magnetic mirror force cancels out. For the case of an anisotropic plasma, ie. when ($p_{\|}\neq p_{\perp}$), I can derive the equilibrium distribution of plasma density from Eq. (2.33). I can rewrite Eq. (2.33) as

$$0 = n_j\mathbf{F}\cdot\hat{s} - \frac{\partial p^j_{\|}}{\partial s} + p^j_{\|}(1-\frac{1}{\gamma_j})\frac{1}{B}\frac{\partial B}{\partial s}, \tag{2.35a}$$

where

$$\gamma_j = \frac{p^j_{\|}}{p^j_{\perp}} = \frac{n_j kT^j_{\|}}{n_j kT^j_{\perp}} = \frac{T^j_{\|}}{T^j_{\perp}}. \tag{2.35b}$$

The index j labels the particle species. The gravitational and centrifugal forces are given by

$$\mathbf{f}_j = (-\frac{GMm_j}{r^2}\hat{r} + m_j\Omega^2 r\cos\lambda\hat{\rho}), \tag{2.36}$$

where the unit vector $\hat{\rho} = \hat{x}\cos\phi + \hat{y}\sin\phi$. The orthogonal unit vectors $(\hat{x},\hat{y},\hat{z})$ define directions along the solar magnetospheric (X,Y,Z) axes with the +X pointing towards the sun and the Y axes lies in the dawn to dusk plane and the +Z axes points along

geographic north. The net non-magnetic forces combined with the electrostatic forces give us

$$n_j \hat{s} \cdot \mathbf{F} = n_j (Z_j e E - f_s^j). \tag{2.37}$$

I will derive the expression for f_s^j in a separate section. Using the result

$$\frac{\partial p_{\|}^j}{\partial s} = k n_j \frac{\partial T_{\|}^j}{\partial s} + k T_{\|}^j \frac{\partial n_j}{\partial s} \tag{2.38}$$

in Eq. (2.35a) and dividing the result by $n_j k T_{\|}^j$, I obtain after simplification,

$$\frac{\partial}{\partial s} ln(\frac{n_j T_{\|}^j}{B}) + A_j = Q_j, \tag{2.39}$$

where

$$A_j = \frac{1}{\gamma_j} \frac{\partial}{\partial s} ln(B) \tag{2.40a}$$

$$Q_j = \frac{1}{k T_{\|}^j} (Z_j e E - f_s^j). \tag{2.40b}$$

Integration of Eq. (2.39) gives us

$$ln(\frac{n_j T_{\|}^j}{B}) - ln(\frac{n_{0j} T_{\|0}^j}{B_0}) = \int_{s_0}^{s} ds\,(Q_j - A_j). \tag{2.41}$$

I can simplify and write the result as

$$n_j = n_{0j} \frac{B}{B_0} \frac{T_{\|0}^j}{T_{\|}^j} e^{\int_{s_0}^{s} ds [\frac{Z_j e E}{k T_{\|}^j} - \frac{f_s^j}{k T_{\|}^j}] - \int_{s_0}^{s} ds \frac{T_{\perp}^j}{T_{\|}^j} \frac{\partial}{\partial s} ln(B)} \tag{2.42}$$

The effect of the magnetic mirror force is seen through the scaling factor $\frac{B}{B_0}$ and the term in the exponent given by

$$- \int_{s_0}^{s} ds \frac{T_{\perp}^j}{T_{\|}^j} \frac{\partial}{\partial s} ln(B). \tag{2.43}$$

In previous fluid models that include the effects of the magnetic mirror force, the term given by Eq. (2.43) is missing. Note, if I assume that the plasma is isotropic, I arrive at

the result for the density profile

$$n_j = n_{0j} \frac{T^j_{\|0}}{T^j_{\|}} e^{\int_{s_0}^{s} \frac{ds}{kT^j_{\|}} (Z_j eE - f^j_s)} \tag{2.44}$$

which is the classical expression obtained for a diffusive equilibrium model. The subscripts zero label quantities at the reference point. However, in order to obtain the density variation along the field lines I need to specify a magnetic field model and a temperature structure and the polarization electric field can be obtained by imposing the condition that charge neutrality hold everywhere along the field line, ie.

$$n_e = \sum_{j=1}^{3} n_j \tag{2.45}$$

where i=(1,2,3) refers to the ion species (O^+, He^+, H^+), respectively.

Gravitational and Rotational Forces

In the present model I have assumed that the rotational and dipole axis are coincident. The expression for the forces along the magnetic field (gravitation plus rotation) has been obtained for a dipole model by Angerami and Thomas (1964), where the expression for the force has been obtained for the case when the field line is in the noon-midnight plane. Since the dipole field is symmetric about the polar axis, the results are valid in general for any azimuth. Care, however must be exercised when working with field models that account for the bending of the magnetic field lines such as Tsyganenko's 1989 model. At any point with coordinates (r, θ, ϕ), the force vector is given by Eq. (2.36) and

the component of the force in the direction of the magnetic field is given by

$$f_s^j = \mathbf{f}_j \cdot \hat{s} = -m_j \frac{GM}{r^2}\frac{B_r}{B} + m_j \Omega^2 r \cos\lambda \frac{B_\rho}{B} \tag{2.46}$$

where

$$B_r = \mathbf{B} \cdot \hat{r} \tag{2.47a}$$

$$B_\rho = \mathbf{B} \cdot \hat{\rho} = \cos\phi\, B_x + \sin\phi\, B_y. \tag{2.47b}$$

Thus, the expression for the force can be written as,

$$f_s^j = -m_j \frac{GM}{r^2}\frac{B_r}{B} + m_j \Omega^2 r \cos\lambda(\cos\phi \frac{B_x}{B} + \sin\phi \frac{B_y}{B}). \tag{2.48}$$

In spherical coordinates, I have the following identities,

$$B_x = B_r \sin\theta\cos\phi + B_\theta \cos\theta\cos\phi + B_\phi(-\sin\phi) \tag{2.49a}$$

$$B_y = B_r \sin\theta\sin\phi + B_\theta \cos\theta\sin\phi + B_\phi \cos\phi. \tag{2.49b}$$

For the case of a dipole, the magnetic field components are

$$B_r = \frac{M_0}{r^3}(-2\cos\theta) \tag{2.50a}$$

$$B_\theta = \frac{M_0}{r^3}(-\sin\theta) \tag{2.50b}$$

$$B_\phi = 0. \tag{2.50c}$$

I can also show the following results

$$B = (B_r^2 + B_\theta^2 + B_\phi^2)^{\frac{1}{2}} = \frac{M_0}{r^3}\Delta \tag{2.51a}$$

where

$$\Delta = (1 + 3\cos^2\theta)^{\frac{1}{2}} \tag{2.51b}$$

and

$$\cos\phi\frac{B_x}{B} = -\frac{3}{\Delta}\sin\theta\cos\theta cos^2\phi. \tag{2.52}$$

Similarly,

$$\sin\phi\frac{B_y}{B} = -\frac{3}{\Delta}\sin\theta\cos\theta\sin^2\phi. \tag{2.53}$$

Adding Eqs. (2.52) and (2.53),

$$\cos\phi\frac{B_x}{B} + \sin\phi\frac{B_y}{B} = -\frac{3}{\Delta}\sin\theta\cos\theta. \tag{2.54}$$

Now, using Eq. (2.54) in Eq. (2.48), I get the result

$$f_s^j = -m_j\frac{GM}{r^2}(\frac{-2\cos\theta}{\Delta}) + m_j\Omega^2 r\cos\lambda(\frac{-3}{\Delta}\sin\theta\cos\theta) \tag{2.55}$$

or

$$f_s^j = \frac{1}{\Delta}[\frac{2GMm_j}{r^2}\cos\theta - 3m_j\Omega^2 r\sin^2\theta\cos\theta] \tag{2.56}$$

which is similar to the result obtained by Angerami and Thomas (1964), apart from the mass term m_j.

Charge Neutrality Condition

When the plasma is isotropic, the density profile for the ions is given by Eq. (2.44)

$$n_j = n_{0j}\frac{T^j_{\|0}}{T^j_{\|}}e^{\chi_j}e^{-I_j} \tag{2.57a}$$

and

$$n_e = n_{0e}\frac{T^e_{\|0}}{T^e_{\|}}e^{-\chi_e}e^{-I_e}, \tag{2.57b}$$

where

$$\chi_j = \int_{s_0}^{s} ds\,\frac{eE}{kT^j_{\|}} \tag{2.58a}$$

$$\chi_e = \int_{s_0}^{s} ds\,\frac{eE}{kT^e_{\|}} \tag{2.58b}$$

$$I_j = \int_{s_0}^{s} ds\,\frac{f^j_s}{kT^j_{\|}} \tag{2.58c}$$

$$I_e = \int_{s_0}^{s} ds\,\frac{f^e_s}{kT^e_{\|}}. \tag{2.58d}$$

For simplicity, assume $T^j_{\|} = T^e_{\|} = T_{\|}$ so that $\gamma_j = \frac{T_{\|}}{T^j_{\perp}}$, $\gamma_e = \frac{T_{\|}}{T^e_{\perp}}$ and

$$\chi_e = \chi_j = \chi = \int_{s_0}^{s} ds\,\frac{eE}{kT_{\|}}. \tag{2.59}$$

Thus, the density distribution for ions and electrons are given by

$$n_j = n_{0j}\frac{T_{\|0}}{T_{\|}}e^{\chi}e^{-I_j} \tag{2.60a}$$

$$n_e = n_{0e}\frac{T_{\|0}}{T_{\|}}e^{-\chi}e^{-I_e}. \tag{2.60b}$$

The condition for charge neutrality gives us

$$e^{-\chi} = (A_1)^{\frac{1}{2}} \tag{2.61a}$$

and

$$A_1 = \sum_j \frac{n_{0j}}{n_{0e}}e^{-I_j}, \tag{2.61b}$$

where terms involving the electron mass have been neglected in Eq. (2.61b). The results just obtained above will be modified for the case when the plasma possesses a temperature

anisotropy. To see this, I rewrite Eq. (2.43) for the density profile of the ions as

$$n_j = n_{0j}\frac{B}{B_0}\frac{T_{\|0}}{T_{\|}}e^{\chi}e^{-I_j}e^{-I_{\gamma j}} \tag{2.62a}$$

and

$$n_e = n_{0e}\frac{B}{B_0}\frac{T_{\|0}}{T_{\|}}e^{-\chi}e^{-I_e}e^{-I_{\gamma e}} \tag{2.62b}$$

for the electrons where

$$I_{\gamma j} = \int_{s_0}^{s} ds\frac{T_{\perp}^{j}}{T_{\|}}\frac{\partial}{\partial s}lnB \tag{2.63a}$$

$$I_{\gamma e} = \int_{s_0}^{s} ds\frac{T_{\perp}^{e}}{T_{\|}}\frac{\partial}{\partial s}lnB. \tag{2.63b}$$

The full specification of the density profile requires the evaluation of the term e^{χ} in Eq. (2.62) which contains the polarization electric field E. Requiring charge neutrality gives us

$$e^{-\chi} = (A_2)^{\frac{1}{2}}, \tag{2.64a}$$

where

$$A_2 = \sum_j \frac{n_{0j}}{n_{0e}}e^{-I_{2j}} \tag{2.64b}$$

$$I_{2j} = I_j + \Delta I_j \tag{2.65a}$$

$$\Delta I_j = I_{\gamma j} - I_{\gamma e} \tag{2.65b}$$

and χ and I_j are defined in Eqs. (2.59) and (2.58c), respectively.

2.3 References

Angerami, J.J. and J.O. Thomas, " Studies of Planetary Atmospheres ", *J. Geophys. Res.*, **69**, 4537-4560, (1964).

Chiu, Y.T., R.M. Robinson, H.L. Collin, S. Chakrabarti and G.R. Gladstone, " Magnetospheric and Exospheric Imaging In The Extreme Ultraviolet ", *Geophys. Res. Lett.*, **17**, pp. 267-270, (1990).

Chiu, Y.T., J.G. Luhmann, B.K. Ching and D.J. Boucher, " An Equilibrium Model of Plasmapheric Composition and Density ",*J. Geophys. Res.*, 84, pp. 909-916, (1979).

Comfort, R.H.," The magnetic mirror force in plasma fluid models", *Modeling Magnetospheric Plasma*", Geophys. Monograph 44, T.E. Moore and J.H. White Jr., Eds., pp. 51-53, American Geophysical Union, Washington, DC, (1988).

Comfort, R.H., I.T. Newberry and C.R. Chappell," Preliminary Statistical Survey of Plasmaspheric Ion Properties From Observations By DE 1/RIMS ", *Modeling Magnetospheric Plasma*", Geophys. Monograph 44, T.E. Moore and J.H. White Jr., Eds., pp. 107-114, American Geophysical Union, Washington, DC, (1988).

Huang, T.S. and T.J. Birmingham, " The Polarization Electric Field and Its Effects in an Anisotropic Rotating Magnetospheric Plasma ",*J. Geophys. Res.*, **97**, pp. 1511-1519, (1992).

Li, W., J.J. Sojka and W.J. Raitt," A Study of Plasmaspheric Density Distribution for Diffusive Equilibrium Conditions ", *Planet. Space Sci.*, **31**, pp. 1315-1327, (1983).

Northrop, T.G. and T.J. Birmingham, " Adiabatic charge particle motion in rapidly rotating magnetospheres ", *J. Geophys. Res.*, **87**, pp. 661-669, (1982).

Tsyganenko, N.A.," A Magnetospheric Magnetic Field Model With a Warped Tail Current Sheet ",*Planet. Space Sci.*, **37**, pp. 5-20, (1989).

Chapter 3 Imaging the Earth's Magnetosphere: Effects of Plasma Flow and Temperature *

3.0 Abstract

We simulate EUV images of the magnetosphere at 83.4 nm for cases where the plasma has a non-zero drift velocity with respect to the Sun and variable plasma temperature. The solar emission in this region is dominated by a blend of nine gaussian shaped lines representing the O^+ triplet and the O^{++} sextuplet contributions (Meier, 1990). The magnetospheric scattering cross-section profile includes only contributions from the O^+ triplet due to the low number density of O^{++} compared to that of O^+ (Chandler et al., 1987). The scattering rate has a complicated structure as a function of bulk velocity and does not possess any symmetry about zero. The scattering rate is reduced for most Doppler shifted cases compared to the case of zero bulk velocity, resulting in a much dimmer image. At some bulk velocities where the scattering cross-section of O^+ peaks at the brighter O^{++} solar line profiles, larger scattering rates occur and the EUV image is brighter. Similarly, due to thermal Doppler spread the scattering rate decreases with increasing plasma temperature. Using a simple model for the O^+ ion number density we present simulated images of the magnetosphere including the radiation belt and plasma sheet for different viewing positions at distances of the order of 50 R_e from the Earth.

*D.E. Garrido, R.W. Smith, D.S. Swift, S-I. Akasofu, Imaging the Earth's Magnetosphere: Effects of Plasma Flow and Temperature; Planet. Space Sci., Vol. 39, pp. 1559-1571, 1991

We show that an EUV magnetospheric image of minimum reasonable quality may be obtained in 1000 s using an electronic imager with an aperture of 750 cm^2. Several comparative cases are shown to illustrate the simulated images in different perspectives and for a selection of bulk plasma velocities and temperatures.

3.1 Introduction

The experimental study of the magnetosphere has proceeded by a process of assembly and careful correlation of point measurements of fields and particles made by satellite instruments in the various plasma regions. Seldom has it been possible to gather an extensive data set for a single geometry or instant in magnetospheric time and space. The contextual information needed to make best use of point measurements of the plasma could be found in an image of the plasma region made optically (Johnson et al., 1971; Meier, 1991; Swift et al., 1989; Chiu et al., 1990) and complementarily by the use of energetic neutral particles (Roelof, 1989). Imaging by optical means gives more information on the lower energy component of the plasma particle population while the energetic neutral particle technique depends upon the higher energy component.

The Sun provides a stream of photons which may be scattered by the ions in the magnetosphere. This scattering is most effective at wavelengths where there is a strong ionic resonance, such as 30.4 nm for He^+ and the triplet at 83.4 nm for O^+. The scattered light enables the observer to determine the shape and position of regions of the magnetosphere where these ions are found and the absolute intensity in any direction gives the line-of-sight column density of the scatterer. This paper is concerned with possible 83.4 nm images of the O^+ densities since information gained from these can be used to study the ionosphere and the magnetosphere. The O^+ found in the magnetosphere

can be assumed to have originated in the ionosphere and to have been advected by the action of coupling processes which link the magnetosphere and the ionosphere.

Swift et al. (1989) and Chiu et al. (1990) showed examples of images at 83.4 nm simulated by computer. Regions of higher density of O^+ in the plasmasphere and plasma sheet show up brighter than their surroundings. In addition, Chiu et al. (1990) show that the ion outflow from the polar caps should also become visible. In both of these earlier papers, no allowance has been made for reduction in scattering efficiency due to high plasma temperature or fast plasma streaming. This paper addresses both these topics giving more realistic simulations of a magnetospheric image and also updated estimate on the imager aperture required for a reasonable frame rate for pictures taken from the moon.

The calculation of the g-factor, expressing the scattering rate of solar emission in photons s^{-1} ion^{-1} has been done by (Meier, 1990) for the 83.4 nm region that incorporates the correct blend of O^+ and O^{++} transitions. The well resolved solar intensity profile is composed of an O^+ triplet and an O^{++} sextuplet. The fractional distribution, b, of the solar intensity into the respective emission lines has also been calculated by Meier et al. (1991) and shown to be b=0.26 for O^+ and b=0.74 for O^{++}. In analyzing the effects of plasma drifts on the cross-section of the ions, the analysis of the scattering rate as a function of bulk velocity, (Meier, 1990) requires an understanding of how the shift in the cross-section line center can affect the scattering rate. Due to close spacing and intermixing of the O^+ and O^{++} lines, a non-zero bulk velocity of the O^+ ions can result in an O^+ cross-section profile overlapping with another line in the O^+ triplet or with a line of the O^{++} sextuplet. An O^+ ion having the right drift speed can resonantly scatter photons emitted from an O^{++} ion. Since some lines in the O^{++} spectrum are much more intense than those in the O^+ triplet, enhanced scattering can occur. This

idea is discussed in detail in a later section. We analyze the structure of the scattering rate as a function of bulk and random velocity by assuming that the cross-section profile for the 83.4 nm wavelength contains only the O^+ triplet.

It will be of great interest to observe the marked changes in the magnetospheric image, say, of the plasma sheet during a substorm by comparing an image observed during 'quiet' times with images obtained during disturbed conditions identified with a marked increase in O^+ number density (Lennartson et al., 1986).

3.2 Brief Review of Atomic and Solar Data

Figure 3.1 shows the energy level diagram corresponding to the O^+ triplet and the O^{++} sextuplet transition (Ho and Henry, 1983). The solar flux I_0 (Hinterreger, 1981) has a magnitude of $.67\times10^9$ photons cm^{-2} s^{-1} and the branching ratios p_n that distribute the solar flux into the nine solar lines can be obtained in terms of the statistical weights of the upper levels of the transitions and also in terms of the Einstein coefficients A_{ln} (for

Table 1: Solar line and atomic data

λ(nm)	$\nu(10^{15}$Hz)	Ju	wu	$\frac{wu}{\sum_u wu}$	$A_{ul}(10^8/s)$	$(\frac{A_{ul}}{\sum_l A_{ul}})_N$	fi	pi	$\sigma_{oi}(cm^2)$
83.4462	3.59513	5/2	6	6/12	7.6	.93	.122	.121	1.5e-13
83.3326	3.60003	3/2	4	4/12	8.2	1.0	.0872	.086	1.1e-13
83.2754	3.60250	1/2	2	2/12	8.2	1.0	.041	.043	5.0e-14
83.2927	3.60175	1	3	3/15	3.3	.59	.102	.087	
83.3742	3.59823	2	5	5/15	4.3	.77	.0748	.189	
83.5096	3.59240	2	5	5/15	1.4	.25	.015	.061	
83.5292	3.59155	3	7	7/15	5.6	1.0	.0816	.345	
83.3715	3.59835	1	3	3/15	2.3	.41	.0245	.061	
83.5059	3.59256	1	3	3/15	.16	.03	.001	.0044	

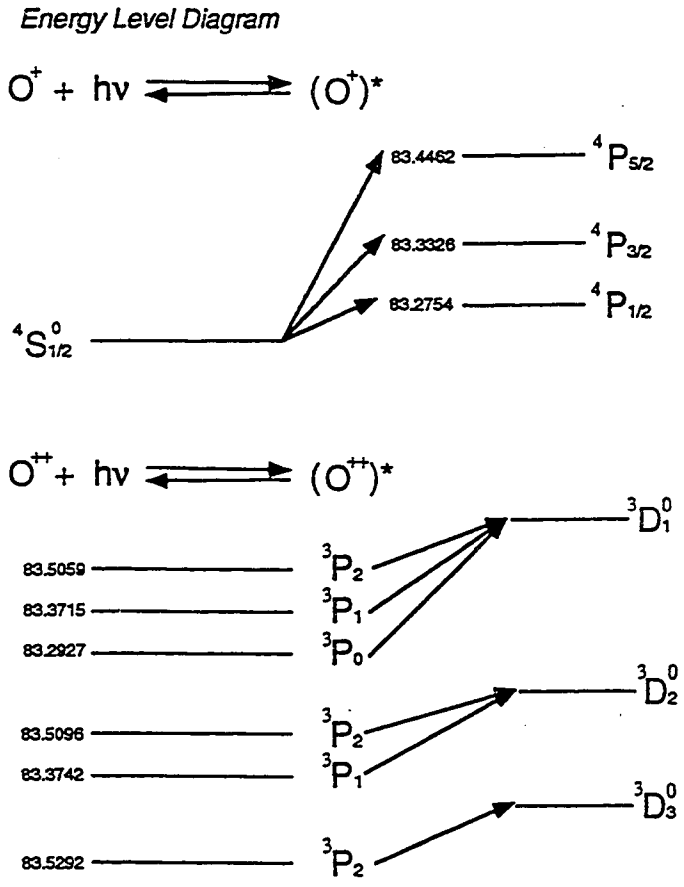

Figure 3.1 Table of Solar and Atomic Data as adopted from Meier (1990). Energy level diagrams are shown explicitly to describe the relevant transitions.

spontaneous emissions to the lower energy levels). The branching ratio p_n is defined by

$$p_n = \frac{w_n}{\sum_i w_i} \frac{A_{ln}}{\sum_l A_{ln}} b_n, \tag{3.1}$$

where

$$\frac{w_n}{\sum_i w_i} = relative\ strength\ of\ statistical\ weights \tag{3.2a}$$

$$\frac{A_{ln}}{\sum_l A_{ln}} = relative\ Einstein\ coefficients \tag{3.2b}$$

and

$$b_n = .26\ for\ n = 1, 3\ (the\ O^+\ lines) \tag{3.3a}$$

$$b_n = .74\ (the\ O^{++}\ lines)\ for\ n = 4, 9. \tag{3.3b}$$

The absorption cross section at line center (ν_{0i}) (see Appendix) is given by

$$\sigma_{0i} = \sigma_i \frac{c}{u_i \nu_{0i} \sqrt{\pi}} \tag{3.4}$$

and is temperature dependent through the thermal speed, $u_i = \sqrt{2kT/m_o}$ of the ions.

The integrated cross-section is defined as

$$\sigma_i = \frac{\pi e^2}{m_e c} f_i, \tag{3.5}$$

where

$$\int_0^\infty \sigma_i^a(\nu)\, d\nu = \sigma_i \tag{3.6}$$

and $\sigma_i^a(\nu)$ is the cross-section profile for a particular transition (where superscript 'a' refers to absorption) and f_i is the oscillator strength. Measured values for the cross-section at line center for O^+ are given by Kumar et al. (1983) for T_i=1000 K. The values for the cross-section obtained using Eq. (3.4) are shown in the last column of the table in Fig. 3.1. The scattering rate at other temperatures were obtained using Eqs. (3.5) and (3.6).

3.3 Analysis of the Scattering Rate g

The theory relevant to the calculation of the g factor (photons per second per ion) is discussed by Meier (1990). Although the method of analysis is familiar, we describe it briefly in the Appendix. Our purpose is to clarify the normalization constants used in our computations. Even though we use the same data, we have obtained slight differences in the values calculated for g. The difference may lie in the temperatures of the ions in the chromosphere. For O^+ we have used T_1= 50000 K and for O^{++} T_2= 130000 K, yielding gaussian widths of .0033 and .0047 nm, respectively. These compare to the values of .0039 and .0054 nm obtained by Meier et al. (1991). Neglecting background light and the effects of solar rotation, the solar line profiles are assumed to be of the form

$$I(\nu) = \sum_{n=1}^{9} I_n \kappa_{0n} e^{-\frac{c^2}{u_n^2 \nu_{0n}^2}(\nu-\nu_{0n})^2}, \tag{3.7}$$

where

$$I_n = I_0 p_n \tag{3.8a}$$

$$\kappa_{0n} = \frac{c}{u_n \nu_{0n} \sqrt{\pi}} \tag{3.8b}$$

and the Doppler shifted cross-section profile is given by

$$\sigma_d^a(\nu) = \sum_{m=1}^{3} \sigma_m \kappa_{0m} e^{-\frac{c^2}{u_m^2 \nu_{0m}^2}(\nu-\nu_m)^2} \tag{3.9},$$

where

$$\nu_m = \nu_{0m}(1 + v_p/c) \tag{3.10a}$$

$$\kappa_{0m} = \frac{c}{u_m \nu_{0m} \sqrt{\pi}}. \tag{3.10b}$$

The subscript n labels quantities of chromospheric origin while m identifies magnetospheric quantities and v_p is the bulk velocity. Our calculations show that the g factor for

the case $v_p = 0$ is 2.45×10^{-7} and 2.67×10^{-7} photons s^{-1} ion^{-1} for plasma temperatures of 1 keV and 10 keV, respectively. This represents an average value which will fluctuate with solar activity. The plot of scattering rate versus drift speed is shown in Fig. 3.2. The complex structure of the g factor shows regions of v_p where g has a significant value and others where it is relatively small.

We analyze both cases where negative drift speeds cause the shifting of the cross-section line centers towards larger wavelengths while positive drift speeds shift the line centers to smaller wavelengths. The varying overlap of the profiles explains the structure of the g factor. The nature of the cross-section and the near resonance of the transitions at 83.4 nm determine the structure of the scattering rate. One can read from Fig. 3.2 the drift speeds at which the g factor is small or large, thus enabling us to infer whether our magnetospheric image is dark or bright. The temperature dependence of g is shown in Fig. 3.2 and the effects on the magnetospheric images are shown in Fig. 3.6. We will discuss the results of the simulations on the images in a later section. As the temperature is increased the absorption cross-section is broadened preserving the total area constant. Fig. 3.2 shows and compares the variation of the scattering rate with drift velocity at various plasma temperatures. The dashed curve represents the structure of the scattering rate when T=100 eV and the solid line represents the case when T=1 keV or T=10 keV. For the case when T=1 keV we see that the scattering rate has a peak around -300 km s^{-1}. The minus sign means that the flow velocity is anti-sunward. Positive velocities will mean that the ion velocities are directed towards the Sun. The value of the scattering rate is seen to decrease as we go towards positive drift speeds up until 100 km s^{-1} where it starts to increase. Another peak in the scattering rate is obtained at speeds of about 300 km s^{-1}. The Doppler effects caused by the ion flow velocities will be shown in Fig.

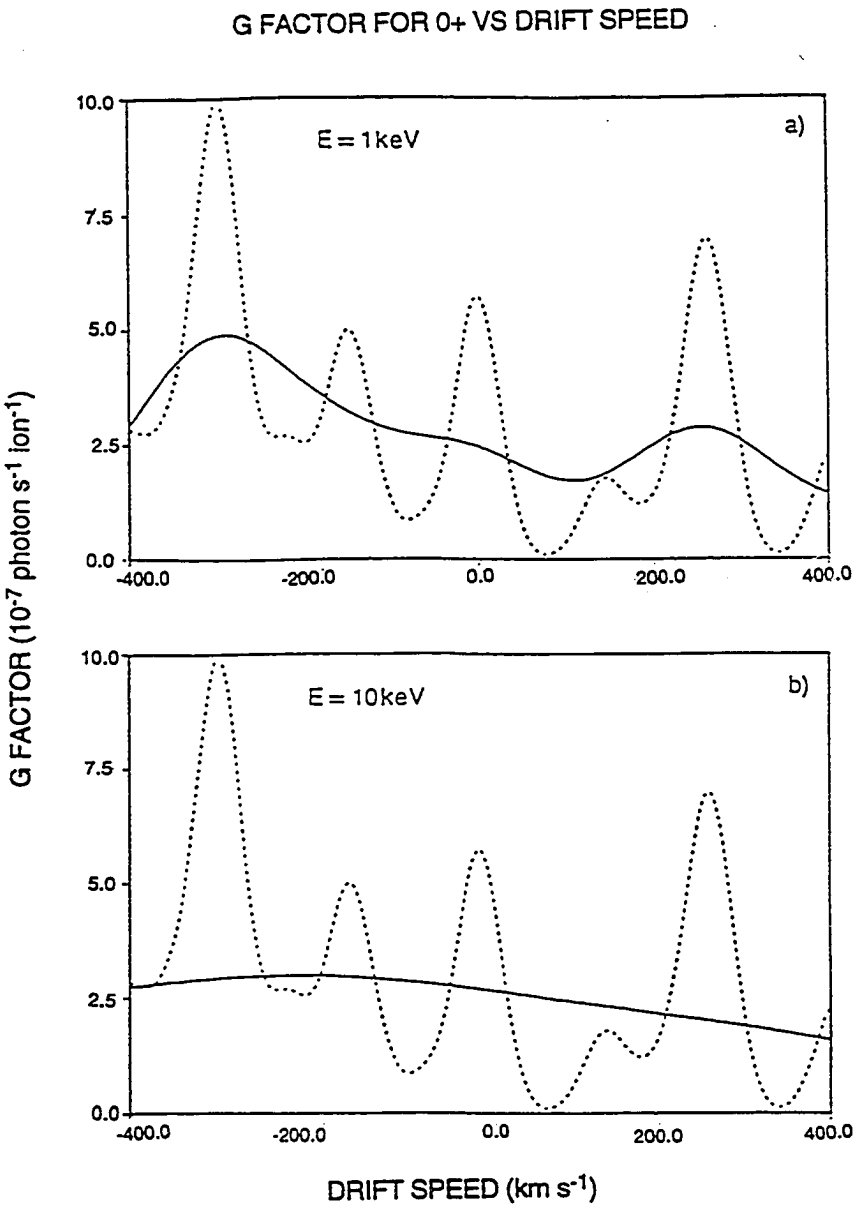

Figure 3.2 Plots of the scattering rate as a function of ion drift velocity. In all cases the dashed curve refers to the case when the plasma temperature T= 100 eV. (a) The solid curve represents the T= 1 keV case. (b) The solid curve represents the T= 10 keV case.

3.4 and Fig. 3.5. The case when v_p=-300 km s^{-1} indicates a maximum value for the scattering rate when T=1 keV and this results in a relatively brighter image.

3.4 Simulation of Magnetospheric Images Using O^+ Emissions

Simulations of global images of the magnetosphere were obtained by Swift et al. (1989) by using resonantly scattered emissions from O^+ ions in the 83.4 nm wavelength band. The images obtained were based on a higher value of the scattering rate than that used here in our simulations. They used a simple model for the O^+ number density and an assymetric radiation belt on dipole magnetic field lines. However, the global features of the magnetosphere that depend on plasma bulk velocity and temperature variations were not analyzed. Due to the unavailability of data at that time on a well resolved solar profile, it was difficult to ascertain the correct line shapes to use in the simulations. The temperatures of the ions in the chromosphere were assumed by Swift et al. (1989) to be of the order of 10^4 K which corresponds to a line width that is much smaller than that used in this paper. In this section, we incorporate the effects of temperature variation and plasma drift speeds on the magnetospheric images. Our model assumes a symmetric dipole field where the geographic and magnetic coordinates coincide. The equation for the magnetic dipole lines of force is given by (Roederer, 1970),

$$r = r_0 \cos^2(\lambda), \tag{3.11}$$

where r_0 is a constant of integration and λ is the magnetic latitude. If we let

$$r_0 = LR_e \tag{3.12}$$

where (R_e=Earth radii), and L the distance of the field line at equatorial crossing in

units of Earth radii, we obtain

$$R = r/R_e = L\cos^2(\lambda). \tag{3.13}$$

The lines of force intersect the surface of the Earth at latitudes given by

$$\cos(\lambda_e) = 1/\sqrt{L}. \tag{3.14}$$

The radiation belt is assumed to extend from L=3 to L=15 with a density profile that varies as

$$n = 1/L \quad (\text{ions cm}^{-3}) \tag{3.15}$$

with a uniform plasma temperature of 10 keV. By assuming the radiation belt (Hess, 1968) to extend between L values of 3 and 15 we have neglected contributions coming from the plasmasphere. The form of the density profile and the extent of the radiation belt is a crude assumption used to illustrate the dipole structure present in the magnetospheric image as illustrated in Fig. 3.3 Case 1, which is discussed below. Uniform L shell populations have been imposed without regard to any redistribution which might occur due to subsequent motions. The plasma sheet is assumed to have the ellipsoidal form

$$\frac{(x+20)^2}{(20)^2} + \frac{y^2}{(15)^2} + \frac{z^2}{(3)^2} = 1 \tag{3.16}$$

with a uniform density of 0.1 cm^{-3}, (Lennartson et al., 1986). The contributions of the ionospheric plasma are blanked out because the ion number densities are much larger than those in the radiation belts and plasma sheet, and this would make it difficult to view the dimmer portions of the magnetosphere. We assume that the Earth hides the plasma behind it from the Sun. In describing our simulation images we denote the satellite positions by cartesian solar magnetospheric coordinates (X_0,Y_0,Z_0) measured in Earth radii. The positive X axis points in the sunward direction and the Z axis is perpendicular to the solar ecliptic plane. The view direction is denoted by coordinates (X_1,0,0). The view direction is represented by a vector directed from the observer's position towards the point (X_1,0,0).

In Figs. 3.3a to 3d we show the grey scale images of the magnetosphere for four different satellite positions. Frame (a) Case 1, is described by the coordinates (X_0=20, Y_0=0, Z_0=0) with view direction at (X_1=0). Frame (b) Case 2, is described by coordinates (X_0=20, Y_0=5, Z_0=-50) also viewing at X_1=-10. Another look at the magnetosphere is shown in frame (c) Case 3 and frame (d) Case 4, which are described by coordinates (X_0=0, Y_0=-10, Z_0=-50, X_1=-10) and (X_0=20, Y_0=10, Z_0=40, X_1=-10), respectively.

In Fig. 3.3, Frame (a) defines Case 1 indicating that the observer has coordinates (20,0,0) (measured relative to the center of the Earth) and is located at 20 Earth radii on the sunward side and viewing directly towards the center of the Earth. We assume that when the picture of the magnetosphere was taken the radiation belt ions have a temperature of 10 keV while the ions in the plasma sheet have T=1 keV. The drift velocities are assumed to be zero in both regions. The central hollow represents the Earth with a small contribution coming from extensions of the radiation belt towards the dayside. The relative brightness seen in the image decreases symmetrically along the dawn to dusk direction. The brightest portions of the ring currents begin at L=3 and the gradual decrease in brightness as we go away from the Earth is governed by the density profile of Eq. (3.15). The maximum image brightness obtained is approximately 1.33×10^{-3} Rayleighs. For Cases 2 to 4 we have also assumed the same temperature and velocity conditions for the radiation belt and plasma sheet. The grey scale bar uses a maximum intensity of 1.33×10^{-3} R and refers to Fig. 3.3a.

Another view of the magnetosphere is shown in Fig. 3.3 frame (b) defining Case 2. The observer is located at (20,5,-50). The view direction (X_1=-10) means that the satellite is looking at a distance 10 R_e behind the Earth in the magnetotail. For this view the maximum image brightness is 3.49×10^{-4} Rayleighs. The grey scale maximum of 4.19×10^{-4} R is used in this case and all other cases discussed below. The radiation belt appears to have a spherical configuration. The sunward portions of the belt appears less bright than portions tailward and the plasma sheet is dim in contrast to the radiation belt. Frames (c) and (d) represent two other viewing perspectives of the magnetosphere. The maximum image brightness are 3.28×10^{-4} and 3.74×10^{-4} R, respectively.

The different views of the magnetosphere shown in Fig. 3.3 allow us to view both the radiation belt and the plasma sheet. The shadowing of the plasma behind the Earth from sunlight is seen to start with a central dark spot representing the Earth and a dim region continuing straight down the magnetotail. The slightly enhanced brightness towards the night side is because the radiation belt and the ellipsoidal plasma sheet overlap and contributions from both regions are additive.

Effects of Doppler Shift

In Figs 3.4 to 3.5, we show how the image structure and intensity vary with changing drift speed for the view direction representing Case 4. In our model we assume that only ions in the plasma sheet are drifting while there are no plasma drifts occurring in the radiation belt. The temperature of the radiation belt ions is 10 keV and the plasma sheet ions has T=1 keV. Fig. 3.4 Frame (a) represents the image when v_p=0 (b) v_p=-100 km s^{-1} (c) v_p=-200 km s^{-1} (d) v_p=-300 km s^{-1}. We can see that as the drift velocities increase in the anti-sunward direction the plasma sheet appears to brighten gradually and begin to show more structure. The enhanced brightness can be explained by Fig. 3.2. The scattering rates for the four cases above are 2.4×10^{-7}, 2.8×10^{-7}, 3.9×10^{-7} and

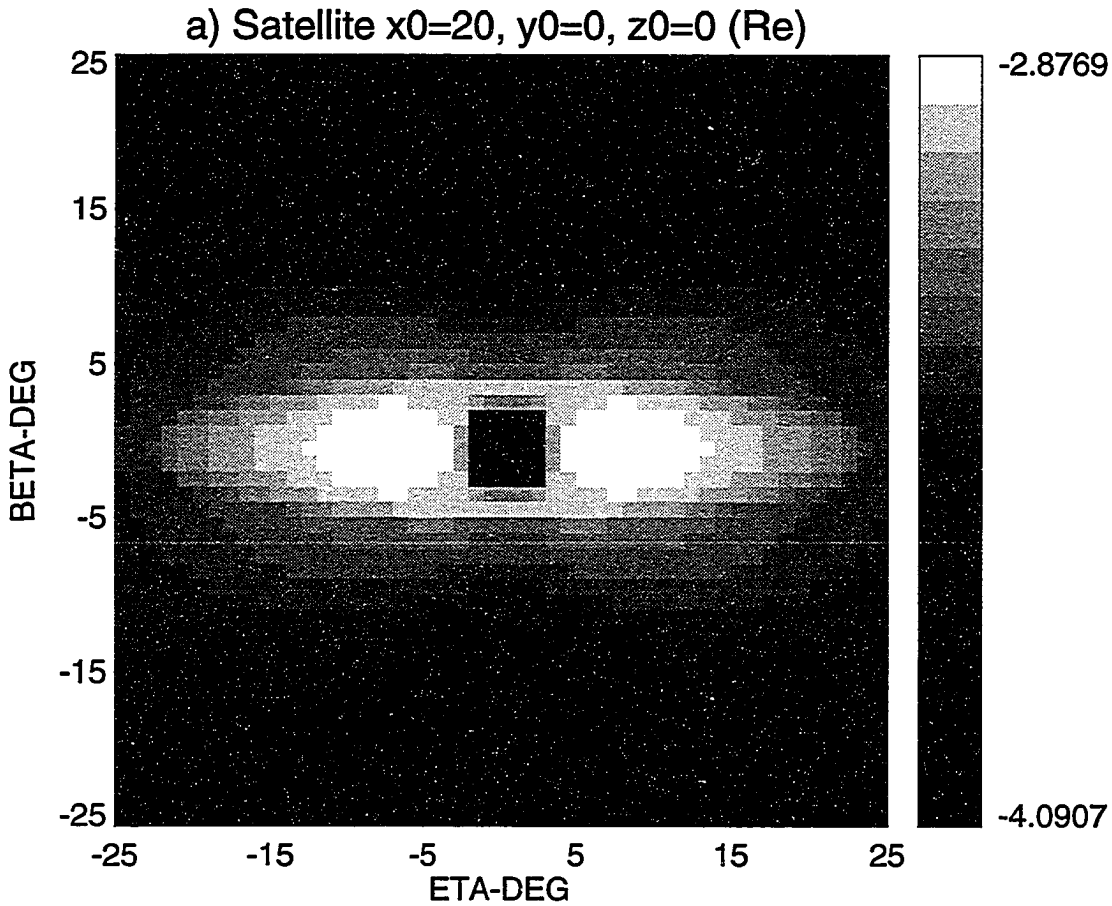

Figure 3.3a Magnetospheric image using satellite position and view direction defined for Case 1. The ions in the radiation belt are assumed to have a temperature and flow velocity of T= 10 keV and v_p= 0 while in the plasma sheet T= 1 keV and v_p= 0. The intensity is in $\log_{10}$Rayleighs. (See Sec. 3.4 for more details).

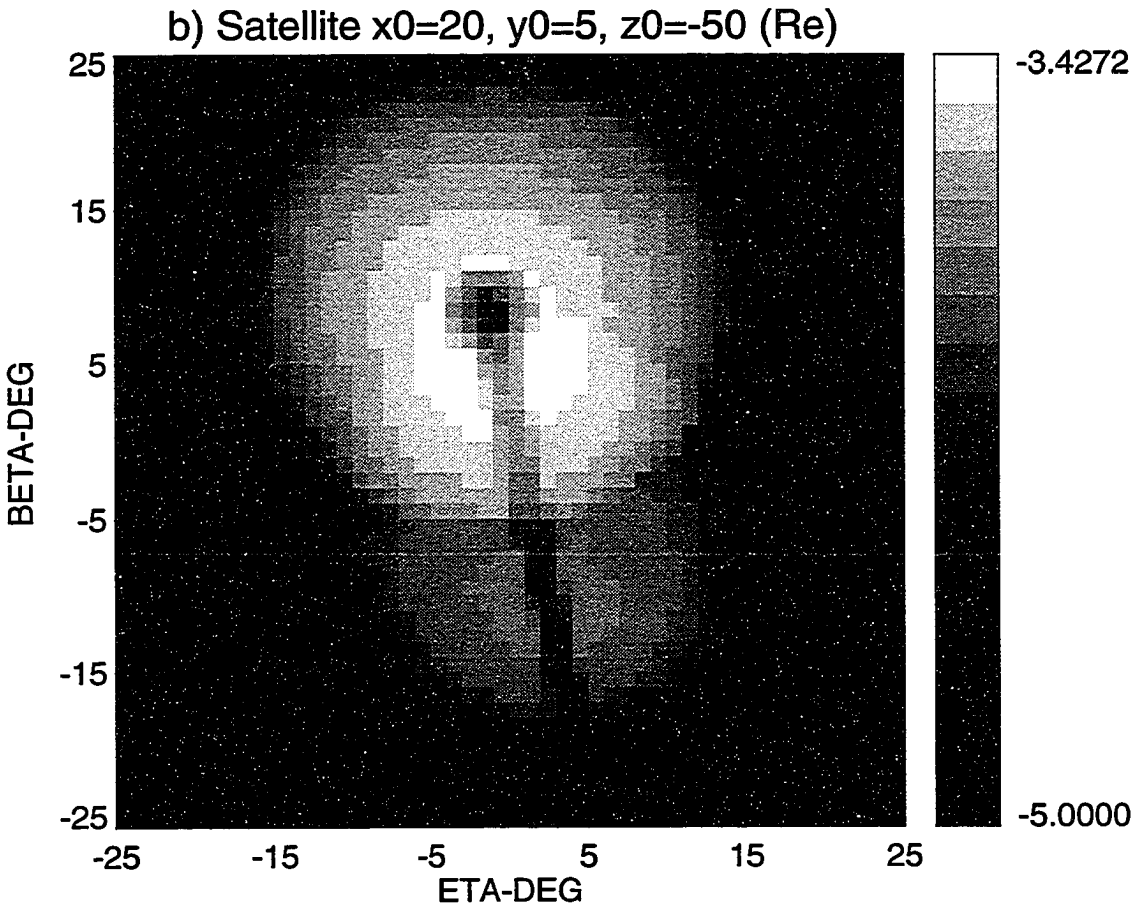

Figure 3.3b Magnetospheric image using satellite position and view direction defined for Case 2. The ions in the radiation belt are assumed to have a temperature and flow velocity of T= 10 keV and v_p= 0 while in the plasma sheet T= 1 keV and v_p= 0. (See Sec. 3.4 for more details).

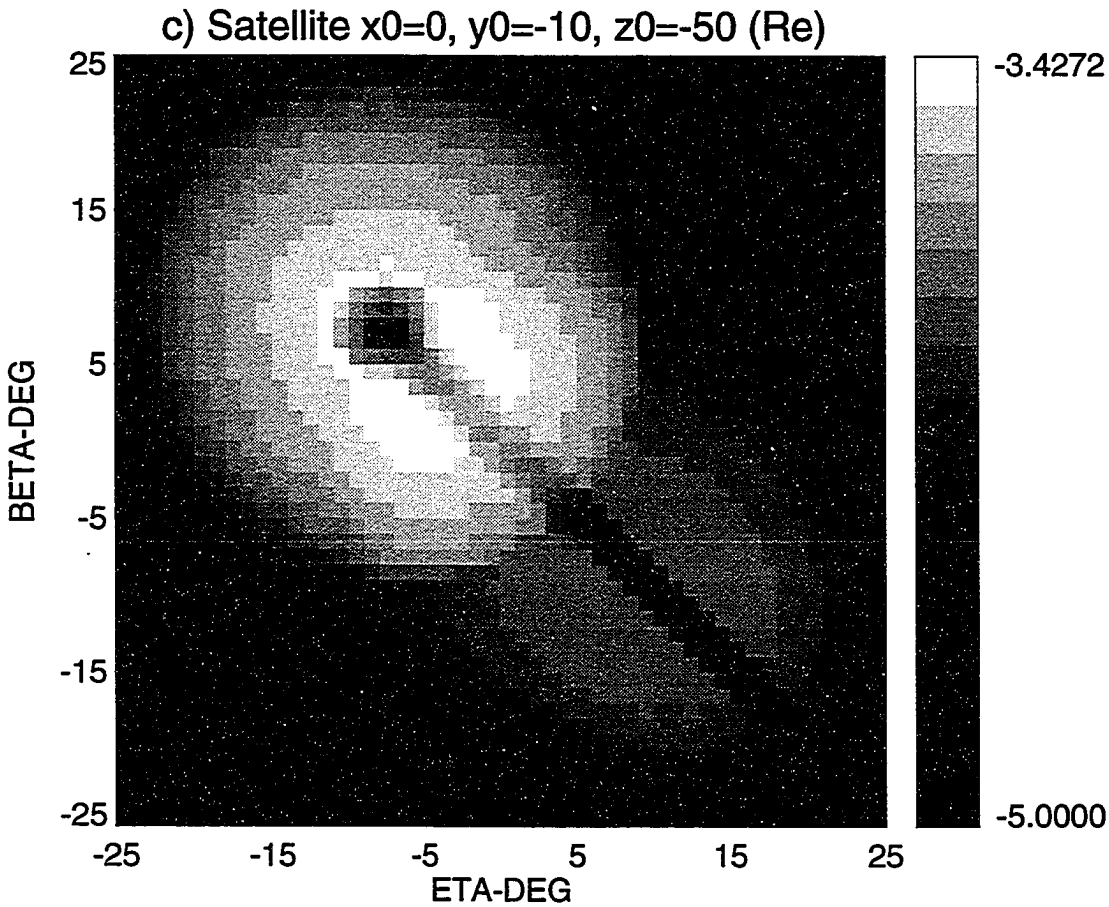

Figure 3.3c Magnetospheric image using satellite position and view direction defined for Case 3. The ions in the radiation belt are assumed to have a temperature and flow velocity of T= 10 keV and v_p= 0 while in the plasma sheet T= 1 keV and v_p= 0. (See Sec. 3.4 for more details).

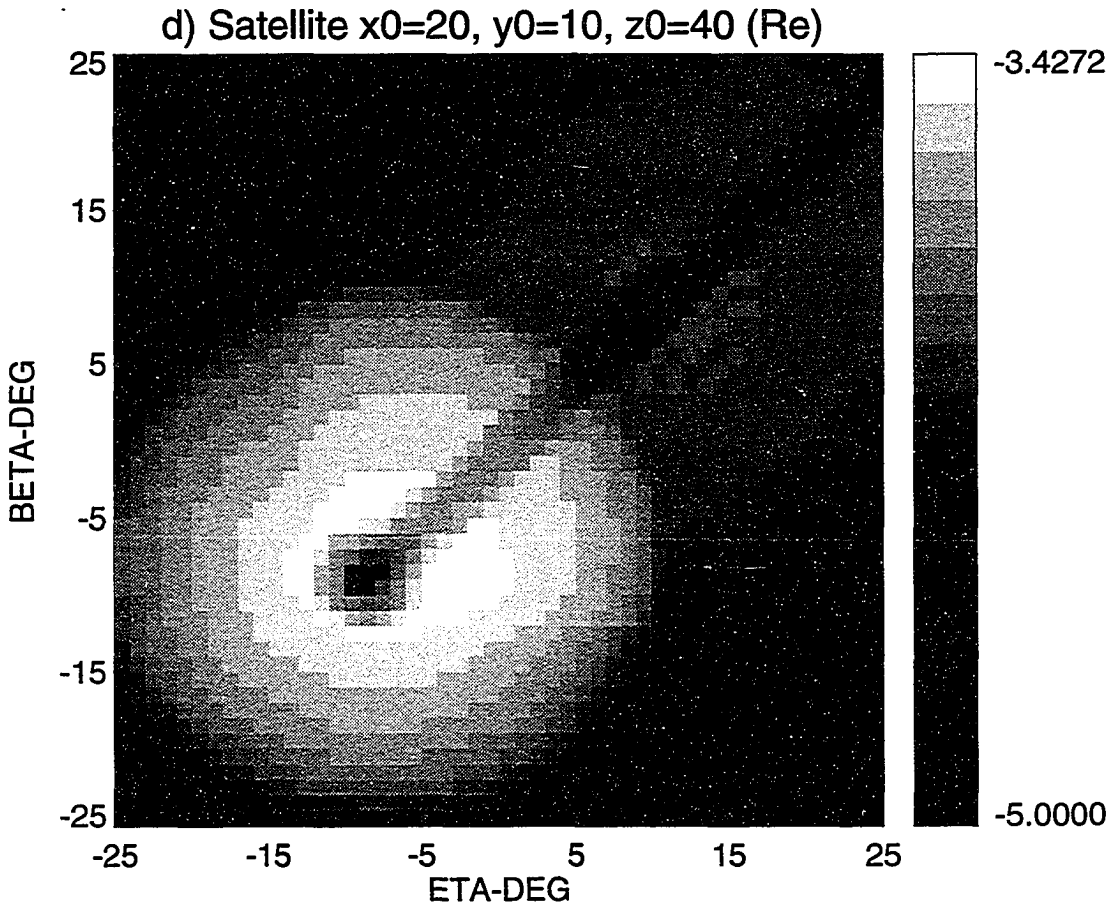

Figure 3.3d Magnetospheric image using satellite position and view direction defined for Case 4. The ions in the radiation belt are assumed to have a temperature and flow velocity of T= 10 keV and v_p= 0 while in the plasma sheet T= 1 keV and v_p= 0. (See Sec. 3.4 for more details).

4.9×10^{-7} photons s^{-1} ion^{-1}, respectively. Since the scattering rate at -300 km s^{-1} is largest the image will appear relatively bright. The maximum image brightness is given by 3.74×10^{-4}, 3.78×10^{-4}, 3.99×10^{-4} and 4.19×10^{-4} R, respectively. For positive (sunward) drift velocities the images obtained for the various flow speeds and their scattering rates in photons s^{-1} ion^{-1} are shown in Fig. 3.5 frame (a) v_p=100 km s^{-1}, g=1.7 $\times10^{-7}$ (b) v_p=200 km s^{-1}, g=2.5×10^{-7} (c) v_p= 300 km s^{-1}, g=2.6×10^{-7} (d) v_p=400 km s^{-1}, g=1.4×10^{-7}. Frame (a) shows a dim image of the plasma sheet while frames (b) and (c) show enhanced brightness of the plasma sheet as reflected from the relative values of the scattering rates. The maximum image brightness obtained is given by 3.60, 3.73, 3.74 and 3.55 times 1×10^{-4} rayleighs, respectively.

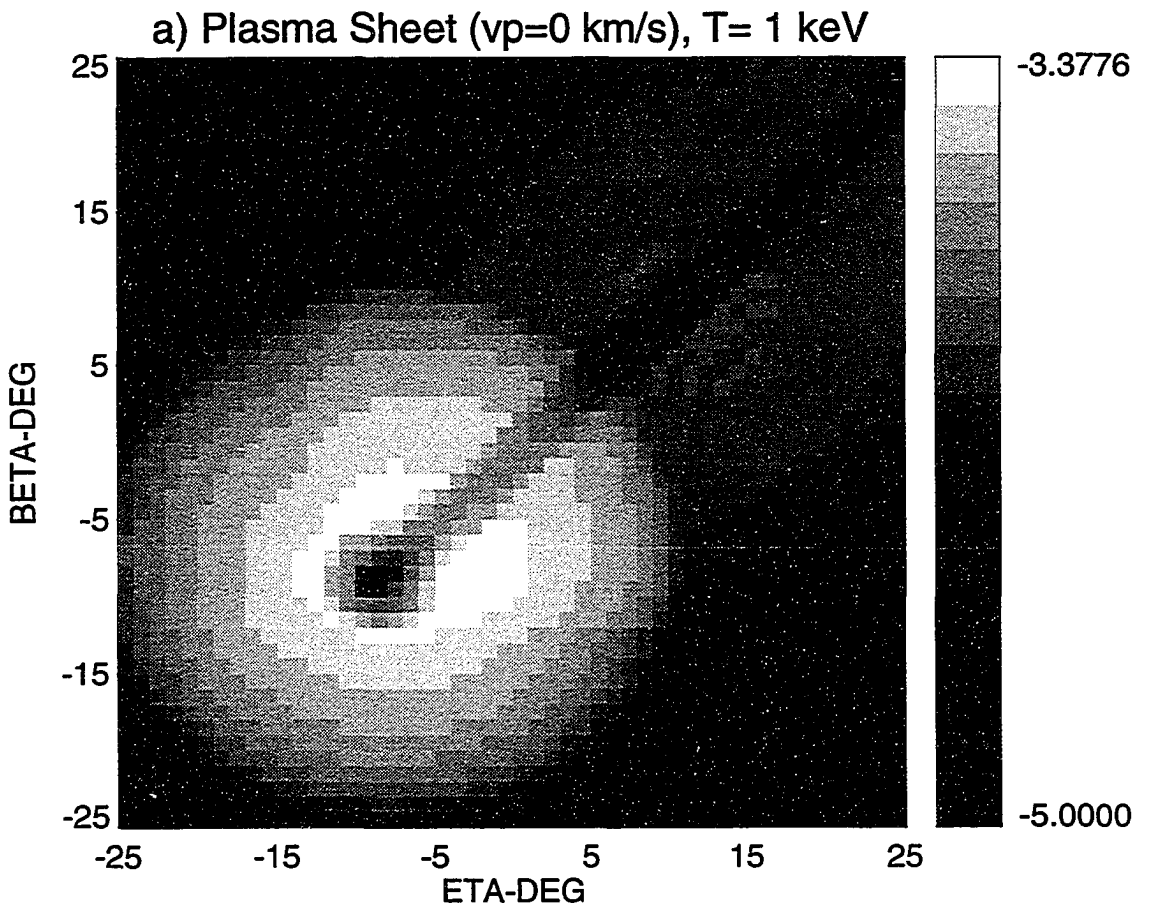

Figure 3.4a Variation of the magnetospheric image when ions in the plasma sheet have an anti-sunward flow velocity v_p= 0 (Case 4). Its temperature is assumed to be 1 keV. The ions in the radiation belt are assumed to have T= 10 keV and v_p= 0.

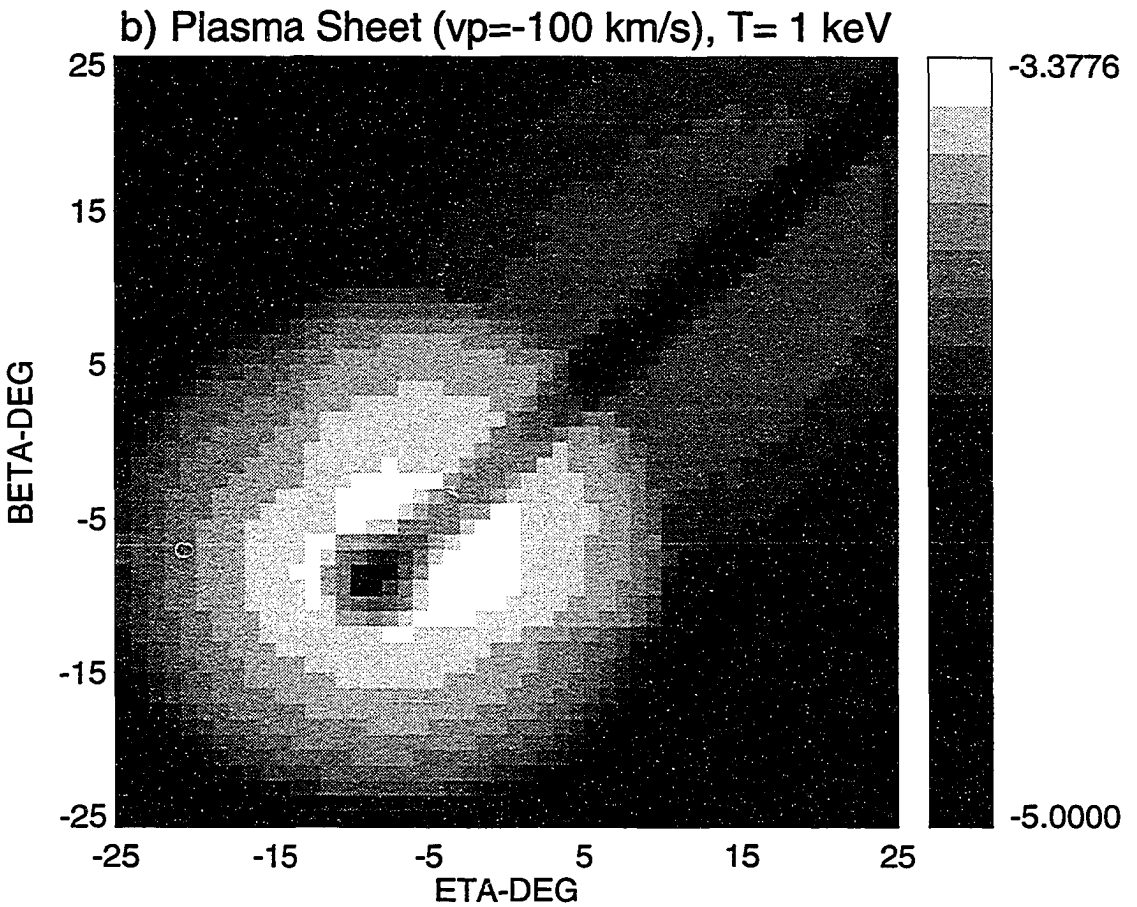

Figure 3.4b Variation of the magnetospheric image when ions in the plasma sheet have an anti-sunward flow velocity v_p= -100 km s^{-1} (Case 4). Its temperature is assumed to be 1 keV. The ions in the radiation belt are assumed to have T= 10 keV and v_p= 0.

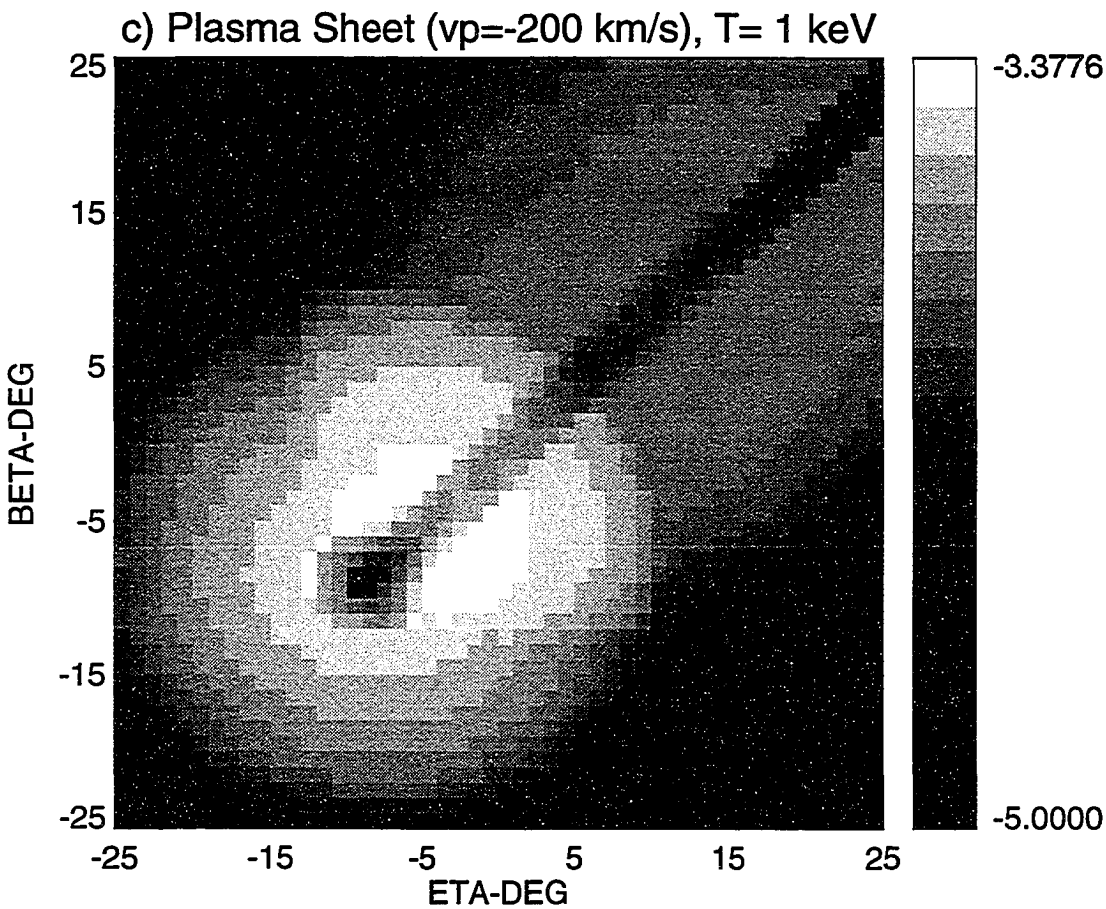

Figure 3.4c Variation of the magnetospheric image when ions in the plasma sheet have an anti-sunward flow velocity v_p= -200 km s^{-1} (Case 4). Its temperature is assumed to be 1 keV. The ions in the radiation belt are assumed to have T= 10 keV and v_p= 0.

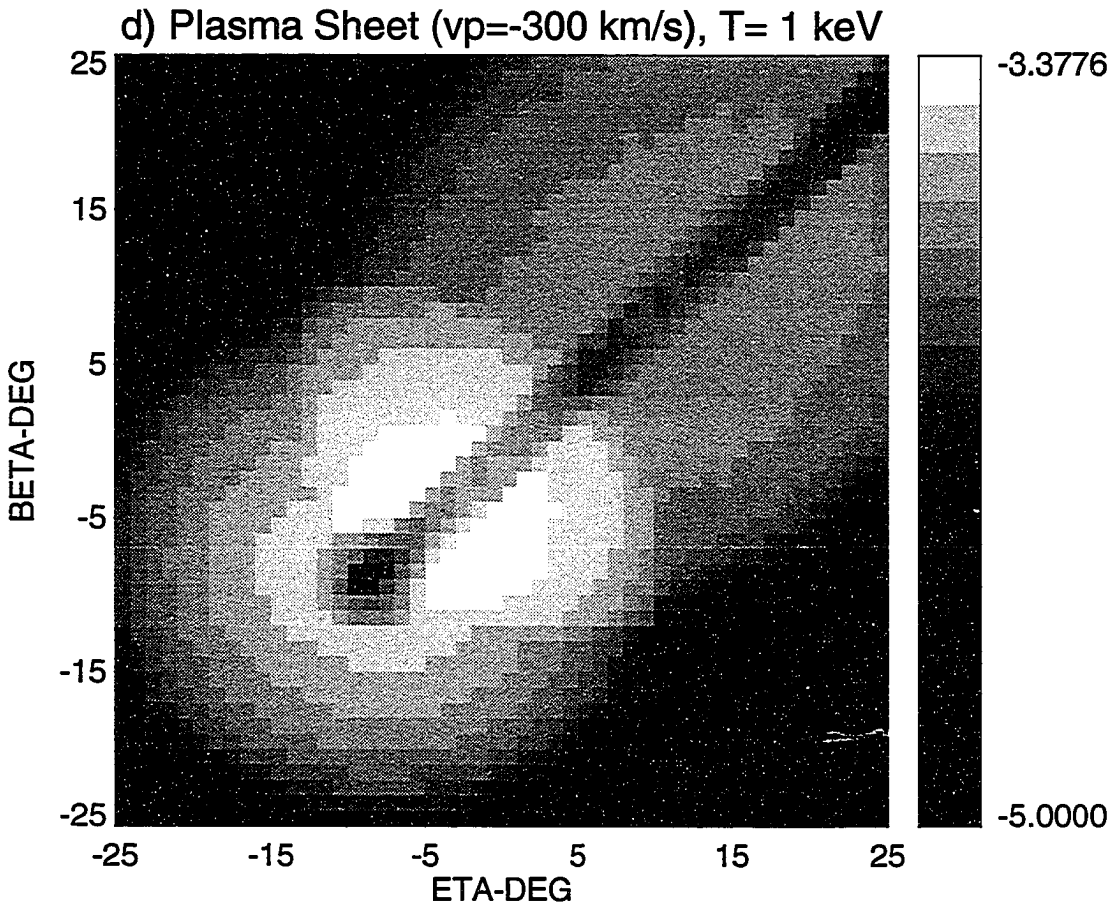

Figure 3.4d Variation of the magnetospheric image when ions in the plasma sheet have an anti-sunward flow velocity v_p= -300 km s^{-1} (Case 4). Its temperature is assumed to be 1 keV. The ions in the radiation belt are assumed to have T= 10 keV and v_p= 0.

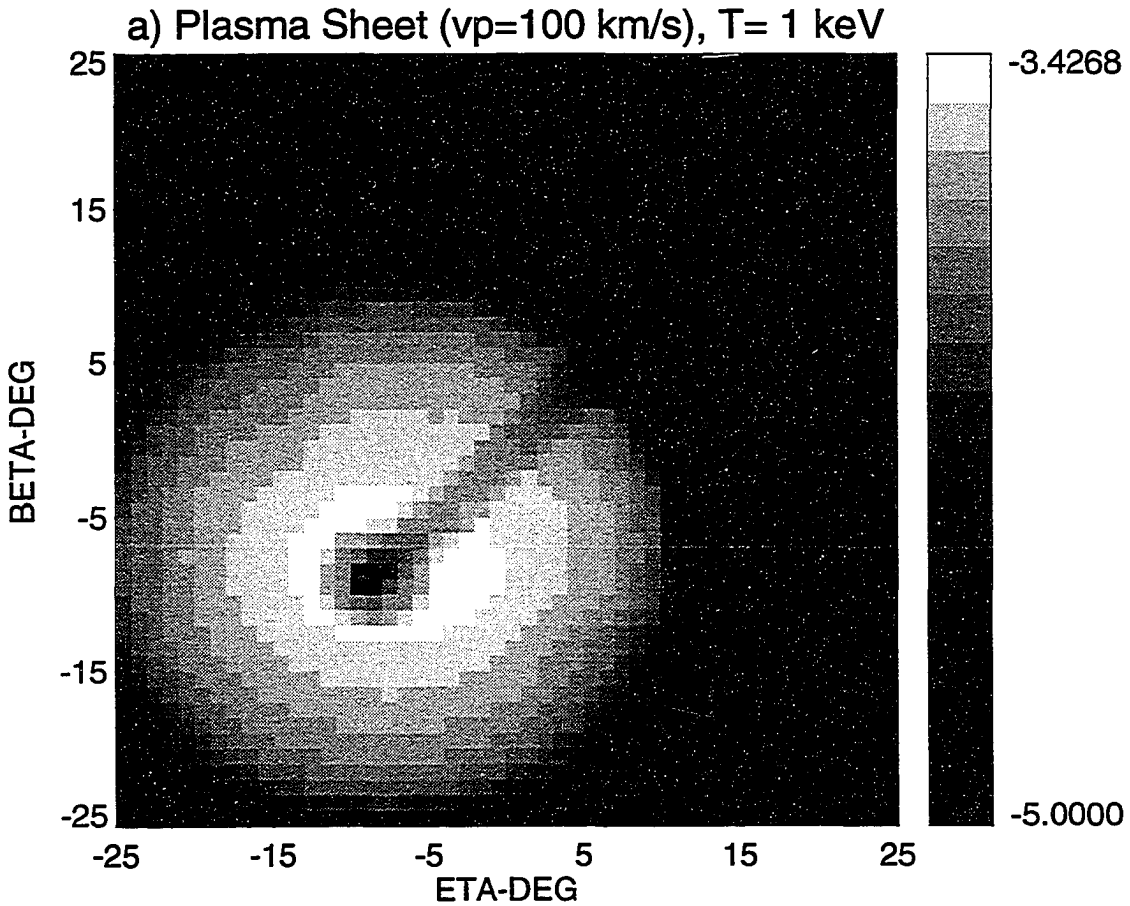

Figure 3.5a Variation of the magnetospheric image when ions in the plasma sheet have a positive (sunward) flow velocity v_p= 100 km s^{-1} (Case 4). The ions are assumed to have T= 1 keV while the ions in the radiation belt are assumed to have T= 10 keV and v_p= 0.

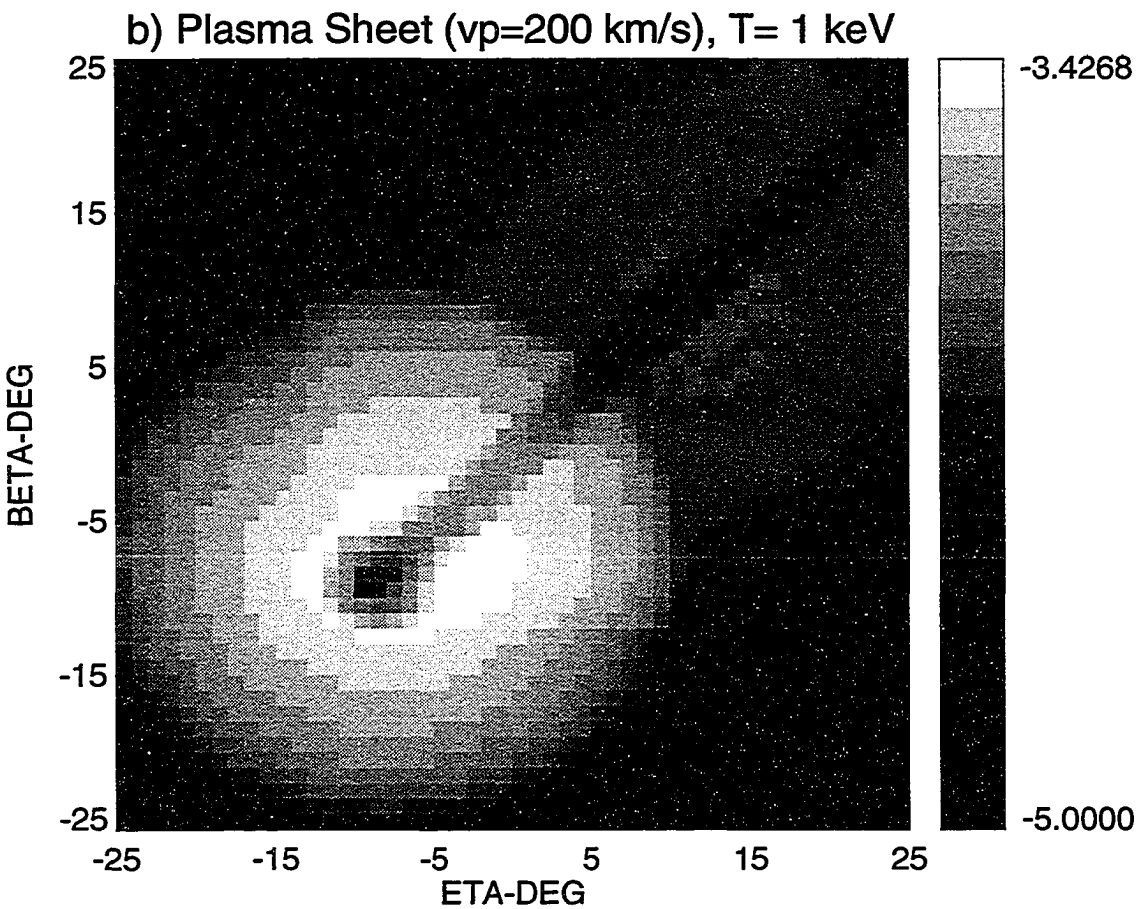

Figure 3.5b Variation of the magnetospheric image when ions in the plasma sheet have a positive (sunward) flow velocity v_p= 200 km s^{-1} (Case 4). The ions are assumed to have T= 1 keV while the ions in the radiation belt are assumed to have T= 10 keV and v_p= 0.

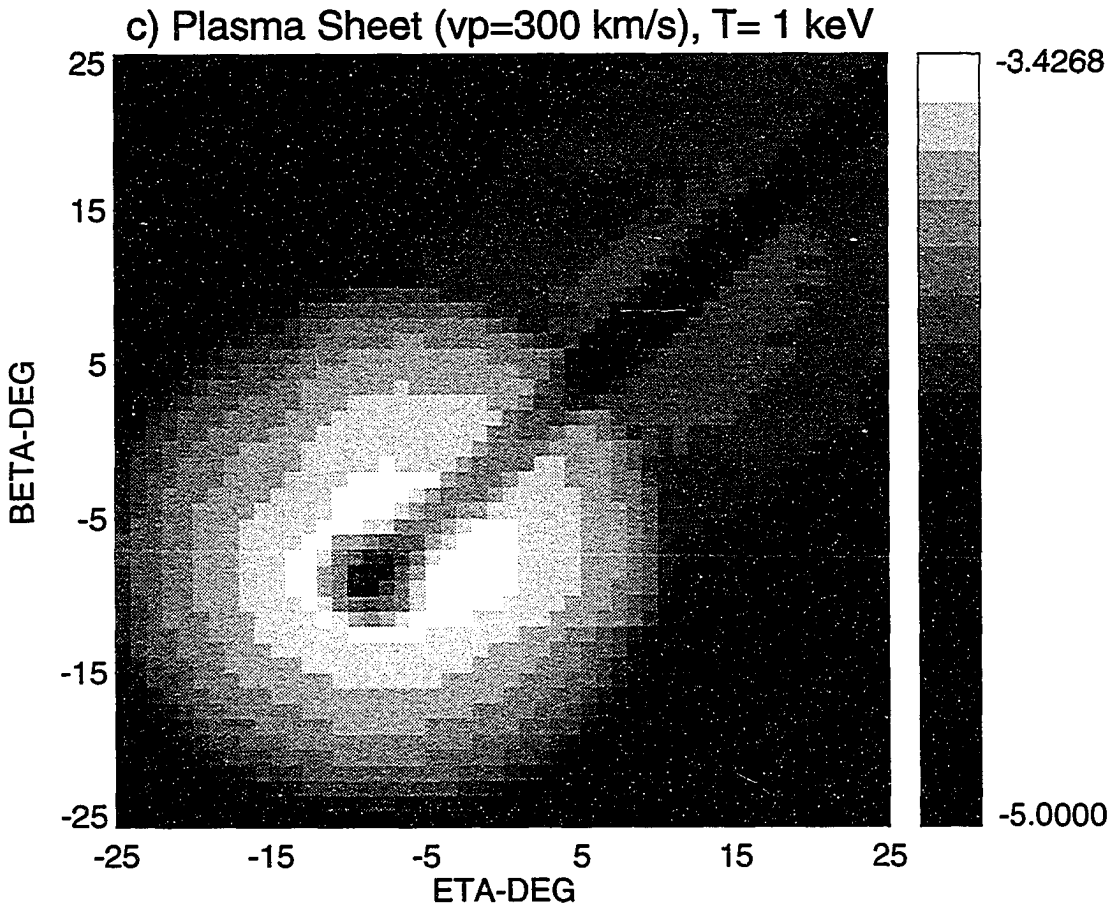

Figure 3.5c Variation of the magnetospheric image when ions in the plasma sheet have a positive (sunward) flow velocity v_p= 300 km s^{-1} (Case 4). The ions are assumed to have T= 1 keV while the ions in the radiation belt are assumed to have T= 10 keV and v_p= 0.

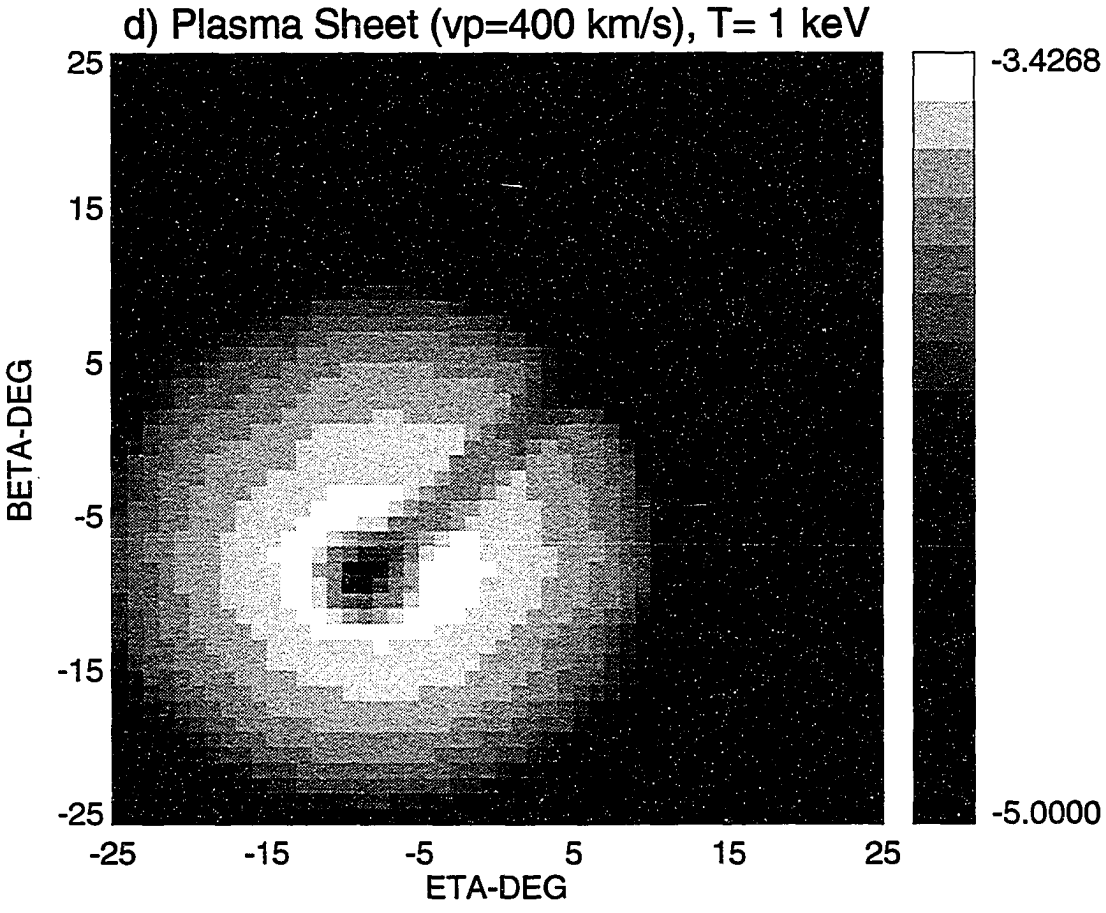

Figure 3.5d Variation of the magnetospheric image when ions in the plasma sheet have a positive (sunward) flow velocity v_p= 400 km s^{-1} (Case 4). The ions are assumed to have T= 1 keV while the ions in the radiation belt are assumed to have T= 10 keV and v_p= 0.

Temperature Variations

The survey of the plasma sheet ion composition done by Lennartson et al. (1986) indicated an average O^+ ion number density of 0.1 cm^{-3}. However, their instrument selected ion energies in the keV range excluding any 'cold ions' in their results. Hence, we have no direct evidence of the cold ion density. We fixed the plasma sheet temperature at 1 keV and allowed the plasma temperature to vary in the radiation belt. The flow velocities are assumed to be zero. The results of the simulations are shown in Fig. 3.6 for Case 2 where Frame (a) T=1 keV (b) T=4 keV (c) T=8 keV (d) T=10 keV. The scattering rates calculated for the radiation belt are 2.45, 2.57, 2.69 and 2.67 times 1×10^{-7} photons s^{-1} ion^{-1}, respectively. The image brightness is almost constant for temperature variations from T=1 keV to T=10 keV. Our simulations indicate the maximum intensities to be 3.24, 3.38, 3.51 and 3.49 times 1×10^{-4} rayleighs, respectively for the four frames above.

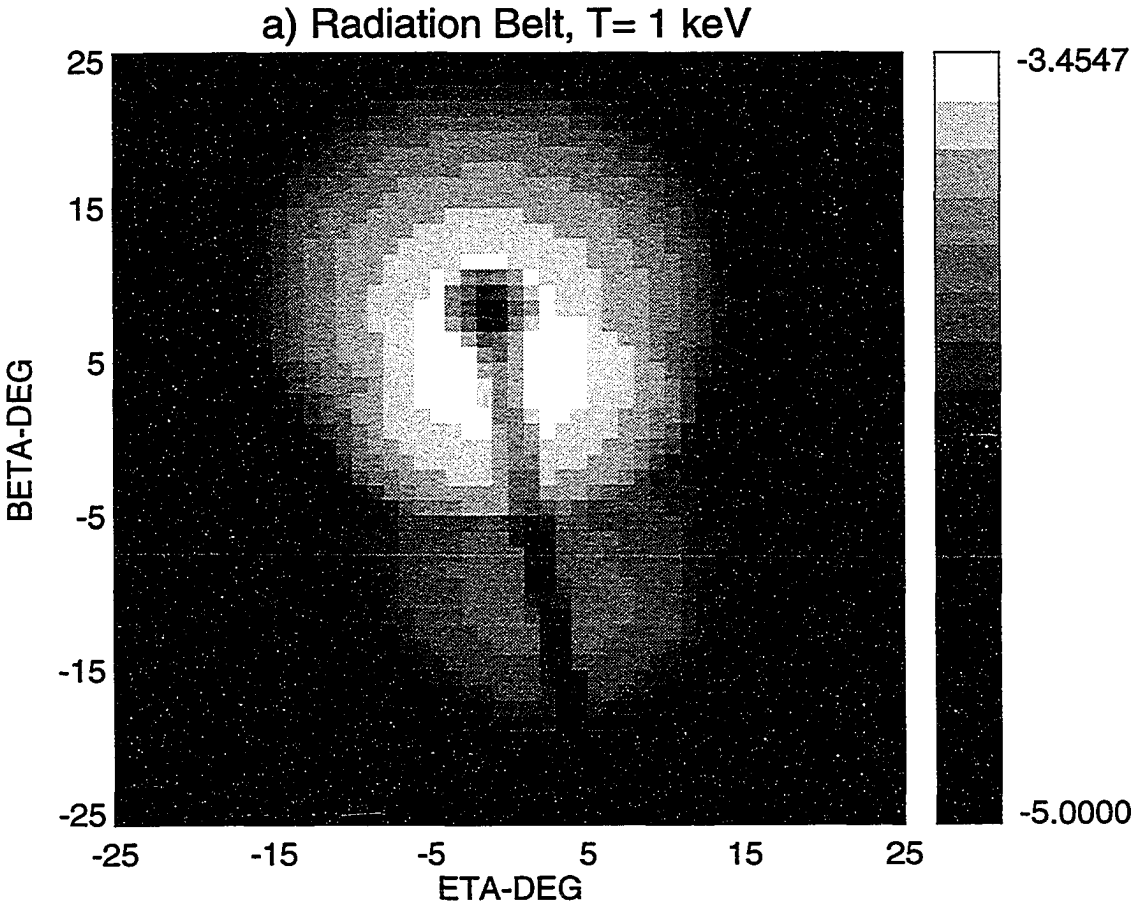

Figure 3.6a Effects of temperature broadening on the magnetospheric image (Case 2, T= 1 keV). The plasma sheet ions are assumed to have a plasma temperature and flow velocity of T= 1 keV and v_p= 0 while in the radiation belt the temperature is allowed to vary. The flow velocity in the radiation belt is taken to be zero.

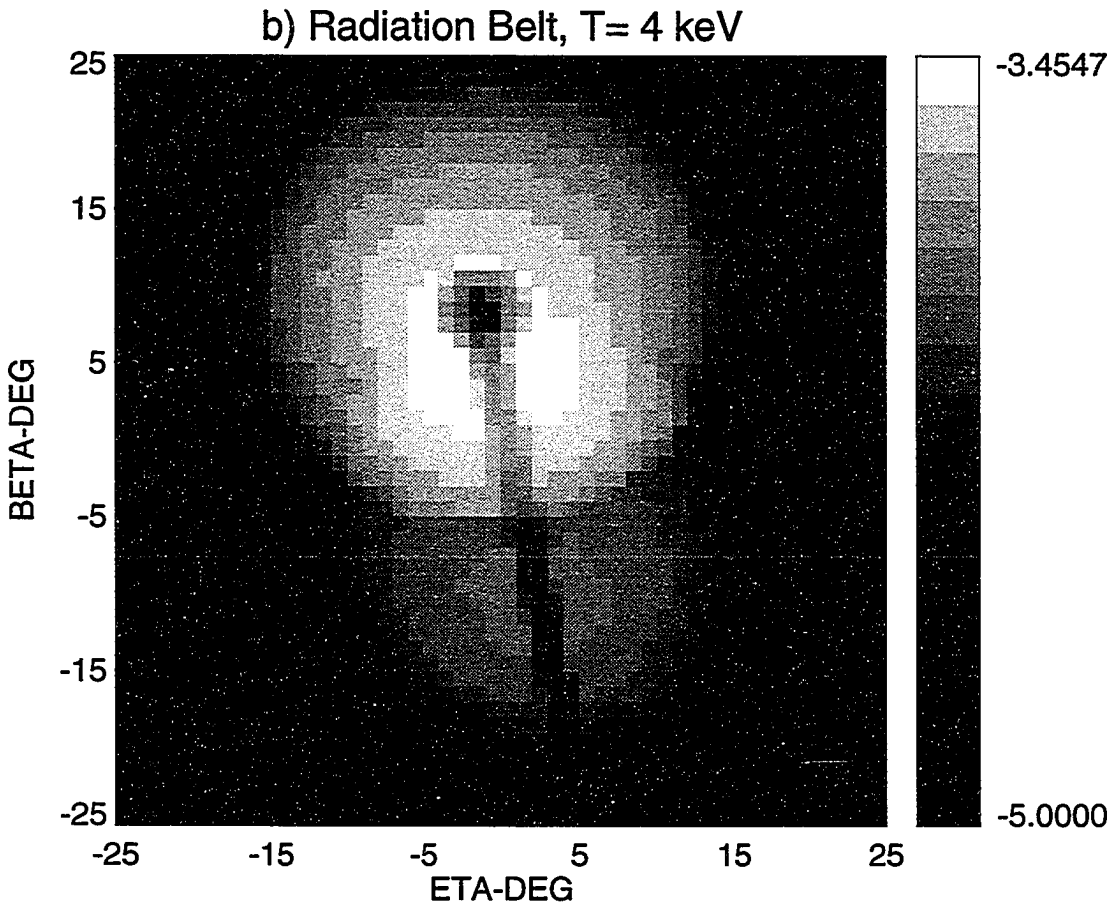

Figure 3.6b Effects of temperature broadening on the magnetospheric image (Case 2, T= 4 keV). The plasma sheet ions are assumed to have a plasma temperature and flow velocity of T= 1 keV and v_p= 0 while in the radiation belt the temperature is allowed to vary. The flow velocity in the radiation belt is taken to be zero.

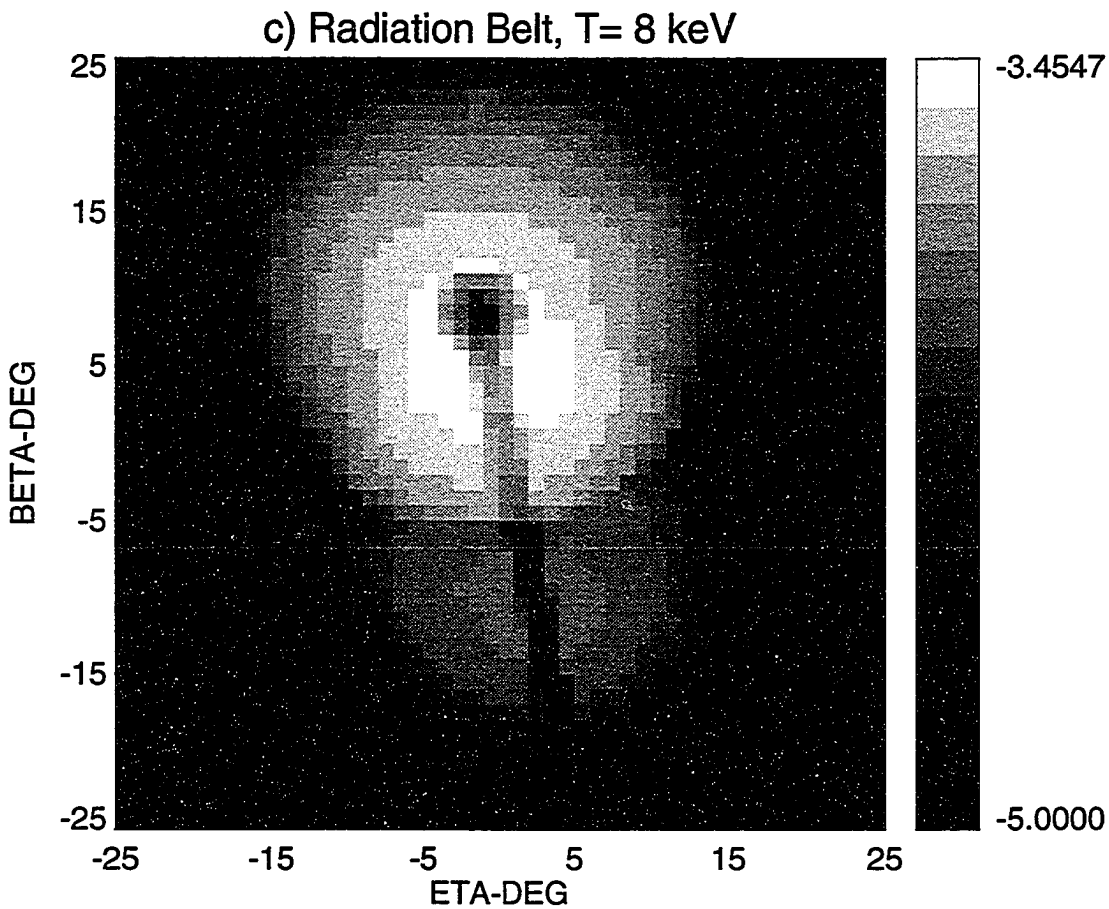

Figure 3.6c Effects of temperature broadening on the magnetospheric image (Case 2, T= 8 keV). The plasma sheet ions are assumed to have a plasma temperature and flow velocity of T= 1 keV and v_p= 0 while in the radiation belt the temperature is allowed to vary. The flow velocity in the radiation belt is taken to be zero.

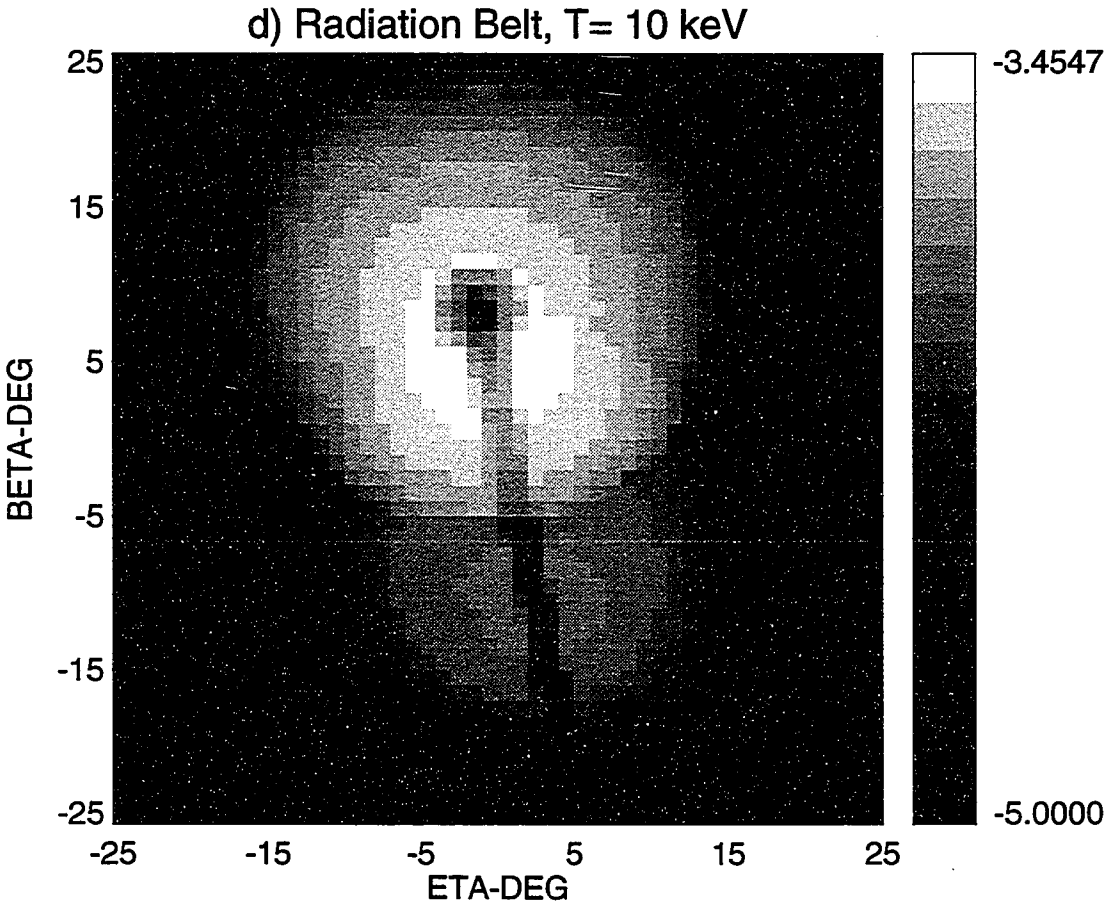

Figure 3.6d Effects of temperature broadening on the magnetospheric image (Case 2, T= 10 keV). The plasma sheet ions are assumed to have a plasma temperature and flow velocity of T= 1 keV and v_p= 0 while in the radiation belt the temperature is allowed to vary. The flow velocity in the radiation belt is taken to be zero.

Imaging the Radiation Belt and Plasma Sheet

One of the objectives of the above analysis is to determine the feasibility of imaging the magnetosphere in the scattered light of O^+. A useful way to summarize the results is to calculate the size of the collecting aperture needed to image the magnetosphere under various circumstances. Assuming a substorm time scale of 1 hour, we shall adopt 1000 sec as a minimal time resolution. The camera is assumed to employ spectrally selective multilayer mirrors of sufficiently narrow passband that no further filtering is required. (Recent work by Seeley (private communication) shows that this is likely to admit an unacceptable amount of Lyman-α contamination). We further assumed an optical transmission of 30% and a detector counting efficiency of 10%, giving an overall system efficiency of 3%.

Using a realistic value of 10 keV for the temperature of the ions in the radiation belt and a plasma sheet temperature of 1 keV, a simulation image was performed for the view direction given by Case 4 using an aperture of 750 cm^2. A randomized image using Poissonian statistics is shown in Fig. 3.7 demonstrating the expected quality for the particular instrument parameters.

3.5 Possible Contributions From O^{++} Ions

The global images of the magnetosphere that we have obtained depended solely on contributions from the O^+ ions. Contributions from the O^{++} ions have been neglected. Results of a model calculation by Chandler (1987) suggest that the O^{++} density is about a factor 20 lower than the O^+ density. However, under certain solar and magnetospheric conditions, if the O^{++} number density becomes comparable to that of O^+ it can contribute to an overall larger emission rate.

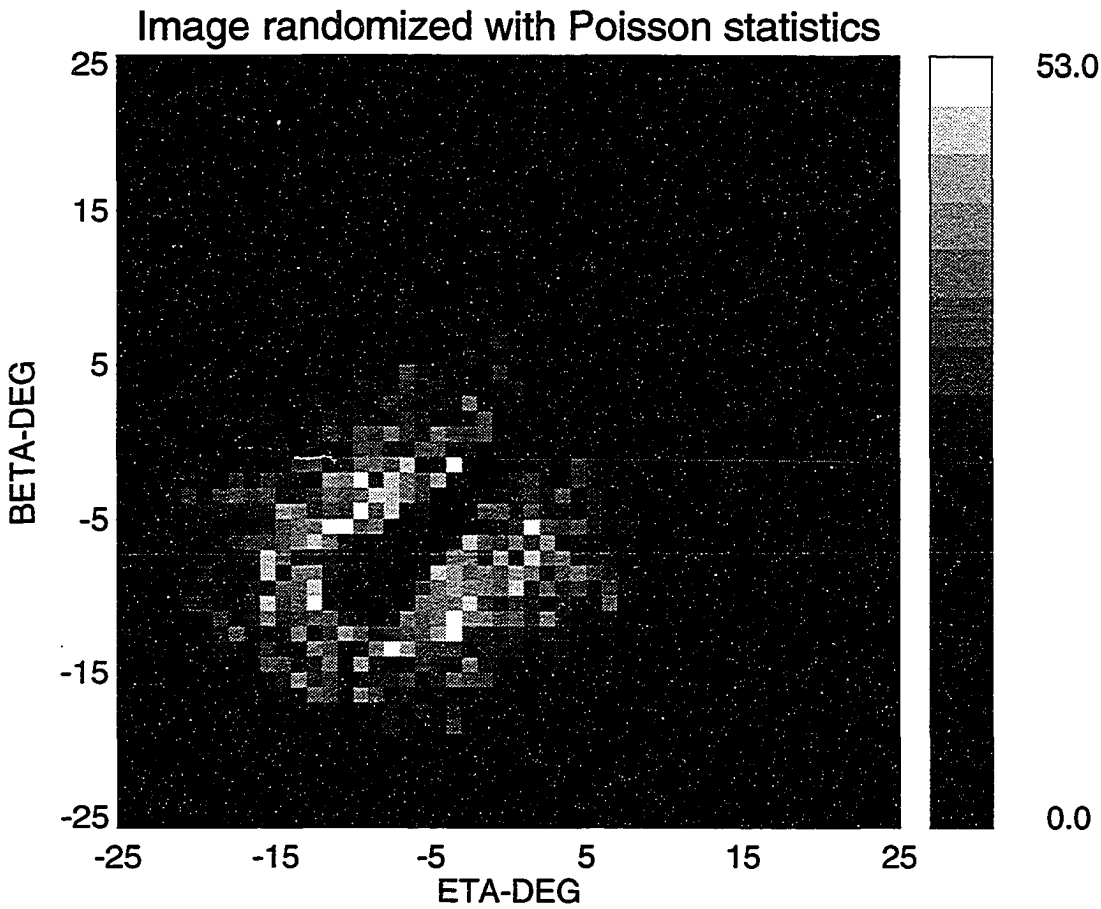

Figure 3.7 The image quality of the radiation belt and plasma sheet as seen with an aperture size of 750 cm^2 (Case 4). The radiation belt ions have T= 10 keV while the plasma sheet ions have T= 1 keV. All flow velocities are assumed zero. The effect of photon statistics on the image quality indicates a maximum of 53 counts for a given pixel at the detector. The scale shown is linear.

3.6 Conclusion

We have investigated the effects of Doppler shift on the line centers of the magnetospheric O^+ cross-section, and explained the resulting structure of the scattering rate as a function of bulk velocity. Whereas the Doppler shift frequently results in a decrease of the scattering rate, it has been demonstrated that for certain drift speeds, the overlap of the cross-section and the solar intensity profile can lead to an increased rate thus enhancing the relative brightness of the image above that obtained when v_p is zero.

Using a dipole field configuration for the magnetic field and a simple model of the O^+ number density profile we are able to obtain simulated images of the magnetosphere and show quantitatively how the magnetospheric image responds to variations in plasma drift speed and temperature. Changes in the brightness of the magnetospheric images will also depend on the variability of the solar flux at 83.4 nm. Assuming a fixed temperature, in regions where there are plasma drifts the brightness in the image is governed by the structure of the scattering rate.

To illustrate how an instrument would respond to a typical magnetospheric source brightness we have shown a randomized image of the radiation belt and plasma sheet. This demonstrates that gross features of those regions can be seen using a camera aperture of at least 750 cm^2.

3.7 Appendix

Analysis of the Cross Section

Because of the ion's thermal speed, the absorption cross-section of a hot plasma containing O^+ ions for a particular line transition will be broadened. Consider an O^+ ion with a temperature T_i and mass m_o. It will have a thermal speed

$$u_i = \sqrt{2kT_i/m_o}. \qquad (A-1)$$

If ν_{0i} is the frequency of radiation emitted by a stationary source then the frequency of radiation absorbed in the rest frame of the ion is given by

$$\nu = \nu_{0i}(1 + v/c). \qquad (A-2)$$

The absorption cross-section is assumed to have a gaussian form

$$\sigma_i^a = c_i e^{-\frac{v^2}{u_i^2}}. \qquad (A-3)$$

Solving for the velocity in (A-2), we get

$$\sigma^a(\nu) = \sum_i c_i e^{-\frac{c^2}{u_i^2 \nu_{0i}^2}(\nu-\nu_{0i})^2}, \qquad (A-4)$$

where the constants c_i are obtained as follows; from Rees (1989), we use the following expressions

$$\sigma_i^a(\nu) = \frac{c^2}{8\pi}\frac{w_u}{w_l}\frac{1}{\nu^2}A_{lu}^i\phi_i(\nu), \qquad (A-5)$$

where

$$\int_{-\infty}^{\infty}\phi_i(\nu)\,d\nu = 1 \qquad (A-6)$$

w_u and w_l are statistical weights of the upper and lower levels for a particular transition and $\phi_i(\nu)$ is the normalized spectral intensity distribution. A_{lu} is the Einstein

coefficient for the transition from upper to lower levels.The normalization for σ_i^a is given by

$$\int_0^\infty \sigma_i^a \, d\nu = \frac{\pi e^2}{m_e c} f_i, \qquad (A-7)$$

where (f_i) is the oscillator strength for the emission of radiation with frequency ν_{0i}. We can obtained A_{lu} by requiring (A-6) to be satisfied, ie.

$$\int_{-\infty}^\infty \frac{c^2}{8\pi} \frac{w_u}{w_l} \frac{A_{lu}}{\nu^2} \frac{m_e c}{\pi e^2 f_i} \phi_i(\nu) \, d\nu = 1 \qquad (A-8)$$

to get

$$A_{lu} = \frac{\pi e^2}{m_e c} f_i \frac{8\pi}{c^2} \frac{w_l}{w_u} \nu^2. \qquad (A-9)$$

Now, using (A-9) into (A-5) we get the result

$$\sigma_i^a(\nu) = \sigma_i \phi_i(\nu) \qquad (A-10)$$

where

$$\sigma_i = \frac{\pi e^2}{m_e c} f_i. \qquad (A-11)$$

Our absorption cross-section profile can then be expressed as a sum of the individual profiles composed of O^+ transitions belonging to the 83.4 nm band. Hence,

$$\sigma^a(\nu) = \sum_i \sigma_i \phi_i(\nu) \qquad (A-12)$$

with

$$\phi_i(\nu) = \kappa_{0i} e^{-\frac{c^2}{u_i^2 \nu_{0i}^2}(\nu - \nu_{0i})^2}. \qquad (A-13)$$

Normalizing $\phi_i(\nu)$ we get

$$\kappa_{0i} = \frac{c}{u_i \nu_{0i} \sqrt{\pi}}. \qquad (A-14)$$

Finally, the absorption cross-section profile is given by

$$\sigma^a(\nu) = \sum_{i=1}^{3} \sigma_i \kappa_{0i} e^{-\frac{c^2}{u_i^2 \nu_{0i}^2}(\nu - \nu_{0i})^2}. \qquad (A-15)$$

The absorption cross-section at line center is then given by the expression $\sigma_{0i} = \sigma_i \kappa_{0i}$ which specifies the constants c_i.When a parcel of plasma is drifting with a bulk velocity

v_p relative to the emitting source, the frequency center of the cross-section profile is shifted by an amount

$$\nu_i = \nu_{0i}(1 + v_p/c).$$

The Doppler shifted cross-section can now be expressed as

$$\sigma_d^a(\nu) = \sum_{i=1}^{3} \sigma_i \kappa_{0i} e^{-\frac{c^2}{u_i^2 \nu_{0i}^2}(\nu - \nu_i)^2}. \qquad (A-16)$$

Calculation of the Scattering Rate

The scattering rate (photons per sec per ion) or the g factor is calculated from the expression

$$g(v_p) = \int_{-\infty}^{\infty} \sigma_d^a(v_p, \nu)\, I(\nu)\, d\nu. \qquad (A-17)$$

Using expressions (7),(8) and (A-16),

$$g = \sum_n \sum_m I_n \kappa_{0n} \sigma_m \kappa_{0m} Q_{nm}, \qquad (A-18)$$

where

$$Q_{nm} = \int_{-\infty}^{\infty} e^{-\delta_{nm}}\, d\nu \qquad (A-19)$$

and

$$\delta_{nm} = c_1^2(\nu_{0n} - \nu)^2 + c_2^2(\nu_m - \nu)^2 \qquad (A-20)$$

$$c_1^2 = \frac{c^2}{\nu_{0n}^2 u_n^2} \qquad (A-21)$$

$$c_2^2 = \frac{c^2}{\nu_{0m}^2 u_m^2}. \qquad (A-22)$$

The indices m and n refer to magnetospheric and solar quantities respectively. We can

simplify δ_{nm} in a form that allows us to integrate Q_{nm} easily, ie.

$$\delta_{nm} = \gamma_0 - \beta\nu + \alpha\nu^2, \qquad (A-23)$$

where

$$\gamma_0 = c_1^2\nu_{0n}^2 + c_2^2\nu_m^2 \qquad (A-24)$$

$$\beta = 2(c_1^2\nu_{0n} + c_2^2\nu_m) \qquad (A-25)$$

$$\alpha = c_1^2 + c_2^2. \qquad (A-26)$$

Integrating Q_{nm} gives us the result

$$Q_{nm} = \sqrt{\frac{\pi}{\alpha}} e^{\frac{(\beta^2 - 4\alpha\gamma_0)}{4\alpha}}. \qquad (A-27)$$

Further simplification leads to the following result

$$\sqrt{\frac{\pi}{\alpha}} = \frac{1}{\kappa_{0m}\sqrt{A}} \qquad (A-28)$$

$$A = \frac{\nu_{0m}^2 u_m^2}{\nu_{0n}^2 u_n^2} + 1. \qquad (A-29)$$

We can finally express g as

$$g = \sum_n \sum_m I_n \sigma_m \frac{\kappa_{0n}}{\sqrt{A}} e^{-\delta_p} \qquad (A-30)$$

with

$$\delta_p = \frac{c^2(\nu_m^2 - 2\nu_{0n}\nu_m + \nu_{0n}^2)}{(\nu_{0m}^2 u_m^2 + \nu_{0n}^2 u_n^2)}. \qquad (A-31)$$

3.8 References

Blake, I.F., *Application to Applied Probability*, Wiley and Son's, 1979.

Chandler, Kozyra, J.U., Horwitz, J.L., Comfort R.H., and Brace, L.H., Modeling of the Thermal Plasma in the Outer Plasmasphere - A Magnetospheric Heat Source, Geophysica Monograph 44, *Modeling Magnetospheric Plasma*, Ed. by Moore, T.E., (1987).

Chiu, Y.T., Robinson, R.M., and Collin, H.L., Magnetospheric and Exospheric Imaging In The Extreme Ultraviolet, *Geophys. Res. Lett.*, **17**, p. 267, (1990).

Chiu, Y.T., Robinson, R.M., Swenson, G.R., Chakrabarti, S.S., and Evans, D.S., Imaging The Outflow of Ionospheric ions into the Magnetosphere, *Nature*, **322**, p. 441, (1986).

Hess, W.N., *The Radiation Belt and Magnetosphere*, Blaisdell Publishing Company, (1968).

Hinteregger, H.E., Fukui, K., and Gilson, B.R., Observational, Reference and Model Data on Solar EUV, From Measurements on AE, E, *Geophys. Res. Lett.*, **8**, p. 1147, (1981).

Ho, Y.K. and Henry, R.J.W., Oscillator Strengths and Collision Strengths for OII and OIII, *Astrophys. J.*, **264**, p. 733, (1983).

Johnson, C.Y., Young, J.M., and Holmes, J.C., Magnetoglow - a New Geophysical Resource, *Science*, **171**, p. 379, (1971).

Kumar, S., Chakrabarti, S.S., Pearsce, F., and Bowyer, S., The O^+ 834 A Dayglow: Satellite Observations and Interpretation with a Radiation Transfer Model, *J. Geophys. Res.*, **88**, p. 9271, (1983).

Lennartson, W. and Shelley, E.G., Survey of .1-16 keV/e Plasma Sheet Ion Composition, *J. Geophys. Res.*, **91**, 3061, (1986).

Meier, R.R., The Scattering Rate of Solar 834 A Radiation By Magnetospheric O^+ and O^{++}, *Geophys. Res. Lett.*, **17**, p. 1613, (1990).

Meier, R.R., Widing, K.G., and Feldman, U., Analysis of the Solar OII/OIII Multiplets at 834 A: Implications for the Emission Measure Distribution in the Vicinity of 40000 K, *Astrophys. J.*, **369**, p. 570, (1991).

Meier, R.R., Ultraviolet Spectroscopy and Remote Sensing of the Upper Atmosphere, *Space Sci. Rev.*, **58**, pp. 1-192, (1991).

Rees, M.H., *Physics and Chemistry of the Upper Atmosphere*, Cambridge University Press, (1989).

Roederer, J., *Dynamics of Geomagnetically Trapped Radiation*, Springer-Verlag, (1970).

Roelof, E.C., Remote Sensing of the Ring Current Using Energetic Neutral Atoms, *Adv. Space Res.*, **9**, No. 12 pp(12)195-(12)(203), (1989).

Swift, D.W., R.W. Smith., S.-I. Akasofu, Imaging The Earth's Magnetosphere, *Planet. Space Sci.*, **37**, No. 4, p. 379, (1989).

Timothy, J.G., The solar spectrum between 300 and 1200 A, in *Solar Output and its Variation*, (Edited by White, O.R.), p. 237, Colorado Associated University Press, Boulder, (1977).

3.9 Acknowlegements

This work was supported in part by NASA grants NAGW 1520 and 1787 and funds from the Geophysical Institute, University of Alaska, Fairbanks. We would like to thank Richard Guritz and Joanne Grooves for their help in producing the images using the University of Alaska Data Visualization and Analysis Laboratory facility. The authors

thank David Kula (University of Alaska summer intern, 1989) for his calculations of scattering efficiency. The authors also thank the referees for their suggestions in revising this paper.

Chapter 4 Magnetospheric Imaging of High Latitude Ion Outflows *

4.0 Abstract

High latitude ion outflows mostly consist of upward streaming O^+ and He^+ emanating from the ionosphere. At heights above 1000 km, these flows consist of cold and hot components which resonantly scatter solar EUV light; however, the ion populations respond differently to Doppler shifts resulting from the large relative velocities between the ions and the Sun. The possibility of optical detection of the Doppler effect on the scattering rate will be discussed for the O^+ (83.4 nm) ions. We have contrasted the EUV solar resonance images of these outflows by simulations of the 30.4 nm He^+ and 83.4 nm O^+ emissions for both quiet and disturbed geomagnetic conditions. Input data for the 1000 km level has been obtained from the EICS instrument aboard the Dynamics Explorer satellite. Our results show emission rates of 50 and 56 milli-Rayleighs at 30.4 nm for quiet and disturbed conditions and 65 and 75 milli-Rayleighs at 83.4 nm for quiet and disturbed conditions, respectively, obtained for a polar orbiting satellite and viewing radially outward. We also find that an imager at an equatorial distance of 9 R_e or more is in a favorable position for detecting ion outflows, particularly when the plasmapause is depressed in latitude. However, an occultation disk may be necessary to obscure the bright plasmaspheric emissions.

---

*D.E. Garrido, R.M. Robinson, Y.T. Chiu, H.L. Collin, R.W. Smith and D.W. Swift, Magnetospheric Imaging of High Latitude Ion Outflows; Annales Geophysicae, in press, 1994

4.1 Introduction

Global imaging of the magnetosphere in the ultraviolet has been discussed by Swift et al. (1989), Chiu et al. (1990), Meier (1991) and Garrido et al. (1991). Swift et al. (1989) constructed images of the plasma sheet and ring current from resonantly scattered sunlight from O^+ ions. Chiu et al. (1990) simulated images of outflowing O^+ (83.4 nm) ions and neutral O (130.4 nm) atoms for a geostationary satellite viewing at a distance of 6.6 R_e in the dusk meridian. They assumed particle motions along a static dipole field with tilt and a density profile that is modeled by a simple magnetic field scaling. A uniform flux distribution over the polar region was assumed with a value derived by averaging outflowing ion fluxes measured by the Energetic Ion Composition Spectrometer (EICS) on Dynamics Explorer 1 (DE-1). The resulting column emission rates were as high as 1 Rayleigh. Effects of gyromotion of the ions and Doppler shift due to the ions' bulk velocity along the Sun-Earth direction were not considered. The calculations of Chiu et al. (1990) also did not include the bright resonant emissions originating from the plasmasphere which can obscure the weaker emissions coming from the high latitude ion fluxes.

Meier (1991) provided a detailed assessment of the possibilities of remote sensing in the ultraviolet over a broad range of wavelengths that includes the 30.4 and 83.4 nm resonant lines of He^+ and O^+, respectively. Using plasmaspheric models based on the observations of Meier and Weller (1972) and Weller and Meier (1974), images of the plasmasphere were constructed for a viewing distance of 10 R_e in the dawn to dusk meridian plane at geographic latitudes 0, 30, 60 and 90 deg. These simulations show that the extent of the plasmapause boundary is visible when viewing at 0 deg latitude and the Earth's shadow becomes evident for higher latitude platforms.

Garrido et al. (1991) simulated images of the radiation belt and plasma sheet from resonant emissions of O^+ ions at 83.4 nm, incorporating Doppler effects due to plasma bulk flows along the Sun-Earth line and variable plasma temperature. From an analysis of the scattering rate as a function of ion drift velocity they showed that enhanced scattering can occur even at drift speeds other than zero. A simple model for the ion density in the radiation belt was assumed without including the dynamics of mirroring particles to illustrate the changes in the image brightness when the plasma temperature is varied. The image brightness did not vary greatly with temperature from 1-10 keV. By simulating images of the radiation belt and plasma sheet they estimated that gross features of those regions can be seen with a camera aperture of 750 cm^2. Calculated values of the intensities from the brighter portions of the model hot magnetosphere is of the order of a few millirayleighs. However, there exists the possibility that undetected cold plasma could increase these intensities considerably.

The purpose of this paper is to improve and extend the simulations of Chiu et al. (1990) by incorporating Doppler effects due to ion drifts along the Sun-Earth line, gravitational and rotational effects, variations in plasma temperature, the non-uniform flux intensities and the effects of plasmaspheric emissions. We investigate the possibility of remotely sensing energetic ion outflows using high altitude satellites. We also show that He^+ (30.4 nm) and O^+ (83.4 nm) ions respond differently to Doppler shifts when the ions are accelerated to high parallel velocities and we study the possibility of observing these effects optically for the O^+ ions.

An earlier paper by Robinson et al. (1992) showed simulated images of extreme ultraviolet (EUV) emissions from energetic outflowing O^+ (83.4 nm) and He^+ (30.4 nm) ions and they also discussed important instrumental considerations for magnetospheric imaging including the sensitivity requirements of detectors for EUV wavelengths.

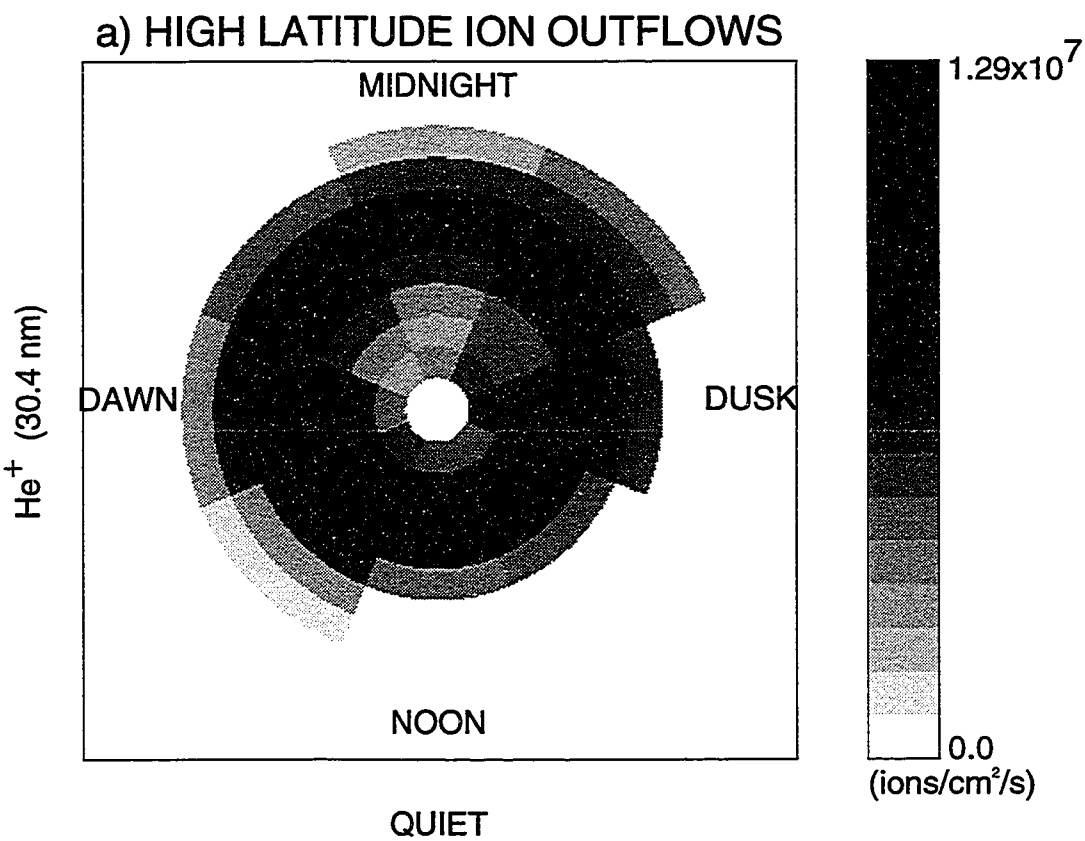

Figure 4.1a MLT-ILAT diagram of He^+ (30.4 nm) ion outflow data for quiet conditions in the 10 eV to 17 keV energy per charge range obtained from the Lockheed Ion Mass Spectrometer on board the DE-1 spacecraft. It shows the grey code scale of the He^+ ion flux intensity distribution at a reference altitude of 1000 km. Due to large statistical uncertainties in the data the ion fluxes in some bins were set to zero.

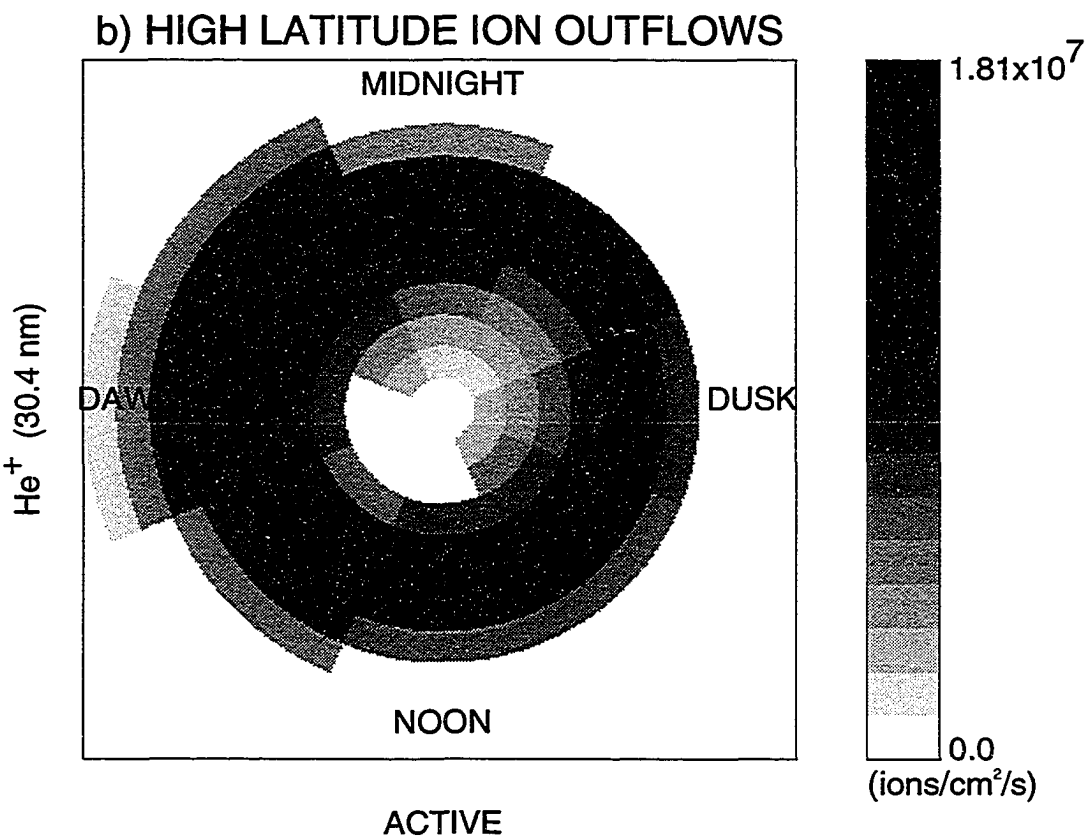

Figure 4.1b MLT-ILAT diagram of He^+ (30.4 nm) ion outflow data for active conditions in the 10 eV to 17 keV energy per charge range obtained from the Lockheed Ion Mass Spectrometer on board the DE-1 spacecraft. It shows the grey code scale of the He^+ ion flux intensity distribution at a reference altitude of 1000 km. Due to large statistical uncertainties in the data the ion fluxes in some bins were set to zero.

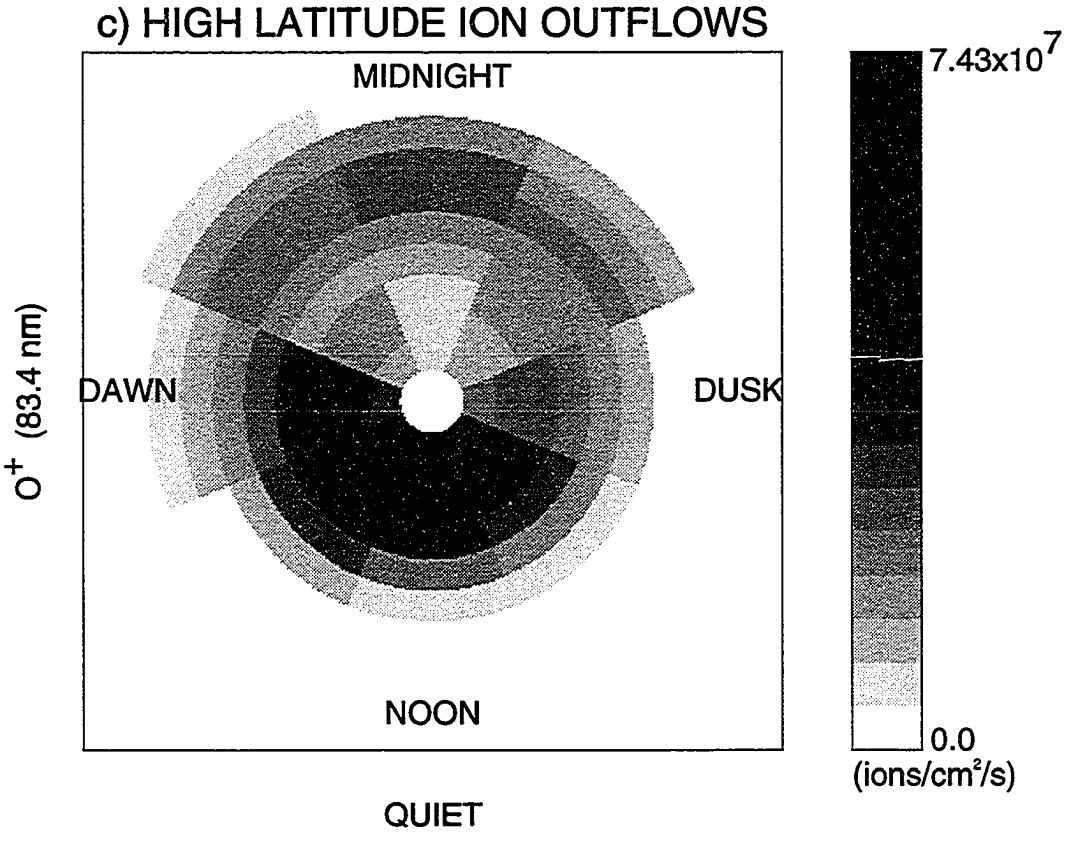

Figure 4.1c MLT-ILAT diagram of O^+ (83.4 nm) ion outflow data for quiet conditions in the 10 eV to 17 keV energy per charge range obtained from the Lockheed Ion Mass Spectrometer on board the DE-1 spacecraft. It shows the grey code scale of the O^+ ion flux intensity distribution at a reference altitude of 1000 km. Due to large statistical uncertainties in the data the ion fluxes in some bins were set to zero.

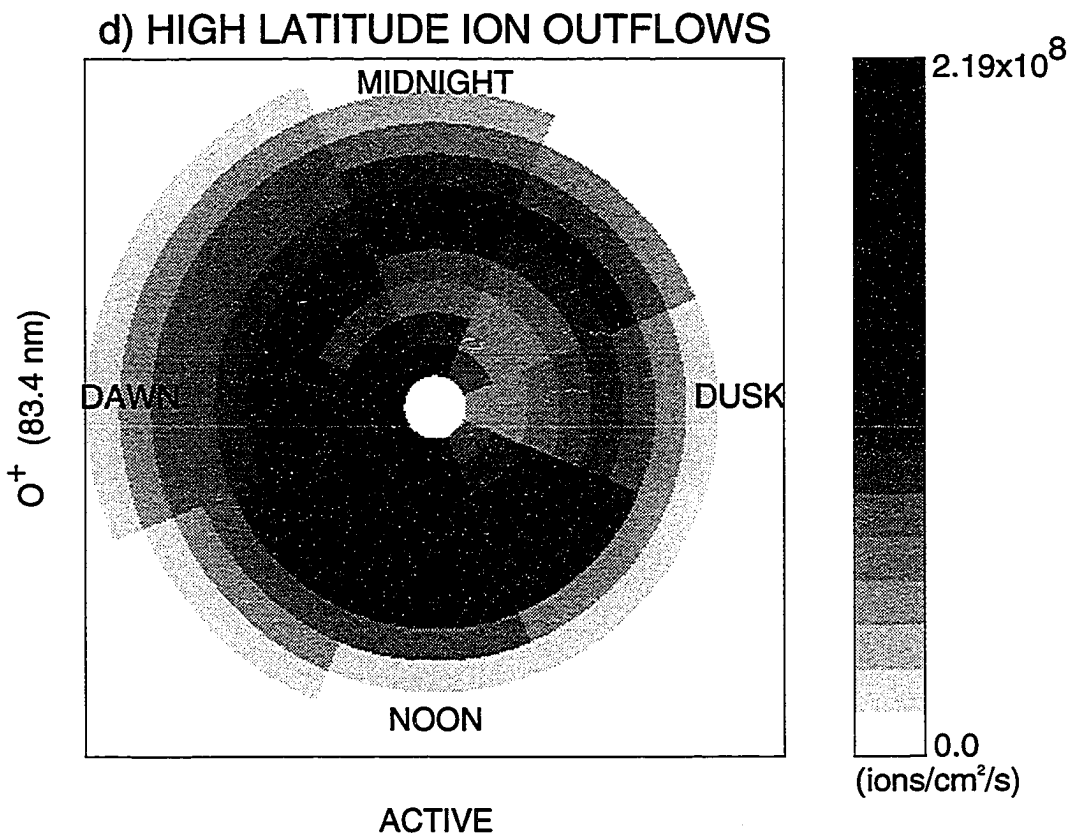

Figure 4.1d MLT-ILAT diagram of O^+ (83.4 nm) ion outflow data for active conditions in the 10 eV to 17 keV energy per charge range obtained from the Lockheed Ion Mass Spectrometer on board the DE-1 spacecraft. It shows the grey code scale of the O^+ ion flux intensity distribution at a reference altitude of 1000 km. Due to large statistical uncertainties in the data the ion fluxes in some bins were set to zero.

4.2 Imaging High Latitude Ion Outflows

The ion outflow data for He^+ and O^+ at two levels of magnetic activity are shown in Figs. 4.1a to 4.1b and Figs. 4.1c to 4.1d, respectively. The outflowing flux intensity distribution is based on data obtained by the EICS instrument on board the DE-1 spacecraft. The upflowing ion fluxes are integrated over energies from 10 eV to 17 keV and over all pitch angles. The fluxes are displayed as a function of magnetic local time (MLT) and invariant latitude (ILAT). These diagrams show the spatial variations of the ionospheric outflows with the magnitudes of the flux intensities displayed in a grey-coded scale. The data were accumulated from EICS measurements made between August, 1981 and the middle of 1986. The data were divided according to the Kp value at the time of measurement with quiet times represented by $0< Kp <3$ and disturbed times corresponding to $Kp >3$. The high latitude ion fluxes are defined for latitudes greater than 56 deg, divided into 10 latitude bins each with a 3 deg width and 8 bins in MLT each having a width of 3 hours. The average fluxes in some bins have large statistical uncertainties and the flux values in these bins are assumed to be zero in our simulations. These results were obtained from a statistical survey of the occurrence of upflowing He^+ and O^+ ions by Collin et al. (1988). Maximum average flux intensities of 1.3×10^7 and 1.8×10^7 ions cm^{-2} s^{-1} for He^+ were obtained for quiet and disturbed conditions, respectively. The maximum average intensities for O^+ shown in Figs. 4.1c to 4.1d are 7.4×10^7 and 2.2×10^8 ions cm^{-2} s^{-1} for quiet and disturbed conditions, respectively. Note the larger variation for O^+ compared to He^+. These data will be used as an ionospheric source to calculate the spatial distribution of outflowing ions in the magnetosphere from which images can be constructed of resonantly scattered emissions from He^+ and O^+ ions.

The images are obtained by simulating a detector with a 50x50 pixel field of view and a resolution of 2 deg. The column integrated intensity along a given line of sight direction with line element ds is

$$4\pi \mathrm{I} = \int e^{-\tau} p(\theta)\, g\, n(\mathbf{r})\, ds \times 10^{-6}(R), \tag{4.1}$$

where I is the column integrated intensity (photons cm^{-2} s^{-1}), τ is optical depth, p(θ) is the phase function, g is the scattering rate (photons s^{-1} ion^{-1}) for solar illumination only and n is the number density in cm^{-3} at position $\mathbf{r}$. The scattering phase function reflects the anisotropy of scattered radiation and is given by

$$p(\theta) = 1 + 1/4(2/3 - \sin^2\theta) \tag{4.2}$$

for He^{+} (30.4 nm) where θ is the angle between the incident direction (Sun-Earth) and scattered radiation in the direction of the observer (Brandt and Chamberlain, 1959). We assume $p(\theta)$ is unity for the 83.4 nm radiation. Since the magnetosphere is optically thin above 1000 km to 30.4 and 83.4 nm radiation, τ can be set to zero. The scattering rate that accounts for Doppler shifts and temperature variations can be calculated from Garrido et al. (1991) or Meier (1990). The ionospheric ion outflows are defined for latitudes greater than 56 deg and we neglect contributions coming from the plasmasphere. The density profile is modeled by a simple magnetic field scaling,

$$n = (J_o/v_o)(B/B_o), \tag{4.3}$$

where J_o and v_o are the flux intensity (ions cm^{-2} s^{-1}) and velocity, respectively at a reference altitude, where the magnetic field strength is B_o. For computational purposes we have assumed an inner and outer spherical boundary of 1.157 and 10 R_e, respectively, and that magnetic and geographic coordinates coincide. All the outflowing ions are assumed to move along static dipole field lines with an average parallel energy of 10 eV. Although

the EICS data are integrated over energy from 10 eV to 17 keV, most of the flux is in the lower energy ions. We also assumed that the flux distribution is symmetric at both poles. In calculating the column intensities we accounted for contributions coming from cold background sources in the high latitude regions (Hoffman et al., 1974). Calculations of the density profile for both ions at high latitudes (Ottley et al., 1980 and Gombosi et al., 1987) allow us to estimate the variation of ion density with altitude. The cold ion density is assumed to decrease exponentially with scale height as

$$n = n_o e^{-(r-r_o)/H}, \tag{4.4}$$

where r_o=1.157 R_e, H is the ion scale height and the densities (n_0) at the reference altitude are given by 10 and 3000 cm^{-3} for He^+ (T=0.1 eV) and O^+ (T=10 eV) ions, respectively. The source densities for the cold ions are assumed to be independent of latitude and magnetic local time (MLT). The scale height for the He^+ ion is 2000 km while for O^+ it is 500 km. In the calculation of intensities from emissions of O^+ (83.4 nm) and He^+ (30.4 nm) ions we have neglected Doppler effects due to the ion's bulk motion along the Sun-Earth line. Doppler effects due to ion drifts and temperature variations will be considered in Sec. 4.4.

4.3 Analysis of the Images

Simulated images of the outflowing He^+ are shown in Figs. 4.2a and 4.2d. The coordinates BETA/ETA are used to locate a particular pixel in the images. The coordinates are defined by considering a reference line from the observer to the center of the image. For convenience, we call this line the central axis. Vertical lines of pixels in the figures are then identified by specifying a line-of-sight direction making an angle ETA with

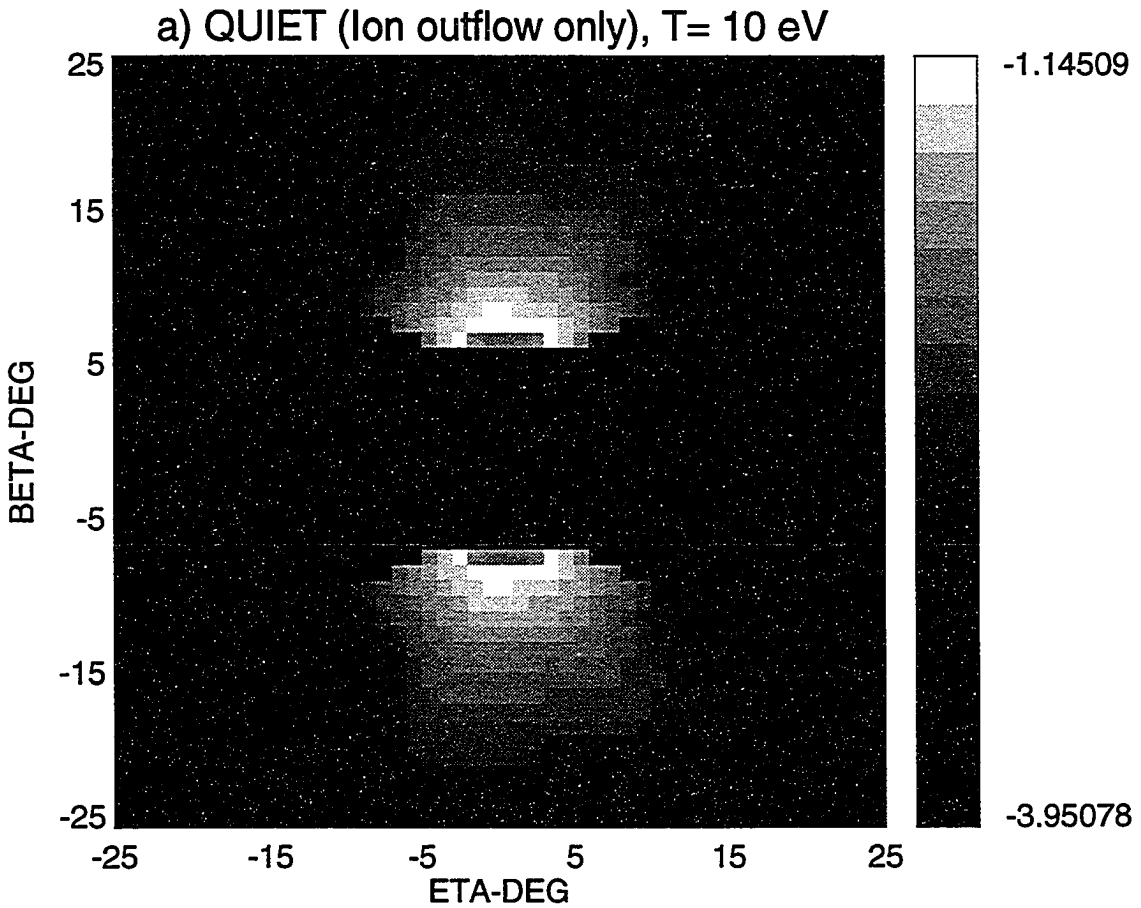

Figure 4.2a Image of outflowing He^+ (30.4 nm) ions (T=10 eV) for quiet conditions that include cold background sources (T=0.1 eV). The satellite is located at a distance of 9 R_e from the center of the Earth in the dusk sector and viewing towards the center of the Earth. In constructing the images Doppler effects due to ion drifts have not been taken into account. Grey scale values are in $\log_{10}$(Rayleighs).

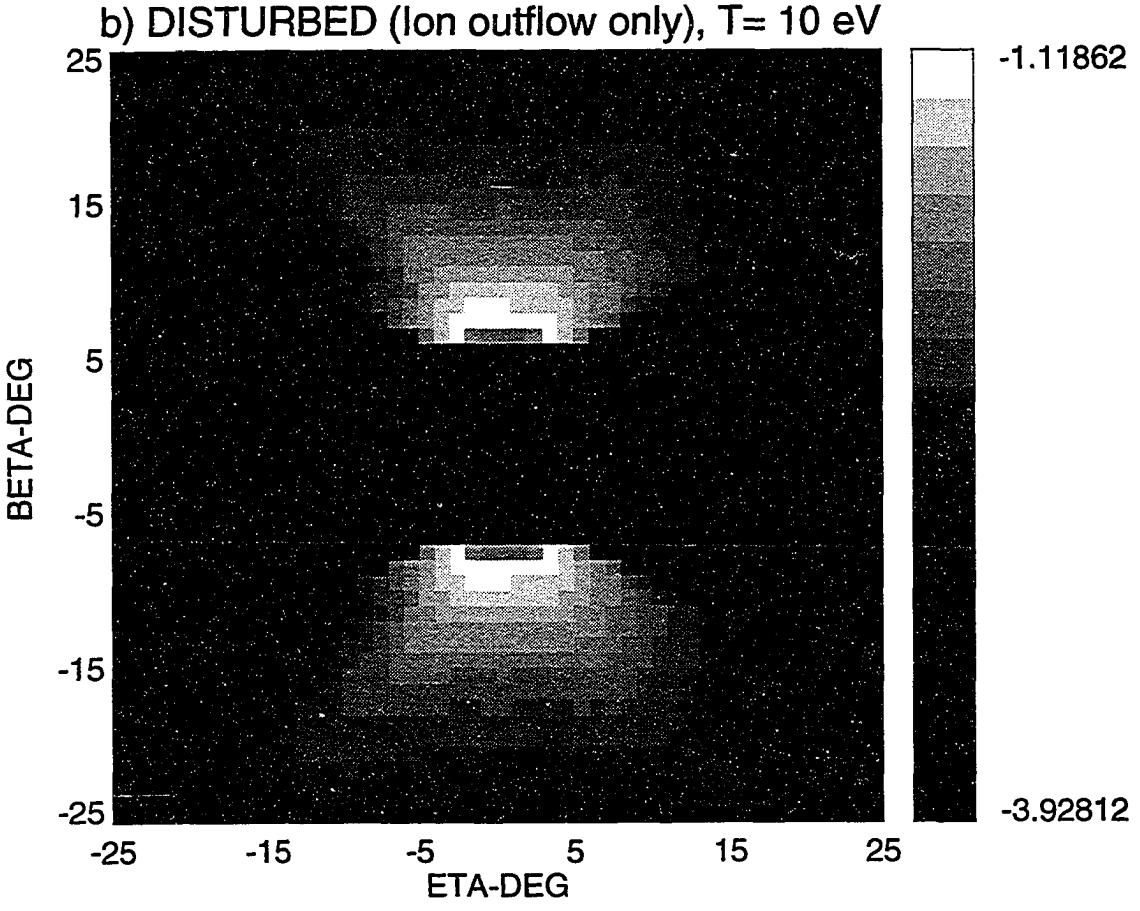

Figure 4.2b Image of outflowing He^+ (30.4 nm) ions (T=10 eV) during disturbed conditions that include cold background sources (T=0.1 eV). The satellite is located at a distance of 9 R_e from the center of the Earth in the dusk sector and viewing towards the center of the Earth. In constructing the images Doppler effects due to ion drifts have not been taken into account. Grey scale values are in $\log_{10}$(Rayleighs).

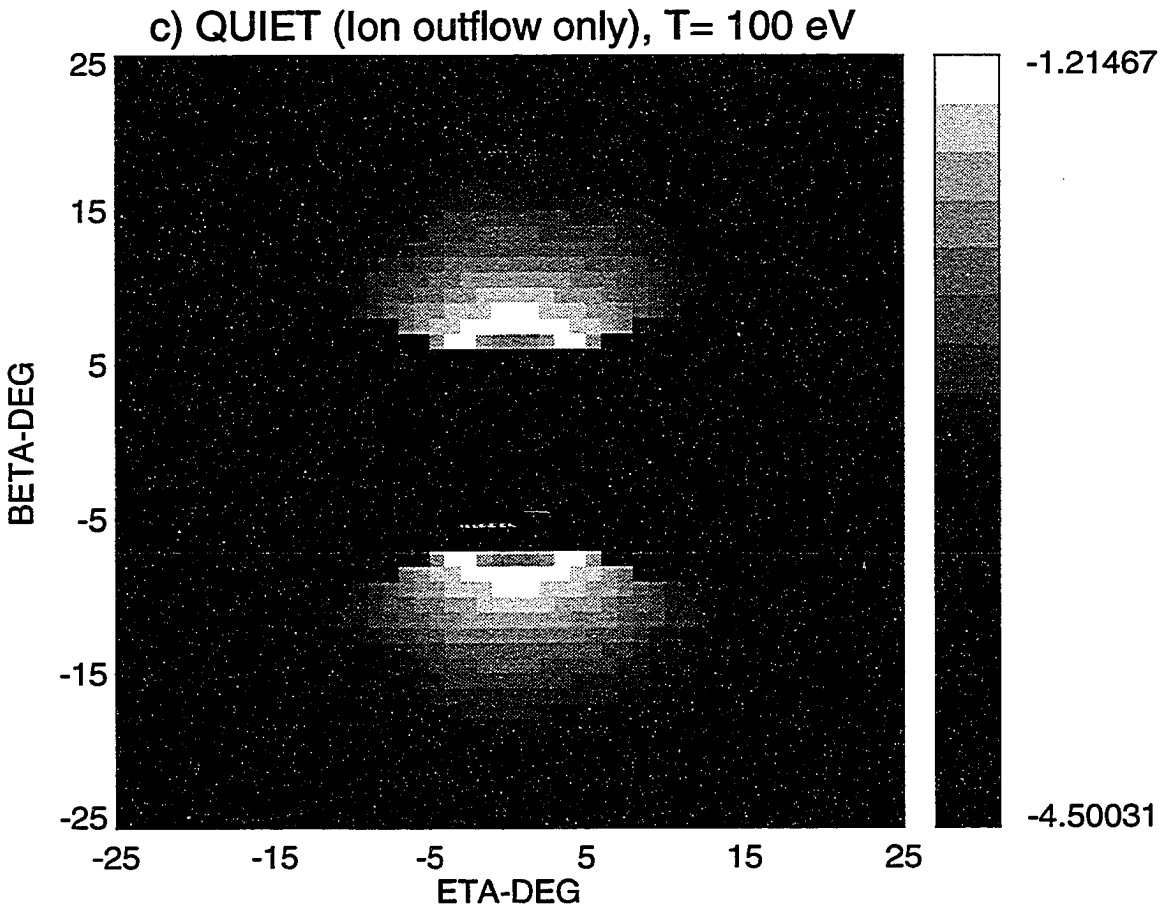

Figure 4.2c Image of outflowing He^+ (30.4 nm) ions (T=100 eV) for quiet conditions that include cold background sources (T=0.1 eV). The satellite is located at a distance of 9 R_e from the center of the Earth in the dusk sector and viewing towards the center of the Earth. In constructing the images Doppler effects due to ion drifts have not been taken into account. Grey scale values are in $\log_{10}$(Rayleighs).

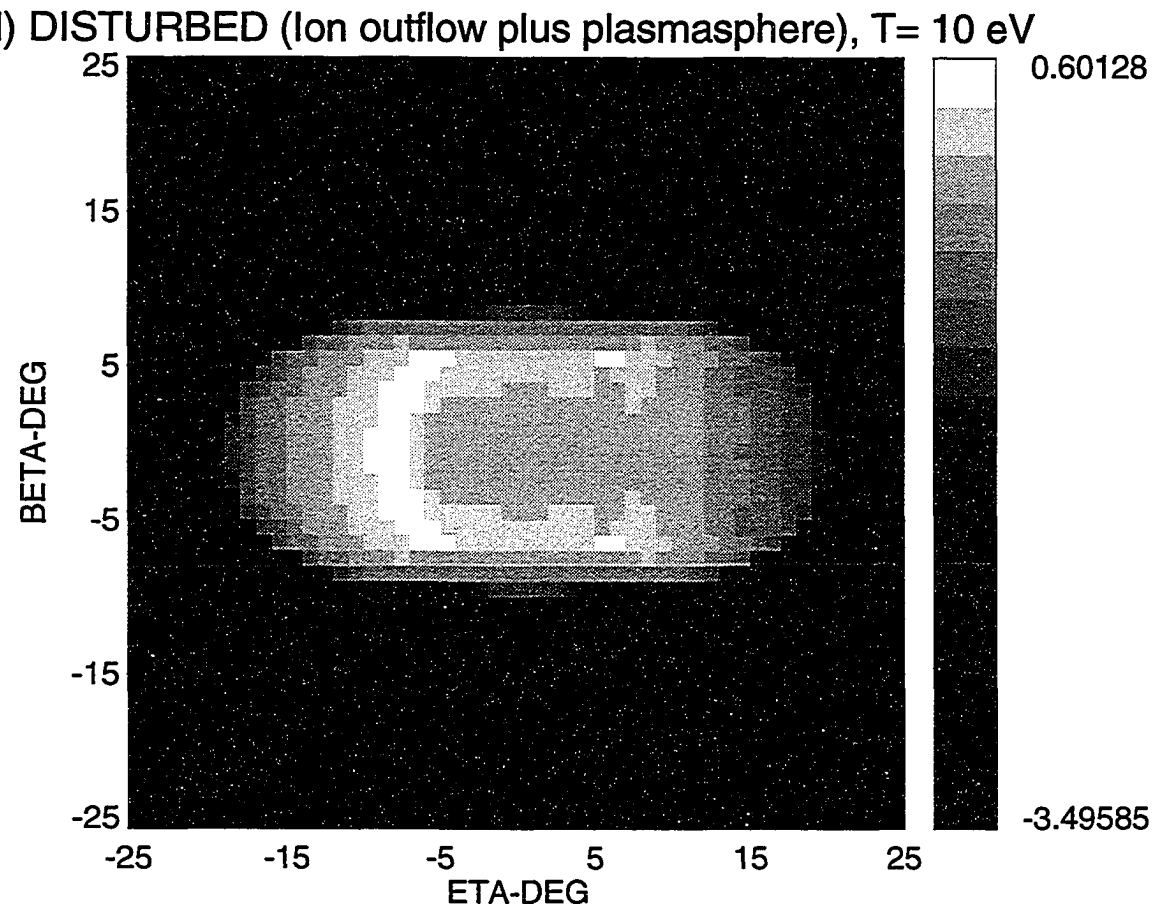

Figure 4.2d Image of outflowing He^+ (30.4 nm) ions (T=10 eV) plus plasmasphere for disturbed conditions that include cold background sources (T=0.1 eV). The satellite is located at a distance of 9 R_e from the center of the Earth in the dusk sector and viewing towards the center of the Earth. In constructing the images, Doppler effects due to ion drifts have not been taken into account. Grey scale values are in $\log_{10}$(Rayleighs). It shows the bright regions of the plasmasphere and the less intense emissions from the ion outflows beyond the plasmapause boundary.

respect to the central axis. Similarly, horizontal lines of pixels are specified by the angle BETA. Thus, any pixel can be specified by the coordinates (BETA, ETA) in deg. With respect to the observer's position, a pixel at the center of the image is said to have coordinates (BETA, ETA)=(0,0) while a pixel in the upper left hand corner is specified by coordinates (-25, 25). In obtaining the images shown in Figs. 4.2a to 4.2c we have neglected the effects of the plasmasphere. Since there is symmetry between the northern and southern hemispheres in all of our images we will only describe the intensities in the northern hemisphere. The effects of a change in temperature on the image brightness for quiet conditions can be seen by comparing Figs. 4.2a and 4.2c. As seen in the grey scale bars, the maximum brightness in Figs. 4.2a and 4.2c is 0.07 and 0.06 R, respectively. For pixels defined by the coordinates -10 < BETA < 15 and ETA > 15 deg, we see that a change in structure and a decrease in the image brightness in Fig. 4.2c occurs. For the same range of BETA the pixels defined by ETA < 15 deg, Fig. 4.2c show only a slight change in magnitude of the intensities. The case of Fig. 4.2b shows the maximum intensity to be .076 R. The image structure in Fig. 4.2b has more details compared to Fig. 4.2a in regions defined by ETA > 15 deg and the image brightness is also enhanced. Now, also consider in Fig. 4.2b the pixel region bounded by coordinates -25 < BETA < -10 and 5 < ETA < 20. It now shows a slight increase in the image brightness in contrast with Fig. 4.2a. The change in the image brightness in Fig. 4.2b is due to the larger ion outflow rates on the dayside during disturbed conditions (See Figs. 4.1a and 4.1b).

In all the figures solar illumination is to the left of the figures and it also defines the direction of the positive x axis. The positive y axis is along dusk and is directed out of the page. The z axis is orthogonal to both x and y axis and completes the right handed solar magnetospheric coordinate system. The coordinate axes are not shown in the figures. Also, in all figures the satellite is located in the dusk sector at a distance of

9 R_e from the center of the Earth and viewing directly towards its center. If we exclude the effects of the plasmasphere in our simulations the image brightness in the dayside coming from the low latitude regions defined by -5 < ETA < 5 deg is less intense than in the night sector. This is a consequence of the absence of statistically significant ion outflow data on the dayside at some latitudes (See Figs. 4.1a to 4.1d).

Although it is not the primary aim of this paper to discuss plasmaspheric imaging we note that it is possible to image the plasmasphere from scattered 30.4 nm radiation. With this viewing geometry, a 30.4 nm imager can determine the size, shape and intensity of emissions of the plasmasphere. To illustrate the effects of plasmaspheric emissions we assumed that the density distribution for the He^+ ions obeys a power law as defined by Paresce et al. (1974). The density is assumed to vary with radial distance as

$$n(He^+) = n_0(He^+)(r_0/r)^{\beta} \tag{4.5}$$

with β=3 or 4. We have adopted a value of 400 ions cm^{-3} for n_0 and β=3 which represents a depleted plasmasphere in contrast to the case when $n_0 = 10^4$ ions cm^{-3} and β=4 or $n_0 = 6 \times 10^3$ ions cm^{-3} and β=3. These latter values were obtained by Paresce et al. by fitting resonant scattering data. The image that includes the plasmasphere and the outflowing ions is shown in Fig. 4.2d. The effects of the Earth's shadow are now manifest on the night sector (right side of image). In some studies it has been shown that under disturbed times the plasmapause contracts, for example, Binsack (1967). This allows relatively brighter portions of the images of the outflowing He^+ ions to be seen. To simulate disturbed conditions we assume the plasmapause boundary to be at L=3. Note that the extent of the plasmasphere in the north-south direction is about +/- 10 deg (-10 < ETA < 10) on the vertical scale in Fig. 4.2d and it is still possible to see the low intensity He^+ emissions coming from the outflowing ions above and below this region. We

also have simulated the case for quiet times assuming a plasmapause boundary at L=4.25 and the extent of the plasmasphere in this case falls within +/- 15 deg (-15 < ETA < 15) field of view thus making it less favorable to view the emissions from the outflowing ions. The result for this case is not shown. In practice, these bright plasmaspheric emissions may be eliminated by introducing an occultation disk in the detector.

The images of outflowing O^+ ions are shown in Figs. 4.3a to 4.3c. The images for quiet and disturbed times are shown in Figs. 4.3a and 4.3b, respectively. The cold ambient and hot outflowing ions are assumed to have an average parallel energy of 10 eV. The same geometry is assumed as in the construction of the He^+ images. Fig. 4.3a represents the image at 83.4 nm for quiet conditions and shows a maximum intensity of 1.02 R while Fig. 4.3c shows a maximum intensity of 1.01 R. Similarly, the maximum intensity in Fig. 4.3b is 1.05 R and represents the disturbed case. Fig. 4.3c also represents quiet conditions but the ion temperature is now 100 eV. For pixels described by ETA > 10 deg, Fig. 4.3c shows only a small decrease in the image brightness and a slight change in the image structure compared to Fig. 4.3a. To compare Figs. 4.3a and 4.3b consider pixels described by coordinates -25 < BETA < -5 and 5 < ETA < 25. We see that the intensities in these regions are more enhanced than in Fig. 4.3a. These enhanced intensities are due to the higher ion outflow rates of O^+ ions during disturbed times (Please refer to Figs. 4.1c and 4.1d).

Photometric Imaging From a Polar Orbiting Satellite

It would be of interest to compare the relative contribution to the emission rate of the cold ambient ions and the energetic ion outflows. For this reason we explored the possibility of imaging ion outflows by viewing outward from a polar orbiting satellite.

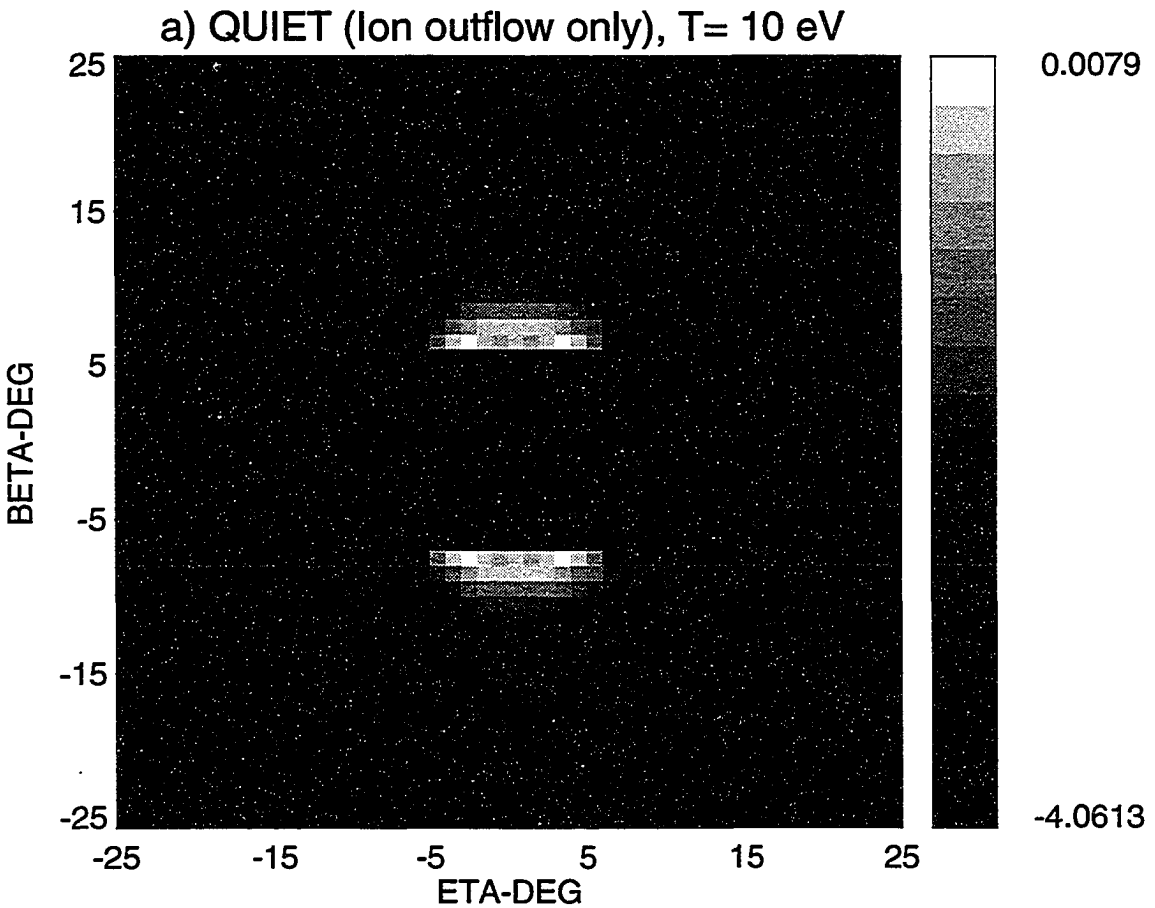

Figure 4.3a Image of outflowing O^+ (83.4 nm) ions (T=10 eV) during quiet times that include cold background sources (T=10 eV). The satellite is located at a distance of 9 R_e from the center of the Earth in the dusk sector and viewing towards the center of the Earth. In constructing the images Doppler effects due to ion drifts have not been taken into account. Grey scale values are in $\log_{10}$(Rayleighs).

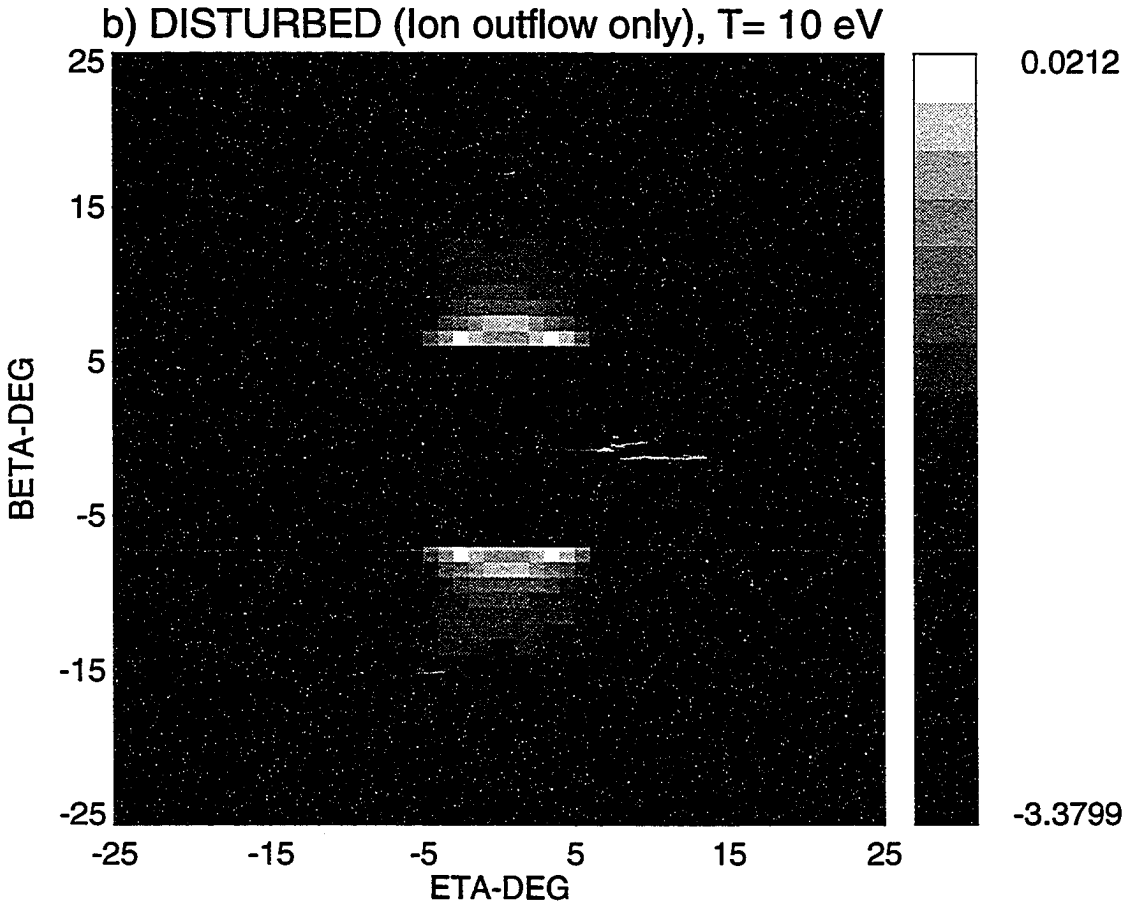

Figure 4.3b Image of outflowing O^+ (83.4 nm) ions (T=10 eV) for disturbed conditions that include cold background sources (T=10 eV). The satellite is located at a distance of 9 R_e from the center of the Earth in the dusk sector and viewing towards the center of the Earth. In constructing the images Doppler effects due to ion drifts have not been taken into account. Grey scale values are in $\log_{10}$(Rayleighs).

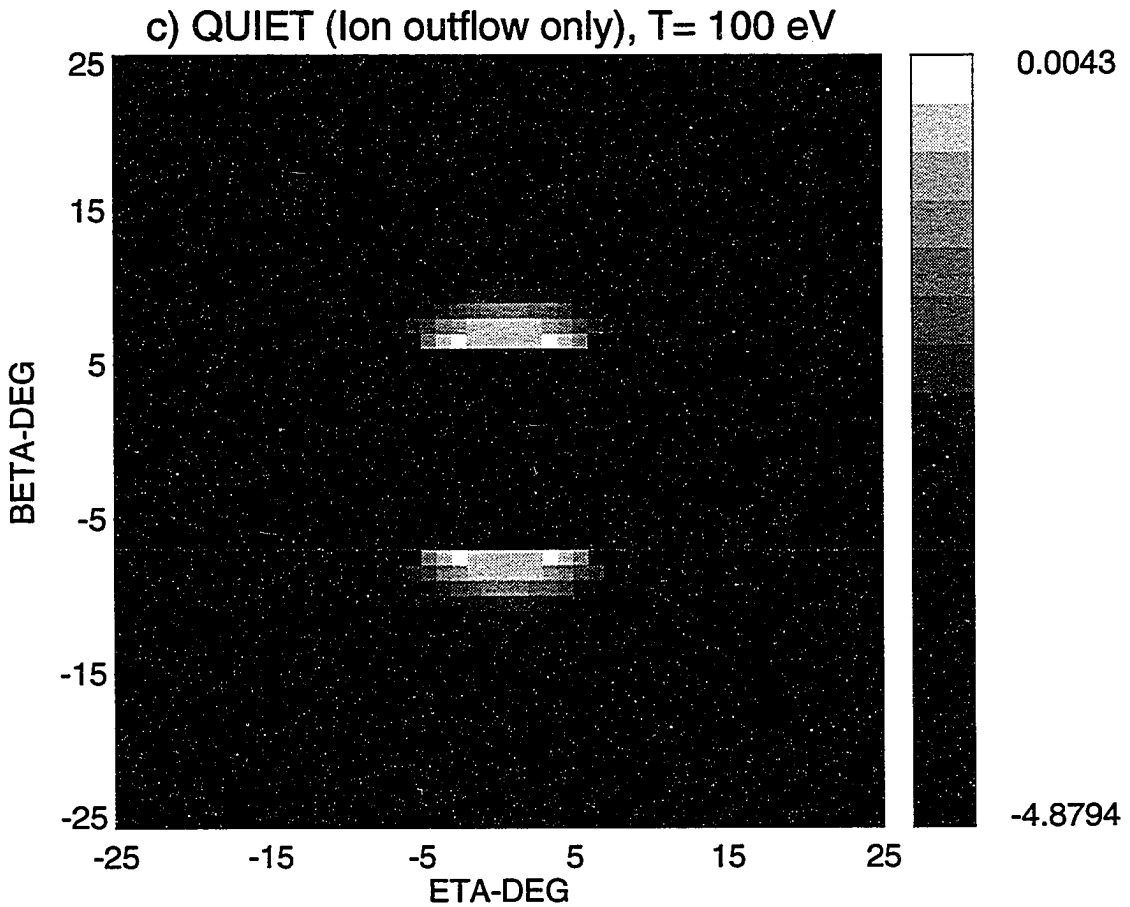

Figure 4.3c Image of outflowing O^+ (83.4 nm) ions (T=100 eV) during quiet times that include cold background sources (T=10 eV). The satellite is located at a distance of 9 R_e from the center of the Earth in the dusk sector and viewing towards the center of the Earth. In constructing the images Doppler effects due to ion drifts have not been taken into account. Grey scale values are in $\log_{10}$(Rayleighs).

To simulate photometric measurements from polar orbiting satellites we adopted a satellite with an orbit and attitude configuration and detector field of view similar to that described by Weller and Meier (1974). The satellite has a circular polar orbit with an altitude of 750 km. Line of sight emission rates were obtained with a satellite viewing radially outward towards the outer magnetosphere. Column emission rates from cold sources and outflowing ions for λ_0=70 deg are 52 and 56 mR (milli-Rayleighs) for quiet and disturbed times for He^+ and 65 and 75 mR for quiet and disturbed times for O^+, respectively. The values obtained for O^+ were calculated for a satellite altitude of 2000 km. Note that the sensitivity of the instrument used to obtain the data modeled by Weller and Meier (1974) was not sufficient to detect this level of emissions. Therefore, the high latitude source was neglected in their modeling.

The column emission rates obtained above represent contributions from both cold and outflowing ions. To determine their relative contributions to the emission rate, we assume that the satellite is located at a fixed latitude of 70 deg. For observation altitudes 1000 and 6000 km, we calculated at each altitude the integrated upward line-of-sight emission rate for both cold and outflowing ions using the density model and scattering rate described in Sec. 4.2. The results are plotted in Figs. 4.4a to 4.4d. In all figures the solid line refers to contributions from outflowing ions and the dashed curve refers to the cold ion contribution. Figs. 4.4a and 4b represent calculated emission rates for He^+ (30.4 nm) during quiet and disturbed times of magnetic activity. For quiet times the cold ion contribution is larger than that coming from the outflowing ions at altitudes up to 3400 km (1.53 R_e) and the contribution from ion outflows begin to dominate beyond this altitude. Note that the horizontal axis is plotted in terms of R_e measured from the center of the Earth. At this transition point cold and outflowing ions contribute 5.3 mR to the emission rate. In Fig. 4.4b during disturbed times, the outflowing ion emission

rates dominate the cold ion contribution even at 1000 km and becomes more significant at higher altitudes. At 1000 km both sources contribute about 25 mR to the emission rate. The emission rates for O^+ (83.4 nm) are shown in Figs. 4.4c and 4.4d during quiet and disturbed times, respectively. The cold ion contribution to the emission rate is larger than contributions from the ion outflows up to altitudes of 2600 km (1.41 R_e) during quiet times while during high levels of magnetic activity the ion outflows contribute larger emission rates starting at an altitude of 1700 km (1.27 R_e). At the transition altitude the emission rates are given by 7 mR and 40 mR for quiet and disturbed times, respectively.

4.4 Doppler Effects and Resonance

In a previous work by Chiu et al. (1990) they constructed images of the outflowing O^+ ions by assuming a uniform upward flux intensity symmetric over both hemispheres. Since Doppler effects were not included in the analysis they obtained an image which is symmetric about the tilted dipole axis. However, it is well known that these outflowing ions can be accelerated to high energies as they are transported to the outer magnetosphere. Horwitz (1987) studied the distribution of O^+ ions in the outer magnetosphere and also calculated their outward parallel velocities. In his simulations he used an intermediate source energy of 50 eV for the ionospheric ions and calculated densities and parallel velocities for different values of the convection electric field with an applied parallel electric field of .5 μV/m. Parallel velocities from 20 to 60 km s^{-1} were obtained for distances of the order of 10 R_e and up to 140 km s^{-1} for distances greater than 10 R_e. The energization of outflowing ions to high parallel velocities would cause the particle scattering rate to vary along its orbit and therefore can affect the intensities of our magnetospheric image. Because of the difference in structure of the solar lines for

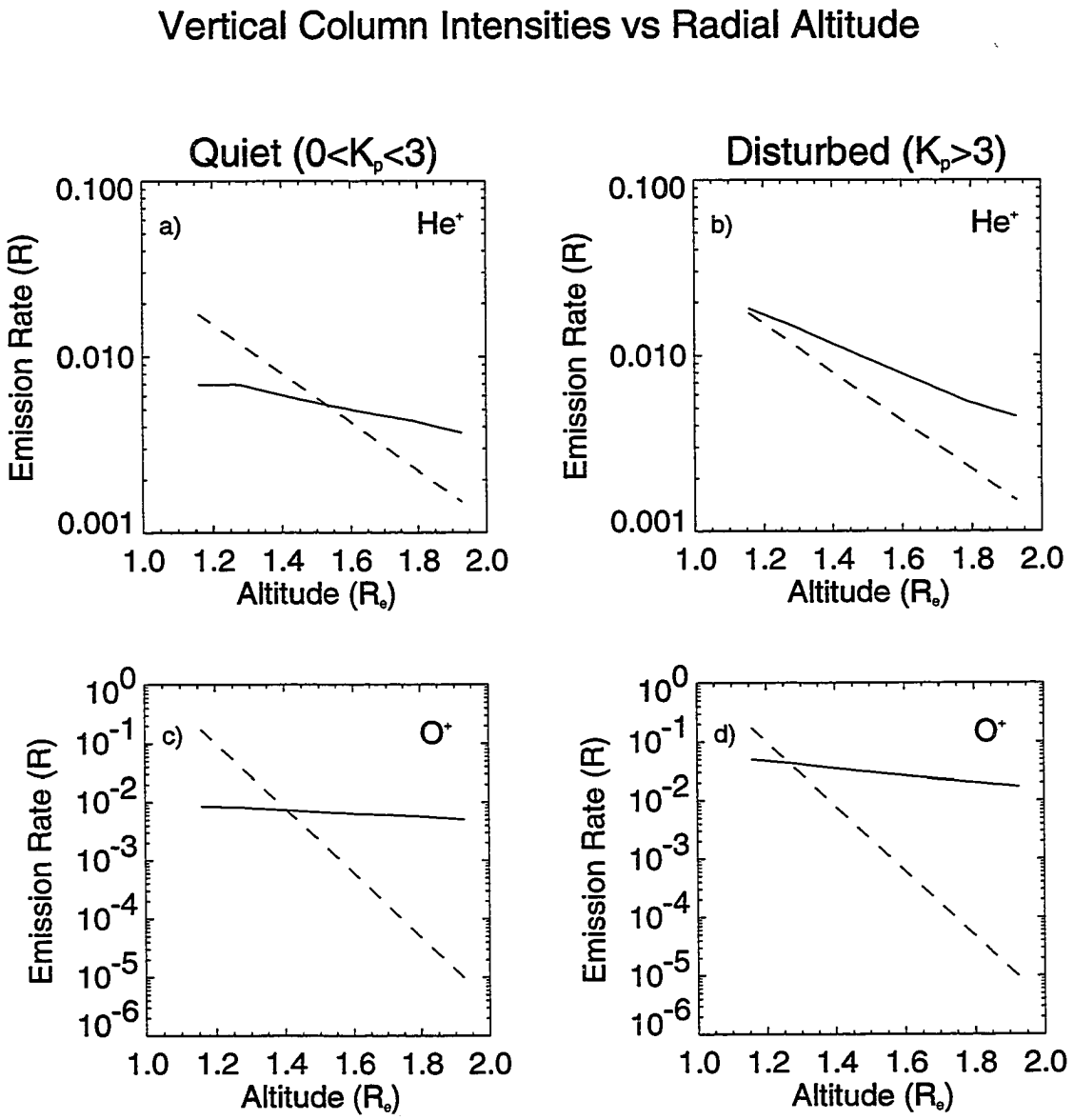

Figure 4.4 Plots of the vertical column emission rate vs satellite altitude starting at 1000 km up to 6000 km. The satellite is at a base latitude of λ_0=70 deg. Figures 4.4a and 4.4c represents the calculated emission rate for He^+ and O^+ for quiet conditions, respectively. Figs. 4.4b and 4.4d represents the calculated emission rate for He^+ and O^+ during disturbed conditions, respectively. In all figures, the solid curve refers to ion outflow sources (T=10 eV) while the dashed curve refers to cold ion contributions.

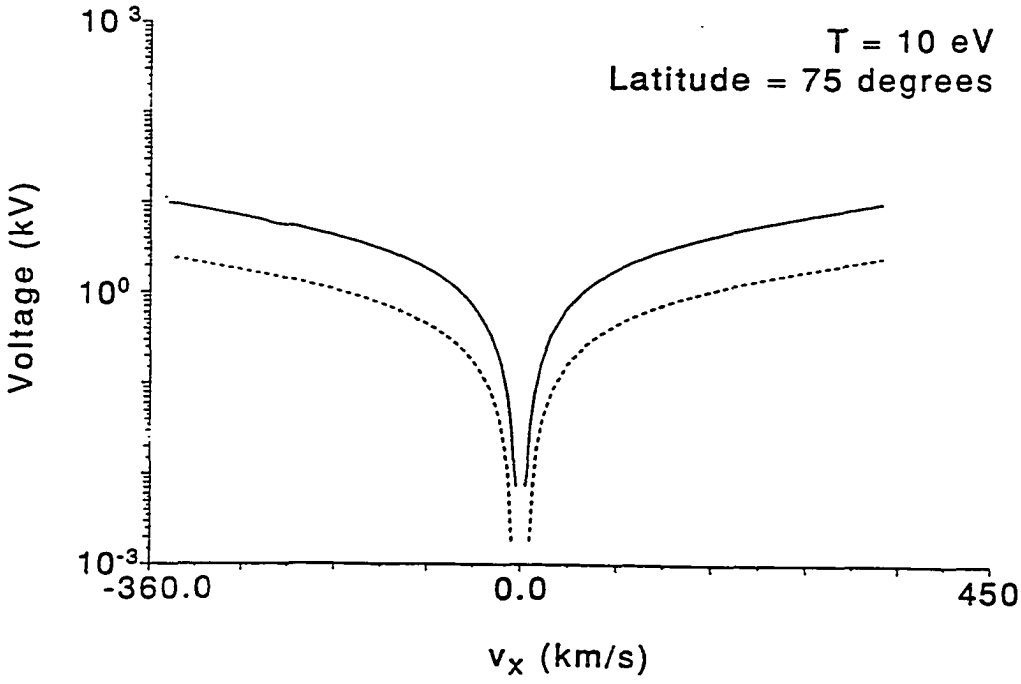

Figure 4.5 Plot of the 'effective' field aligned potential difference vs the x component of the particle's velocity. The 'effective' voltage is assumed to vary linearly with distance along the field line and increases from 0-10 kilovolts for O^+ (solid curve) and 0-2.5 kilovolts for He^+ (dashed curve). Both ions have source energies of 10 eV and initially located at a base latitude of λ_0=75 deg.

O^+ and He^+ we examine how the scattering rates would vary if the ions are energized along their orbits. Also, it is of interest to determine the extent to which these energy inputs can lead to maximum scattering rates or resonance conditions.

To contrast the effect on the scattering rates for He^+ and O^+ we consider motion along field lines in the noon-midnight plane. The ionospheric boundary is defined at 1.157 R_e. We assume that the total energy and magnetic moment of the particle is conserved. In the total energy expression the gravitational and electrostatic potential energies are included. The relevant expressions are listed in Eqs. (4.10)-(4.14) and will be described later in Sec. 4.5. While not advocating that an actual linear gradient of potential difference exists along the field line, we have, nevertheless assumed so for convenience. To distinguish this assumed potential difference from any other we call it an 'effective potential difference'. To explain Fig. 4.5 we refer to Eqs. (4.10)-(4.14). The voltage or effective potential difference is defined by ϕ-ϕ_0. The component of the ion's velocity along x (ie. v_x) is obtained from Eq. (4.13) but neglecting the second term. Thus, Fig. 4.5 is obtained by inputting the voltages in Eq. (4.14) and calculating v_x using Eqs. (4.13) and (4.14). Without the effective potential difference the effects of the dipole field are accounted for in the unit vector along the field line $\hat{s}$. In Fig. 4.5 we show the effective potential difference plotted against the x component of the particle's velocity for the two ions. The solid curve refers to O^+ and shows the effective voltage to vary from 0-10 kV and the dashed curve refers to He^+ and the effective voltage varies from 0-2.5 kV. Knight (1973) assumed that if the thermal properties and density distributions of the electrons are different at both ends of a field line then the effective field aligned potential differences of up to 10 kilovolts are possible. The scattering rate as a function of v_x is shown in Fig. 4.6 for He^+ and O^+. The results in Fig. 4.6a show the scattering rate for He^+ (dashed) for the case when T=10 eV and λ_0=75 deg. The curve is symmetric about zero

velocity and decreases as v_x increases in both directions. Note that positive and negative values of v_x refer to motion towards and away from the sun, respectively. The scattering rate for O^+ (solid) is complicated by the structure of the solar profile for the 83.4 nm radiation. Since the He^+ ion has a single resonance line, Doppler effects would shift the ion's cross-section line center away from its solar line in both directions for v_x giving symmetrical values of the scattering rate and decreasing in magnitude with increases in v_x. The curve for O^+ has interesting features in that it contains dips and peaks in the scattering rate. Note that this section may contain some elements of previous work by Meier (1990) and Garrido et al. (1991) but detailed application towards energization of O^+ ions along field lines is presented for completeness.

Resonance peaks that give scattering rates that are comparable or greater in magnitude than that when v_x equals zero can also occur. The peaks in Fig. 4.6a (solid curve) for $v_x > 0$ occur roughly at 146, 204 and 257 km s^{-1} with effective voltages of 3.4, 5.02 and 6.7 kV, respectively, while for $v_x < 0$ the peaks occur at -61, -144, -218 and -301 km s^{-1} with effective voltages of 1.1, 3.3, 5.4 and 8.2 kV, respectively. Large decreases in the magnitude of the scattering rate occur between 28-106 km s^{-1} corresponding to the range of potential differences from 0.34 to 2.3 kV. Also for v_x greater than 290 km s^{-1} with impressed voltages greater than 7.7 kV the scattering rates are very low. Fig. 4.6b shows the case when T=100 eV and λ_0=75 deg. The He^+ curve shows a slower decline in the value of the scattering rate as v_x increases. The O^+ curve indicates that the maximum scattering rate can still be attained although the magnitudes are smaller compared to the case when T=10 eV. For both curves (He^+ and O^+), the slower decline in the magnitude of the scattering rate at certain range of values of v_x is due to the fact that at a higher temperature the cross-section profile of the ions is broadened so that when it's line center is shifted the overlap with the solar profile is greater than when it

is at a lower temperature. For the case of Fig. 4.6b the maximum resonance condition could not be obtained even though a large potential drop is present. Cladis (1986) has shown that the presence of an ionospheric convection electric field can also provide a mechanism that will energize and accelerate ions to higher energies. Thus, for the range of velocities obtained above we showed that the structure of the scattering rate for the O^+ (83.4 nm) and He^+ (30.4 nm) behave in a different way to different variations in v_x. Note also that in obtaining the scattering rate, we neglected the effects of gravity and rotation.

4.5 Kinetic Model

In previous sections simulated images were constructed based on a density profile that depends on a magnetic scaling factor and the scattering rate was also calculated for the case when the temperature was constant along the field lines. We also neglected the effects of the plasma corotating with the Earth. Lemaire and Scherer (1974) have shown that rotational effects can affect the distribution of densities in the outer regions of the magnetosphere. In this section, we describe the kinetic model due to Huang and Birmingham (1992). The model provides a simple expression for plasma density, incorporates temperature anisotropy, effects of gravity and rotation and also contains the magnetic scaling factor. We will also show that the effects of rotation on the scattering rate is small and can be neglected in the calculation of intensities.

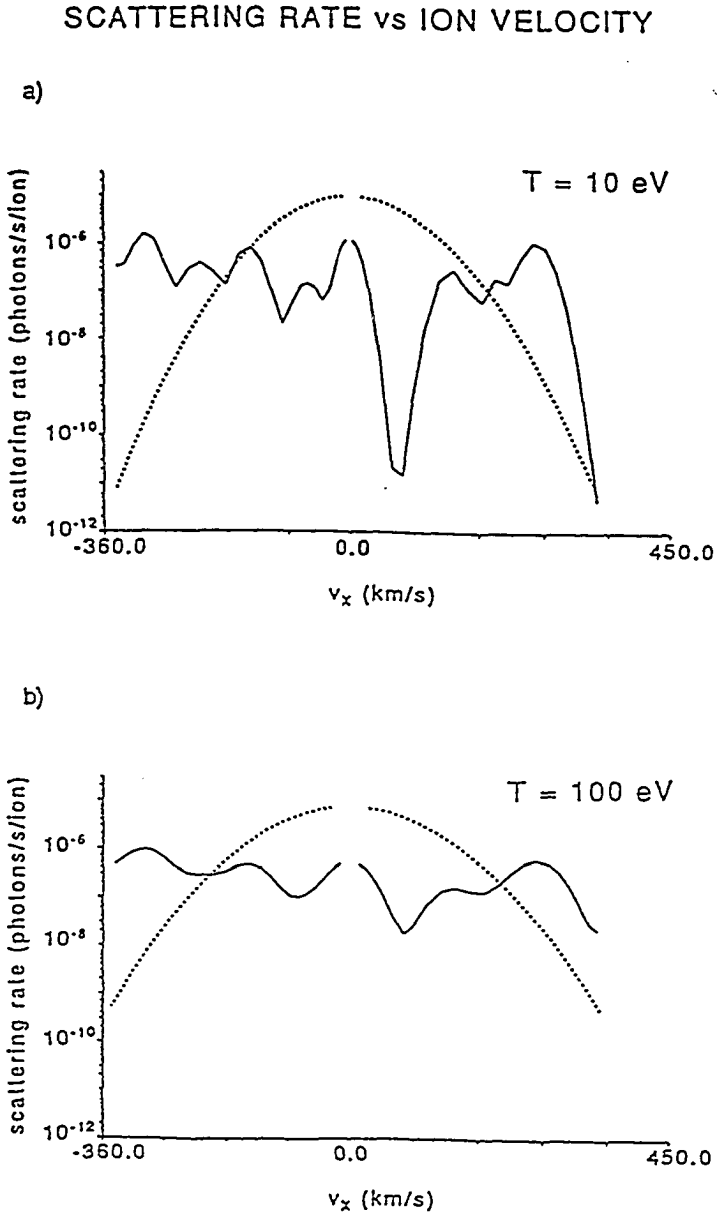

Figure 4.6 Plots showing the variation of the g-factor with v_x for motion along the field line for cases when T=10 eV and T=100 eV (λ_0= 75 deg). Fig. 4.6a represent the case when T=10 eV while Fig. 4.6b represent the case when T= 100 eV. The solid curve refers to O^+ and the dashed curve refers to He^+.

Huang and Birmingham (1992) derived expressions for the spatial distribution of densities of ions and electrons along a field line by assuming the particle velocity distribution has a bi-Maxwellian form with a given parallel and perpendicular temperature. By application of Liouville's Theorem in conjunction with the conservation of energy and magnetic moment they showed that the parallel temperature remains constant

$$T_{\|} = T_{\|0} \tag{4.6a}$$

and the perpendicular temperature varies along the field line as

$$T_{\perp} = T_{\perp 0} \frac{1}{[\frac{1}{\gamma_0} + (1 - \frac{1}{\gamma_0})\eta]} \tag{4.6b}$$

$$\gamma_0 = \frac{T_{\|0}}{T_{\perp 0}} \tag{4.6c}$$

$$\eta = \frac{B_0}{B}, \tag{4.6d}$$

where $T_{\|0}$ and $T_{\perp 0}$ are parallel and perpendicular temperatures at the reference altitude, respectively. The density distribution along the field line can be written as

$$n = n_0 \frac{T_{\perp}}{T_{\perp 0}} e^{\frac{-m\Delta v^2}{2kT_{\|0}}} e^{-\chi} \tag{4.7}$$

and can be recast in the form

$$n = n_0 \epsilon \frac{B}{B_0} e^{-\chi} e^{\frac{-m\Delta v^2}{2kT_{\|0}}} \tag{4.8}$$

$$\epsilon = \frac{1}{[1 + \frac{1}{\gamma_0}(\frac{1}{\eta} - 1)]} \tag{4.9a}$$

$$\chi = \frac{e\Delta\psi}{kT_{\|0}} \tag{4.9b}$$

$$\Delta\psi = \phi - \phi_0, \tag{4.9c}$$

where k=Boltzmann constant, ϕ=electric potential and n_0 is the source density.

Northrop and Birmingham (1982) showed also that the conservation of energy can be written as

$$v^2 = v_0^2 + \frac{2e}{m}(\phi_0 - \phi) - \Delta v^2 \tag{4.10}$$

$$\Delta v^2 = 2C_0(1 - \frac{r_0}{r}) - \Omega^2 r^2(1 - \frac{r_0^2 \cos^2 \lambda_0}{r^2 \cos^2 \lambda}) \tag{4.11}$$

$$C_0 = \frac{GM}{r_0}, \tag{4.12}$$

where G, M and λ are the gravitational constant, Earth's mass and latitude, respectively. Also, m is the ion mass and Ω is the angular frequency of the Earth's rotation. The ion's bulk velocity can be written as

$$\mathbf{v} = v_{\parallel}\hat{s} + \mathbf{v}_{\perp} + \mathbf{\Omega} \times \mathbf{r}, \tag{4.13}$$

where $v_{\perp}^2 = \frac{v_{\perp 0}^2}{\eta}$ and $\hat{s}$=unit vector along the field line directed away from the ionosphere and the parallel velocity is given by

$$v_{\parallel}^2 = v_{\parallel 0}^2 + v_{\perp 0}^2(1 - \frac{1}{\eta}) + \frac{2e}{m}(\phi_0 - \phi) - \Delta v^2. \tag{4.14}$$

The 'zero' subscript labels quantities at the reference altitude r_0. Note that by assuming the distribution to have a temperature anisotropy, we are able to obtain an expression for the density distribution that contains the magnetic scaling factor and the effects of gravity and rotation. Note, that Eqs. (4.8) and (4.9a) were included above to show the difference in form of the density profile from Eq. (4.3) that contains only the magnetic scaling factor.

For comparison purposes we show in Fig. 4.7 the variation of the ion density along the field line using the model described in Eq. (4.7) and the model described by Eq. (4.3). At an altitude of 1000 km and λ_0=75 deg and for $T_{\|0}$=10 eV, γ_0=2 and $J_0 = 2.7 \times 10^6$ ions cm^{-2} s^{-1} we get a source density of 2.47 ions cm^{-3}. Note that the above value for J_0 is typical of values for a source located within the latitude range 65-75 deg. During disturbed conditions a maximum flux intensity of 2.28×10^8 ions cm^{-2} s^{-1} leads to a source density of 200 ions cm^{-3}. The model density described by Eq. (4.3) that depends on the magnetic scaling factor (dashed curve) decreases faster with distance along the field line than the bi-Maxwellian model density described by Eq. (4.7) (solid curve) for the parameters assumed above. Assuming the same conditions in the calculation of the scattering rate the bi-Maxwellian model density gives a larger contribution to the intensities from sources in the outer magnetosphere than when using the model with a magnetic scaling factor.

The earlier model Eq. (4.3) used to describe Figs. 4.2 and 4.3 was presented for historical reasons. As described in the last paragraph of the Introduction, the present article is an extension of the work done by Chiu et al. (1990). They used a density model that contains the magnetic scaling factor while the model discussed in this section is presented to show from a more elaborate analysis how a density profile with the magnetic scaling factor can be obtained. Other features like rotation, gravitation and electric field are also present. We have shown that the model described here gives a higher estimate for the emission rate than the simple model of Eq. (4.3).

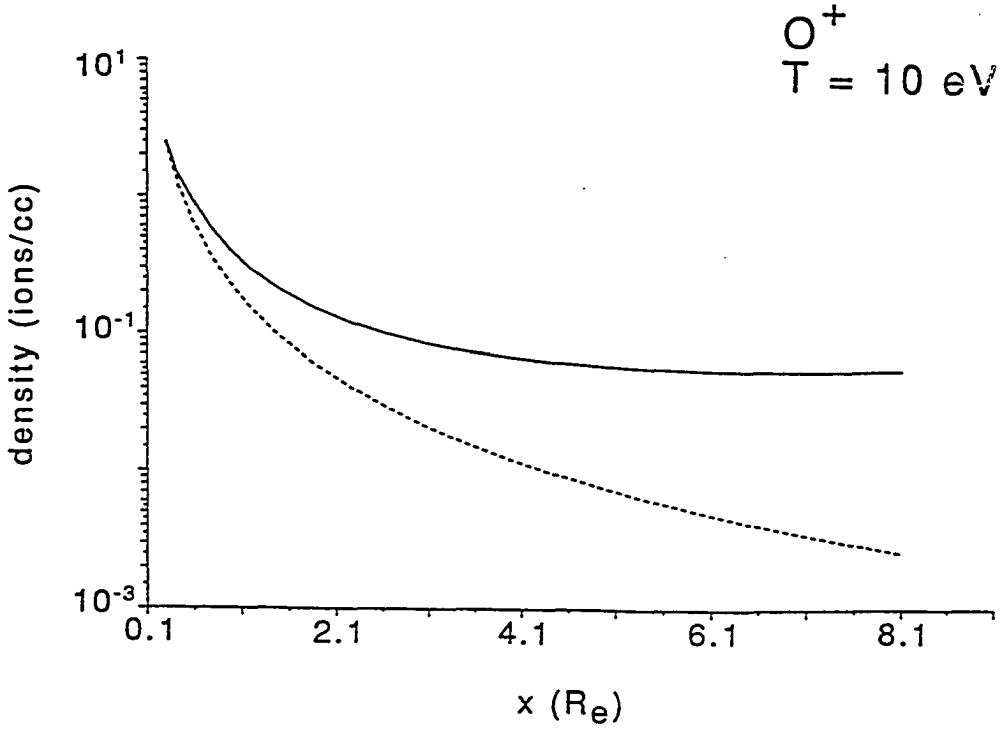

Figure 4.7 Plot of the variation of the ion density of O^+ along the field line versus the x component of the position along the field line. The solid curve refers to the density profile using a bi-Maxwellian distribution and the dashed curve represents the density profile using a magnetic scaling factor.

Effects of Rotation on the Scattering Rate

To illustrate the effects of rotation on the scattering rate we consider ions with $T_{\|0}$=10 eV moving up along field lines in the meridian plane defined by ϕ=135 and ϕ=315 deg. In our coordinate system ϕ=0 points sunward and ϕ=90 deg is directed towards dusk. Assume also that a small parallel electric field equal to .5 μV/m is present along the field line and that the dipole and rotational axis coincide. The x component of the velocity that causes a Doppler shift of the absorption line center away from the solar line center can be obtained from Eq. (4.13). The contribution from the term $v_\perp$ decreases rapidly along the field line and can be neglected, however, the effects of rotation tend to increase the magnitude of the scattering rate for large values of r. We show in Figs. 4.8a and 4.8b plots of the scattering rate vs the x component of the ion's position along the field line for the case when $T_{\|0}$=10 and 50 eV, respectively. The solid curve refers to the case when rotation is present and the dashed curve refers to the case with no rotation. Positive values of x identify the field line defined by ϕ=315 deg and negative values of x refer to the field line defined by ϕ=135 deg. Both figures indicate that the scattering rate is larger for the case when rotation is included. Results of our calculation show that at the point x=5.5 R_e we obtained (with rotation, solid curve) the values v_x=15.2 km s^{-1} and g=5.47$\times 10^{-7}$ photons s^{-1} ion^{-1} and without rotation (dashed curve) v_x=17.72 km s^{-1} and g=4.2$\times 10^{-7}$ photons s^{-1} ion^{-1}, respectively. Note that the effects of rotation tend to decrease the magnitude of v_x (within the range of distances assumed in this paper) hence leading to a larger scattering rate. The effects of rotation are greatest in the dawn to dusk meridian plane and least in the noon-midnight plane. For the case when $T_{\|0}$=50 eV, the scattering rate tends to decrease faster with distance compared to the case when $T_{\|0}$=10 eV. Thus, the effect of rotation on the scattering rate is small compared to the effect due to Doppler shifts, and can be neglected in the calculation of intensities.

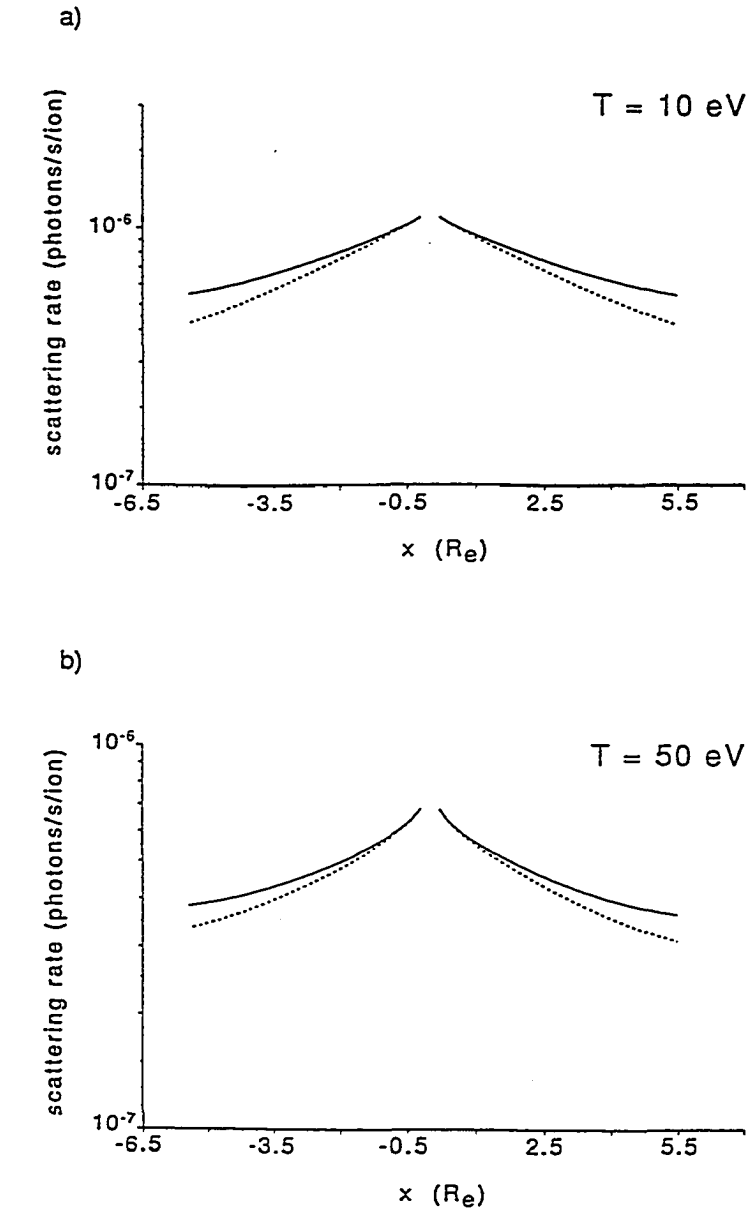

Figure 4.8 Plots of the scattering rate of O^+ vs the x component of position along field line. The solid curve refers to the model calculation with rotation and the dashed curve refers to the case with no rotation. Fig. 4.8a represent the case when T=10 eV and Fig. 4.8b refers to the case when T=50 eV.

4.6 Observational Effects Due to Parallel Acceleration

The high latitude regions where energetic ion outflows occur as a result of the auroral acceleration process is fertile ground from which the dynamics of ion transport and energization can be studied. Horwitz (1987) modeled ion transport of O^+ ions into the outer magnetosphere using a kinetic model that assumes a bi-Maxwellian source distribution at a reference altitude of 3000 km. He calculated bulk parameters of ion density and parallel velocities for different source energies and applied convection electric field. The radial decline of the source densities and the increase in parallel velocities of the ions out in the tail are in reasonable agreement with observations. He assumed the energization process to occur over a small latitude range in the polar cap from 70 to 80 deg. From the results of his simulations and also observations of Candidi et al. (1982) tailward velocities of O^+ from 50 to 250 km s^{-1} have been reported. Thus, in the high latitude regions the ions can be energized to high parallel velocities and the discussion in Sec. 4.4 shows that for O^+ ions such a range of velocities can affect the ion's ability to resonantly scatter photons as they accelerate relative to the sun.

In this section we study how the large decrease in magnitude of the scattering rate can be observed optically from emissions of accelerating O^+ (83.4 nm) ions. To simulate the acceleration process, we energize the ions at each step along its orbit in energy units $\Delta E = E_0(\frac{s}{l})$ where E_0=1.6 keV and s is the distance of the ions along the field line measured from the ionosphere and l is the total length of the field line. For the latitude range assumed , l is of the order of 11 R_e. Note that when s=0, ΔE=0 and at the end of our boundary (s=l), we have $\Delta E = E_0$. Parallel velocities can be calculated by modifying Eq. (4.14), replacing the term $2\frac{e}{m}(\phi_0 - \phi)$ by $\frac{2}{m}\Delta E$. The magnitude of the parallel velocities obtained are consistent with the results of Horwitz. In constructing an

image, we adopt the density profile described in Sec. 4.5 but modified by setting χ=0. The decline of the source densities along the field line is in qualitative agreement with the simulations of Horwitz and the density scatter diagrams of Candidi et al. (1982). Using the EICS data, we get source densities from 3 to 200 ions cm^{-3} and densities of 0.02 to 4 ions cm^{-3} in the tail at a distance of 10 R_e. Our model does not assume particle drifts perpendicular to the field lines as a result of the convection electric field and our aim is not to reproduce the 'tongue' features in the density contours obtained by Horwitz. Assuming that a steady convection of ions occurs, eventually in time, the magnetosphere will be populated with ions with different temperatures and parallel velocities reflecting their energization. When the ions are accelerated to high velocities, Doppler effects on the scattering rate can result in very low intensities. Our aim is to show that such effects may be seen optically in 83.4 nm. Our model does not reflect the exact distribution of spatial densities along field lines and we are not concerned in obtaining the exact structure of the magnetospheric image. If we assume that there are no major depletions in the ion densities as a result of the energization process, the rapid decline in the image brightness will be due to the resonance dip in the scattering rate for O^+.

The effects of particle energization on the scattering rate for O^+ ions with source energies T=10, 20, 50 and 100 eV is shown in Fig. 4.9. Note, that Fig. 4.6 shows how the scattering rate varies with v_x as the ion moves along the field line. These figures, however, emphasize the difference in response of the scattering rates for He^+ (30.4 nm) and O^+ 83.4 nm to Doppler shifts caused by the ions' motion along the field lines. However, in Fig. 4.9 (gravitational and rotational terms included) we emphasize the relative changes in the scattering rate with temperature variations. The scattering rate is plotted vs v_x to reflect the motion in the dayside ($v_x > 0$) and motion in the night sector ($v_x < 0$). The scattering rate for negative velocities is roughly within an order of magnitude of the

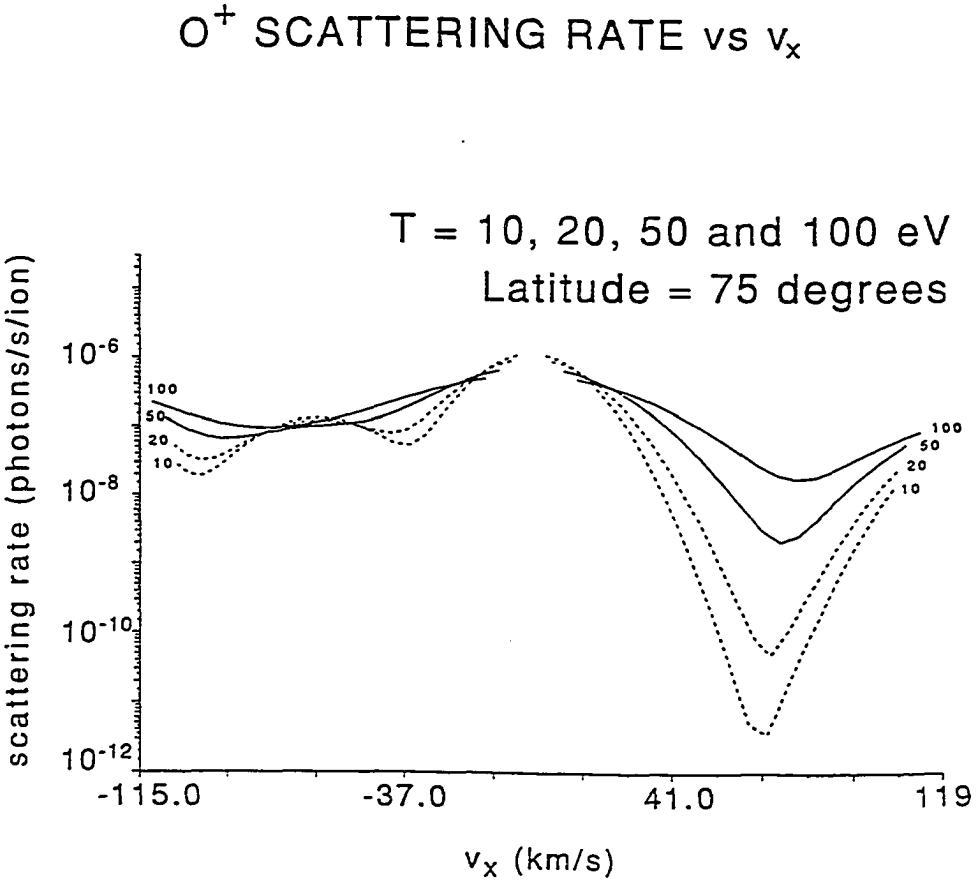

Figure 4.9 Plot showing the variation of the O^+ scattering rate versus v_x for various source energies T=10, 20, 50, and 100 eV. The dashed curves refer to the case when T=10 and 20 eV and the solid curve refers to the case when T=50 and 100 eV. The ions are assumed to be energized from 0 eV at the foot of the field line at base latitude λ_0=75 deg to 1.6 keV at the end of the field line.

maximum scattering rate while for positive velocities, resonance wells in the scattering rate occur at velocities from 67 to 78 km s^{-1}. The decline in magnitude of the scattering rate is significant for ions with temperatures T=10, 20 or 50 eV. The maximum scattering rate occurs at 1.07×10^{-6} photons s^{-1} ion^{-1} (T=10 eV) and for the 10 and 20 eV ions we obtained minimum scattering rates of 3.65×10^{-12} and 5×10^{-11} photons s^{-1} ion^{-1}, respectively. For the 50 and 100 eV ions we get 2.16×10^{-9} and 1.75×10^{-8} photons s^{-1} ion^{-1}, respectively. To see the effect on a magnetospheric image, we consider a thin region in the polar cap defined by the latitude range from λ_0=70-80 deg where acceleration of the particles is assumed to take place. We assume the spatial distribution of densities along the field lines is described by the kinetic model in Sec. 4.5 while parallel velocities are obtained using Eq. (4.14). We also assume that the densities are symmetric about the equator.

Figures 4.10 and 4.11 show images of 83.4 nm scattered light assuming the only source of illumination is sunlight. We recognize that the ionosphere will provide additional source of illumination but we have ignored it here in our simulations. Hence, in this sense, the O^+ (83.4 nm) intensities are lower limits of what should be expected. Our aim in Figs. 4.10 and 4.11 is to show what to expect in the image intensities using available information on the ion scattering rates and observations made on the density distribution of the ions. The efficiency of the scattering rate for the 83.4 nm line is very sensitive to Doppler shifts at certain values of v_x and we have shown that in regions where bulk acceleration may occur we expect a sudden drop in the emission rate of the ions. Although emission rates from the outflowing regions may be small based on our present analysis we recognize that it is technologically possible to detect these weak emissions given sufficient integration time. Fig. 4.10 also reconsiders the case of Fig. 4.3b when $T_{\|0}$=10 eV for the outflowing O^+ ions. However, we have included an acceleration region

in latitudes ranging from 70 to 80 deg and a small parallel electric field (.5 μV/m) is applied. Fig. 4.10 shows a maximum intensity of 1.05 R and its image structure does not vary very much from Fig. 4.3b despite proper accounting of Doppler shifts due to acceleration. However, for pixels described by ETA > 15 deg the image brightness in Fig. 4.10 is more enhanced than that of Fig. 4.3b indicating that the density model in Sec. 4.5 results in a higher estimate of the intensities at larger distances from the poles.

In describing Fig. 4.11 we will refer to Fig. 4.10 for comparison purposes. Figs. 4.11a and 4.11b show simulated images of the magnetosphere for the case when $T_{\|0}$=10 and 50 eV and have maximum intensities of 1.05 and 1.03 Rayleighs, respectively. In Figs. 4.11a and 4.11b we have assumed the energization to take place in flux tube regions defined by latitudes 70 to 80 deg while in Figs. 4.11c and 4.11d the acceleration region occurs at lower latitudes (65 to 75 deg). The results shown in Figs. 4.11c and 4.11d are for the cases when $T_{\|0}$=10 and 50 eV, respectively. Figs. 4.11c and 4.11d also show maximum intensities of 1.05 and 1.03 Rayleighs, respectively. We see that the image brightness in Figs. 4.11a to 4.11d has decreased significantly in contrast with Fig. 4.10 in those flux tubes where energization occurs. Note, also that for pixels defined by ETA > 10 deg, in those flux tube regions where energization occurs, the image brightness in Fig. 4.11b (T= 50 eV) is more enhanced than that of Fig. 4.11a (T= 10 eV). Fig. 4.9 shows that the scattering rate at T=10 eV decreases faster with v_x than when T= 50 eV. A similar conclusion holds for Figs. 4.11c and 4.11d, in that the effects of energization in the image intensities also show up in flux tube regions at lower latitudes.

For clarity, the images in Figs. 4.10 and 4.11a were obtained by using the same density model described in Sec. 4.5 and the same viewing geometry as in Fig. 4.3. In the calculation of the ion scattering rate Doppler effects due to v_x are taken into account by replacing ϕ_0-ϕ by $E_{||}$ s in Eq. (4.14) where s is the arc length distance along the field lines. The image intensities in Fig. 4.10, however, do not show a significant change in brightness in those flux tube regions where energization has been assumed to take place. In Fig. 4.11a (also true in Figs. 4.11b to 4.11d) the ions are energized according to the discussion in Sec. 4.6 (see also Fig. 4.9). The image intensities in Fig. 4.11a now show a marked decrease in image brightness in those flux tube regions where energization was assumed to take place in contrast with that of Fig. 4.10.

4.7 Discussion

In our analysis of the images of He^+ (30.4 nm) and O^+ (83.4 nm) we have ignored contributions from the ionosphere and have focused only on regions above 1000 km. Inclusion of the scattered sunlight from the ionosphere would increase the total brightness of our images for both lines but would not alter the conclusions in this paper. In the images of the 83.4 nm line, we also neglected the plasmasphere and the effects of multiple scattering. Images of the plasmasphere in both 30.4 nm and 83.4 nm have also been obtained by Gladstone (1992). See also Roelof and Mauk (1992). The intensities in the images for O^+ are underestimated because we have neglected ionospheric and plasmaspheric sources. Gladstone estimated the emissions from plasmaspheric and upflowing O^+ ions to be in the range from .1 to 1 R. For the high latitude regions our estimates of the emission rates may be reasonable. The ion density models we have used are consistent with observations of ion densities.

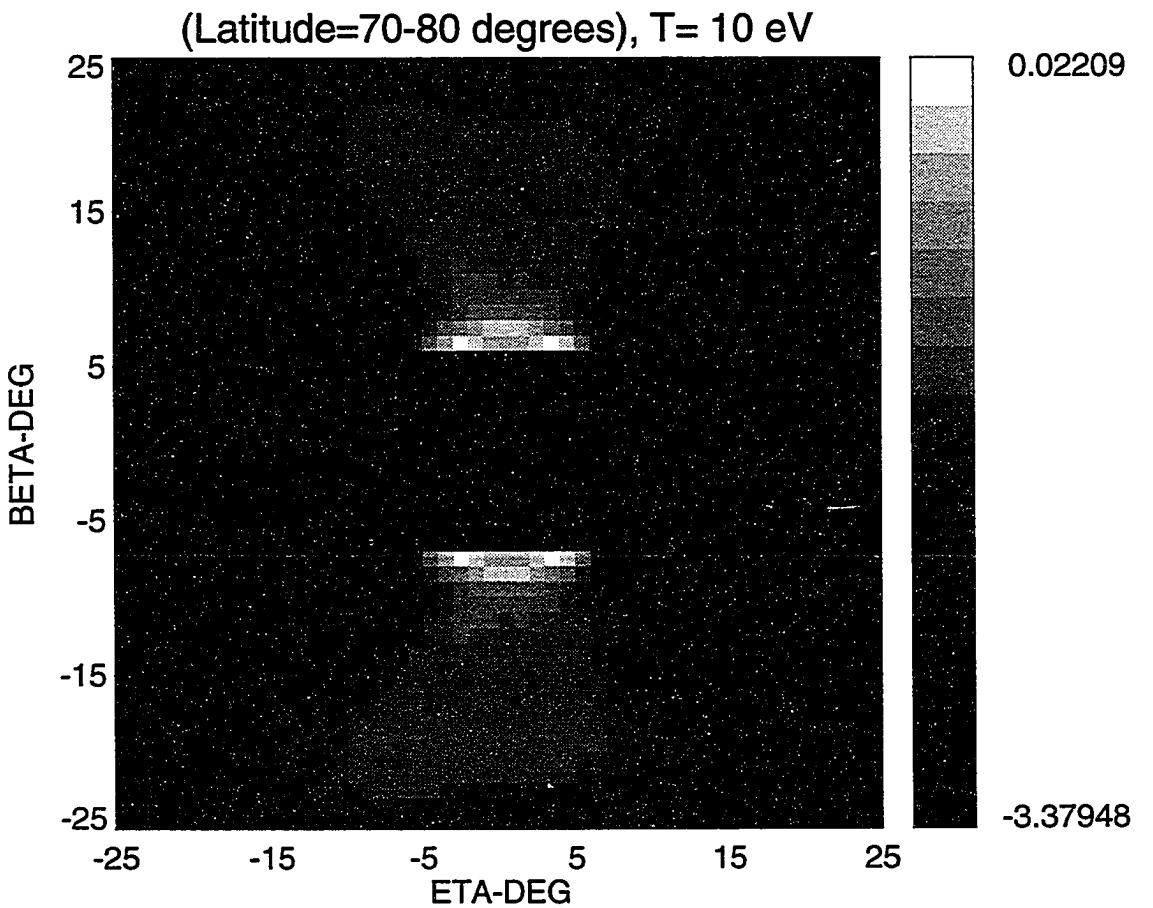

Figure 4.10 Magnetospheric image of O^+ (83.4 nm) emissions with a small applied parallel electric field. The density distribution for outflowing ions is bi-Maxwellian. Acceleration due to a small applied parallel electric field (.5 μV/m) is assumed to occur over the latitude range from 70 to 80 deg in the polar cap. The satellite has coordinates (0,9,0) and is viewing towards the center of the Earth. The Sun is to the left of the figure. The grey scale values are in $\log_{10}$(Rayleighs). Compare with Fig. 4.3b.

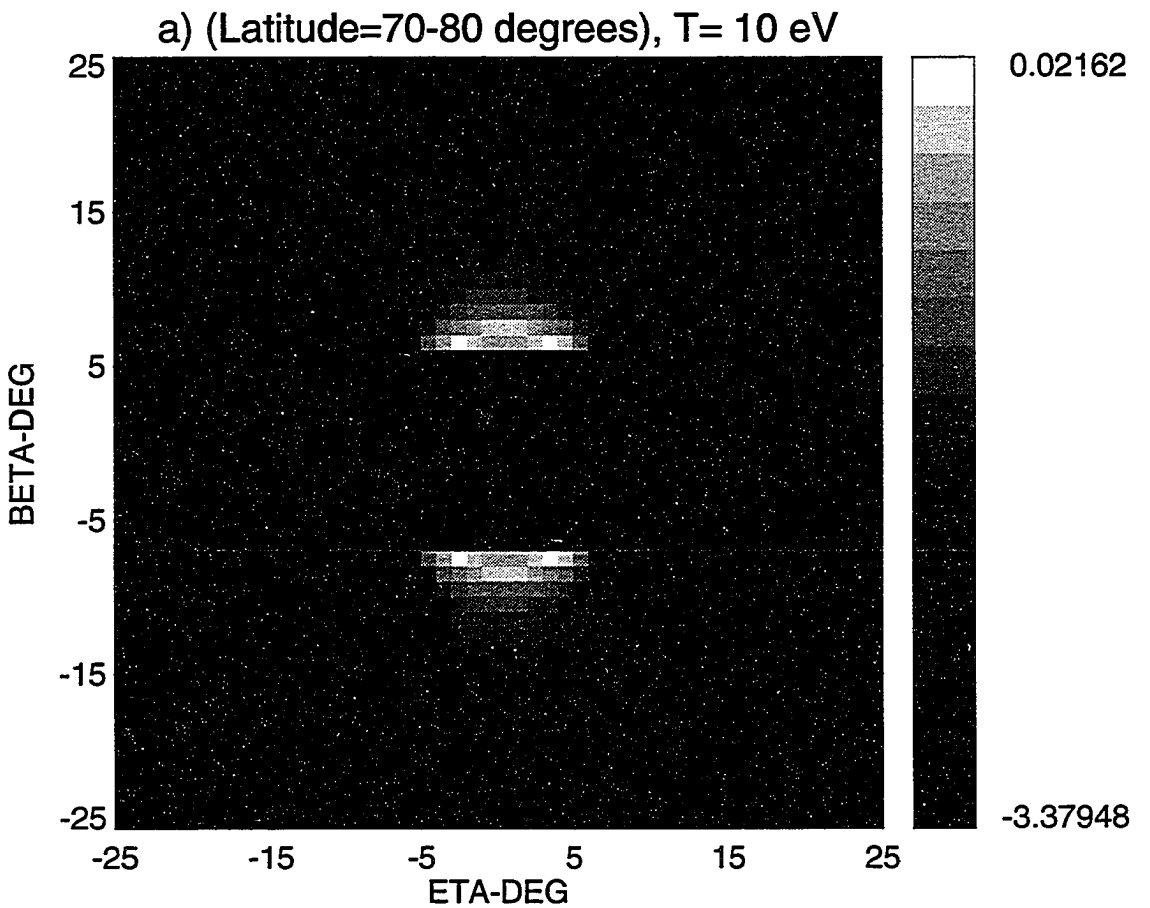

Figure 4.11a Magnetospheric image of O^+ (83.4 nm) emissions during disturbed times and acceleration occurs over the latitude range from 70 to 80 deg for ions with a source energy of 10 eV. Ions are assumed to be energized from 0 eV to 1.6 keV along the field lines. Doppler effects due to ion drifts have been taken into account. The grey scale values are in $\log_{10}$(Rayleighs). The satellite has the same viewing geometry as in Fig. 4.10.

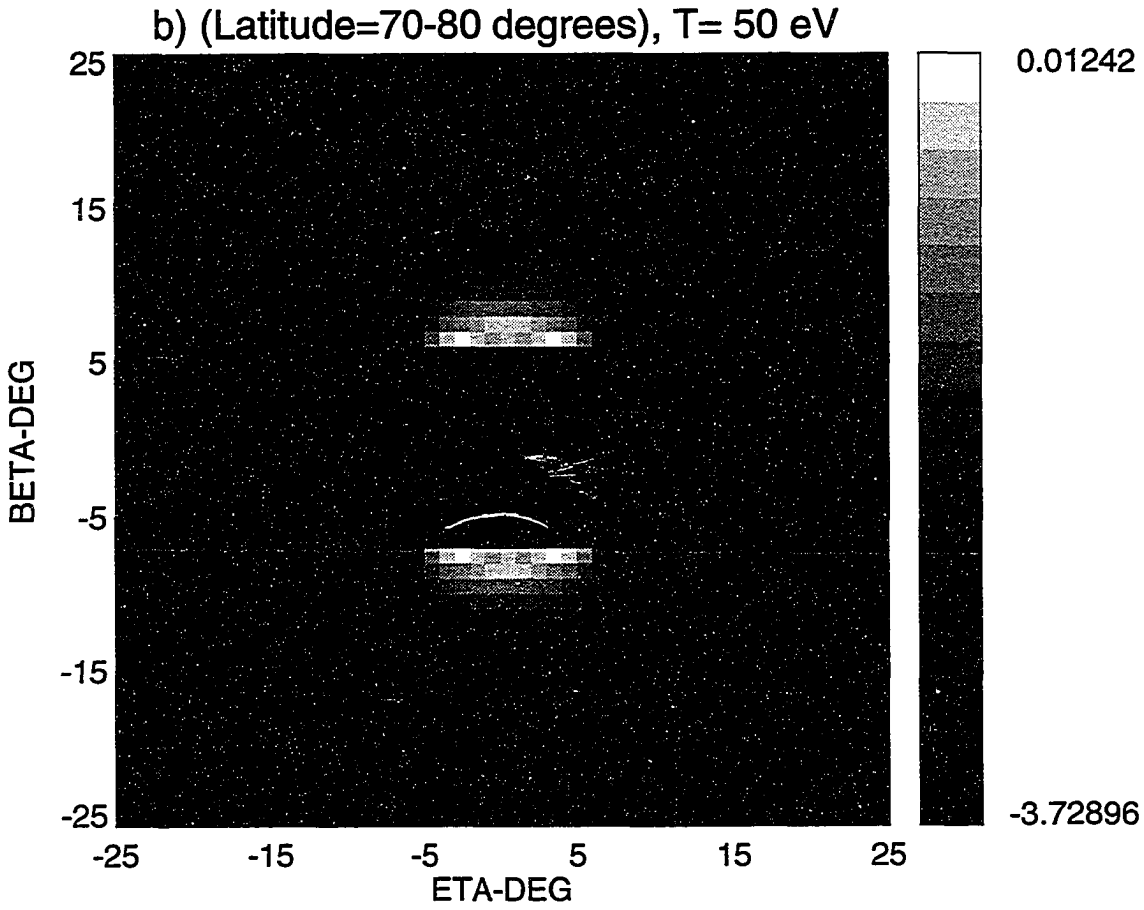

Figure 4.11b Magnetospheric image of O^+ (83.4 nm) emissions during disturbed times and acceleration occurs over the latitude range from 70 to 80 deg for ions with a source energy of 50 eV. Ions are assumed to be energized from 0 eV to 1.6 keV along the field lines. Doppler effects due to ion drifts have been taken into account. The grey scale values are in $\log_{10}$(Rayleighs). The satellite has the same viewing geometry as in Fig. 4.10.

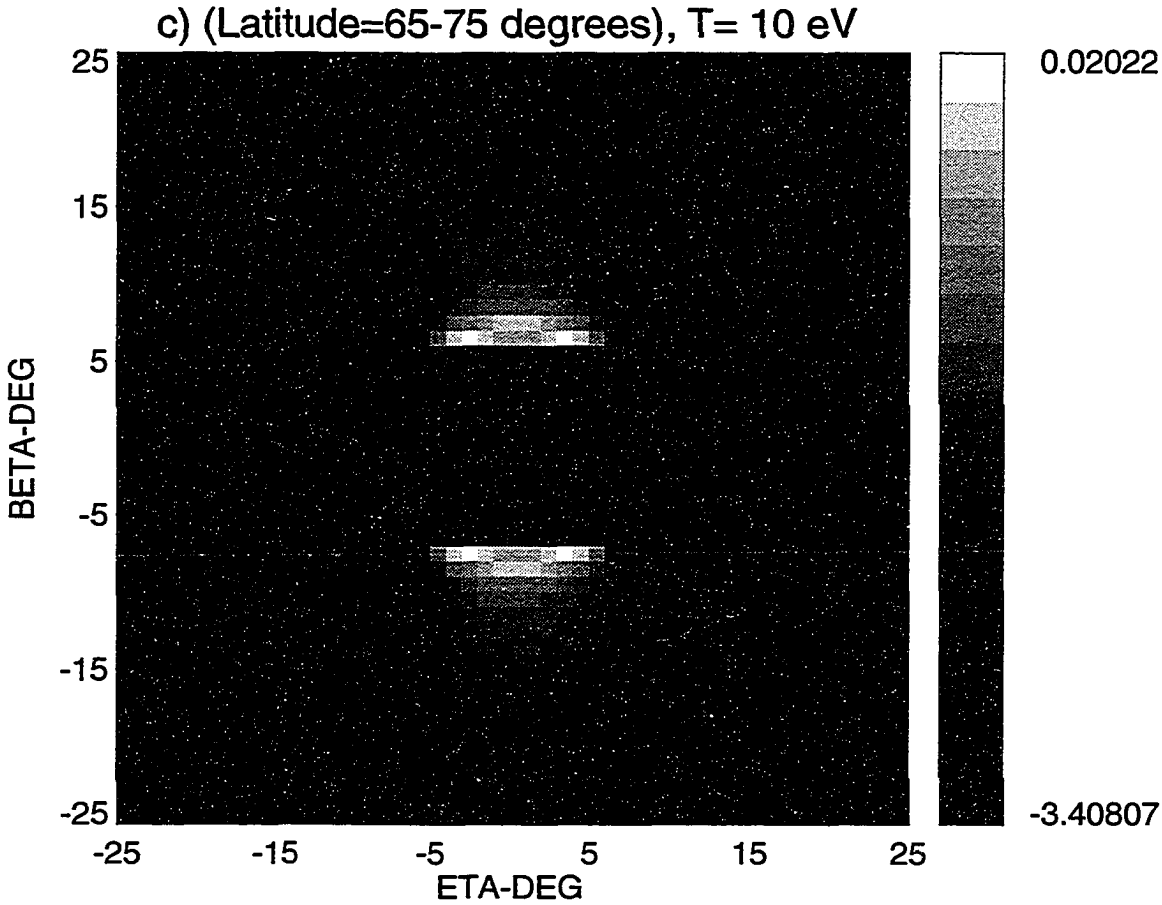

Figure 4.11c Magnetospheric image of O^+ (83.4 nm) emissions during disturbed times and acceleration occurs over the latitude range from 65 to 75 deg for ions with a source energy of 10 eV. Ions are assumed to be energized from 0 eV to 1.6 keV along the field lines. Doppler effects due to ion drifts have been taken into account. The grey scale values are in $\log_{10}$(Rayleighs). The satellite has the same viewing geometry as in Fig. 4.10.

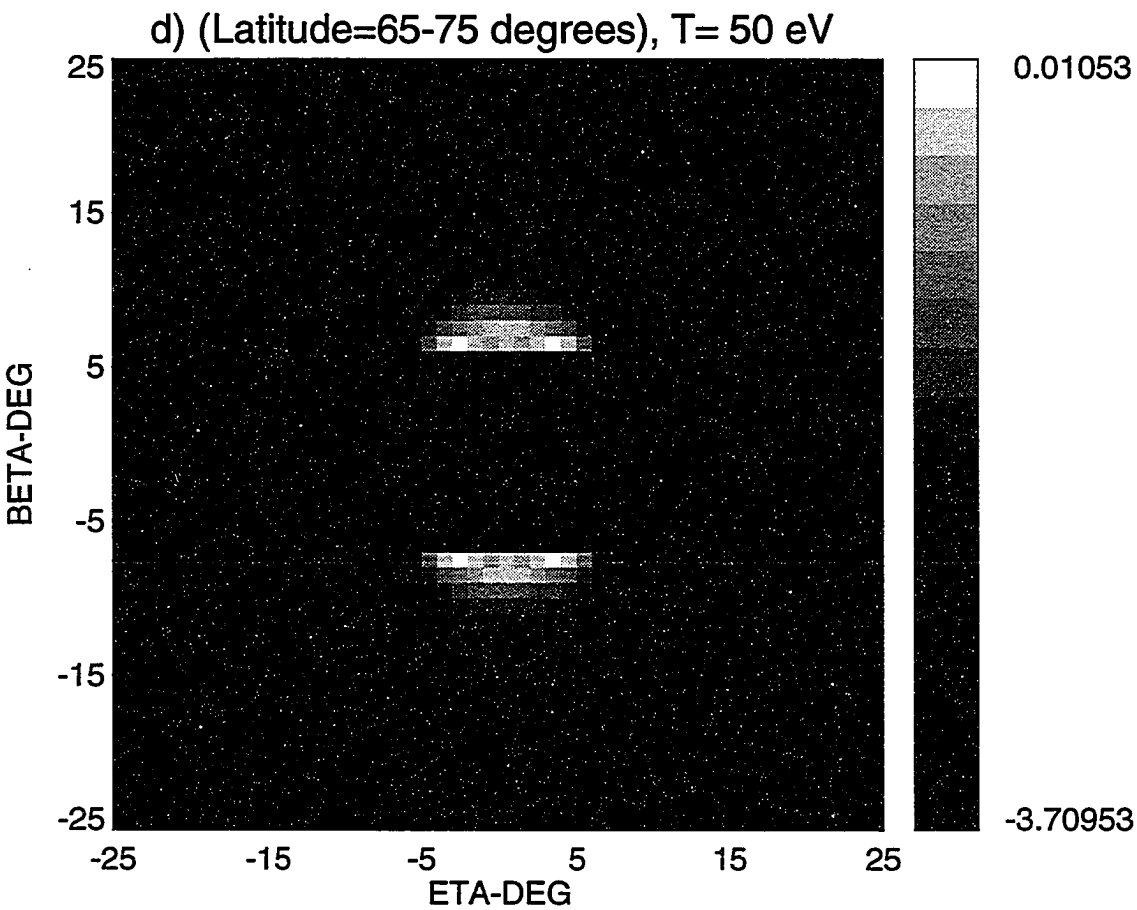

Figure 4.11d Magnetospheric image of O^+ (83.4 nm) emissions during disturbed times and acceleration occurs over the latitude range from 65 to 75 deg for ions with a source energy of 50 eV. Ions are assumed to be energized from 0 eV to 1.6 keV along the field lines. Doppler effects due to ion drifts have been taken into account. The grey scale values are in $\log_{10}$(Rayleighs). The satellite has the same viewing geometry as in Fig. 4.10.

4.8 Conclusions

We have constructed images from resonant emissions of upward flowing He^+ (30.4 nm) and O^+ (83.4 nm) ions at high latitudes taking into account the non-uniform flux intensity distribution of the source obtained from the Lockheed EICS instrument on board the DE-1 spacecraft and also have contrasted the images during quiet and disturbed geomagnetic conditions.

An imager viewing at an equatorial distance of 9 R_e or more is in a favorable position to see the regions of ion outflow. Observations made during times when the plasmapause is depressed make conditions favorable in detecting emissions from the outflowing ions. However, it is necessary to include an occultation disk in the detector to mask the bright emissions coming from plasmaspheric He^+ (30.4 nm) ions.

A satellite with an orbit attitude configuration similar to that used in Weller and Meier (1974) was used to measure emission rates, and maximum intensities obtained are low (less than 0.1 R) thus requiring high sensitivity instruments for imaging ion outflows. Photometry from polar orbiting satellites at altitudes greater than 1000 km is a means of remotely sensing energetic ion outflows.

The large drift velocities of He^+ and O^+ ions relative to the sun cause the scattering rates of the ions to behave in a different way showing that the scattering rate for He^+ (30.4 nm) decreases slowly with increasing velocity compared to that of O^+ (83.4 nm) ions. When O^+ (83.4 nm) ions are accelerated to velocities from 67 to 78 km s^{-1} a very large drop in the ion's scattering rate occurs resulting in a very low intensity emission. The sudden drop in image brightness is detectable in the simulated images. Note that the acceleration of ions in the high latitude regions represents a dynamic process that

can be observed in an image of the outflowing ions. We have demonstrated this effect in our simulations for the O^+ (83.4 nm) ions.

The emphasis in this paper is placed on the simulation of images of outflowing ions assuming the exclusion of the nearby bright plasmaspheric emissions. The data base used is confined to that of energetic ion upflows. Total ion data, upflow plus trapped populations, are known to be of much higher density, especially in the crucial regions of the plasma trough and plasmapause. We plan to examine such data in the near future.

Ion gyromotion has also been neglected in our analysis. We have assumed that the ion motion is described mostly by their parallel velocities because our aim is to show the maximum effects on the scattering rates due to Doppler shifts along the Sun-Earth line. If significant gyromotion takes place with pitch angle equal to 45 deg (for instance) the scattering efficiency may increase. Since the scattering rate for He^+ (30.4 nm) decreases very slowly with v_x we believe that the effects of ion gyromotion will be small. Ion gyromotions using realistic magnetic field geometry (Tsyganenko, 1989) and models that include the external convection electric field (Cladis, 1986) should be considered in obtaining realistic density profiles in constructing the images, thus allowing us to understand better the dynamics of ion transport into the outer magnetosphere via the images and hence enhancing our understanding of ionospheric-magnetospheric coupling processes.

4.9 References

Binsack, J.H., Plasmapause Observations with the MIT experiment on Imp 2, *J. Geophys. Res.*,**72**, 5231-5237, 1967.

Brandt, J.C. and J.W. Chamberlain, Interplanetary gas, 1, Hydrogen radiation in the night sky,*Astrophys J.*,**130**, 670-682, 1959.

Candidi, M., S. Orsini and V. Formisano, The Properties of Ionospheric O^+ ions as observed in the Magnetotail Boundary Layer and Northern Plasma Lobe, *J. Geophys. Res.*, **87**, 9097-9106, 1982.

Chiu, Y.T., R.M. Robinson, H.L. Collin, S. Chakrabarti and G.R. Gladstone, Magnetospheric and Exospheric Imaging In The Extreme Ultraviolet, *Geophys. Res. Lett.*, **17**, 267-270, 1990.

Cladis, J.B., Parallel Acceleration And Transport of Ions From Polar Ionosphere To Plasma Sheet, *Geophys. Res. Lett.*, **13**, 893-896, 1986.

Collin, H.L., W.K. Peterson, J.F. Drake and A.W. Yau, The Helium Components of Energetic Terrestial Ion Upflows: Their Occurrence, Morphology and Intensity, *J. Geophys. Res.*, **93**, 7558-7564, 1988.

Garrido, D.E., R.W. Smith, D.W. Swift and S.-I. Akasofu, Imaging The Earth's Magnetosphere: Effects of Plasma Flow and Temperature, *Planet. Space Sci.*, **39**, 1559-1571, 1991.

Gladstone, G.R., Simulated images of the plasmasphere, *Instrumentation for Magnetospheric Imagery*, S. Chakrabarti, Editor, Proc. SPIE 1744, 171-176, 1992.

Gombosi, T.I. and T.L. Killeen, Effects of Thermospheric Motions on the Polar Wind: A Time-Dependent Numerical Study, *J. Geophys. Res.*,**92**, 4725-4729, 1987.

Hoffman, J.H., W.H. Dodson, C.R. Lippincott and H.D. Hammack, Initial Ion Composition Results From Isis 2 Satellite, *J. Geophys. Res.*, **79**, 4246-4251, 1974.

Horwitz, J.L., Model For The Geomagnetic Ion Spectrometer In The Magnetotail Lobes, *Magnetotail Physics*, Anthony T.Y. Lui, Ed., 291-294, Johns Hopkins University Press, 1987.

Huang, T.S. and T.J. Birmingham, The Polarization Electric Field and Its Effects in an Anisotropic Rotating Magnetospheric Plasma,*J. Geophys. Res.*, **97**, 1511-1519, 1992.

Knight, L., Parallel Electric Fields, *Planet. Space Sci.*, **21**, 741-750, 1973.

Lemaire, J. and M. Scherer, Exospheric Models of The Topside Ionosphere, *Space Sci. Rev.*, **15**, 591-640, 1974.

Meier, R.R., The Scattering Rate of Solar 834 A Radiation By Magnetospheric O^+ and O^{++}, *Geophys. Res Lett.*, **17**, 1613-1616, 1990.

Meier, R.R., Ultraviolet Spectroscopy and Remote Sensing of the Upper Atmosphere, *Space Sci. Rev.*, **58**, 1-192, 1991.

Meier, R.R. and C.S. Weller, EUV Resonance Radiation from Helium Atoms and Ions in the Geocorona, *J. Geophys. Res.*, **77**, 1190-1204, 1972.

Northrop, T.G. and T.J. Birmingham, Adiabatic charged particle motion in rapidly rotating magnetospheres, *J. Geophys. Res.*, **87**, 661-669, 1982.

Ottley, J. Alan and R.W. Schunk, Density and Temperature Structure of Helium Ions in the Topside Polar Ionosphere for Subsonic Outflows, *J. Geophys. Res.*, **85**, 4177-4190, 1980.

Paresce, F., C.S. Bowyer and S. Kumar, On the Distribution of He^+ in the Plasmasphere From Observations of Resonantly Scattered He II 304-A Radiation, *J. Geophys. Res.*, **79**, 174-178, 1974.

Robinson, R.M., Y.T. Chiu, R.C. Catura, H.L. Collin, D.E. Garrido, and R.W. Smith, Instrumental and observational requirements for space-based imaging of magnetospheric emissions, *Instrumentation for Magnetospheric Imagery*, S. Chakrabarti, Ed., Proc. SPIE 1744, 13-18, 1992.

Roelof, E.C. and Barry H. Mauk, Instrument requirements for imaging the magnetosphere in extreme ultraviolet and energetic neutral atoms derived from computer-simulated images, *Instrumentation for Magnetospheric Imagery*, S. Chakrabarti, Ed., Proc. SPIE 1744, 19-30, 1992.

Swift, D.W., R.W. Smith and S.-I. Akasofu, Imaging The Earth's Magnetosphere, *Planet. Space Sci.*, **37**, 379-384, 1989.

Tsyganenko, N.A., A Magnetospheric Magnetic Field Model With a Warped Tail Current Sheet, *Planet. Space Sci.*, **37**, 5-20, 1989.

Weller, C.S. and R.R. Meier, First Satellite Observations of the He^+ 304-A Radiation and Its Interpretation, *J. Geophys. Res.*, **79**, 1572-1574, 1974.

4.10 Acknowledgements

This work was supported by NASA contract NASW-4529 to Lockheed by the Lockheed Independent Research Program, Geophysical Institute funds from the University of Alaska-Fairbanks and Alaska Space Grant Program. We would like to thank Dr. J.B. Cladis for useful discussions and Dr. Juan Roederer for the field tracing programs that we used in some calculations in this paper. We also thank Richard Million (System Manager), Evelyn Trabant, Debrah Shrider and Doug Sigler (Photo-Graphics Service Center) all from the Geophysical Institute, University of Alaska for their help in printing

the figures. The authors also thank the referees for their comments in improving this paper.

Chapter 5 Imaging the Plasmasphere and Trough Regions in the Extreme Ultraviolet *

5.0 Abstract

EUV images from emissions of O^+ (83.4 nm) and He^+ (30.4 nm) distributions in the plasmasphere and trough regions are constructed for a satellite at 9 R_e (where R_e is Earth radii). A diffusive equilibrium model is used to describe the density distribution along the field lines for ions in the plasmasphere, and a kinetic collisionless model is assumed to calculate ion densities in the high latitude regions beyond the plasmapause. In our model of the plasmasphere we assume that ions move along a static dipole field. Observational data on O^+ and He^+ densities in the ionosphere are used as boundary conditions to calculate spatial distribution of densities along the field lines. Assuming that the day and night boundary conditions are asymmetric and exobase densities vary with latitude we will discuss how this would be reflected in the intensities and structure of the magnetospheric images.

*D.E. Garrido, R.W. Smith, D.S. Swift and S-I. Akasofu, R.M. Robinson and Y.T. Chiu, Imaging the Plasmasphere and Trough Regions in the Extreme Ultraviolet; Optical Engineering, Vol. 33, pp. 371-382, 1994

5.1 Introduction

Satellite observations of thermal ion composition in the near-equatorial plasmasphere show the relative abundance of the He^+ ion to be typically from 5 to 10 percent and sometimes 25 percent or more of the total ion density. These high ion concentrations (Horwitz, 1982) increase the feasibility of imaging the plasmasphere from resonant scattering of sunlight at 30.4 nm by He^+. Observations of the He^+ 30.4 nm line have been obtained by detectors aboard low altitude rockets (Paresce et al., 1974; Weller and Meier, 1974; Meier and Weller, 1972) and also by the EUV telescope on the Apollo-Soyuz spacecraft (Chakrabarti et al., 1982). The intensities of the emissions can be explained by using a density model of the plasmasphere and knowledge of the scattering rate of the ions. However, line-of-sight intensities do not reveal the global nature of the ion distribution. In this paper, we study how the global distribution of ionization will be reflected in the images constructed from resonant scattering of sunlight by He^+ (30.4 nm) ions.

Magnetospheric imaging of the Earth's magnetosphere by resonant scattering at 83.4 nm by O^+ ions has been discussed in an earlier paper (Swift et al., 1989) and has been extended (Garrido et al., 1991) to incorporate realistic temperatures (radiation belt) and Doppler shifts (plasmasheet) due to the ions bulk motion relative to the Sun-Earth line. Contributions from the plasmasphere were neglected and maximum intensities of a few millirayleighs were obtained, indicating that hot plasmas of O^+ ions in the plasmasheet and radiation belt are less likely to be detected. Note, however, that undetected cold plasma may enhance the intensities considerably.

Other researchers (Chiu et al., 1990) have also simulated images of outflowing O^+ (83.4 nm) ions and neutral O (130.4 nm) atoms for a geostationary satellite by means of a uniform flux distribution over the polar regions and have obtained intensities as high as 1 rayleigh (R). These simulations were also extended (Garrido et al., 1994) by incorporating realistic non-uniform flux intensities, Doppler effects due to ion bulk motion, gravitational and rotational effects, variations in plasma temperature and effects of the bright plasmaspheric emissions on the images of the outflowing ions. They also constructed images of the outflowing ions from resonant scattering by O^+ (83.4 nm) and He^+ (30.4 nm) ions for both quiet and disturbed times. The results show that the change in intensity is small but the redistribution of intensities is dramatic because of the extent in MLT over which the ion fluxes have increased during times of high magnetic activity and may represent a good signature of substorm related processes. They also showed that the effects of acceleration of O^+ ions on the scattering rate may be detected in the images of the outflowing ions. Thus, analysis of the intensity distribution of the images of outflowing O^+ ions may give some insights and understanding about dynamical processes originating in the high latitude regions of the ionosphere.

Simulated images of the plasmasphere (Meier, 1991) were also constructed from resonant scattering by He^+ (30.4 nm) ions from different perspectives in the dusk meridian from a satellite viewing at 10 Earth radii (R_e). However, only the densities of ions bounded by L shells between 3 and 4.25 were considered. Maximum intensities of up to 20 R were obtained indicating a large amount of ionization present in these flux tubes and suggesting that the feasibility of imaging the inner plasmasphere in 30.4 nm emissions is favorable.

In this paper, our aim is to simulate images of the distribution of O^+ and He^+ ions along closed field lines using realistic ionospheric densities as boundary conditions at the foot of the field lines. In the construction of the images we adopt an empirical density model that gives values of densities that are consistent with observations. Our model is not aimed at replacing self-consistent or hydrostatic models that have been successful in explaining physical processes occuring in the plasmasphere. To be self-contained, we briefly review the calculation of the scattering rates for both O^+ (83.4 nm) and He^+ (30.4 nm) ions in Sec. 5.2. In Sec. 5.3 we provide a brief description of the kinetic and diffusive equilibrium model for the density. In Sec. 5.4 we discuss relevant observations on ion densities and composition ratios for purposes of comparison with our simulations. In the remainder of the paper we discuss how the images are constructed and show how our choice of boundary conditions and model densities will be reflected in the intensity distribution of the images.

5.2 Calculation of Scattering Rate for He^+ and O^+

In the calculation of the scattering rate ie., the number of photons scattered per second by each ion for resonance scattering at EUV wavelenghts, knowledge of the shape of the solar intensity and absorption cross-section profile is important. For the O^+ (83.4 nm) emission the calculation of the scattering rate is discussed in detail in connection with Doppler shifts (Garrido et al., 1994; Meier, 1990) of the oxygen lines. Due to the complex blend of O^+ and O^{++} lines, Doppler effects due to temperature variations and bulk drifts along the Sun-Earth line must be accounted for, and the calculation of intensities becomes complex. However, for He^+ at 30.4 nm, the calculation of the scattering rate is less complicated because the He^+ (30.4 nm) emission is a single line.

Previous calculations of the scattering rate for He^+ have only considered contributions from the line center, and this was reasonable because the plasma under consideration was cold. Since the temperature of the cold ions in the plasmasphere may be higher than 10 eV, we must account for temperature effects on the scattering rate. Although the largest scattering rates may come from the colder ions, hot ions may enhance the overall contribution to the intensities. For the inner regions of the plasmasphere, the ion temperatures range from 3000-5000 K and slowly rise to values up to 10^5 K in the trough regions. Such temperature characteristics have also been reported (Horwitz et al., 1986; Comfort et al., 1988). We show in the foregoing discussions how temperature variations can be accounted for in the calculation of the scattering rate, and we also illustrate the calculation for stationary He^+ (30.4 nm) and O^+ (83.4 nm) ions.

The solar intensity profile for He^+ is assumed to be of the form

$$(\pi F_\lambda) = (\pi F_\lambda)_0 e^{\frac{-(\lambda-\lambda_0)^2}{\Delta\lambda_n^2}} \tag{5.1}$$

where the full width at half maximum (FWHM) of the He^+ solar profile is $\Delta\lambda$=.012 nm, λ_0=30.4 nm (wavelength at line center), and $(\pi F_\lambda)_0$ is the solar flux at line center which has a value of 5.4×10^{10} photons $cm^{-2}s^{-1}A^{-1}$ (Feldman and Behring, 1974; Doschek et al., 1974), which is appropriate for solar minimum conditions. The value for solar maximum conditions is 1×10^{11} photons $cm^{-2}s^{-1}A^{-1}$ which is about twice the value for solar minimum conditions. The width $\Delta\lambda$ is related to the thermal width $\Delta\lambda_n$ through the relation

$$.5\Delta\lambda = \sqrt{\ln 2}\Delta\lambda_n \tag{5.2a}$$

$$\Delta\lambda_n = \lambda_0 \frac{u_n}{c} = \frac{\lambda_0}{c}\sqrt{\frac{2kT_n}{m}} \tag{5.2b}$$

where u_n and c are the thermal speed and the speed of light, respectively. The index n labels quantities of solar origin, k is the Boltzmann constant, m and T_n are the mass and

temperature of the He^+ ions, respectively. From Eq. (5.1)

$$(\pi F_\lambda)_0 = \frac{I_{0n}}{\sqrt{\pi}\Delta\lambda_n}, \tag{5.3}$$

where I_{0n} is the solar flux in photons cm^{-2} s^{-1}. From Eq. (5.2) and the value of $\Delta\lambda$, we get

$$I_{0n} = (\sqrt{\pi}\Delta\lambda_n)(\pi F_\lambda)_0$$

which equals 6.9×10^9 and 1.28×10^{10} photons cm^{-2} s^{-1} for solar minimum and maximum conditions, respectively. Note that our derived values compare well with the 30.4 nm flux values of Hinteregger (1969) which are 6×10^9 and 1.1×10^{10} photons cm^{-2} s^{-1} for solar minimum and maximum conditions, respectively. The absorption cross-section can be obtained from

$$\sigma_0 = \frac{\pi e^2}{m_e c} f_{12} \tag{5.4}$$

where e and m_e are the mass and charge of the electron, respectively, and f_{12}=.4162 is the oscillator strength for the He^+ transition. Thus, the magnitude of the integrated cross-section is given by .01102 (cm^2Hz). The scattering rate can be calculated from

$$g_0 = (\pi F_\nu)_0 \sigma_0 \tag{5.5a}$$

and $(\pi F_\nu)_0$ can be obtained from the relation

$$(\pi F_\nu)_0 = \frac{I_{0n}}{\sqrt{\pi}\Delta\nu_n}, \tag{5.5b}$$

where

$$\Delta\nu_n = \frac{c}{\lambda_0^2}\Delta\lambda_n = 2.339 \times 10^{12} \text{ Hz}. \tag{5.6}$$

Using Eqs. (5.3) and (5.6) we get $(\pi F_\nu)_0 = 1.664 \times 10^{-4}$ and 3.087×10^{-3} photons cm^{-2} s^{-1} Hz^{-1} for solar minimum and maximum conditions, respectively. Thus, the g-factor or scattering rate for stationary He^+ ions has a value $g_0 = 1.83 \times 10^{-5}$ and

3.4×10^{-5} photons s^{-1} ion^{-1} for solar minimum and maximum conditions, respectively. To incorporate the effects of temperature variation and bulk drifts of the scattering ions, we assume that the absorption line and solar intensity profile to have the form

$$\sigma(\nu) = \sigma_0 \kappa_{0m} e^{\frac{-(\nu-\nu_m)^2}{\Delta\nu_m^2}} \tag{5.7}$$

$$I(\nu) = I_{0n} \kappa_{0n} e^{\frac{-(\nu-\nu_n)^2}{\Delta\nu_n^2}}, \tag{5.8}$$

where

$$\kappa_{0m} = \frac{1}{\sqrt{\pi}\Delta\nu_m} \tag{5.9a}$$

$$\kappa_{0n} = \frac{1}{\sqrt{\pi}\Delta\nu_n}. \tag{5.9b}$$

The index m labels quantities of magnetospheric origin and ν_m or ν_n are given by Eq. (5.2b). They can also be written as

$$\Delta\nu_m = \nu_0 \frac{u_m}{c} = \frac{\nu_0}{c}\sqrt{\frac{2kT_m}{m}}, \tag{5.9c}$$

where ν_0 is the frequency at line center and T_m is the temperature of the He^+ (30.4 nm) ions in the magnetosphere. The Doppler-shifted frequency due to the ion's bulk motion relative to the Sun-Earth direction is given by

$$\nu_m = \nu_0(1 + \frac{v_x}{c}). \tag{5.10}$$

Using Eqs. (5.7) and (5.8) the g-factor can be obtained by integration over the entire

frequency range

$$g = \int_{-\infty}^{\infty} I(\nu)\sigma(\nu)\, d\nu \tag{5.11}$$

and the result of integration gives us

$$g = I_{0n}\sigma_0 \frac{1}{\sqrt{\pi}\Delta\nu_n} \frac{1}{\sqrt{1+\frac{T_m}{T_n}}} e^{-\delta_p}, \tag{5.12}$$

where

$$\delta_p = \frac{v_x^2}{u_n^2} \frac{1}{(1+\frac{T_m}{T_n})}. \tag{5.13}$$

Finally, Eq. (5.12) can be simplified further as

$$g = g_0 \frac{1}{\sqrt{1+\frac{T_m}{T_n}}} e^{-\delta_p}, \tag{5.14}$$

where g_0 is given in Eq. (5.5a). We illustrate the effects of temperature on the scattering rate when the ions have no bulk drifts. Consider a plasma of He^+ ions to have T_m= 10 eV. The solar temperature can be calculated from Eq. (5.2) and is given roughly by $T_n = 1.22 \times 10^6$ K. Thus, Eq. (5.14) gives us $g = .9952 g_0 = 1.825 \times 10^{-5}$ photons s^{-1} ion^{-1} for solar minimum conditions.

The calculated values of the scattering rates for O^+ (83.4 nm) for T=.1 eV has been tabulated (Meier, 1991) and the atomic and solar data needed in the calculation of the scattering rate for O^+ have also been discussed (Meier, 1990). We apply the results just obtained above for He^+ to calculate the scattering rate for O^+. The solar flux I_0 at 83.4 nm has a magnitude (Hinteregger, 1969) of $.67 \times 10^9$ photons cm^{-2} s^{-1} for solar minimum conditions and the fraction of I_0 that goes into the O^+ lines is given by the branching ratio p_i (Garrido et al., 1991). At solar maximum the flux Hinteregger measured was 1.7×10^9 photons cm^{-2} s^{-1} which is about 2.5 times larger than the solar minimum value. For the wavelengths λ_{0i}=(83.4462, 83.3326 and 83.2754 nm) the branching ratios and oscillator

strengths are given by 0.121, 0.086, 0.043 and 0.122, 0.0872, 0.041, respectively. The FWHM for O^+ is given by $\Delta\lambda$=.0065 nm, and the thermal width can be obtained from Eq. (5.2). We illustrate the calculations for the wavelength λ_{01}=83.4462 nm. The solar flux at line center is calculated from Eq. (5.5b) where $I_{0n} = I_0 p_n$ and n=1, 2, 3 refers to the three wavelengths described above. For n=1, we have

$$\Delta\nu_1 = \frac{c}{\lambda_{01}^2}\Delta\lambda_n = \frac{c}{\lambda_{01}^2}\frac{.5\Delta\lambda}{\sqrt{\ln 2}}$$

or

$$\Delta\nu_1 = 1.682 \times 10^{11} \text{ Hz}.$$

Thus,

$$(\pi F_\nu)_0 = \frac{(.67 \times 10^9)(.121)}{\sqrt{\pi}\, 1.682 \times 10^{11}}$$

$$= 2.72 \times 10^{-4} \text{ photons cm}^{-2}\text{s}^{-1}\text{Hz}^{-1}$$

Using the oscillator strength f_1=.122, the absorption cross-section in Eq. (5.4) is now given by $\sigma_0 = 3.23 \times 10^{-3}$ cm^2 Hz. Hence, the scattering rate is given by

$$g_1 = (\pi F_\nu)_0 \sigma_0 = 8.79 \times 10^{-7} \text{ photons s}^{-1}\text{ ion}^{-1}.$$

Similarly, for λ_{02} and λ_{03} we obtained g-factors of 4.46×10^{-7} and 1.26×10^{-7} photons per second per ion, respectively. Thus, the total scattering rate for stationary O^+ is 1.45 $\times 10^{-6}$ photons s^{-1} ion^{-1}. The effects of temperature variation and plasma bulk drifts on the scattering rate for O^+ and its effect on the magnetospheric images are described in an earlier work (Garrido et al., 1991).

5.3 Calculation of Densities

For the calculation of intensities used in constructing the images of the plasmasphere we need a density model that gives values of the ion densities that are consistent with observations. We will describe both the kinetic and fluid models below. We also describe briefly the main results of the two models and show in later sections that the kinetic model is appropriate in describing plasmas outside the plasmapause or in the trough regions, and a diffusive equilibrium model gives ion densities that are consistent with observations made inside the plasmasphere.

Kinetic Description

In describing the density profile of the ions along the field lines beyond the plasmapause, we adopt a kinetic model (Huang and Birmingham, 1992) that assumes the particle velocity distribution function to be a bi-Maxwellian at a reference point with a given parallel and perpendicular temperature. Liouville's Theorem with the conservation of energy and magnetic moment allows us to calculate the density distribution everywhere along the field lines. Also, in the analysis of the dynamics of charged particles in a rotating magnetosphere (Northrop and Birmingham, 1982) one can show that the conservation of energy can be expressed in the form

$$v_0^2 = v^2 + \frac{e}{m}(\phi - \phi_0) + \Delta v^2, \tag{5.15a}$$

where

$$\Delta v^2 = -\Omega^2(r^2 cos^2\lambda - r_0^2 cos^2\lambda_0) + 2C_0(1 - \frac{r_0}{r}) \tag{5.15b}$$

and

$$C_0 = \frac{GM}{r_0}, \tag{5.16}$$

where r_0 defines the ionospheric boundary, which we assumed to be at an altitude of 1000

km, e and ϕ are the electron charge and potential, respectively, m is the ion mass, v is the velocity, G is the gravitational constant, M is the Earth's mass, λ is the latitude, and Ω is the angular frequency of the Earth's rotation. The subscript '0' refers to quantities defined at a reference point which we define to be in the ionosphere at 1000 km. From an analysis of the distribution function (Huang and Birmingham, 1992) one can also show that the parallel temperature remains constant, ie.

$$T_{\parallel}^{j} = T_{\parallel 0}^{j} \tag{5.17}$$

and the perpendicular temperature varies along the field line as

$$T_{\perp}^{j} = T_{\perp 0}^{j} \frac{1}{[\frac{1}{\gamma_0^j} + (1 - \frac{1}{\gamma_0^j})\eta]}, \tag{5.18}$$

where $\gamma_0^j = \frac{T_{\parallel 0}^j}{T_{\perp 0}^j}$, $\eta = \frac{B}{B_0}$ and $T_{\parallel 0}^j$, $T_{\perp 0}^j$ are parallel and perpendicular temperatures while B_0 is the magnetic field at the reference point, respectively. The density distribution along the field line can be written as

$$n_j = n_{0j} \frac{T_{\perp}^j}{T_{\perp 0}^j} \exp -[Z\chi_j + \frac{m_j \Delta v^2}{2kT_{\parallel 0}^j}], \tag{5.19}$$

where n_{0j} is the source density and $\chi_j = \frac{e(\phi - \phi_0)}{kT_{\parallel 0}^j}$. The index j labels the particle species and Z=1 for ions and Z=-1 for electrons.

Fluid Description

Previous researchers (Chiu et al., 1979; Li et al., 1983) have discussed fluid models describing plasma flow along magnetic field lines pointing out the importance of the magnetic mirror force in describing the spatial distribution of densities; however, the anisotropy in the fluid properties of the plasma have not been accounted for. When the plasma is isotropic (Comfort, 1988) the effects of the mirror force cancel out. However, in a plasma that possesses a temperature anisotropy the effects of the mirror force will be evident in the magnetic scaling factor present in the expression for the density profile of the ions. This result can be derived from the parallel equation of motion for the ions but we need not pursue this matter here. In Comfort's analysis, he showed that the parallel equation of motion for the plasma is given by

$$nm(\frac{\partial \mathbf{v}}{\partial t} + \mathbf{v}\cdot\nabla\mathbf{v})_{\|} = n\mathbf{F}\cdot\hat{s} - \frac{\partial p_{\|}}{\partial s} + \frac{(p_{\|}-p_{\perp})}{B}\frac{\partial B}{\partial s}, \tag{5.20}$$

where n is the number density, m is the mass of species, $p_{\|}$ and $p_{\perp}$ are the parallel and perpendicular pressures, $\hat{s} = \frac{\mathbf{B}}{B}$ is the unit vector along the field line and $\mathbf{F}$ is the net nonmagnetic force. We consider the case of diffusive equilibrium ($\mathbf{v}$=0) for plasmas in flux tubes from the ionosphere all the way to the equatorial plane. If the plasma is isotropic, then $p_{\|} = p_{\perp}$ and Eq. (5.20) becomes

$$n\mathbf{F}\cdot\hat{s} - \frac{\partial p_{\|}}{\partial s} = 0. \tag{5.21}$$

Thus, the effect of the magnetic mirror force cancels out. The gravitational and centrifugal forces are given by

$$\mathbf{f}_j = (-\frac{GMm_j}{r^2}\hat{r} + m_j\Omega^2 r\cos\lambda\hat{\rho}), \tag{5.22}$$

where the unit vector $\hat{\rho} = \hat{x}\cos\phi + \hat{y}\sin\phi$. The orthogonal unit vectors $(\hat{x},\hat{y},\hat{z})$ define directions along the solar magnetospheric (X,Y,Z) axes with the +X pointing towards

the Sun and the Y axes lies in the dawn to dusk plane and the +Z axes points along geographic north. The net nonmagnetic forces combined with the electrostatic forces give us

$$n_j \hat{s} \cdot \mathbf{F} = n_j (Z_j e E - f_s^j), \tag{5.23}$$

where E is the parallel electric field and f_s^j is the component of the combined gravitational and rotational forces in the direction of the magnetic field and is derived in the next discussion. Note that if we assume that the plasma is isotropic, we arrive at the result for the density profile,

$$n_j = n_{0j} \frac{T_{\|0}^j}{T_{\|}^j} \exp[\int_{s_0}^{s} \frac{ds}{kT_{\|}^j} (Z_j e E - f_s^j)] \tag{5.24}$$

which is the classical expression obtained for a diffusive equilibrium model. The subscript zero labels quantities at the reference point. However, to obtain the density variation along the field lines, we need to specify a magnetic field model and a temperature structure, and the polarization electric field can be obtained by imposing the condition that charge neutrality holds everywhere along the field line, ie.,

$$n_e = \sum_j n_j. \tag{5.25}$$

Gravitational and Rotational Forces

In our present model we have assumed that the rotational and dipole axis are coincident. The expression for the forces along the magnetic field (gravitation plus rotation) has been obtained for a dipole model (Angerami and Thomas, 1964) where the expression for the force has been obtained for the case when the field line is in the noon-midnight plane. Since the dipole field is symmetric about the polar axis, the results are valid, in general, for any azimuth. However, care must be exercised when working with field models that account for the bending of the magnetic field lines (Tsyganenko, 1989). At any point with coordinates (r, θ, ϕ), the force vector is given by Eq. (5.22) and the component of the force in the direction of the magnetic field is given by

$$f_s^j = \mathbf{f}_j \cdot \hat{s} = -m_j \frac{GM}{r^2} \frac{B_r}{B} + m_j \Omega^2 r \cos\lambda \frac{B_\rho}{B}, \tag{5.26}$$

where

$$B_r = \mathbf{B} \cdot \hat{r} \tag{5.27a}$$

$$B_\rho = \mathbf{B} \cdot \hat{\rho} = \cos\phi\, B_x + \sin\phi\, B_y. \tag{5.27b}$$

Thus, the expression for the force can be written as

$$f_s^j = -m_j \frac{GM}{r^2} \frac{B_r}{B} + m_j \Omega^2 r \cos\lambda (\cos\phi \frac{B_x}{B} + \sin\phi \frac{B_y}{B}). \tag{5.28}$$

For the case of a dipole, the magnetic field components are given by

$$B_r = \frac{M_0}{r^3}(-2\cos\theta) \tag{5.29a}$$

$$B_\theta = \frac{M_0}{r^3}(-\sin\theta) \tag{5.29b}$$

$$B_\phi = 0, \tag{5.29c}$$

where M_0 is the magnetic moment. We can also show the following results:

$$B = (B_r^2 + B_\theta^2 + B_\phi^2)^{\frac{1}{2}} = \frac{M_0}{r^3}\Delta \qquad (5.30a)$$

where

$$\Delta = (1 + 3\cos^2\theta)^{\frac{1}{2}} \qquad (5.30b)$$

and

$$f_s^j = \frac{1}{\Delta}[\frac{2GMm_j}{r^2}\cos\theta - 3m_j\Omega^2 r\sin^2\theta\cos\theta], \qquad (5.31)$$

which is similar to a previous result obtained by Angerami and Thomas, (1964) apart from the mass term m_j.

5.4 Observational Data

Our current understanding of the distribution of ions of ionospheric origin within the Earth's inner magnetosphere has been made possible with measurements obtained from the energetic ion composition experiments on spacecrafts such as GEOS, SCATHA, ISEE, and Dynamics Explorer (DE). Also, cold plasma of ionospheric origin have been observed with ion mass spectrometers on the OGO-1 and OGO-5 spacecraft (Taylor et al., 1965; Chappell, 1972).

For purposes of comparison with our simulations, we examine the plasma density profile (Horwitz et al., 1981) shown in Fig. 5.1 plotted vs L shell. Data were obtained for the outbound ISEE 1 passes on December 4 (day 338) and (day 341), 1977. In the upper panel of the Fig. 5.1, the Kp index is plotted versus universal time (UT). For the December 4 pass, the Kp index is moderately high (about 3+) while the December 7 pass Kp is low (less than 1). The density profiles are shown as dashed and solid curves, respectively. The steep density gradient at L=4 defines the plasmapause within which densities are large and of the order from 100 to 1000 ions cm^{-3}. For the dashed curve

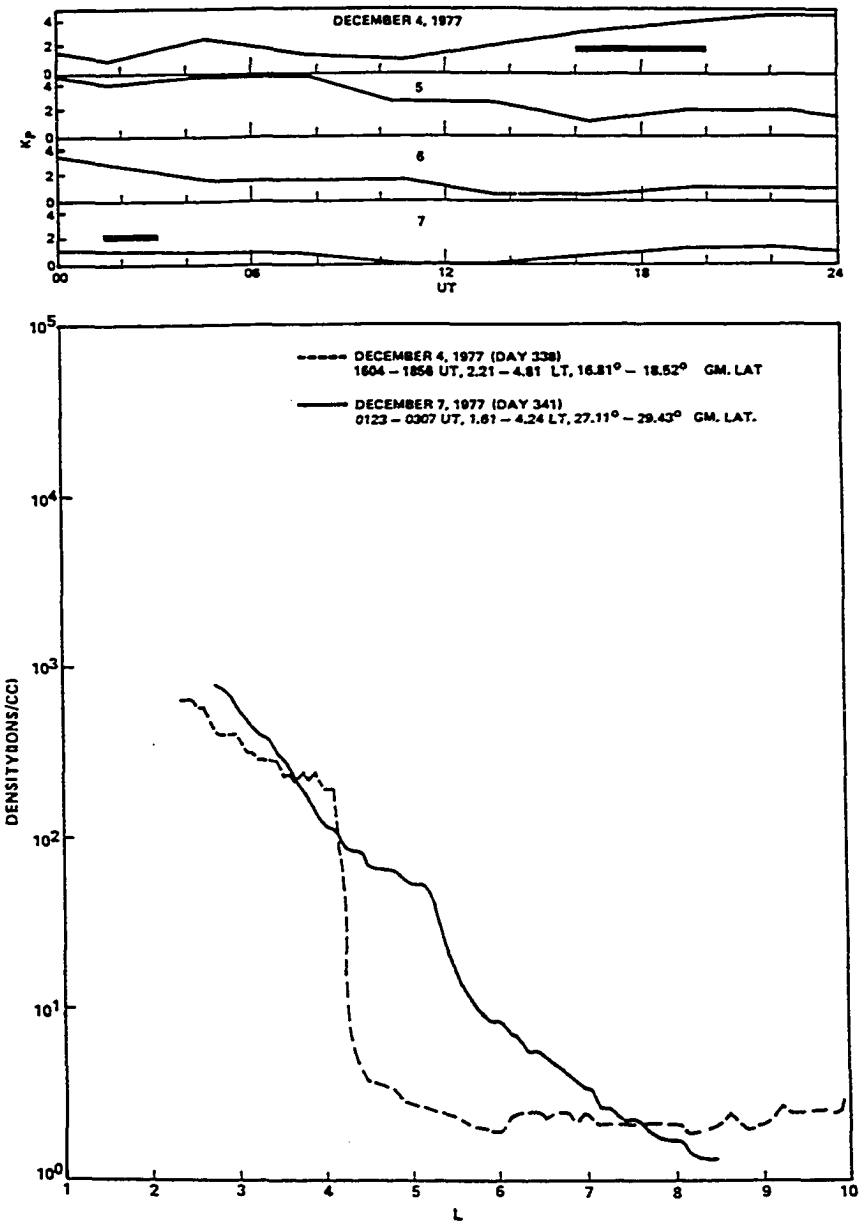

Figure 5.1 Plasma density profiles for two successive ISEE 1 outbound passes in the postmidnight sector. The Kp history vs UT is shown in the upper panel of the figure (Horwitz et al., 1981).

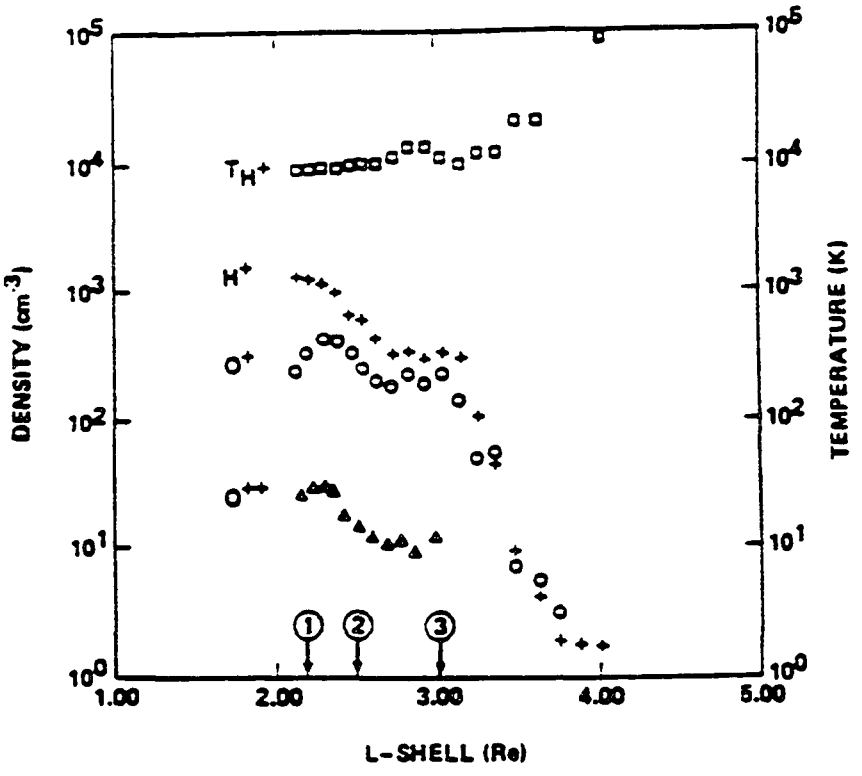

Figure 5.2 Density profile versus L shell for the ions H^+, O^+ and O^{++}. The temperature structure for H^+ is also shown (Chandler et al., 1988).

outside of L=4 the flux tubes are depleted of ions, and for the solid curve the flux tubes are filled with plasma. The steep density gradient in the density profile is a characteristic feature during periods of high magnetic activity, and the profile defined by the solid curve is characteristic of long quiet times. Our aim is to simulate conditions during disturbed times.

The density profile (Chandler et al., 1988) shown in Fig. 5.2 represents plasma observations of ion composition, density, and temperature at high altitudes obtained from the DE 1 retarding ion mass spectrometer instrument. The densities of the H^+, O^+ and O^{++} ions are plotted versus L shell. The data were taken for L values of 2.2, 2.5 and 3 on October 23, 1981 at approximately 21 hours magnetic local time. The density ratio $\frac{O^+}{H^+}$ varied roughly from 0.5 to 1 for L shells less than 3 and is equal to 1 for L between 3 and 4.

The heavy ion and light ion density ratios (Comfort et al., 1988) $\frac{O^+}{H^+}$ and $\frac{He^+}{H^+}$ are shown in Figs. 5.3a and 5.3b, respectively. The data are averaged values obtained from more than 100 transits of the plasmasphere by DE 1 in two local time regions defined by the morning side (7 to 11 hours) and evening side (18 to 22 hours). The measurements were obtained during a period of high solar activity and moderate but variable magnetic activity.

In constructing magnetospheric images that include the plasmasphere and trough regions, we adopt the ionospheric densities previously reported by Hoffman et al. (1974). The ion densities for O^+, He^+, and H^+ were measured in a nearly constant altitude of 1400 km. The ion densities are shown to vary over latitude from pole to pole in both day and night sectors. We use the data as boundary values in the calculation of densities along field lines. In our simulations we define our exobase densities to lie on field lines that intersect L shells between 1.52 and 8.25. In latitude they translate from 29 to 68 deg.

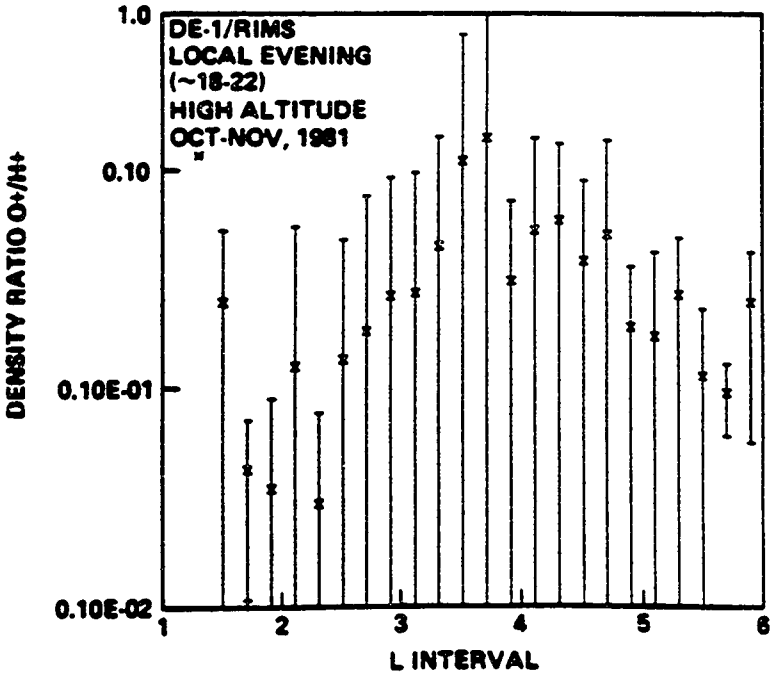

Figure 5.3a Mean profiles of density ratios O^+/H^+. See Comfort et al, 1988.

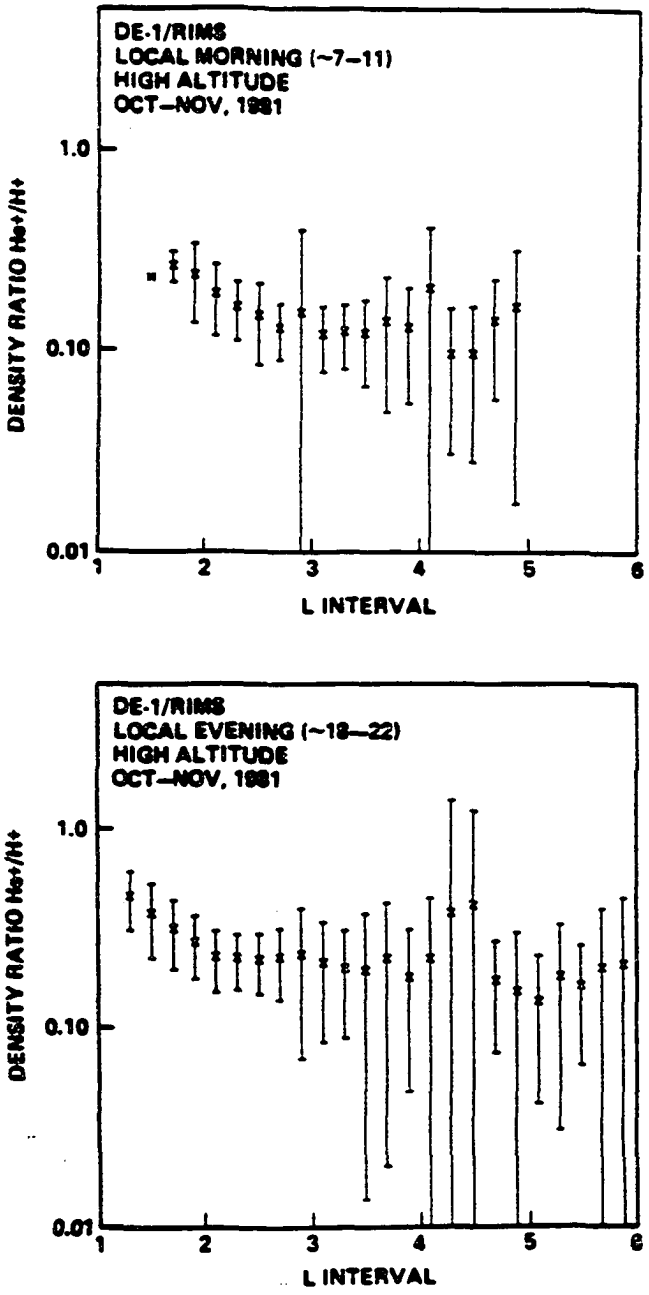

Figure 5.3b Mean profiles of density ratios He^+/H^+. See Comfort et al, 1988.

In our model we assume that ion densities are symmetric with respect to the equator. To illustrate the effects of the asymmetry for day and night conditions, we adopt the daytime and nighttime concentrations of the upper hemisphere shown in Figs. 5.4a and 5.4b,respectively. Figure 5.4a shows that O^+ is the dominant ion for latitudes greater than 20 deg and has an almost constant value at 10^4 ions cm^{-3} all the way up to the poles, in contrast to the He^+ and H^+ ions, which show a steep gradient at about λ_0=50 deg or roughly at L=3 suggesting a plasmapause boundary.

Note that for the latitude range assumed, the He^+ and H^+ ion concentrations follow an almost identical profile with a $\frac{He^+}{H^+}$ density ratio almost at 0.1. It seems that such ratios are also maintained at the equator. It still remains an open problem why such characteristic ratios consistently exist in the plasmasphere. Figure 5.4b also shows a similar steep gradient at L=3 in the density for the He^+ and H^+ ions. Note that below λ_0=50 deg, He^+ becomes much more dominant than O^+. Inside the plasmapause, the O^+ concentration is depleted but starts increasing with latitude beyond the plasmapause. Note that such depletions of plasma could result in a dim region within the plasmasphere if imaged under 83.4 nm light. We will discuss more on this topic in a later section.

5.5 Boundary Conditions

The kinetic model adopted here may be compared with the kinetic models reviewed elsewhere (Lemaire and Scherer, 1974). In constructing the magnetospheric images from emissions coming from regions beyond the plasmapause, the kinetic model (Lemaire and Scherer, 1974) is applicable but requires more computational labor than the model we describe in this paper, and will be considered in a future study. To serve our motivation, we briefly review some of their results that are useful in our analysis and construction

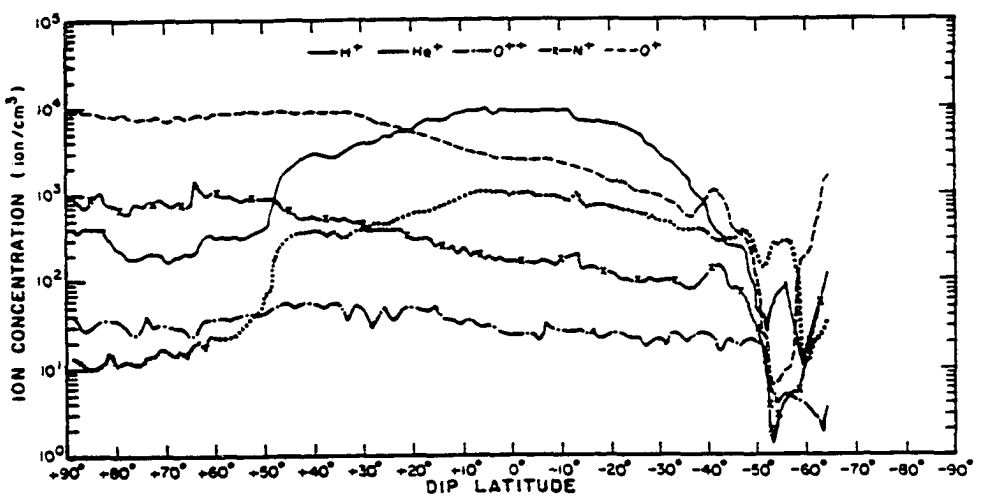

Figure 5.4a Pole-to-pole plot of daytime ion densities. Northern summer is to the left and winter (south) is to the right. Local time is 1713-1810. Satellite altitude is essentially constant at 1400 km (Hoffman et al., 1974).

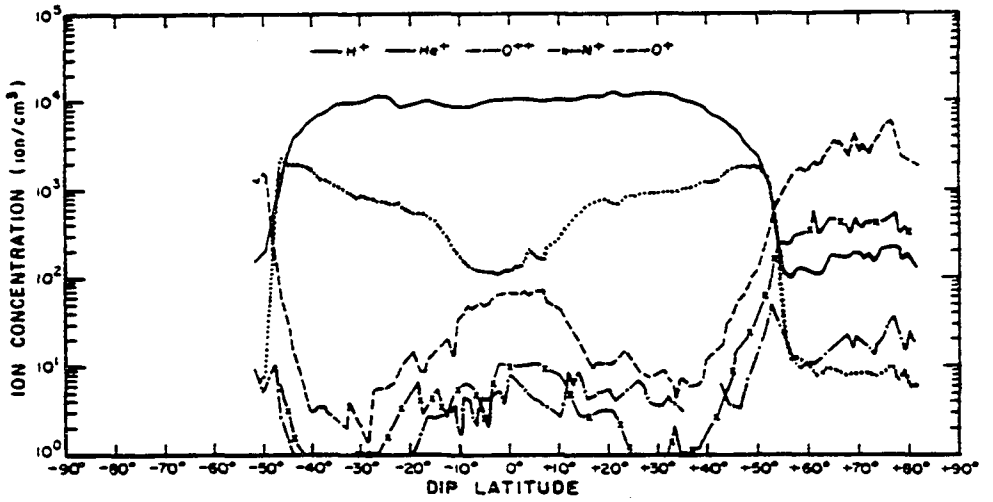

Figure 5.4b Pole-to-pole plot of nighttime ion concentrations. Summer is to the right and winter to the left. Local time is 0500 (Hoffman et al., 1974).

of the images. Reference to Fig. 5.5 shows the latitudinal variation of the ionospheric densities for O^+ and H^+ obtained by the OGO-6 polar orbiting satellite at an altitude that varied from 700 to 1100 km. The magnetic conditions at the time of measurement indicated a Kp index of 0^+. Using the ionospheric densities as boundary conditions and adopting a kinetic as well as diffusive equilibrium model to calculate equatorial densities for the H^+ ion, the results of their simulations as shown in Fig. 5.6 indicate that the diffusive equilibrium model gave substantially larger values of the equatorial density than that obtained from a kinetic model. The calculations were compared with measurements of H^+ equatorial density obtained by the OGO-5 satellite. The magnetic conditions at the time of measurement indicated a Kp index of 4, and the density profile reflected a plasmapause boundary value equal to 3.5. Although the magnetic conditions were different at the time of measurement of the ionospheric and equatorial densities, the results of their simulations are in good agreement with the observations. The results showed that the diffusive equilibrium model values are in agreement with observed values for L shells below the plasmapause and the kinetic model values are in approximate agreement for equatorial distances beyond the plasmapause. This analysis suggests the validity of the kinetic model in describing the spatial densities in the trough regions and the diffusive equilibrium model to be applicable in regions within the plasmapause. Thus, theoretically one can infer the plasmapause boundary by noting the point at which the equatorial density of H^+ show a sharp decline in magnitude.

Temperature Boundary Conditions

For the temperature profile in the plasmasphere, we adopt the following expression (Chiu et al., 1979),

$$T_{\|}(s) = T_{\|0} + T_1(\frac{L-1}{L_0})^{\alpha}(\frac{s}{l})^{\beta}, \tag{5.32}$$

where $T_{\|0}$=2000 K, T_1=2500 K, α=.5, β=.5, L_0=2. Also l is the length of the field line measured from the ionosphere to the equator and, s is the distance along the field line defined to be positive as measured from the ionosphere. The parameters α, β, L_0 or T_1 can be chosen in such a way that $T_{\|}$(s) fits with observation at the equator. We also assume that the temperature of the ions is the same and the temperature boundary values are given by $T_{\|0}$ and are symmetric with respect to the equator. The temperature profile in Eq. (5.32) gives values from 3000 to 5000 K in the inner plasmasphere and is consistent with previous measurements (Horwitz et al., 1986). For the trough regions, the He^+ ion is assumed to have T=1 eV, O^+ has T=10 eV, and H^+ has T=1 eV. Here, $T_{\|0}$ is defined as T and for the anisotropy term we take γ_0^j=2 for both H^+ and He^+ ions.

5.6 Empirical Model Results

The density profile for H^+ vs L shell using the boundary conditions shown in Figs. 5.4a and 5.4b are plotted in Fig. 5.7. The solid curve refers to densities calculated using daytime boundary conditions, and the circles denote densities calculated using nighttime conditions. In both curves, the plasmapause boundary occurs at L=3. The densities for H^+ and He^+ inside L=3 were obtained using the model density described by Eq. (5.24) and using the boundary conditions in Fig. 5.4. For densities above L=3, the kinetic model described by Eq. (5.19) in Sec. 5.3 was used. In both models the ambipolar electric field E was calculated by assuming that the charge neutrality condition to be satisfied

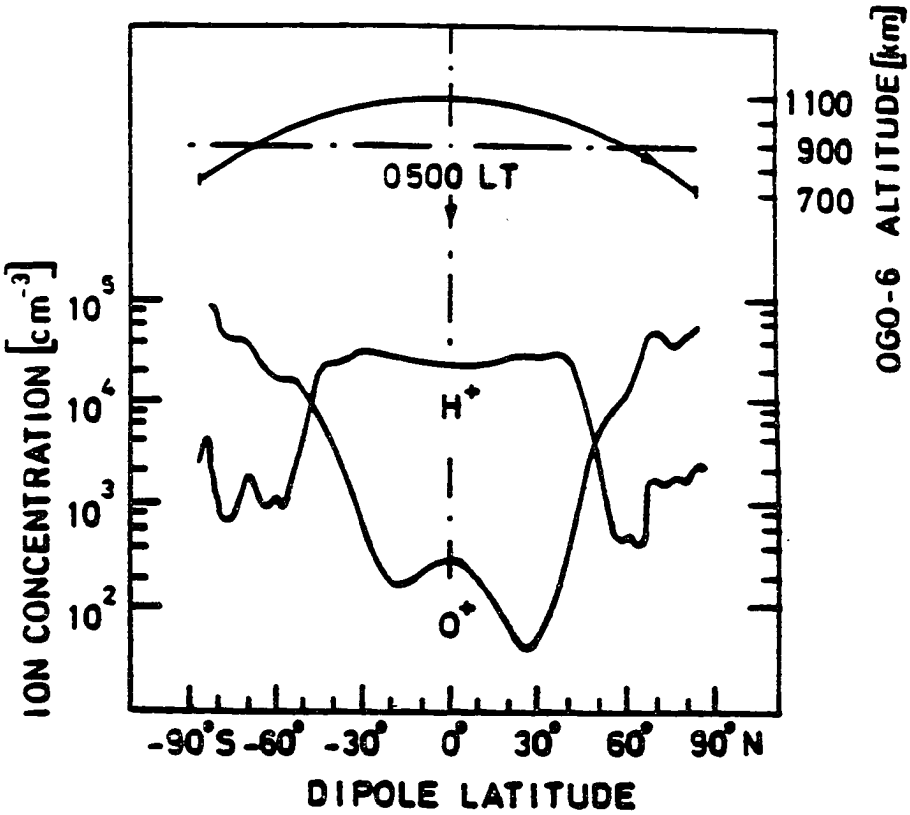

Figure 5.5 Variation of exobase densities of O^+ and H^+ ions with latitude from OGO 6 made on September 23, 1969. The Kp index was low (Lemaire and Scherer, 1974).

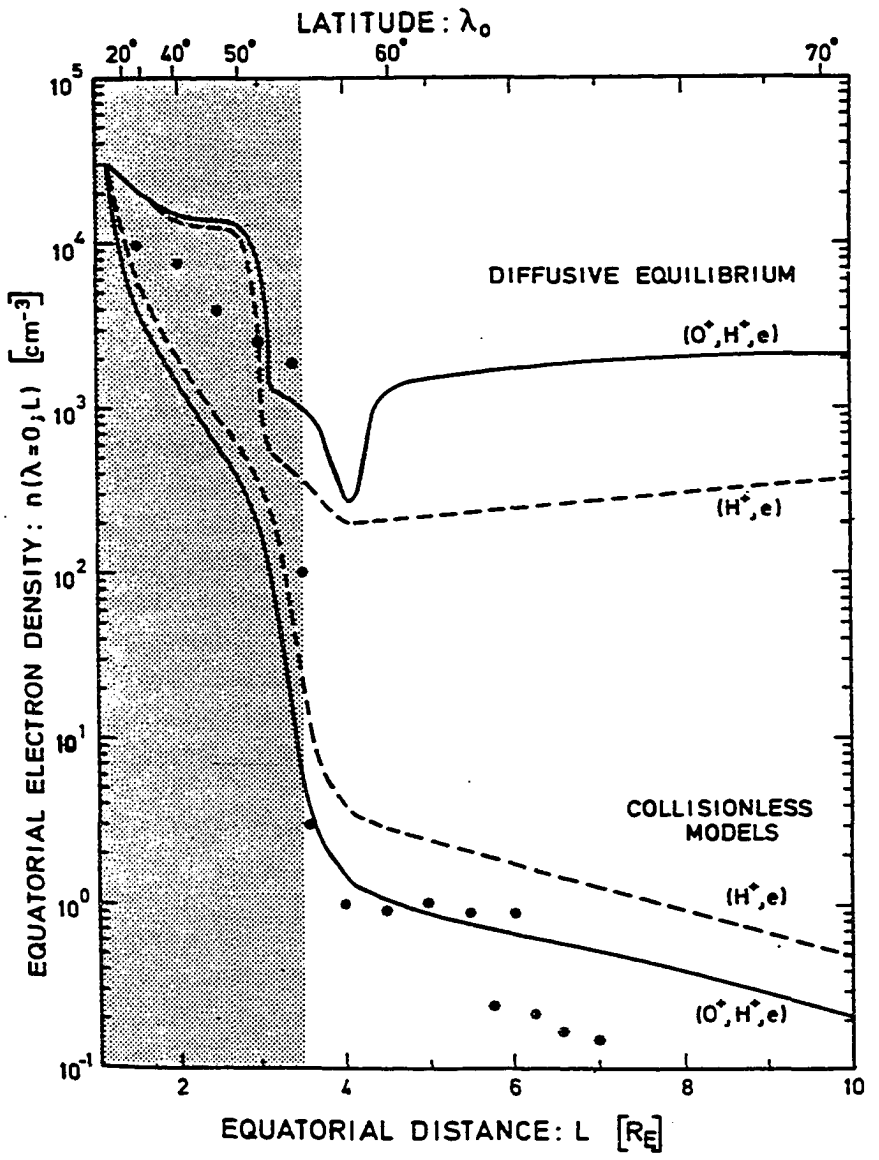

Figure 5.6 Effects of the variation of exobase densities with latitude. Diffusive equilibrium and kinetic models are shown by the upper and lower set of curves, respectively (Lemaire and Scherer, 1974). Shaded region defines the plasmasphere.

everywhere along the field lines. The calculated $\frac{He^+}{H^+}$ density ratios for day and night conditions are shown in Fig. 5.8. The density ratios are larger in the evening case than in the day case. This seems reasonable because the nighttime ion concentrations in the ionosphere are much higher than their daytime counterparts. The range of values for the ratios varies from 0.02 to 0.8 with lower ratios obtained for larger L shells. The composition ratios shown in Fig. 5.8 are within the range of measured values shown in Fig. 5.3 despite the sudden decrease of the ratios at the trough in Fig. 5.8. Also, OGO-5 profiles (Harris et al., 1970) and OGO-1 profiles (Taylor et al., 1965) have shown consistently that for L less than 2.5, $\frac{He^+}{H^+} \sim 0.1$ and for L greater than 2.5, $\frac{He^+}{H^+} \sim 0.01$, thus, our results are consistent with observations.

For the O^+ ions, we treat this case separately. Note that the O^+ ions have densities which are large compared to H^+ and He^+ so that a straightforward application of the diffusive model of Sec. 5.4 would give large values for the densities at the equator. To be consistent with the density profile shown in Fig. 5.2 for O^+, we assume that the O^+ densities obey the hydrostatic law

$$n = n_0 exp[-\frac{(r - r_0)}{h}], \tag{5.33}$$

where h is the scale height, n_0 is the source density, r_0 defines the ionospheric boundary, and r is the radial distance. Both distances are measured from the center of the Earth in units of Earth radii. For the day boundary condition we assume a scale height of 2400 km for densities inside L=3 and above L=3 we assume $n(O^+) = n(H^+)$ for simplicity in accordance with Fig. 5.2. Note that our night boundary conditions, which show a depletion of O^+ ions, do not fit the observations shown in Fig. 5.2. Although the data shown in Fig. 5.2 were obtained for the evening sector, they are suitable for comparison purposes with our calculations using the day boundary conditions. For nighttime boundary conditions,

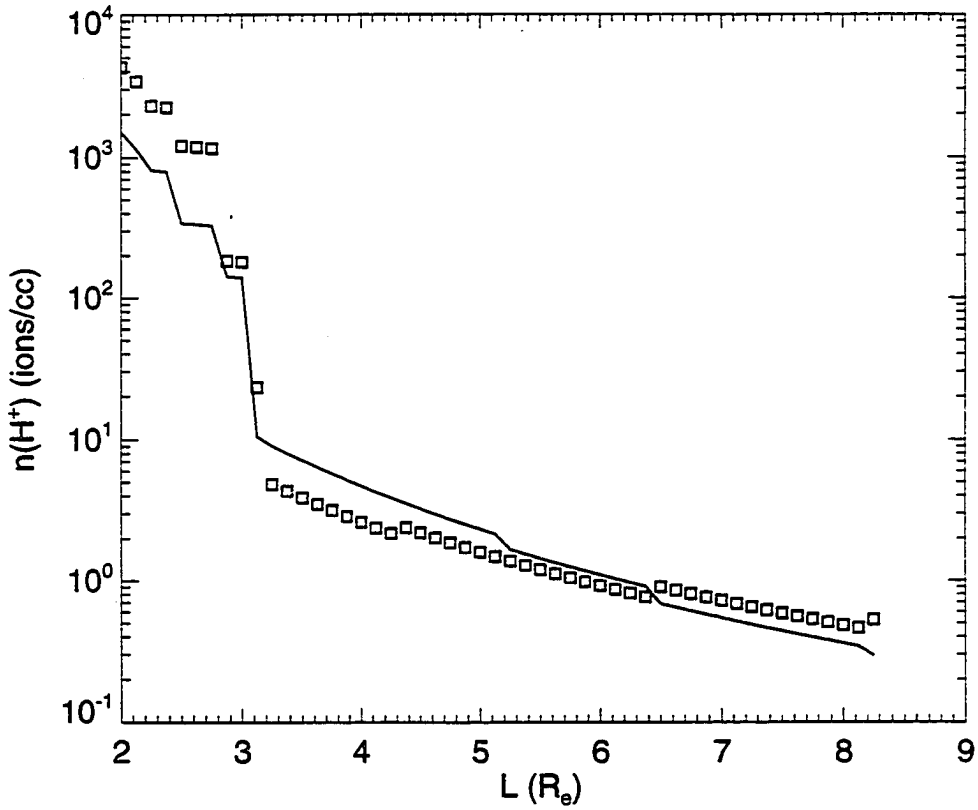

Figure 5.7 H^+ density profile versus L shell. Results for day and night are shown by the solid and dashed curves, respectively. The model was diffusive inside L=3 and kinetic outside.

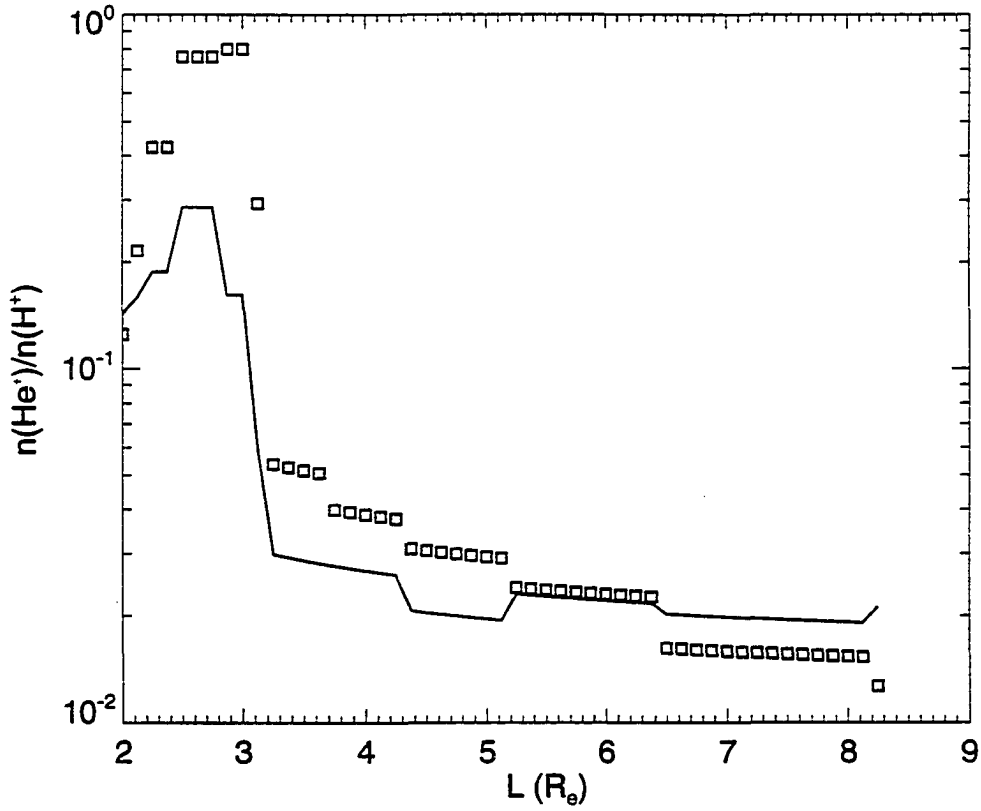

Figure 5.8 He^+ and H^+ density ratio profiles versus L shell. Results for day and night are shown by the solid curve and circles, respectively. The model was diffusive inside L=3 and kinetic outside.

we assume h=2600 km inside L=3 and h=2000 km outside L=3. The density ratio $\frac{O^+}{H^+}$ using the preceeding assumptions is plotted in Fig. 5.9 in circles. The results shown in Fig. 5.9 seem to be consistent with the observations plotted in Fig. 5.3a up to L shells equal to 6.

5.7 Images of The Plasmasphere in the EUV Region

Simulated images of the plasmasphere as seen in the wavelengths 83.4 nm and 30.4 nm from resonant scattering of O^+ and He^+ ions are shown in Figs. 5.10 and 5.11, respectively. The images are obtained by simulating a detector with a 50x50 pixel field of view and a resolution of 2 deg. The column integrated intensity in Rayleighs (R) along a given line-of-sight direction with line element ds is

$$4\pi I = \int e^{-\tau}\, p(\theta) g\, n(\mathbf{r})\, ds \times 10^{-6}(R) \tag{5.34}$$

where I is the column integrated intensity (photons cm^{-2} s^{-1}), τ is optical depth, $p(\theta)$ is the phase function, g is the scattering rate (photons per second per ion), and n is the number density in cm^{-3} at position $\mathbf{r}$. The scattering phase function reflects the anisotropy of scattered radiation and is given by

$$p(\theta) = 1 + 1/4(2/3 - sin^2\theta) \tag{5.35}$$

for He^+ (30.4 nm) where θ is the angle between the incident direction (Sun-Earth) and scattered radiation in the direction of the observer (Brandt and Chamberlain, 1959). We assume $p(\theta)$ is unity for the 83.4 nm radiation. Since the magnetosphere is optically thin above 1000 km to 30.4 and 83.4 nm radiation, τ can be set to zero. In the calculation of intensities we neglect multiple scattering.

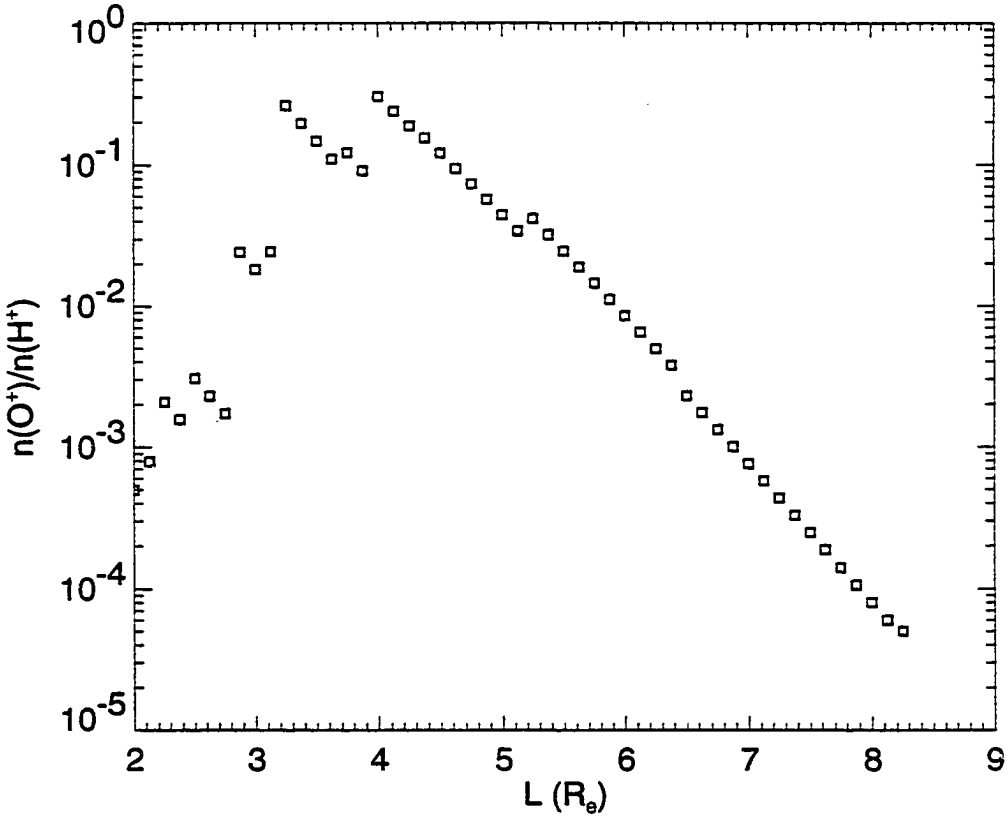

Figure 5.9 Density ratio profile vs L shell for O^+ and H^+ ions. The circles represent density ratios calculated using nighttime conditions.

In the construction of plasmaspheric images we assume a satellite at a distance of 9 R_e located in the dusk plane with a view toward the center of the Earth. Note that solar illumination is to the left of the figures. The satellite configuration has the advantage of showing the day and night as well as pole-to-pole asymmetries that may be evident in the intensity distribution of the images. Figure 5.10 shows simulated images of the plasmasphere and trough regions in 83.4 nm wavelengths for day (left side) and night (right side) conditions, respectively. Note that the image intensities are brighter in the day than in the night sector indicating a larger scattering source of O^+ ions. The sudden change from bright to moderate brightness in the near- Earth regions reflects the density fall-offs due to the ion scale heights we have assumed in the model. Maximum intensities as high as 12 R are obtained during the day. Moderate intensities from 1 to 5 R dominate the inner plasmasphere and the extent of the plasmapause falls within the half-angle field of view of about 8 deg measured vertically and 20 deg horizontally. Outside the plasmapause the intensities are of the order of a few millirayleighs to tens of millirayleighs. The left side of Fig. 5.10 shows that the inner regions of the plasmasphere are dim and the intensities seem to increase gradually with latitude, reflecting the same parallel increase in the ionospheric source density with latitude as shown in Fig. 5.4b.

Simulated images of the plasmasphere in 30.4 nm wavelengths are shown in Fig. 5.11 for the day (left side) and night (right side) conditions, respectively. It is evident that the image is brighter in the night sector than in the day reflecting a large amount of cold He^+ (30.4 nm) ions contained in the inner plasmasphere. A maximum intensity of 37.8 R and a minimum intensity of the order of 1 mR were obtained. The relative brightness in the images is also consistent with the density ratio profile shown in Fig. 5.8, indicating a higher $\frac{He^+}{H^+}$ ratio in regions within the plasmapause.

Note also that in the images for both O^+ (83.4 nm) and He^+ (30.4 nm) ions the shadowing of the plasma behind the Earth is also evident. The dim region in the night sector of Fig. 5.10 is due to the depletion of O^+ ions, and in Fig. 5.11 the relatively brighter intensities in the night sector reflect the effects of the nighttime boundary conditions, which are much higher than the day boundary conditions. We also have neglected the effects of asymmetry in the boundary conditions of the northern and southern hemisphere as well as its variation with longitude.

5.8 Future Prospects

Inherent in the study of imaging in the EUV region is the goal of understanding the underlying physical processes that would explain the distribution of O^+ and He^+ ions that resonantly scatter at 83.4 and 30.4 nm wavelengths. Such processes may implicitly be reflected in the distribution of intensities in the images. We also want to emphasize the importance of using appropriate boundary conditions. As previously discussed (Lemaire and Scherer, 1974) in Sec. 5.6 we were able to show reasonable agreement between equatorial H^+ densities measured when the magnetic activity was moderately high and model densities calculated using ionospheric boundary conditions obtained when the magnetic activity was low. This may, however, lead to difficulties in the interpretation of observed data. A plasmaspheric model (Waite et al., 1984) was developed and aimed at understanding the enhanced He^+ ion concentrations observed in the equator. The observed plasmapause boundary during the time of measurement was at L=4 as reflected in the averaged data (Hoffman and Dodson, 1980) from ISIS 2. Model calculations of densities for H^+, He^+ and O^+ incorporating effects of thermal diffusion (Schunk and Walker, 1969) were made using the ISIS 2 data as lower boundary conditions, and their results were

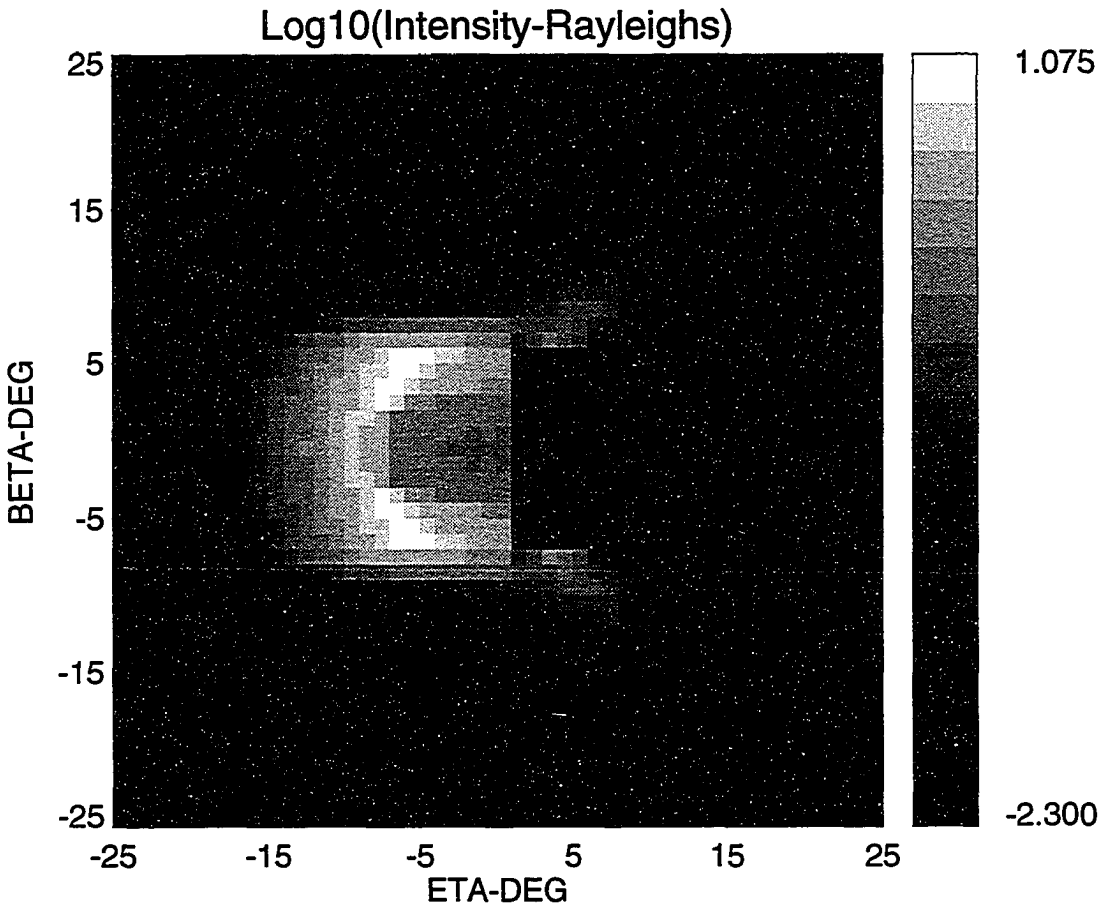

Figure 5.10 Image of the plasmasphere in resonantly scattered emissions by O^+ (83.4 nm) ions. The left side refers to the day sector and the right side refers to the night sector. The image was constructed from a satellite at 9 R_e in the dusk sector and viewing towards the center of the Earth. The gray scale bar is in base 10 log values. The maximum and minimum intensities are about 12 R and a few millirayleighs, respectively.

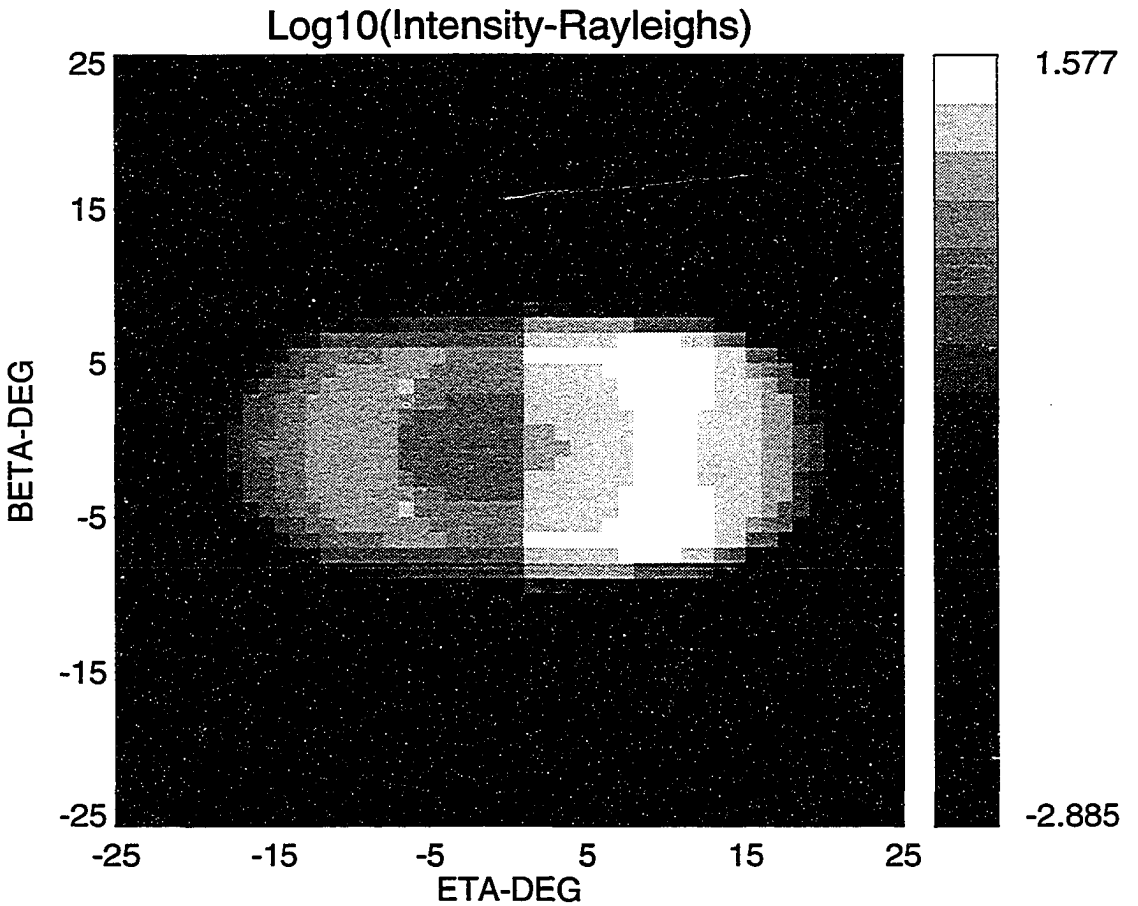

Figure 5.11 Image of the plasmasphere in resonantly scattered emissions by He^+ (30.4 nm) ions. The left side refers to the day sector and the right side refers to the night sector. The image was constructed from a satellite at 9 R_e in the dusk sector and viewing towards the center of the Earth. The scale bar are in base 10 log values. Maximum and minimum intensities are about 38 R and a few millirayleighs, respectively.

compared to equatorial values of $\frac{He^+}{H^+}$ density ratios obtained from ISEE 1 experiments. The ISEE 1 measurements at that time indicated a plasmapause boundary that was far out, nearly L=7.5. Thus, the lower boundary conditions have to be adjusted to higher invariant latitudes. The results of the analysis have shown mixed success in explaining the density ratios. We want to point out that ion densities for He^+, H^+ and O^+ in the ionosphere and their corresponding values at the equator measured simultaneously are appropriate boundary values that may provide a realistic estimate of the structure and intensity distribution of the magnetospheric images. Since simultaneous measurements of the ionosphere and plasmasphere are rare (Horwitz et al., 1986), averaged data under similar conditions (ie. magnetic activity, etc.) for the ion densities in the ionosphere and equator may be adequate for use in estimating the density falloffs or ion scale heights along field lines. Thus, for instance in the simulated images constructed for the O^+ (83.4 nm) ions, our assumptions regarding the ion scale heights may vary depending on available data. We plan to use a more extensive data set in a future analysis. We also note that contributions from energetic ions with energies greater than 10 eV have been neglected and their overall contributions to the intensities may be considerable, especially in the high latitude regions (Garrido et al., 1994).

5.9 Conclusions

We have simulated images of the plasmasphere and trough regions from resonant scattering by O^+ (83.4 nm) and He^+ (30.4 nm) ions that incorporate realistic boundary values, variation of the exobase densities with latitude and realistic ion temperatures. A maximum intensity of 12 R was obtained for O^+ and about 38 R was obtained for He^+. Because of these high intensities imaging in both 83.4 and 30.4 nm wavelengths

is feasible. However, the larger scattering rate of cold He^+ ions and the almost stable $\frac{He^+}{H^+}$ density ratios (suggestive of enhanced He^+ ion concentrations) in most regions in the plasmasphere make imaging using 30.4 nm light more favorable than imaging at 83.4 nm.

5.10 References

Angerami, J.J. and J.O. Thomas, " Studies of planetary atmospheres," *J. Geophys. Res.*, **69**, 4537-4560 (1964).

Brandt, J.C. and J.W. Chamberlain, "Interplanetary gas, 1, hydrogen radiation in the night sky," *Astrophys. J.*, **130**, 670-682 (1959).

Chakrabarti, S., F. Paresce, S. Bowyer, Y.T. Chiu and A. Aikin, " Plasmaspheric helium ion distribution from satellite observations of He II 304-A," *Geophys. Res. Lett.*, **9**, 151-154 (1982).

Chandler, M.O., J.U. Kozyra, J.L. Horwitz, R.H. Comfort and L.H. Brace, " Modeling of the thermal plasma in the outer plasmasphere-a magnetospheric heat source," *Modeling Magnetospheric Plasma*, Geophys. Monograph 44, T.E. Moore and J.H. Waite Jr., Eds., pp. 101-105, American Geophysical Union, Washington, DC, (1988).

Chappell, C.R., " Recent satellite measurements of the morphology and dynamics of the plasmasphere," *Rev. Geophys. Space Phys.*, **10**, 951-979 (1972).

Chiu, Y.T., R.M. Robinson, H.L. Collin, S. Chakrabarti, G.R. Gladstone, " Magnetospheric and exospheric imaging in the extreme ultraviolet," *Geophys. Res. Lett.*, **17**, 267-270 (1990).

Chiu, Y.T., J.G. Luhmann, B.K. Ching, and D.J. Boucher, Jr., " An equilibrium model of plasmaspheric composition and density," *J. Geophys. Res.*, **84**, 909-916 (1979).

Comfort, R.H., I.T. Newberry and C.R. Chappell, "Preliminary statistical survey of plasmaspheric ion properties from observations by DE 1/RIMS," *Modeling Magnetospheric Plasma*, Geophys. Monograph 44, T.E. Moore and J.H. Waite Jr., Eds., pp. 107-114, American Geophysical Union, Washington, DC, (1988).

Comfort, R.H., " The magnetic mirror force in plasma fluid models," *Modeling Magnetospheric Plasma*, Geophys. Monograph 44, T.E. Moore and J.H. Waite Jr., Eds., pp. 51-53, American Geophysical Union, Washington, DC, (1988).

Doschek, G.A., W.E. Behring and U. Feldman, " The widths of the solar He I and He II lines at 584, 537 and 304 A," *Astrophys. J.*,**190**, L141-L142 (1974).

Feldman, U. and W.E. Behring, " Solar coronal line profiles in the extreme-ultraviolet," *Astrophys. J.*, **189**, L45-L46 (1974).

Garrido, D.E., R.W. Smith, D.W. Swift and S.-I. Akasofu, " Imaging the earth's magnetosphere: effects of plasma flow and temperature," *Planet. Space Sci.*, **39**, 1559-1571 (1991).

Garrido, D.E., R.M. Robinson, Y.T. Chiu, H.L. Collin, R.W. Smith, and D.W. Swift, " Magnetospheric imaging of high latitude ion outflows," (Annales Geophysica, in press, 1994).

Harris, K.K., G.W. Sharp and C.R. Chappell, " Observations of the plasmapause from OGO 5," *J. Geophys. Res.*, **75**, 219-224 (1970).

Hinteregger, H.E., " Effects of solar XUV radiation on the earth's atmosphere," in *Annals of the IQSY*, Strickland, A.C., Ed., **5**, pp. 305-321, MIT Press, Cambridge, Massachusetts, (1969).

Hoffman, J.H., W.H. Dodson, C.R. Lippincott and H.D. Hammack," Initial ion composition results from Isis 2 satellite," *J. Geophys. Res.*,**79**, 4246-4251 (1974).

Hoffman, J.H. and W.H. Dodson, " Light ion concentrations and fluxes in the polar regions during magnetically quiet times," *J. Geophys. Res.*, **85**, 626-632 (1980).

Horwitz, J.L., " The ionosphere as a source for magnetospheric ions," *Rev. Geophys. Space Phys.*, **20**, 929-952 (1982).

Horwitz, J.L., L.H. Brace, R.H. Comfort and C.R. Chappell," Dual- spacecraft measurements of plasmasphere-ionosphere coupling," *J. Geophys. Res.*,**91**, 11,203-11,216 (1986).

Horwitz, J.L., C.R. Baugher, C.R. Chappell, E.G. Shelly, D.T. Young and R.R. Anderson, " ISEE 1 observations of thermal plasma in the vicinity of the plasmasphere during periods of quieting magnetic activity," *J. Geophys. Res.*, **86**, 9989-10,001 (1981).

Huang, T.S. and T.J. Birmingham," The polarization electric field and its effects in an anisotropic rotating magnetospheric plasma,"*J. Geophys. Res.*,**97**, 1511-1519 (1992).

Lemaire, J. and M. Scherer," Exospheric models of the topside ionosphere," *Space Sci. Rev.*,**15**, 591-640 (1974).

Li, W., J.J. Sojka and W.J. Raitt, " A study of plasmaspheric density distributions for diffusive equilibrium conditions," *Planet. Space Sci.*, **31**, 1315-1327 (1983).

Meier, R.R. and C.S. Weller, " EUV resonance radiation from helium atoms and ions in the geocorona," *J. Geophys. Res.*, **77**, 1190-1204 (1972).

Meier, R.R., " Ultraviolet spectroscopy and remote sensing of the upper atmosphere," *Space Sci. Rev.*, **58**, 1-192 (1991).

Meier, R.R., " The scattering rate of solar 834 A radiation by magnetospheric O^+ and O^{++}," *Geophys. Res. Lett.*, **17**, 1613-1616 (1990).

Northrop, T.G. and T.J. Birmingham, " Adiabatic charged particle motion in rapidly rotating magnetospheres," *J. Geophys. Res.*, **87**, 661-669 (1982).

Paresce, F., C.S. Bowyer and S. Kumar, " On the distribution of He^+ in the plasmasphere from observations of resonantly Scattered He II 304-A radiation," *J. Geophys. Res.*, **79**, 174-178 (1974).

Schunk, R.W. and J.C.G. Walker, " Thermal diffusion in the topside ionosphere for mixtures which include multiply-charged ions," *Planet. Space Sci.*, **17**, 853-868 (1969).

Swift, D.W., R.W. Smith and S.-I. Akasofu, " Imaging the earth's magnetosphere," *Planet. Space Sci.*, **37**, 379-384 (1989).

Taylor Jr., H.A., H.C. Brinton and C.R. Smith, " Positive ion composition in the magnetoionosphere obtained from the OGO-A satellite,"*J. Geophys. Res.*,**70**, 5769-5781 (1965).

Tsyganenko, N.A., " A magnetospheric magnetic field model with a warped tail current sheet," *Planet. Space Sci.*, **37**, 5-20 (1989).

Waite Jr., J.H., J.L. Horwitz and R. H. Comfort, " Diffusive equilibrium distributions of He^+ in the plasmasphere," *Planet. Space Sci.*, **32**, 611-618 (1984).

Weller, C.S. and R.R. Meier," First satellite observations of the He^+ 304-A radiation and its interpretation," *J. Geophys. Res.*, **79**, 1572-1574 (1974).

5.11 Acknowledgements

This work was supported by funds from the Geophysical Institute, University of Alaska, Fairbanks. We would also like to thank Dr. Juan Roederer for useful discussions, Dr. T.S. Huang and T.J. Birmingham for providing us with a manuscript of their paper, and the referees for their comments in improving the paper.

Chapter 6 Inversion of Photometric He^+ (30.4 nm) Intensities to obtain He^+ distributions *

6.0 Abstract

Radiation from He^+ at 30.4 nm, which is emitted close to the Earth, comes from three distinct regions; the ionosphere, the plasmasphere and the polar cap. Published observational data on He^+ 30.4 nm have shown that the intensities from polar regions are relatively smaller than the other regions. Polar emissions are believed to be due to resonance scattering of sunlight from ions flowing away from the ionosphere. A 1982 rocket flight from Poker Flat, Alaska has shown that line-of-sight 30.4 nm emission rates are relatively strong in the direction of the pole. Since the roll of the rocket afforded many different observing directions, we have used the variety of viewing geometries to extract ionospheric source densities from the photometric intensity data assuming that the He^+ ion densities vary with distance along dipole field lines according to a particular functional form. A least squares inversion method is used to extract the source densities. The results give density variations over a range of latitudes including samples from each of the regions mentioned above. The results show the presence of a trough in both the southern and northern hemispheres for the first period of the rocket's rotation and the

*D.E. Garrido, R.W. Smith, C.A. Marsh, A.B. Christensen, and S. Chakrabarti, Inversion of Photometric He^+ (30.4 nm) Intensities to obtain He^+ distributions; submitted to Optical Engineering, 1994

density varied rapidly for other periods of rotation. The results also show enhanced ion concentrations near the polar cap.

6.1 Introduction

Observations of the He^+ 30.4 nm line have been obtained by detectors aboard low altitude rockets (Paresce et al., 1974; Weller and Meier, 1974) and also have been observed by the extreme ultraviolet telescope on the Apollo-Soyuz spacecraft (Chakrabarti et al., 1982). The intensities of the emissions can be explained by using a density model for the plasmasphere and knowledge of the scattering rate of the ions. In studies of plasmasphere-ionosphere coupling (Horwitz et al., 1990) satellite observations of thermal ion composition were made and compared directly with calculations of ion density profiles using the field line interhemispheric plasma (FLIP) model (Richards and Torr, 1988; Newberry et al., 1989). The model shows general agreement with observations. We will use results consistent with the FLIP model as a guide in the analysis of observed intensity data.

Photometric measurements of optically thin emissions provide emission rates integrated along the line-of-sight. The problem of obtaining volume emission rates from the measured intensities in some observational scenarios is related to the technique known as tomography. The technique is applied in such areas as remote sensing and medical computerized tomography. The methods of analysis vary in mathematical approach such as the Cormack inversion (Cormack, 1963; 1964), Radon Transforms (Ghosh Roy, 1984) and algebraic reconstruction techniques (Herman, 1979). However, the method of sampling many line integrals of the emission function is common to all these techniques in that the many line-of-sight integrations are obtained at various locations. A tomographic

method using the Cormack inversion has been used in the analysis of photometric measurements of atmospheric airglow from orbit (Solomon et al., 1984; 1985). Tomographic experiments, although important, make space-borne applications impractical and very expensive. In this paper we propose a least squares inversion method from which the density distribution of ions can be obtained from the observed intensities for the case when a rocket moves in space and has a rolling motion. This geometry has the advantage that many observation directions allow the sampling of many spatial regions that include the ionosphere, plasmaspheric and trough regions and the regions of ion outflow in the polar cap. If the average behaviour of the plasmasphere does not vary rapidly over one period of rotation of the rocket then our method provides a way of obtaining He^+ ion densities at a chosen reference height (500 km). The extent of the distribution covered many latitude regions that include both the northern and southern hemisphere.

6.2 Photometric Intensity Profiles

The intensity profile vs zenith angle during one period of rotation (29.5 seconds) obtained from an EUV photometer at 30.4 nm from a rocket which reached an altitude of 435.7 km flown in 1982 from Poker Flat Range, Alaska. The rocket flight viewing geometry showing representative line-of-sight vectors is shown in Fig. 6.2. We defined cartesian (X_1, Y_1) coordinates fixed with the rocket but are not shown. The vertical Y_1 axis represents the upward zenith direction and β, the zenith angle is measured clockwise. β=0 is in the zenith and the horizontal positive X_1 axis defines the β=90 deg position and is directed towards the northern pole. For an observer viewing down the figure, the rocket's spin is clockwise starting at β=90 deg. The dashed curve represents the raw intensity profile while the solid curve represents the smoothed intensity profile. Our analysis will

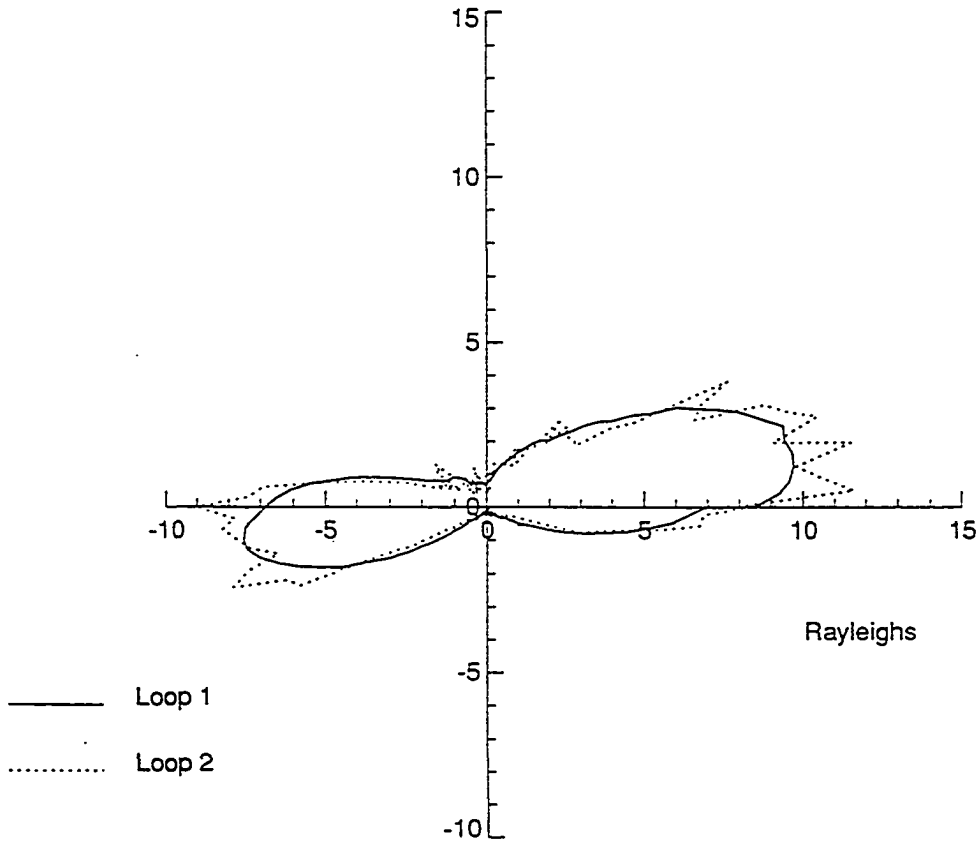

Figure 6.1 Photometric He^{+} (30.4 nm) Intensity vs Roll Angle. The solid curve (loop 1) is the smooth profile while the dashed curved (loop 2) is the raw data.

be concerned only with large scale phenomena, hence, we will use the smoothed curve shown in Fig. 6.1. A maximum intensity of 9.8 R (where R means rayleigh) occurs at β=80 deg viewing towards the northern hemisphere while a maximum intensity of 7.6 R occurs at β=-94.7 deg viewing towards the southern hemisphere. For observation angles in the negative Y_1 axis the rapid decline in the intensities begin at β= 114 deg continuing down to β=180 (also -180 deg) and then until β= -110 deg from which the effects of the Earth's occultation are present. We shall investigate the variation of the ion densities with altitude in their respective flux tubes in the different regions of space that will reproduce the line-of-sight emission rate profiles shown in Fig. 6.1.

We start our analysis by assuming that the ionosphere is divided into 25 different latitude regions each having a width in degrees as defined below. Their respective base densities are defined at an altitude of 500 km and we assume that they act as ionospheric source densities. The regions are broken down as follows:

$$(Latitude\ Range\,(Deg),\quad Source\ Label)$$

$$z > 0,\ (Night)$$

$$(85 \leq \lambda_0 < 90,\quad 1)$$

$$(80 \leq \lambda_0 < 85,\quad 2)$$

$$(70 \leq \lambda_0 < 80,\quad 3)$$

$$(68 \leq \lambda_0 < 70,\quad 4)$$

$$(65 \leq \lambda_0 < 68,\quad 5)$$

$$(63 \leq \lambda_0 < 65,\quad 6)$$

$$(60 \leq \lambda_0 < 63, \quad 7)$$

$$(55 \leq \lambda_0 < 60, \quad 8)$$

$$(50 \leq \lambda_0 < 55, \quad 9)$$

$$z < 0, \ (Night)$$

$$(-60 \leq \lambda_0 < -50, \quad 10)$$

$$(-62 \leq \lambda_0 < -60, \quad 11)$$

$$(-64 \leq \lambda_0 < -62, \quad 12)$$

$$(-66 \leq \lambda_0 < -64, \quad 13)$$

$$(-68 \leq \lambda_0 < -66, \quad 14)$$

$$(-70 \leq \lambda_0 < -68, \quad 15)$$

$$(-80 \leq \lambda_0 < -70, \quad 16)$$

$$z > 0, \ (Day)$$

$$(86 \leq \lambda_0 < 90, \quad 17)$$

$$(83 \leq \lambda_0 < 86, \quad 18)$$

$$(80 \leq \lambda_0 < 83, \quad 19)$$

$$(77 \leq \lambda_0 < 80, \quad 20)$$

$$(74 \leq \lambda_0 < 77, \quad 21)$$

$$(72 \leq \lambda_0 < 74, \quad 22)$$

$$(70 \leq \lambda_0 < 72, \quad 23)$$

$$(68 \leq \lambda_0 < 70, \quad 24)$$

$$(65 \leq \lambda_0 < 68, \quad 25)$$

Also, the shadow region where the scattering rate is assumed to be zero is defined by $-50 \leq \lambda_0 < 50$ and $-89 \leq \lambda_0 < -80$ for X>0. The rocket is located approximately at an altitude of 435.7 km, θ=24.1 and ϕ=167.25 deg (in geographic coordinates). The choice for the number and width of source regions is arbitrary. We have chosen the number of source regions to be 25 and we label the unknown source densities n_{0I} where I=1 to 25 which are values at an altitude of 500 km. The base of the flux tube is set at 100 km and the density everywhere within the flux tube can be obtained from $n_I = n_{0I}\phi_I(s)$ where the shape function $\phi_I(s)$ may be an increasing or decreasing function of the arc length s within a given flux tube. In one rotation period of the rocket there are 148 intensity data points, thus leading to the problem of inverting a 148×25 matrix. Thus, preparatory to the analysis of inverting a 148×25 matrix equation we define the roll angles shown in Fig. 6.2 and label them by the index m. The roll angles equal to 89.647 and 91.82 deg are labeled by m=1 and m=2, respectively. Also, the roll angle equal to 109.532 deg is labeled by m=9 and is also grazing the Earth in the northern hemisphere. The roll angle of -109.567 deg defines the line-of-sight directed towards the southern hemisphere and almost grazes the surface of the Earth and is labeled by m=66. Likewise, roll angles -90.043 and 0 deg are labeled by m=74 and m=111, respectively. Thus, the rotation of the rocket proceeds in a clockwise manner starting with m=1 stepping through m=148. In common with previous researchers, we assume that these intensity data may be analyzed

on the basis of an optically thin atmosphere. The column emission rate for an optically thin emission line at (30.4 nm) is given by

$$4\pi I = \int \mathrm{gn\,dl\ (photons\,cm^{-2}\,s^{-1})10^{-6}\,(R)} \qquad (6.1)$$

n is the density in ions cm^{-3} and the scattering rate g for cold He^+ 30.4 nm ions is 9.16×10^{-6} photons s^{-1} ion^{-1} (Garrido et al., 1992; 1994). Also, dl is the differential distance along a given line-of- sight.

6.3 The Motivation Behind Our Approach

The available photometric intensity data does not conveniently fit into presently known methods of analysis of obtaining altitude profiles for the density of He^+ (30.4 nm) ions over all the latitude regions covered by the rocket's spin motion. A single line-of-sight observation contains emissions from several flux tubes and in principle we don't know how much each flux tube contributes to the total emission rate. We also don't know the exact shape of the altitude profiles of the ion densities in each flux tube region. However, simulations using the FLIP model have obtained altitude profiles in the plasmasphere that are consistent with observations and FLIP type profiles also arise in the analysis of ion distribution in the high latitude regions (Ottley and Schunk, 1980). We are not emphasizing any particular dynamical model in the description of the ion densities but it is reasonable to expect the spatial distribution of the densities in each flux tube to be consistent with the results of the FLIP model. For the geophysical regions considered here, we asume that each magnetic flux tube in the high latitude regions and the low latitude plasmasphere has ionization distributed with altitude according to a functional form that is consistent with the FLIP model. This assumption greatly simplifies the

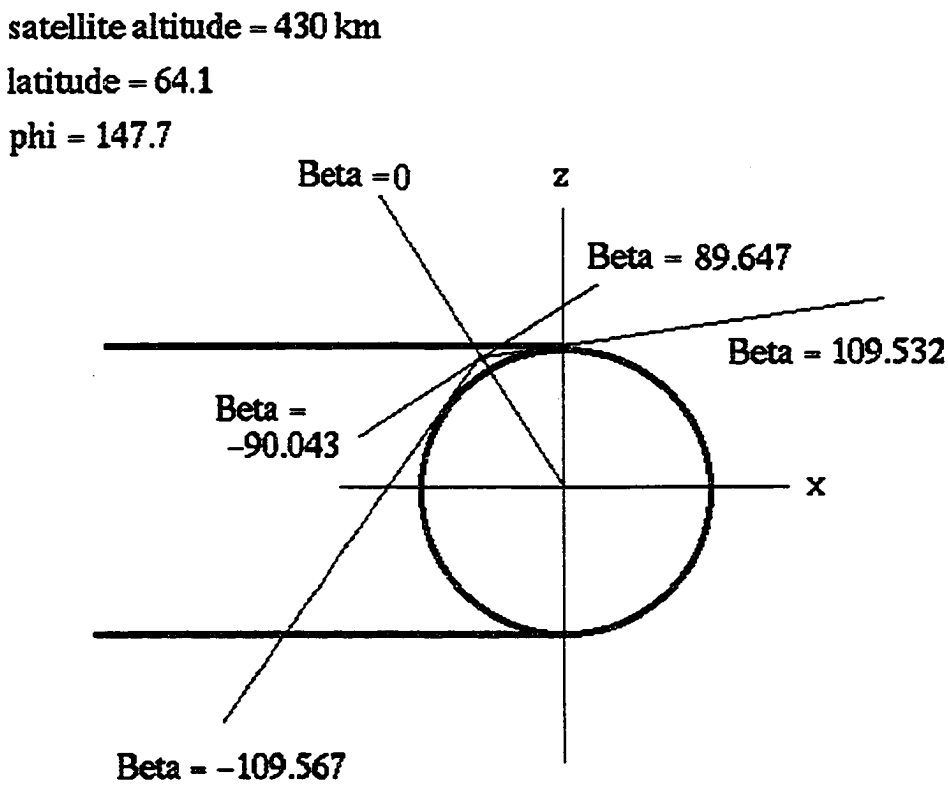

Figure 6.2 Rocket geometry showing representative line-of-sight view angles (β) and geographic coordinates for a spinning rocket. The shadow region is to the left of the figure.

problem to only determining the source densities at the reference altitude once the shape of the spatial distribution of ion densities is assumed to be known. We will describe in Sec. 6.4 the procedure of how the relative contribution of each flux tube to the emission rate may be obtained. The shape function that describes the spatial distribution of ion densities will be described in Sec. 6.5.

6.4 Derivation of the Matrix Coefficients

At any point along a line-of-sight the density is calculated from

$$n = n_{0I}\phi_I(s) \tag{6.2}$$

where ϕ_I(s) is a function of the arc length s along a field line and may be assumed to increase or decrease with increasing distance s from the ionospheric base. Also, the particular source region may be obtained by tracing back to the ionosphere using the equation for the line of force for a dipole field

$$R_0 = L\cos^2\lambda_0 \tag{6.3}$$

where L is the distance of the equatorial crossing of a field line from the center of the Earth, λ_0=base latitude and R_0 is the radial distance of the ionospheric base given in units of Earth radii (R_e).

In particular, the line-of-sight intensities may be written as a sum of terms reflecting contributions from the different source regions, ie.,

$$4\pi I_m = \int_{R_{m,1}} gndl + \int_{R_{m,2}} gndl + ... + \int_{R_{m,25}} gndl \tag{6.4}$$

or in general

$$4\pi I_m = \sum_I \int_{R_{m,I}} gndl \tag{6.5}$$

where R_{mI} defines the region of integration for a specific source location identified by the index I and line-of-sight 'look' angle index m. Eqs. (6.4) or (6.5) may be expressed in terms of the unknown densities n_{0I}

$$4\pi I_m = A_{m,1} n_{01} + A_{m,2} n_{02} + ... + A_{m,25} n_{025} \tag{6.6}$$

Eq. (6.6) may also be expressed in matrix form as

$$\sum_I A_{m,I} x_I = b_m \tag{6.7}$$

where b_m refer to the input intensities, $A_{m,I}$ are coefficients that depend on the g-factor, dl and the model function ϕ_I(s) and x_I assume the role of the unknown densities n_{0I}. As an illustration, for the view direction at 109.532 deg (m=9)

$$4\pi I_9 = \sum_{I=18}^{25} A_{9,I} n_{0I} \tag{6.8}$$

where the remaining coeficients $A_{m,I}$ are zero because the line-of-sight ray only traces back to the source regions 18, 19, 20, 21, 22, 23, 24 and 25. The coefficients A_{mI} are

calculated numerically as follows

$$\int_{R_{9,18}} \text{gndl} = \text{n}_{018}\text{A}_{9,18} \tag{6.9}$$

where

$$A_{9,18} = \frac{\Delta l}{2} \sum_{k=1}^{k=nk(9,18)} (g_k \phi_{18}(s_k) + g_{k+1}\phi_{18}(s_{k+1})) \tag{6.10}$$

Similarly,

$$\int_{R_{9,19}} \text{gndl} = \text{n}_{019}\text{A}_{9,19} \tag{6.11}$$

where

$$A_{9,19} = \frac{\Delta l}{2} \sum_{k=nk(9,18)-1}^{k=nk(9,19)} (g_k \phi_{19}(s_k) + g_{k+1}\phi_{19}(s_{k+1})) \tag{6.12}$$

For the terms in the sum, k=1 labels the starting point and nk(m,I) is the integer that defines the last term that is contained within the flux tube defined by the source region I. The other $A_{m,I}$ coefficients for the different 'look' directions are calculated numerically as discussed in Eqs. (6.9)-(6.12) and is summarized in the following sparse matrix

$$m = 1-2,\ A_{m,I} = (\text{x},\text{x},\text{x},\text{x},0,0,0,0,0,0,0,0,0,0,0,0,\text{x},\text{x},\text{x},\text{x},\text{x},\text{x},\text{x},\text{x},\text{x})$$

For convenience, we can explicitly write out only the non zero elements and their respective labels and view angle ranges, ie.,

$m = 1-2$, $\beta = (89.65, 91.82)$, $A_{m,I}$=(1,2,3,4,17,18,19,20,21,22,23,24,25)

$m = 3-8$, $\beta = (94.7, 107.4)$, $A_{m,I}$=(1,2,3,17,18,19,20,21,22,23,24,25)

$m = 9$, $\beta = 109.5$, $A_{m,I}$=(18,19,20,21,22,23,24,25)

$m = 66-74$, $\beta = (-109.567, -90.04)$, $A_{m,I}$=(10,11,12,13,14,15,16)

$m = 75-78$, $\beta = (-87.5, -80.3)$, $A_{m,I}$=(11,12,13,14,15,16)

$m = 79$, $\beta = -77.75$, $A_{m,I}$=(7,12,13,14,15,16)

$m = 80$, $\beta = -75.22$, $A_{m,I}$=(6,7,13,14,15,16)

$m = 81$, $\beta = -73.05$, $A_{m,I}$=(5,6,7,14,15,16)

$m = 82$, $\beta = -70.16$, $A_{m,I}$=(3,4,5,6,7,8,16)

$m = 83 - 88$, $\beta = (-67.98, -55.69)$, $A_{m,I}$=(3,4,5,6,7,8,9)

$m = 89 - 94$, $\beta = (-53.52, -41.2)$, $A_{m,I}$=(3,4,5,6,7,8)

$m = 95 - 98$, $\beta = (-38.7, -31.47)$, $A_{m,I}$=(3,4,5,6,7)

$m = 99 - 101$, $\beta = (-28.94, -23.88)$, $A_{m,I}$=(3,4,5,6)

$m = 102 - 107$, $\beta = (-21.71, -9.78)$, $A_{m,I}$=(3,4,5)

$m = 108 - 115$, $\beta = (-6.88, 10.11)$, $A_{m,I}$=(2,3,4,5)

$m = 116 - 122$, $\beta = (12.64, 27.09)$, $A_{m,I}$=(1,2,3,4,5)

$m = 123$, $\beta = 29.27$, $A_{m,I}$=(1,2,3,4)

$m = 124 - 128$, $\beta = (31.8, 41.5)$, $A_{m,I}$=(1,2,3,4,17)

$m = 129 - 132$, $\beta = (44.1, 51.3)$, $A_{m,I}$=(1,2,3,4,17,18)

$m = 133 - 135$, $\beta = (53.8, 58.5)$, $A_{m,I}$=(1,2,3,4,17,18,19)

$m = 136 - 138$, $\beta = (61.1, 65.4)$, $A_{m,I}$=(1,2,3,4,17,18,19,20)

$m = 139 - 141$, $\beta = (67.9, 73.0)$, $A_{m,I}$=(1,2,3,4,17,18,19,20,21)

$m = 142 - 143$, $\beta = (75.2, 77.7)$, $A_{m,I}$=(1,2,3,4,17,18,19,20,21,22)

$m = 144 - 145$, $\beta = (80.2, 82.8)$, $A_{m,I}$=(1,2,3,4,17,18,19,20,21,22,23)

$m = 146 - 147$, $\beta = (85.3, 87.5)$, $A_{m,I}$=(1,2,3,4,17,18,19,20,21,22,23,24)

$m = 148$, $\beta = 89.65$, $A_{m,I}$=(1,2,3,4,17,18,19,20,21,22,23,24,25)

where the x values reflect the source regions that contribute to the line-of-sight intensities for a given view angle. The notation used above for labelling the case m=1-2 means that the first four positions occupied by x also refers to the source regions 1, 2, 3, and 4, respectively. Similarly, the remaining positions filled by x refer to the regions 17 through 25. The case m=1 refers to the view direction with β=89.65 deg while m=2 refers to β= 91.82 deg and the elements in the array $A_{m,I}$ reflect the source regions involved that contribute to the column intensity, ie., regions 1 through 4 and 17 through 25. The cases m=3-8 refer to the view angle range from β= 94.7 deg (m=3) to β=107.4 deg (m=8) and the entries in the array refer to the source regions involved. We also take note that the m=1 and m=148 labels refer to the same view direction but differ in time by one period of rotation of the rocket and the value of the intensities at these times may have changed. We did not list the cases for m=10 to m=65 because these view directions are occulted by the Earth. The case m=10 refers to the view direction occulted by the Earth in the northern hemisphere while m=65 refers to the view direction occulted in the southern hemisphere. For source regions that are shadowed by the Earth, the scattering rate has been set to zero so that they are not part of the system of equations. Note, that the above example corresponds to a dipole field with 0 deg tilt. We have not listed the values of the corresponding matrix elements indicated above.

6.5 The Density Shape Function

In each flux tube we define a shape function that describes the subregions between s=0 to s=1 and for s > 1. All distances are measured in units of R_e. Since our description for the other source regions pertaining to different flux tubes are similar we omit the label I. Thus, the subscripts used here refer to the subregions in a given flux tube.

$$S_3 : 0 < s < s_2,\ n = n_0\phi_3(s),\ \phi_3(s) = a_3s^2 + b_3s + c_3$$

$$S_2 : s_2 \leq s < s_3,\ n = n_0\phi_2(s),\ \phi_2(s) = a_2s + b_2$$

$$S_1 : s_3 \leq s < s_5,\ n = n_0\phi_1(s),\ \phi_1(s) = a_1s^2 + b_1s + c_1$$

$$S_0 : s_5 \leq s \leq s_7,\ n = n_0\phi_0(s),\ \phi_0(s) = a_0s^2 + b_0s + c_0$$

From the arc distances s_i (i=1 to 7) we choose s_1=100 km s_3=500 km and s_7= 6371 km. The remaining s_i are chosen as free parameters in the inversion process. This will be evident when we discuss results obtained after the inversion in a later section. Defining $n(s_1) = n_1$ and $n(s_3) = n_0$, we obtained the following equations for region S_3; assuming

that n=0 at s=0, we get c_3=0. At s_1 and s_2 we have

$$a_3 s_1^2 + b_3 s_1 = \frac{n_1}{n_0} \tag{6.13a}$$

$$a_3 s_2^2 + b_3 s_2 = \frac{n_2}{n_0} \tag{6.13b}$$

Similarly, for region S_2 at s_2 and s_3 we obtained the following equations

$$a_2 s_2 + b_2 = \frac{n_2}{n_0} \tag{6.14a}$$

$$a_2 s_3 + b_2 = 1 \tag{6.14b}$$

Also, for region S_1 we obtained the set of equations

$$a_1 s_3^2 + b_1 s_3 + c_1 = 1 \tag{6.15a}$$

$$a_1 s_4^2 + b_1 s_4 + c_1 = \frac{n_4}{n_0} \tag{6.15b}$$

$$a_1 s_5^2 + b_1 s_5 + c_1 = \frac{n_5}{n_0} \tag{6.15c}$$

and for region S_0 we obtained the set of equations

$$a_0 s_5^2 + b_0 s_5 + c_0 = \frac{n_5}{n_0} \tag{6.16a}$$

$$a_0 s_6^2 + b_0 s_6 + c_0 = \frac{n_6}{n_0} \tag{6.16b}$$

$$a_0 s_7^2 + b_0 s_7 + c_0 = \frac{n_7}{n_0} \tag{6.16c}$$

The unknown coefficients above can easily be solved in terms of the density ratios and the arc distances. Finally, for the region s > 1 we assume the density to decrease according to

$$n = \frac{n_7}{s^\alpha} \tag{6.17a}$$

where

$$n_7 = n_0(a_0 s_7^2 + b_0 s_7 + c_0) \tag{6.17b}$$

Thus, for all points within a given flux tube the density profile depends on the scale parameter α, the 7 arc distances s_i and the 6 density ratios $\frac{n_i}{n_0}$.

6.6 Inversion of Intensities by the Least Squares Method

In the calculation of the matrix elements defined in Sec. 6.4 we set the scattering rate g_k equal to the constant g, Δl=.02 R_e and use the expressions for the shape function discussed in Sec. 6.5. The elements of the column vector b_m in Eq. (6.7) are given by the 148 intensity data points that we have chosen earlier as discussed in Sec. 6.2. Since the intensities are in rayleighs we divide our matrix elements by the factor 10^6 photons cm^{-2} s^{-1}. We also define the error or residual matrix as ϵ=Ax-b. We proceed with the inversion process by inputing initial values for the scale parameter α, s_i and n_i/n_0 in each of the 25 source regions. Before we specify the parameters, we state our assumptions, 1) The rocket is fixed in space while spinning on its axis. 2) The rocket's line-of-sight rays lie in the plane of rotation of the rocket. 3) The contribution to the line-of-sight intensity comes from different flux tube regions. 4) In each flux tube region the density varies as n=$n_0\phi$(s) where ϕ(s) is a quadratic function described in Sec. 6.4 and s is the arc length. The quadratic function is assumed to have the FLIP type shape and the model parameters are given in the appendix. 5) The cold plasma distribution would include the ionosphere, high latitude outflow regions and the plasmasphere. 6) The intensities are calculated under optically thin conditions. 7) The plasmasphere does not vary over one period of the rocket's rotation.

Now, the model parameters n_i/n_0, α and s_i are specified in the appendix and the forward method of inversion is done by first assuming initial values for the densities n_{0l} in all the 25 source regions and then calculating the intensities for all the different view angles and compare these values with the observed intensities and note the square of the error ϵ. The densities are then adjusted and the procedure repeated until a minimum value for ϵ^2 is attained. For convenience, since it is cumbersome to be adjusting the

densities in 25 source regions at a time, we calculated the intensities in a limited range of view angles first and then adjusted the densities in the relevant source regions until the smallest value for ϵ^2 has been obtained for that range of view angles and then repeated the calculations above for the other remaining view angles until a small error is obtained. A look at the matrix elements in Sec. 6.4 can show how cumbersome the procedure is in the adjustment of the densities in the source regions involved for a given range of view angles. Note that the minimum error is obtained when any other adjustment in the densities leads to an increase in the magnitude of ϵ^2. When an increase results, the previous value for the densities is defined as the solution to our problem.

Inherent in the discussion of the density shape function is that by an appropriate choice of the density ratios n_i/n_0 and the arc distances s_i, the altitude profiles would resemble the shape of altitude profiles obtained from results using the FLIP model, which has been successful in the description the plasmasphere. In the FLIP model, the densities would increase from 100 km to a maximum at roughly 500 km and decrease with altitude, thereafter.

6.7 Time-Dependent Intensity Profiles

The intensity profiles for 7 periods of the rocket's rotation are shown in Fig. 6.3. The intensity profile for the first period is the innermost profile (loop 1, solid) and the outermost profile (seventh period) is referred to as loop 7 and is also indicated by a solid curve. The intensity profiles reflect the dynamic changes in the plasmasphere and qualitatively show up in the plasmaspheric and outflow regions. Note that the horizontal axis in Fig. 6.3 which is the case m=74 with a view direction angle β=-90.04 deg (see Sec. 6.4) and the source regions involve are regions 10 to 16 and by referring back to the definitions in Sec.

6.2, it shows that the regions in the southern hemisphere and mid-latitude plasmasphere are involved and give the largest relative contribution to the intensity. For the first period of rotation (loop 1), the left horizontal axis indicates a maximum intensity of 9 R and in the next period the intensity has increased to 12 R. For the remaining periods of rotation the intensity has increased even more up to 14 R. The sudden increase in intensities in a time period of three minutes is suggestive of 'dynamical changes' occuring at high altitudes (greater than 6000 km) in the plasmaspheric regions. The contributions from the high latitude regions are reflected in the view direction about β=17 deg where regions 1, 2, 3, 4, and 5 are involved and with the largest contribution to the intensity coming from regions 1 and 2 which are high latitude outflow regions in the northern hemisphere and in the night sector. For period 1 the intensity is about 1.25 R and has now increased roughly to 2, 4, 5, 5.5, 5.6 and 7 R for the remaining periods 2 to 7, respectively. We also take note that the intensity change from period 1 to period 2 from the outflow regions (1.25 to 2 R) is not very significant except in the mid-latitude regions where we see an increase in intensity from 9 to 12 R. However, from period 2 to period 3 only a small increase in intensity occurs in the mid-latitude regions. Also, another significant feature occurs in the intensity profile for period 3 (loop 3, dashed). For the view angle range from β=60 to 86 deg the largest intensity is 12.7 R which occurs for β= 75 deg where the regions that contribute the largest are regions 21 and 22. For the remaining periods 4 to 6 the intensity has dropped to about 10.2 R and then increased again to 11.8 R for period 7. Assuming that the ion's scattering rate remains constant at these times these oscillatory features in the intensity profiles suggests that the ion distribution at higher altitudes are very dynamic. It is also interesting to note that the intensity profiles for periods 4, 5 and 6 represent globally an almost 'constant configuration' of the plasmasphere during these periods (1.5 minutes) (see also Fig. 6.4) and then a sudden expansion occurs in the

last period. We will discuss the corresponding changes in the density profiles in a later section.

6.8 Interpretation of n(500) vs latitude graphs

A plot of the He^+ ion density at 500 km vs latitude is shown in Figs. 6.5 and 6.6 for the northern and southern hemispheres, respectively. The angle from the equator is plotted so that the pole crossing can come out explicitly. Hence, an angle greater than 90 deg means that the location is over the pole.

A look at the Northern Hemisphere plot shows a) All curves have the same basic shape. b) There is a clear trough feature centered near 75 deg for the first period, but an enhancement grows (or moves) in the field of view with steadily increasing concentration. There seems to be an increase of He^+ ions by a factor of 8, just at about 69 deg latitude. c) A consistent peak of Helium ion concentration appears near 108 deg (72 deg latitude on the sunlit side). This might be accepted as due to ionization in sunlight. The decrease beyond 110 deg is probably not real but due to the minimal observation of that field line, rather high up. d) The increase in concentration going to lower latitudes is as expected apart from the apparent time dependence. Since such a large change in a short time is not expected,we may suspect that the measurement may not be simply interpreted as we had thought.

A look at the Southern Hemisphere plot shows that a) The concentrations are much higher than the northern hemisphere. b) A trough appears as in the northern hemisphere. c) The poleward increase of He^+ ion concentration is conjugate to the aurora seen near the rocket in the northern hemisphere, and the time dependence is very similar. d) The bottom of the trough is rather stable, unlike the behaviour in the northern hemisphere.

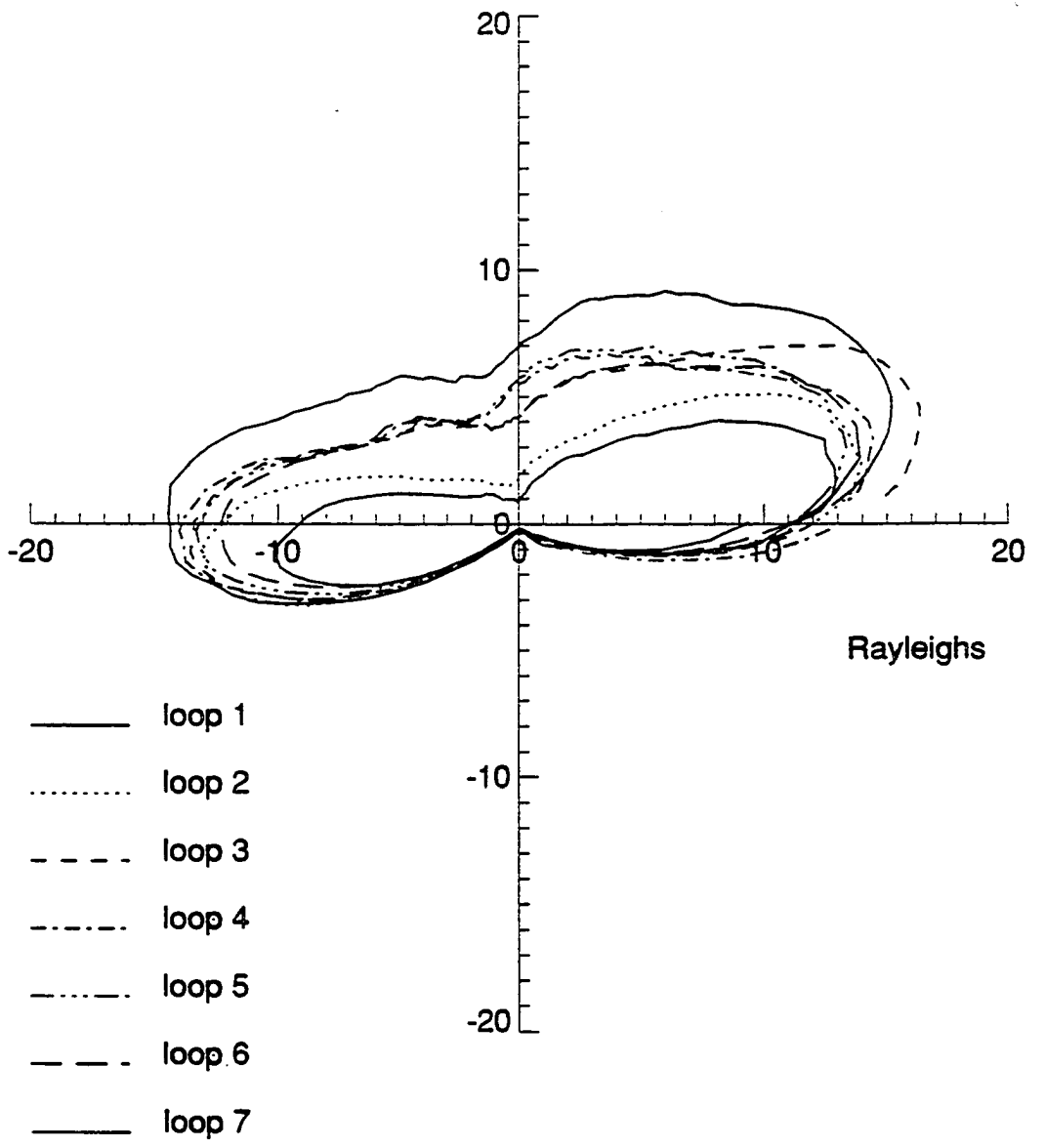

Figure 6.3 Photometric He^+ (30.4 nm) Intensity vs Roll Angle for 7 periods of rotation of the rocket. The innermost loop (loop 1, solid) represents the first period of the rocket's rotation and the outermost loop (loop 7, also solid) refer to period 7.

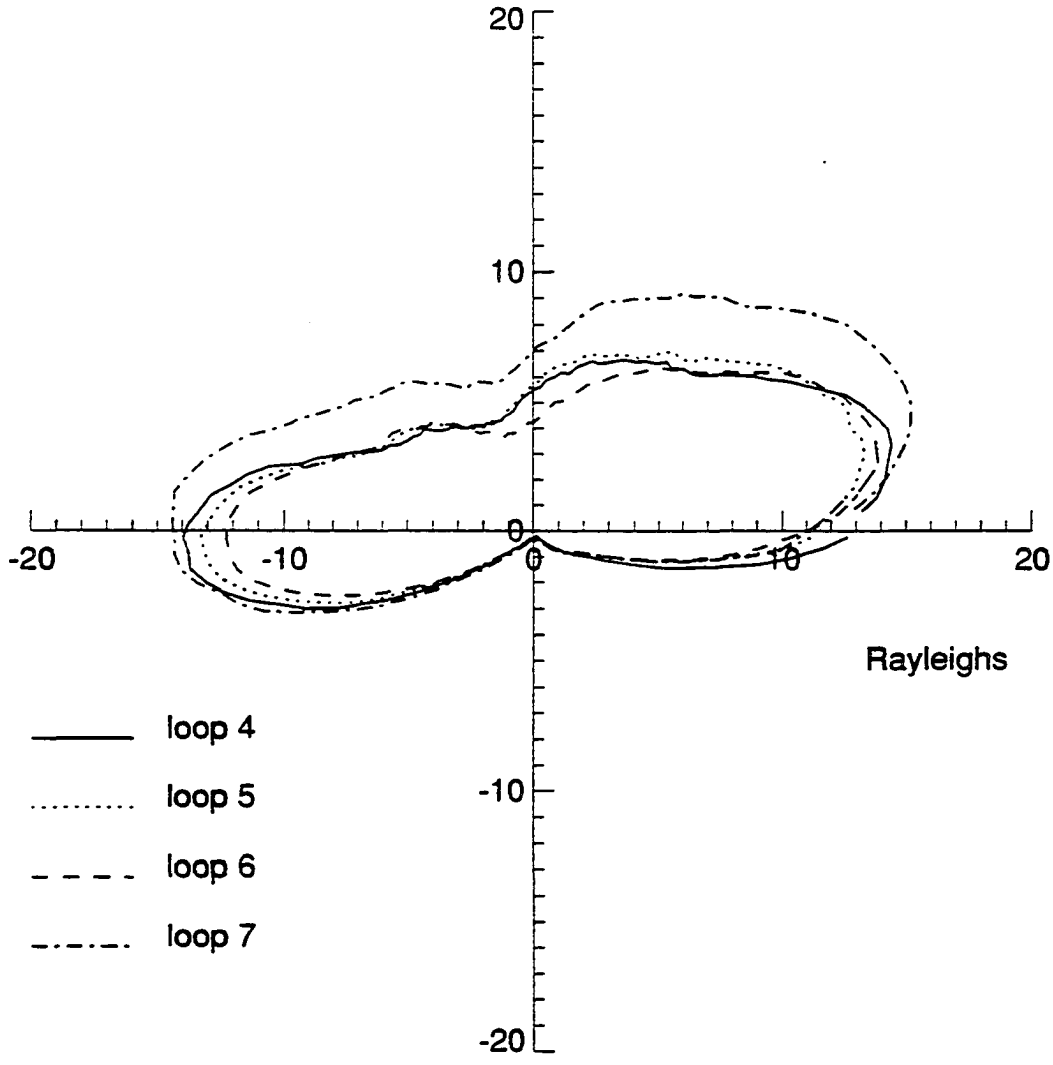

Figure 6.4 Photometric He^+ (30.4 nm) Intensity vs Roll Angle for periods 4, 5, 6 and 7 of the rocket's rotation. Note that the intensity profiles for periods 4, 5 and 6 represent an almost constant configuration for the plasmaphere and a final inflated profile for period 7. The period of the rocket's rotation and the outermost loop (loop 7, solid) refer to period 7.

Note that each profile is not unreasonable by itself and features were found similar to reports by other observers. Derivation of the n(500) values from data obtained at greater altitudes, using an equilibrium standard ion profile, seems to work reasonably well. While the sudden changes just north of the rocket are acceptable because of the presence of an aurora, time dependencies at lower latitudes are difficult to relate to our present understanding.

6.9 Time-Dependent Altitude Profiles

In each region the time variation of the altitude profiles during the 7 periods of the rocket's rotation is shown in Figs. 6.7 to 6.11 and we made plots for some representative regions. Note that regions 1, 2 and 3 of Fig. 6.7 are high latitude regions in the night sector while regions 17, 18 and 19 of Fig. 6.8 correspond to the high latitude regions in the day side. Figs. 6.7 and 6.8 represent regions in the northern hemisphere. Note, also that for each time dependent plot in each region the solid curve refers to both period 1 and period 7 with the latter having the largest intensities. It seems evident that in both figures the altitude profiles for periods 4, 5 and 6 in these regions have not varied significantly and seem to be consistent with the intensity profiles shown in Figs 6.3 or 6.4. The contrast between Fig. 6.7 and Fig. 6.8 for the first period of rotation show that the relative magnitude of the densities in the day sector is larger than in the night sector and may be reasonable due to more ionization in the dayside. The altitude profiles in the mid-latitude regions in the night sector are shown in Fig. 6.9 for regions 7, 8 and 9 (northern hemisphere) and in Fig. 6.10 for regions 11, 12 and 13 (southern hemisphere). Figure 6.10 shows a relatively larger distribution of ionization (latitude ranges from -60 to -66 deg) compared to the regions described in Fig. 6.9 (latitude ranges from 50 to 63

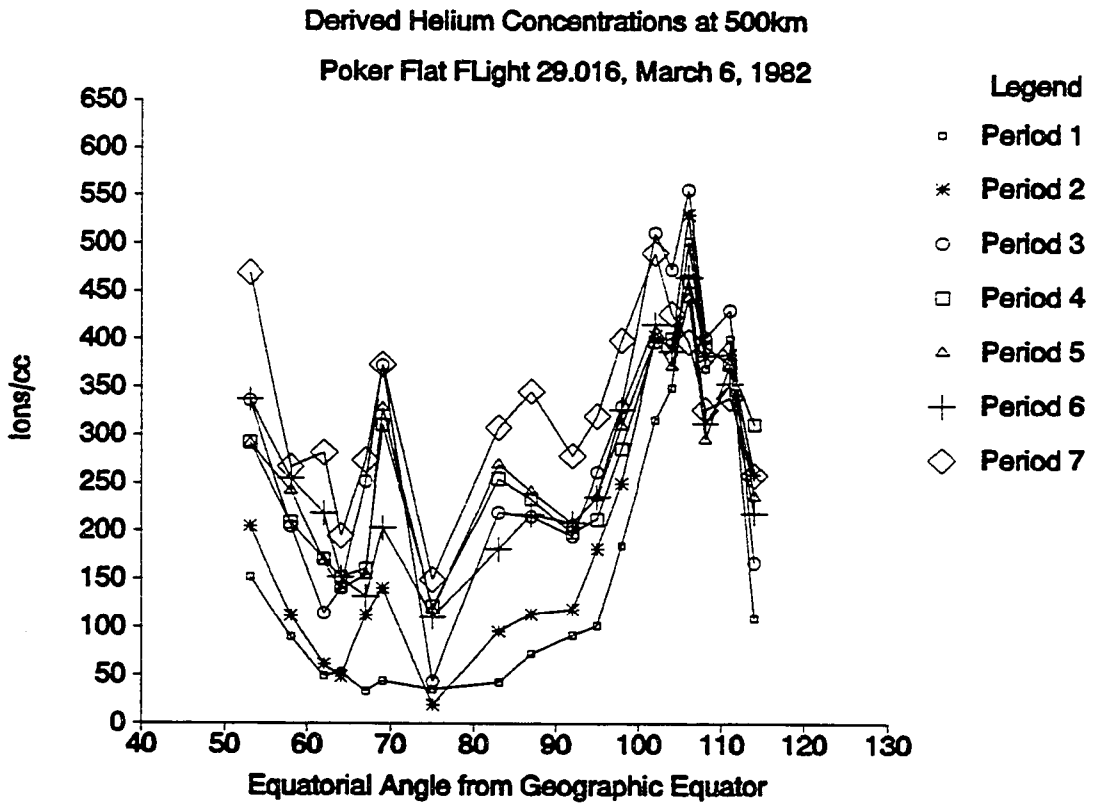

Figure 6.5 He^+ (30.4 nm) ion concentration vs latitude for the northern hemisphere for 7 periods of rotation of the rocket. Latitude angles are measured from the equator.

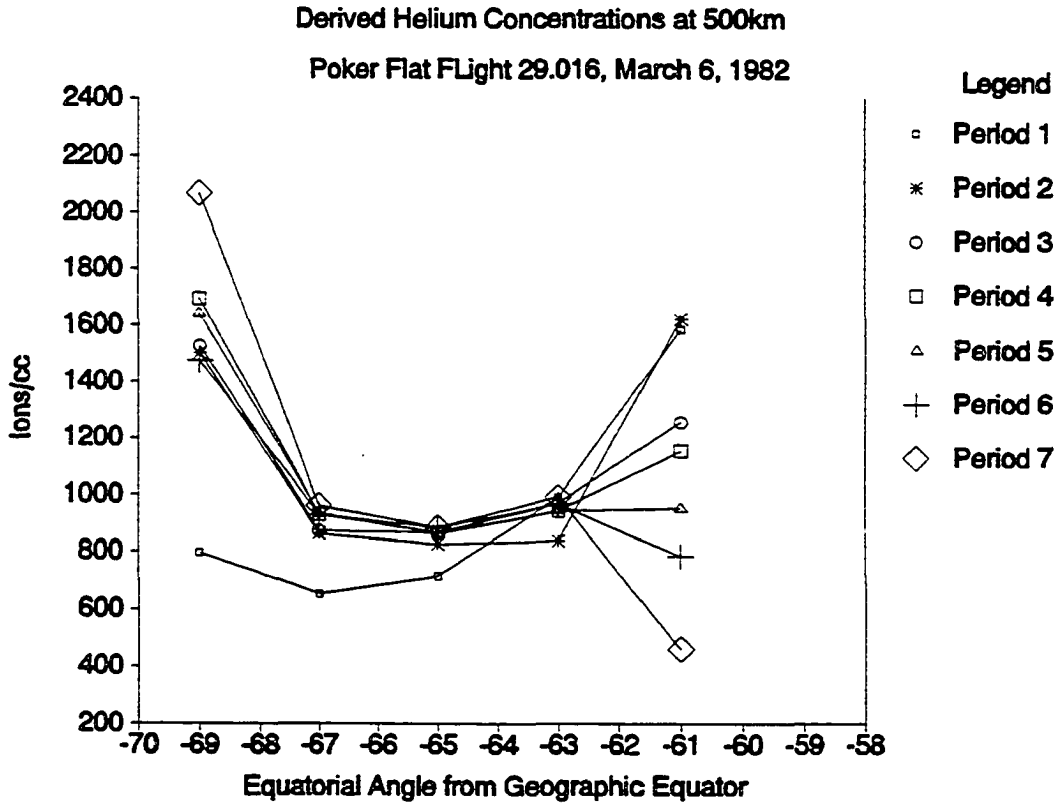

Figure 6.6 He^+ (30.4 nm) ion concentration vs latitude for the southern hemisphere for 7 periods of rotation of the rocket. Latitude angles are measured from the equator.

deg). Regions 12 and 13 show an almost unchanging density behaviour which may be expected of the plasmasphere in a diffusive equilibrium state while in region 11 the ion density varies 'slightly' about 1000 ions cm^{-3}. However, the altitude profiles in Fig. 6.9 reflect a more dynamic behaviour in the densities in contrast to Fig. 6.10 and since these measurements are high altitude observations we have at present no model to explain these results. The altitude profiles for the mid-latitude plasmasphere (latitude ranges from 65 to 72 deg) in the dayside is shown in Fig. 6.11 and regions 23 and 24 show an almost constant profile for the 7 periods of the rocket's rotation.

6.10 Comparison With Observations

Now, we can use the coefficients defined in Sec. 6.4 and the model parameters listed in the Appendix and the inverted density distribution shown in Figs. 6.7 to 6.11 to recalculate the intensity profiles for all the available data observation angles. The results are shown in Fig. 6.12 where the solid curves (loop 1) represent the calculated intensities and the dotted curves (loop 2) are the smoothed data profile while the dashed curves (loop 3) are raw data. Note that for the first five periods all three curves are superposed while for periods 6 and 7 we did not superpose the raw data. We see, however, excellent agreement between calculated and observed data. There is range of view angles where the field of view of the instrument is not completely filled. These are points where the field of view crosses the shadow line and is not filled with light from the source, thus, the measured intensity will be reduced from the proper value. These view angles range roughly from -74 to -62 deg so that the calculated intensities for these view directions would cause a dip in the intensity profile in contrast to that shown in Fig. 6.12 and no adjustment in the densities in the relevant source regions can compensate for these

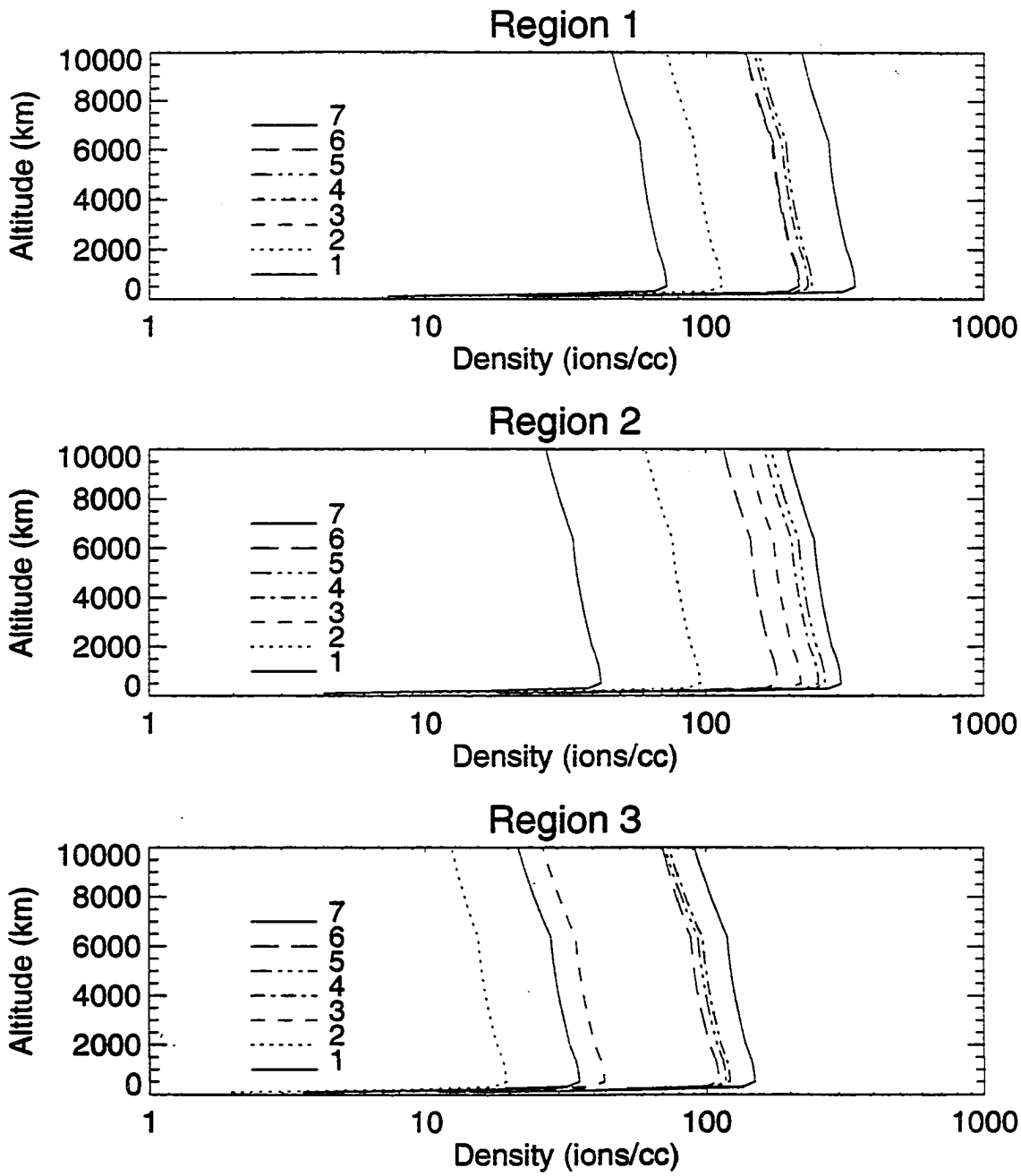

Figure 6.7 Altitude profiles for He^+ (30.4 nm) number densities in regions 1, 2 and 3. They refer to the high latitude regions in the night sector and northern hemisphere. In each region the altitude profiles for the ion densities are also plotted for the 7 periods of rotation of the rocket.

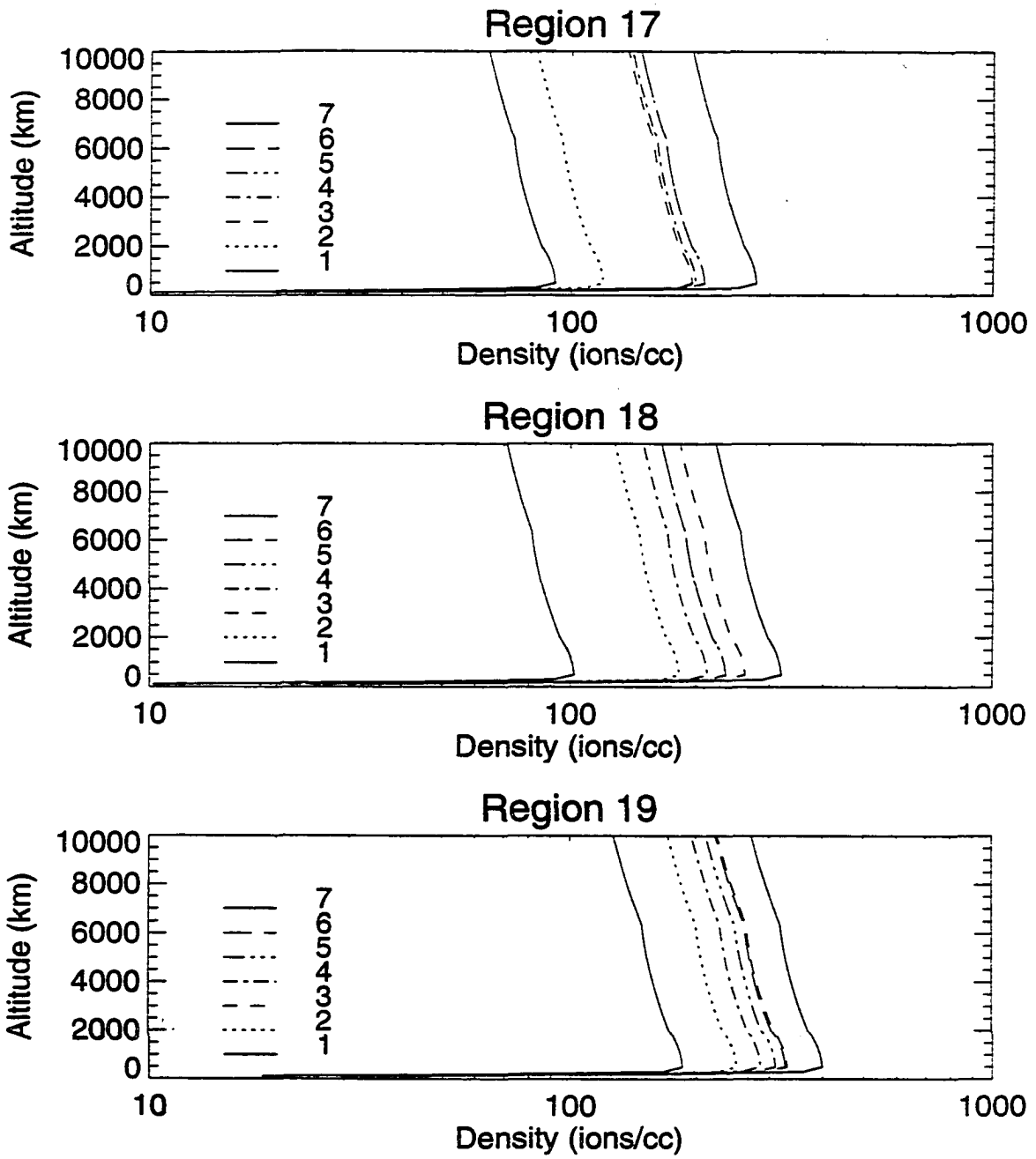

Figure 6.8 Altitude profiles for He^+ (30.4 nm) number densities in regions 17, 18 and 19. They refer to the high latitude regions in the day sector and northern hemisphere. In each region the altitude profiles for the ion densities are also plotted for the 7 periods of rotation of the rocket.

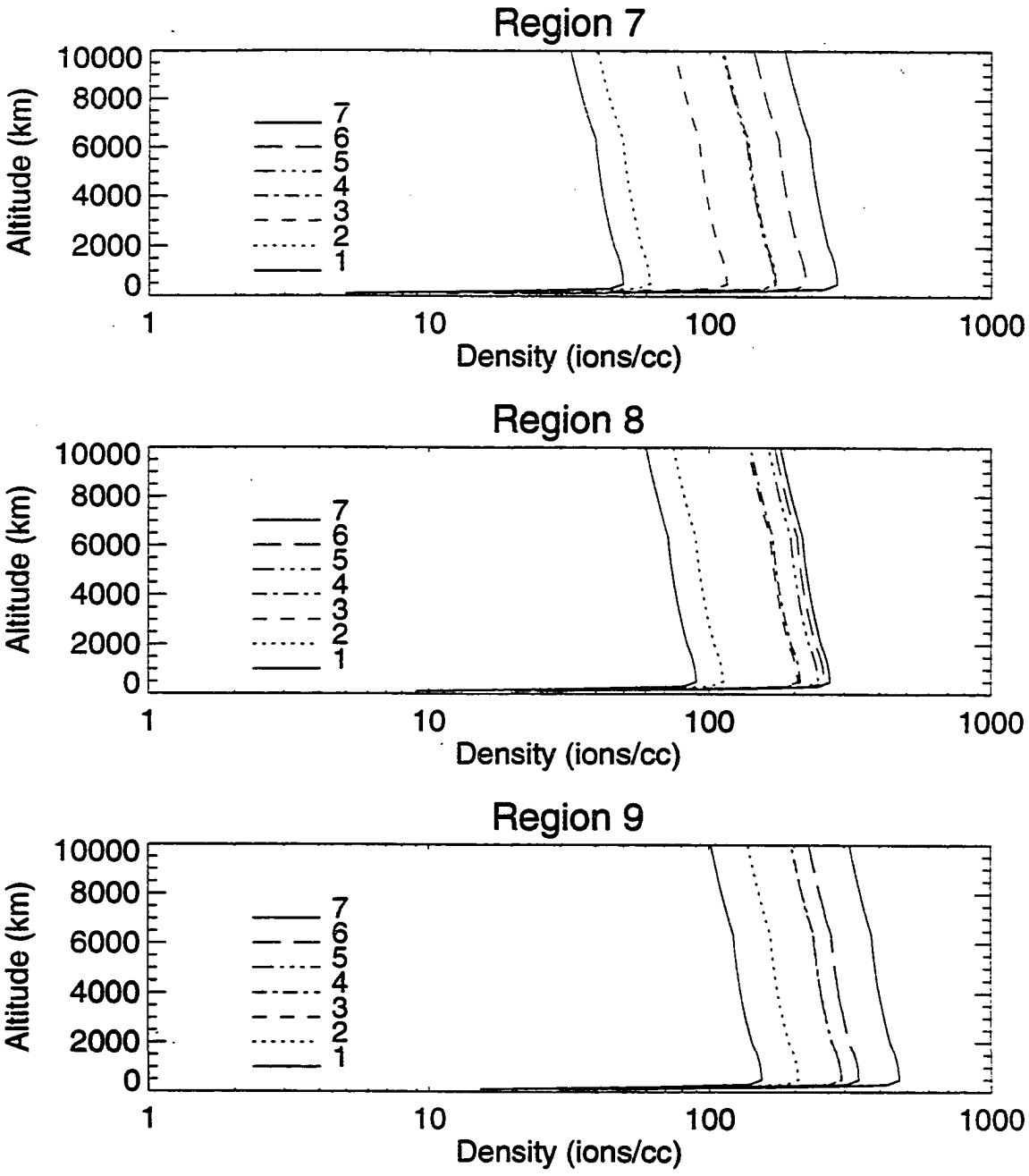

Figure 6.9 Altitude profiles for He^+ (30.4 nm) number densities in regions 7, 8 and 9. They refer to the mid-latitude plasmasphere in the night sector and northern hemisphere. In each region the altitude profiles for the ion densities are also plotted for the 7 periods of rotation of the rocket.

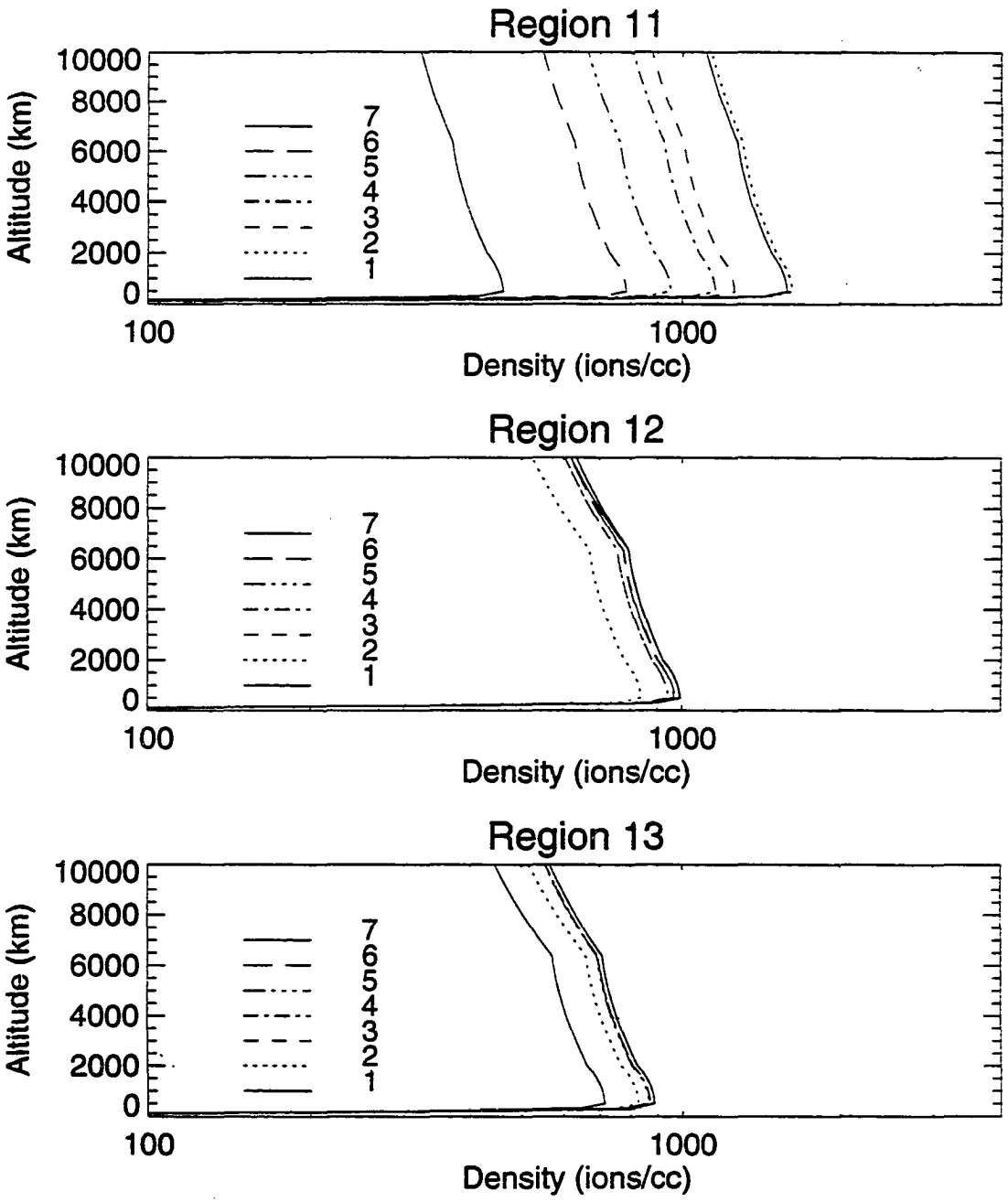

Figure 6.10 Altitude profiles for He^+ (30.4 nm) number densities in regions 11, 12 and 13. They refer to the mid-latitude plasmasphere in the night sector and southern hemisphere. In each region the altitude profiles for the ion densities are also plotted for the 7 periods of rotation of the rocket.

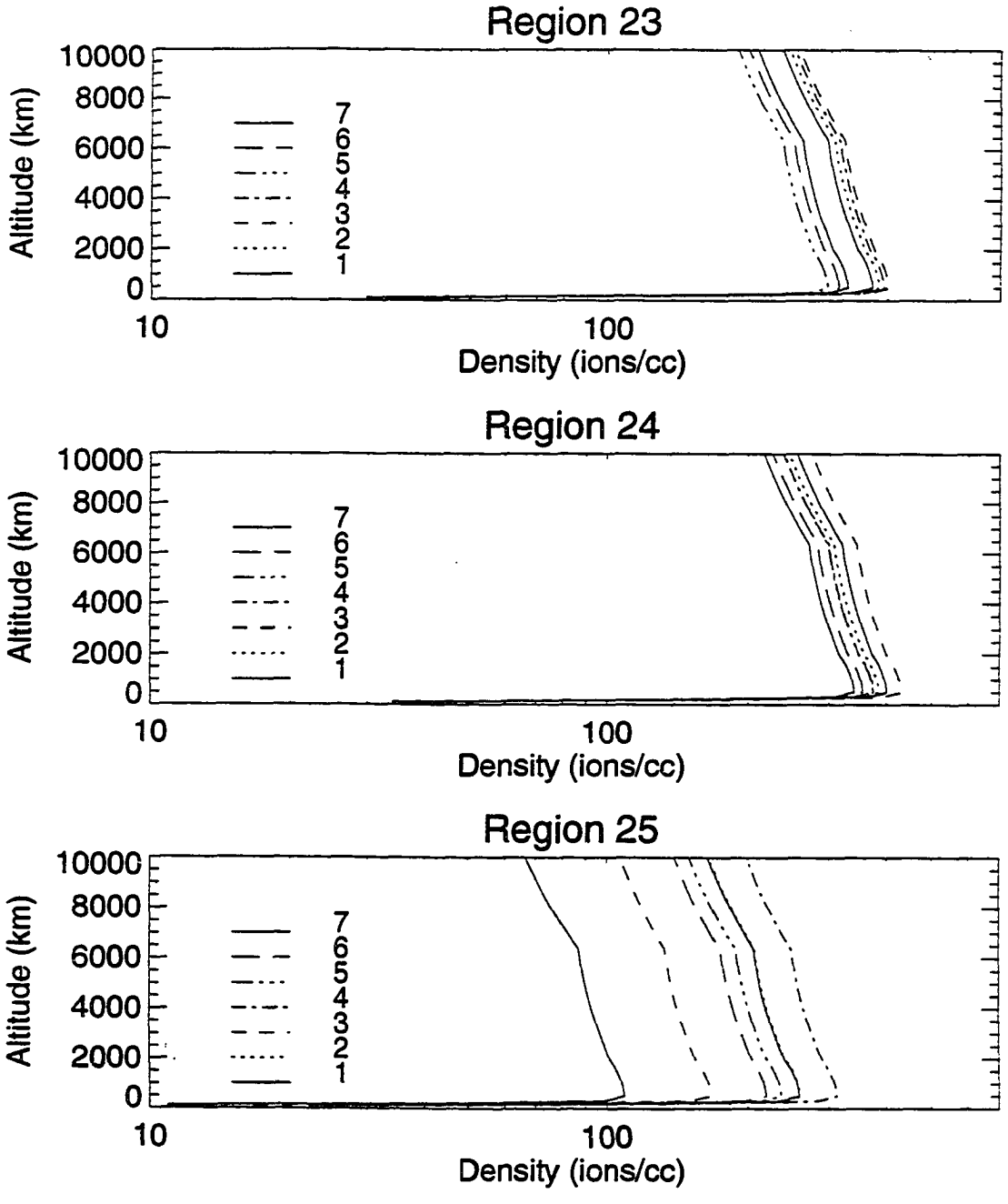

Figure 6.11 Altitude profiles for He^+ (30.4 nm) number densities in regions 23, 24 and 25. They refer to the mid-latitude plasmasphere in the day sector and northern hemisphere. In each region the altitude profiles for the ion densities are also plotted for the 7 periods of rotation of the rocket.

dips. For these view angles which are labeled m, we calculated the intensity I_m to be the average $(I_{m-1} + I_m + I_{m+1})\times(f/3)$ where f=1+η and η is a small factor much less than 1.

6.11 Discussion

The particular viewing geometry of the rocket used here with its rolling motion allows a wide coverage of many plasma regions; however, the available photometric intensity data is insufficient to determine the uniqueness of the extracted densities. In purely tomographic methods, the available data is sufficient to enable complete inversion because of the number and distribution of observations. By employing altitude profiles that are consistent with dynamical models such as the FLIP model we are able to invert the measurements and reproduce the observed intensity profiles. The product of this analysis is a set of densities at a chosen reference height. Since we do not know the exact shape of the altitude profiles as well as the relative shape of the density distribution in each flux tube, the choice of parameters to describe that shape is arbitrary and the number of parameter is large. Note that an arbitrary change in parameters (See Section 13, Appendix) can also change the relative magnitude of the extracted densities at the reference height (500 km); however, we do not expect major changes in our conclusions. From our results we are able to infer the presence of an aurora, the trough feature, and showed enhanced He^+ ion densities in the polar cap. No account has been taken of a possible change in altitude profile of the ions in the presence of an aurora.

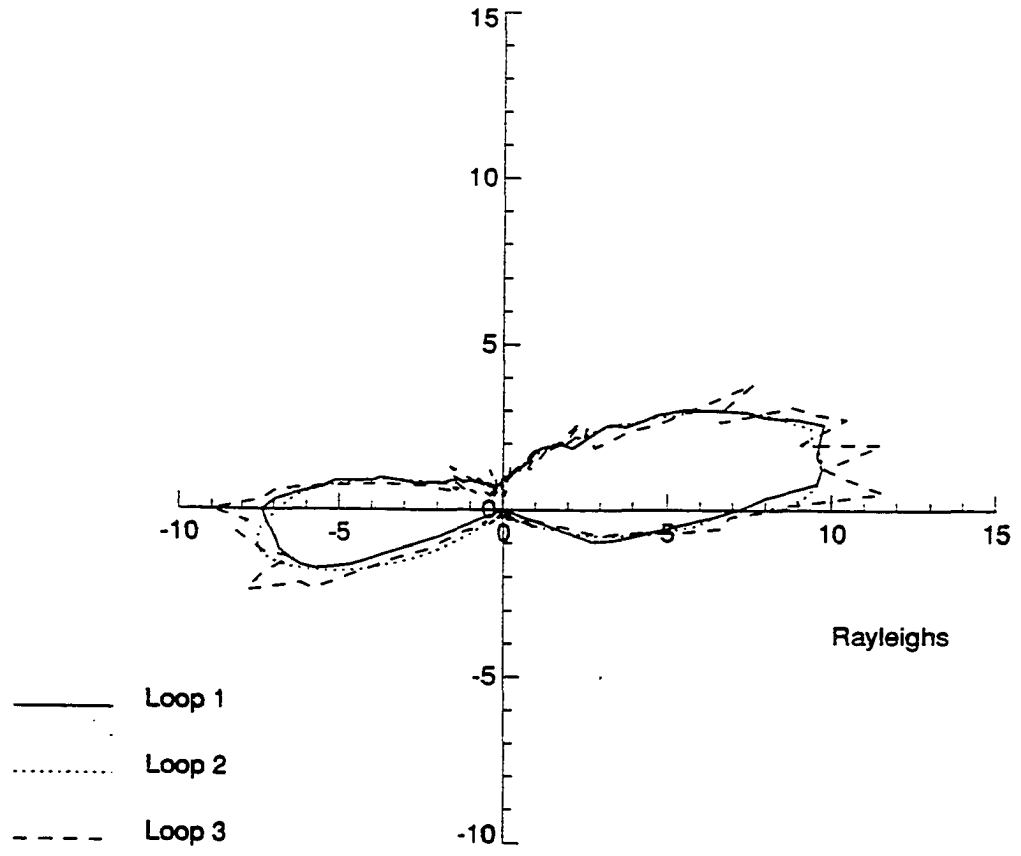

Figure 6.12a Photometric He^+ (30.4 nm) Intensity vs Roll Angle for period 1. The dotted curve is the smooth profile (loop 2) while the dashed curve (loop 3) is unsmooth and are superposed over the calculated profile (loop 1, solid).

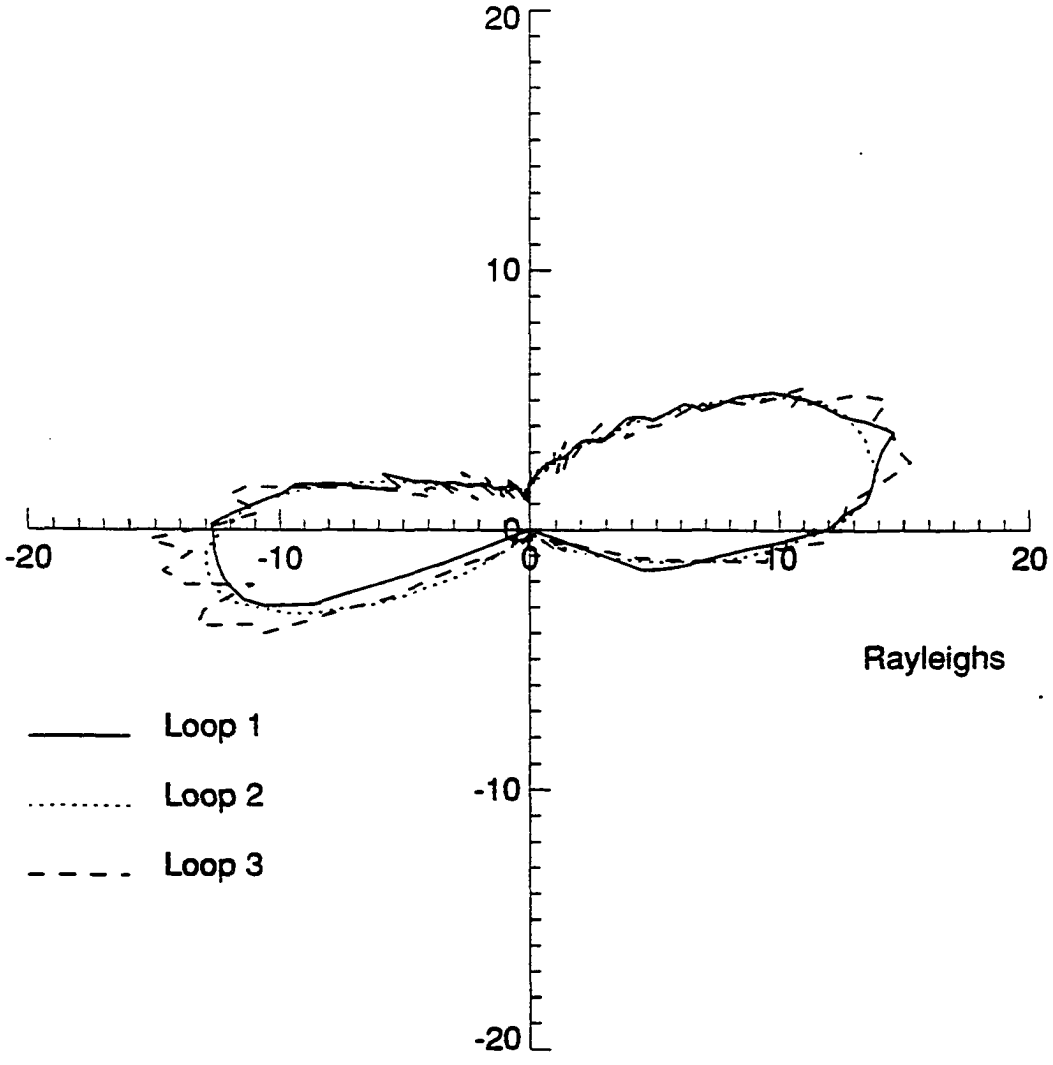

Figure 6.12b Photometric He^+ (30.4 nm) Intensity vs Roll Angle for period 2. The dotted curve is the smooth profile (loop 2) while the dashed curve (loop 3) is unsmooth and are superposed over the calculated profile (loop 1, solid).

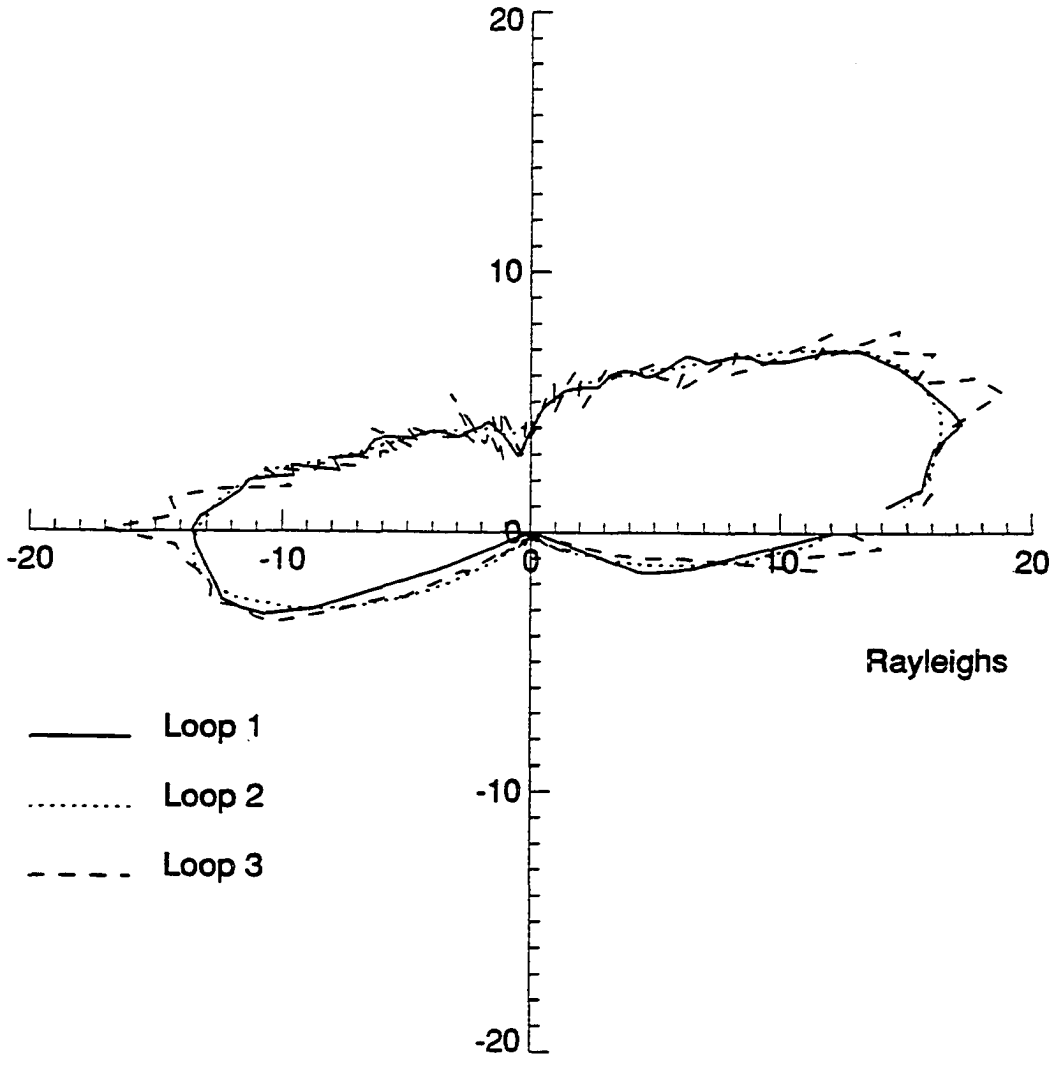

Figure 6.12c Photometric He^+ (30.4 nm) Intensity vs Roll Angle for period 3. The dotted curve is the smooth profile (loop 2) while the dashed curve (loop 3) is unsmooth and are superposed over the calculated profile (loop 1, solid).

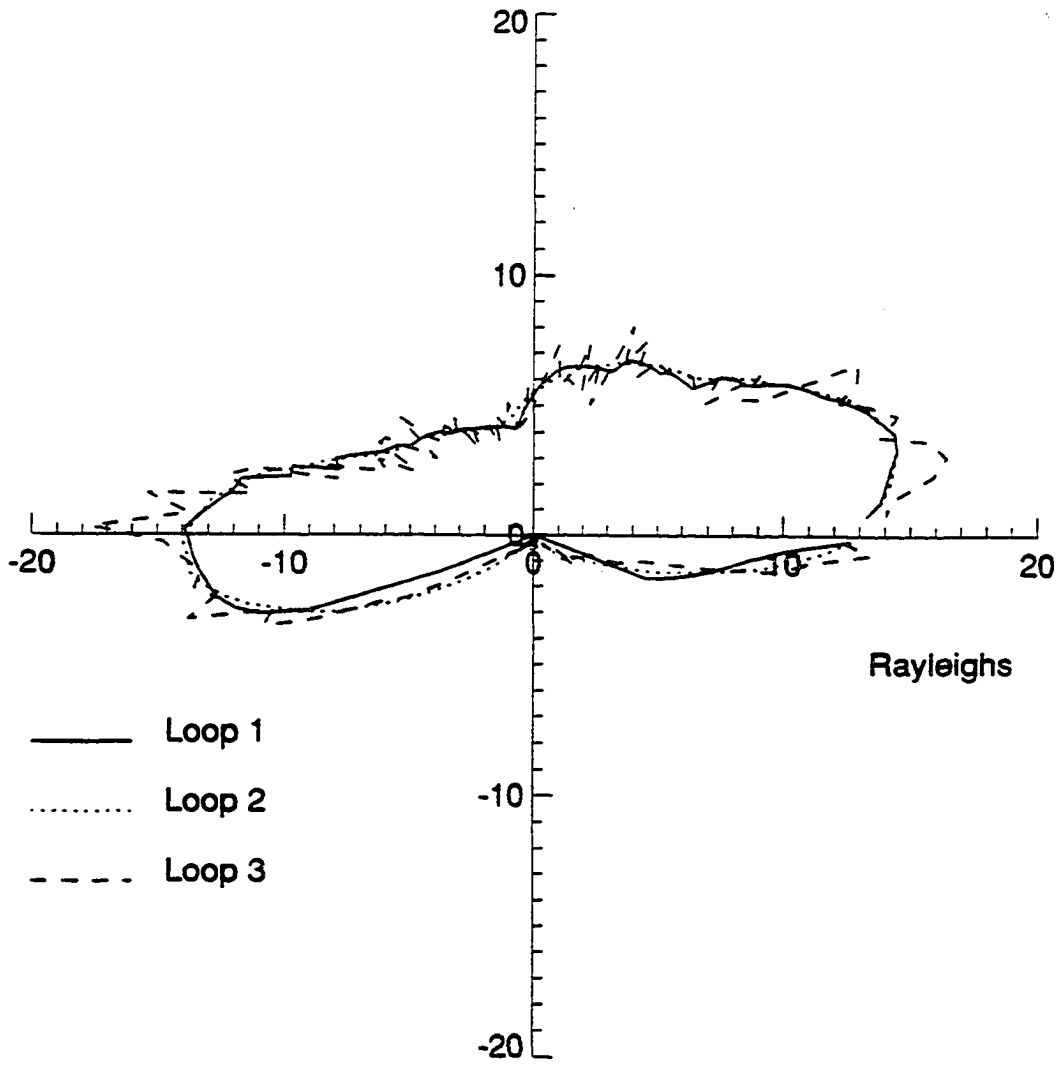

Figure 6.12d Photometric He^+ (30.4 nm) Intensity vs Roll Angle for period 4. The dotted curve is the smooth profile (loop 2) while the dashed curve (loop 3) is unsmooth and are superposed over the calculated profile (loop 1, solid).

Our method of inverting observed intensities to obtain density distributions may be applied in studies regarding the refilling and depletion of plasmas from flux tubes in the plasmasphere and the outflow of ions at high latitudes in the polar cap. The inflated shapes of the profiles in other loops represent a dynamical change in the density distribution of the He^+ ions in the regions observed. The relative magnitude of the densities in each flux tube region will give us an indication about which source regions have significant ion depletions or outflows. Our results show that since most of the observed intensities come from higher altitude regions the relative change in the intensities during the 7 periods of the rocket's motion may not be attributed directly to the changes in the ionospheric densities at 500 km. If the plasmasphere varies rapidly in time during the rotational period of the rocket our method may not be applicable; however, important advances in instrumentation such as coded aperture imagers (Curtis et al., 1992) are presently being developed that may resolve this problem. A single observation in time allows the imager to obtain many line- of-sight integrations (1-D slice) within the field of view of the instrument. Thus, many 1-D slices of the magnetosphere can be obtained in a relatively shorter time by adjusting the 'look' direction of the imager.

6.12 Conclusions

Under the assumption that the plasmasphere does not vary rapidly within one period of the rocket's rotation we are able to recover density profiles of He^+ (30.4 nm) ions in many different plasma regions that includes the plasmasphere and the high latitude outflow regions. We introduced a forward inversion method that used all the intensity data points and a least squares method that minimizes the error between observed and calculated intensity profiles. We also derived matrix elements that contains information

on the particle scattering rate and the density shape function. The matrix elements indicate the different source regions and their relative contribution to the densities in a given line-of-sight direction.

The latitude variation of the densities at 500 km in the night sector show a trough region starting roughly at a latitude of 64 deg and a steady enhancement of the He^+ ion concentration by a factor of 8 just north of the rocket just at about 69 deg latitude. These density enhancements may be reasonable and attributed to the presence of an aurora but time dependencies at lower latitudes are difficult to relate to our present understanding.

The computed intensity profiles for He^+ (30.4 nm) ions are in excellent agreement with observations for all periods of rotation of the rocket.

The assumption of FLIP type shapes for the altitude profiles of the ions in each flux tube region is reasonable because these profiles have been shown to be consistent with observations. Furthermore, this assumption together with the parameters defined in the Appendix effectively reduces the problem to just the determination of the density parameters at 500 km. Note, that the densities obtained with our method of analysis are also dependent on dipole tilt, magnetic field model, the rocket's spatial location, detector field of view and the rocket's orbital motion. The assumption of a static plasmasphere may be removed if intensity observations are obtained simultaneously.

The densities that we have obtained by the least squares method lead to consistent intensity profiles; however, densities at lower altitudes obtained from the simulation still need to be compared with low altitude observations. Since intensity measurements were obtained at high altitudes, the changes in the intensities directly correlate to changes in the density distribution in these regions. We, however, still have difficulty in interpreting dynamic changes in ion densities occurring in the ionosphere.

6.13 Appendix: Model Parameters

For the case when the dipole has 0 deg tilt, we have used the following arc distances in km; s_1=100, s_2=300, s_3=500, s_4=1000, s_5=2000, s_6=4000 and s_7=6371. For the density ratios, let $l_i = n_i/n_0$ (i=1,7) so that the model parameters for all regions R_I (I=1,25) may be written as follows,

$$R_I = (l_1, l_2, l_3, l_4, l_5, l_6, l_7)$$

Thus, for all flux tube regions we have used

$$R_I = (0.1, 0.9, 1.0, .99, .93, .85, .80)$$

Also, the scale parameters α_I have values that are adjustable between 0.3 to 0.5.

6.14 References

Chakrabarti, S., F. Paresce, S. Bowyer, Y.T. Chiu and A. Aikin, "Plasmaspheric Helium Ion Distribution from Satellite Observations of He II 304-A," *Geophys. Res. Lett.*, **9**, 151-154 (1982).

Cormack, A.M., "Representation of a Function by Its Line Integrals, with Some Radiological Applications," *J. Appl. Phys.*, **34**, 2722-2727 (1963).

Cormack, A.M., "Representation of a Function by Its Line Integrals, with Some Radiological Applications. II," *J. Appl. Phys.*, **35**, 2908-2912 (1964).

Curtis, C.C., K.C. Hsieh, B.R. Sandel and V. A. Drake, " Coded aperture devices for viewing extended objects from space," *Instrumentation for Magnetospheric Imagery*, Supriya Chakrabarti, Editor, Proc. SPIE 1744, 138-147 (1992).

Garrido, D.E., R.W. Smith, D. W. Swift, S.I. Akasofu, R.M. Robinson and Y.T. Chiu, " Imaging the plasmasphere and trough regions in the extreme ultraviolet," *Instrumentation for Magnetospheric Imagery*, Supriya Chakrabarti, Editor, Proc. SPIE 1744, 117-136 (1992).

Garrido, D.E., R.W. Smith, D. W. Swift, S.I. Akasofu, R.M. Robinson and Y.T. Chiu, " Imaging the plasmasphere and trough regions in the extreme ultraviolet," *Optical Engineering*, **33**, February, (1994).

Ghosh Roy, D.N., " Radon Inversion of Spectral Intensities Emitted by an Asymmetric and Absorbing Plasma," *J. Quant. Spectrosc. Radiat. Transfer*, bf 31, 15-21 (1984).

Herman, G.T., Editor, Image Reconstruction from Projections (Implementation and Applications), Springer-Verlag, New York (1979).

Horwitz, J.L., R.F. Comfort, P.G. Richards, M.O. Chandler, C.R.Chapell, P. Anderson, W.B. Hanson and L.H. Brace, " Plasmasphere-Ionosphere Coupling 2. Ion Composition Measurements at Plasmaspheric and Ionospheric Altitudes and Comparison With Modeling Results," *J. Geophys. Res.*, **95**, 7949-7959 (1990).

Newberry, T., R.H. Comfort and P.G. Richards, " Thermal He^+ in the Plasmasphere: Comparison of Observations with Numerical Calculations I," *J. Geophys. Res.*, **94**, 15265-15276 (1989).

Ottley, J. Alan, R.W. Schunk, " Density and Temperature Structure of Helium Ions in the Topside Polar Ionosphere for Subsonic Outflows," *J. Geophys. Res.*, **85**, 4177-4190 (1980).

Paresce, F., C.S. Bowyer and S. Kumar, " On the Distribution of He^+ in the Plasmasphere From Observations of Resonantly Scattered He II 304-A Radiation,"*J. Geophys. Res.*, **79**, 174-178 (1974).

Richards, P.G. and D.G. Torr, " Ratios of photoelectron to EUV ionization rates for aeronomic studies," *J. Geophys. Res.*, **93**, 4060-4066, (1988).

Solomon, S.C., P.B. Hays and V.J. Abreu, " Tomographic inversion of satellite photometry," *Appl. Opt.*, **23**, 3409-3414 (1984).

Solomon, S.C., P.B. Hays and V.J. Abreu, " Tomographic inversion of satellite photometry. Part 2," *Appl. Opt.*, **24**, 4134-4140 (1985).

Weller, C.S. and R.R. Meier, " First Satellite Observations of He^+ 304-A Radiation and Its Interpretation," *J. Geophys. Res.*, **79**, 1572-1574 (1974).

6.15 Acknowledgements

This work was supported by the Alaska Space Grant Program and funds from the Geophysical Institute, University of Alaska-Fairbanks. The authors also thank D.L. Hampton for technical assistance.

Chapter 7 Inversion of EUV 30.4 nm images to obtain 3-D He^+ densities

7.1 Introduction

A large number of in situ experiments have been carried out over many years in many component regions around the Earth's Magnetosphere and the present global picture has been an average picture. Since measurements of ion populations have been accumulated over long periods of time and at different regions, because of the time variability of the different magnetospheric processes from one pass of a satellite to the next the interpolated information may not be accurate; hence, the current picture may not be reliable. Ions like He^+ and O^+, however, have been found to have large scattering rates and their resonant emissions may be used to trace the ion distributions.

The ionosphere and the plasmasphere have been observed to be heavily populated with plasma constituents such as He^+ (30.4 nm) and O^+ (83.4 nm) ions which are suitable candidates for imaging in the EUV region. It has been discussed in the previous chapter that extracting quantitative information like density distributions from photometric intensities using tomographic techniques may be expensive and impractical and requires many simultaneous observations at various locations. I introduce a method of analysis that removes the technical difficulties involved in carrying out tomographic analysis. In the next section I undertake a computer experiment to illustrate the method and also state my assumptions.

7.2 The Source Distribution

In Chapter 5, I simulated an image of the plasmasphere in He^+ 30.4 nm light using boundary conditions that represented source densities in the ionosphere and the density distribution everywhere in the flux tubes was obtained by using the kinetic model to describe the densities in the polar regions and the fluid model to describe the plasmasphere. The boundary conditions have been assumed to vary in latitude but to be constant in MLT. I have also assumed that I have a symmetrical north and south hemispheric distribution.

I simulate another experiment by adopting the day boundary conditions in Chapter 5 and using them as boundary conditions for both day and night sectors for my present problem and now assume the source densities to be 'data' at 500 km. I also assume that there is symmetry between northern and southern hemispheres. The He^+ source density is shown as an image distribution in Fig. 7.1. The source distribution is divided into 11 latitude sectors which are 8 deg wide and there are 8 MLT sectors which are 45 deg wide each. The annular regions show areas assumed to be constant in distribution over MLT. The latitude variation of the densities shows a plasmapause at L=3 with a minimum density of 10 ions cm^{-3} in the polar cap and a maximum density of 900 ions cm^{-3} around the equator (See Fig. 5.4a). Looking from above the northern hemisphere the bottom portion of Fig. 7.1 represent the day sector while the top portion of Fig. 7.1 refer to the night sector. Also, the left and right side of the Fig. 7.1 refer to the dawn and dusk sectors, respectively.

7.3 The Image Distribution

The image distribution corresponding to the source boundary conditions defined by Fig. 7.1 is shown in Fig. 7.2. The shadowing of the plasma in the night sector (right side of Fig. 7.2) is reflected in the relatively dimmer intensity in contrast to the day sector (left side of Fig. 7.2). Recall that the 50×50 pixel image was obtained by simulating an imager at 9 R_e in the dusk sector viewing towards the center of the Earth. The brightest intensity is about 38 Rayleighs and the darkest regions are of the order of a few hundreths of a Rayleigh. I will assume that the image of Fig. 7.2 to be input data. Note that photon statistics in the detector have not been considered and that 100 % detector efficiency has been assumed.

7.4 The Inversion Method

The image of Fig. 7.2 is now considered as input data to be analyzed and my aim is to recover the source distribution of Fig. 7.1. Note that a single pixel in Fig. 7.2 can be defined by field of view coordinates (eta,beta) where the upper right hand corner pixel has coordinates (25,25) and the middle right side corner has coordinates (25,0), and both pixels are all in the night sector. Recall, that the key assumption that I used in Chapter 6 to recover the densities is to assume that the density profile of the ions have a 'FLIP' type shape so that if the source density in the ionosphere is given, then the density distribution everywhere inside the flux tube can be calculated. The use of the FLIP type model to describe plasmaspheric densities may not be fully justified; however, it is convenient to use and it accounts for a large amount of observations in the plasmasphere.

The decrease in densities along the flux tubes away from the ionosphere is also consistent with observed behaviour in these regions. Thus, the model is simple and reasonable.

I indicated in Chapter 6 that a given line-of-sight includes contributions from different flux tube regions whose sources can be traced down along magnetic field lines to the ionosphere into various latitude sectors. A group of pixels in Fig. 7.2 which has field of view coordinates ranging from (-10, 25) to (-10,-25) may be defined as a 'slice' in the image distribution at eta = -10 deg. Each pixel coordinate in this slice represents a given direction within the imager's field of view and the column intensity represent integrated intensity sources from diffferent flux tube regions. The relevant matrix elements (See Chapter 6) also give the relative magnitude of the contributions to the densities from the different latitude sectors. The source densities affected in the line-of-sight integrations can be adjusted and the column intensities recalculated and compared with the original data. The procedure is reiterated many times until minimum error is obtained in the least squares sense. Since there is symmetry between the northern and the southern hemispheres it is possible to consider only a slice in the upper hemisphere.

A source distribution such as shown in Fig. 7.1 can be used as an initial source distribution and also assuming the FLIP type density model to describe the ion distribution everywhere, the line-of-sight intensities can be recalculated using the same viewing geometry as was used to obtain Fig. 7.2 and compared with the original image. The problem may be iterated many times until the error is minimized. Each hemispherical source region is divided into 88 component regions (11 latitude sectors and 8 MLT sectors) which makes the procedure tedious. Furthermore, the amount of time for image minimization to be achieved is enormous. However, to illustrate my purpose, I simplify the procedure by considering only specific slices in the analysis. I have chosen to analyze the image distribution in slices which are 5 deg apart but the line-of-sight integrations still cover

the entire source distribution. Thus, for simplicity the image minimization is performed one slice at a time until the whole image is covered and the procedure repeated until error minimization is achieved.

7.5 The Extracted Source Distribution

The results of the error minimization procedure that I have applied is shown in the image distribution of Fig. 7.3 and the recovered source distribution is shown in Fig. 7.4. I see in Fig. 7.4 that the shape of the plasmasphere, its plasmapause, maximum intensities in the bright regions in the day sector are reasonably obtained, and the shadowing of the plasma in the night sector is still evident. I also note that some bright regions in the plasmasphere (day sector, about eta=-9 deg) are not present and this results because I used only a partial number of slices in the image distribution during the minimization procedure. The recovered source distribution is shown in Fig. 7.4. I see that in some regions, there are differences between Fig. 7.1 and Fig. 7.4. Note that the plasmaspheric regions and the polar regions are fairly recovered where the number of ions cm^{-3} is now zero for latitudes greater than 77 deg.

The discrepancy between the original and extracted source distribution is expected because in the minimization procedure illustrated above, the calculated image may not be the true minimum image. Although the results above are very promising, I need to improve the computer codes in the image analysis. This simulated experiment was done to show that I have the ability to extract quantitative information from 2-D images with a spacecraft making an observation in an instant of time and in one location in space.

7.6 Future Work

In future work, I will continue to assume the FLIP type model to describe the density distribution everywhere inside the flux tubes and divide the source distribution into zonally averaged sectors. I may start with 11 latitude sectors with each latitude region having the same source distribution in MLT (zonally averaged). The symmetry between the northern and southern hemispheres reduces the laborious iterative procedure described above. I therefore have only a few unknown source densities (unknowns) to adjust in performing the image minimization. The entire image distribution is calculated and compared with the original image and the procedure is iterated until a minimum error in the least squares sense is obtained. The resultant source distribution is now broken into 22 independent subregions (day sector has 11 and night sector has 11), thus, introducing a day-night asymmetry. The minimization procedure is repeated where there are now more independent parameters involved; however, I need to adjust all sectors at once: say, all sectors in the night are either increased or decreased in content simultaneuosly, and then all day sectors are adjusted until a minimum is achieved. Note that I have made only two adjustments. As another minimum is achieved, I now introduce a dawn-dusk and a noon-midnight asymmetry and so on. I believe that this procedure leads to the minimum image desired and the source distribution extracted will then be unique in the least squares sense.

Note that the labor of repeatedly calculating the entire image distribution in each step in the minimization procedure is still present. The computer code to calculate the image needs to be optimized.

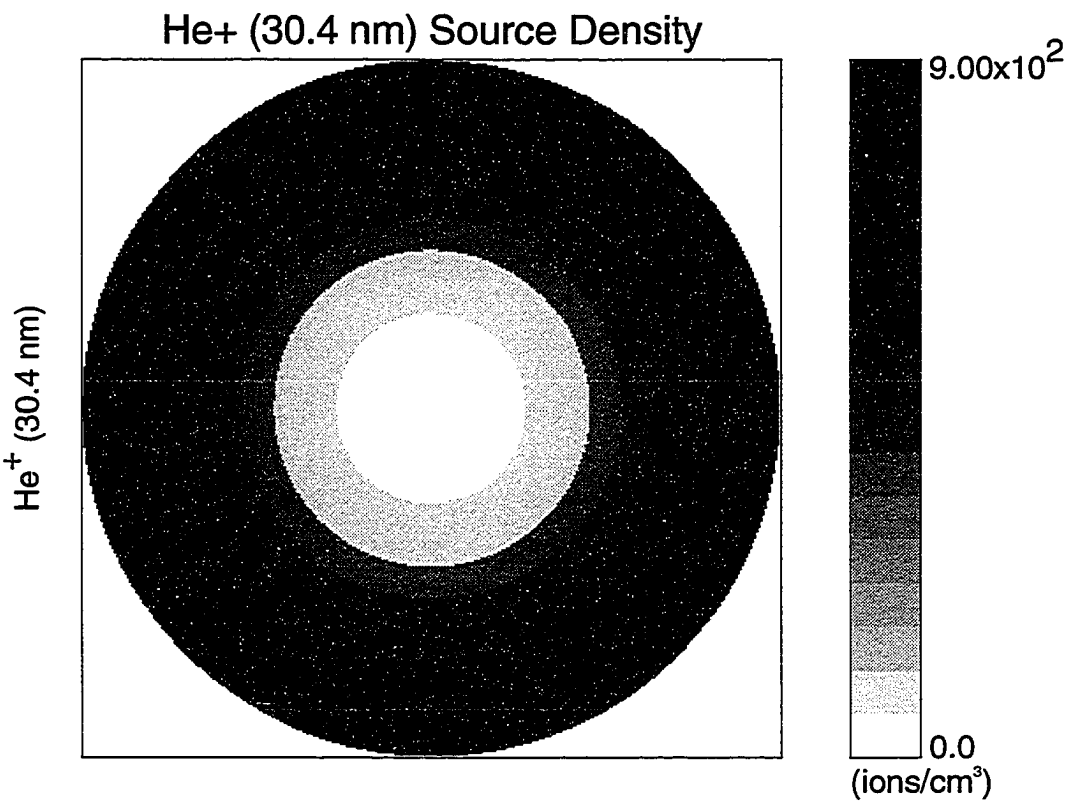

Figure 7.1 He^+ (30.4 nm) source distribution at 500 km divided into 11 latitude zones. The bottom portion of the figure is in the noon sector.

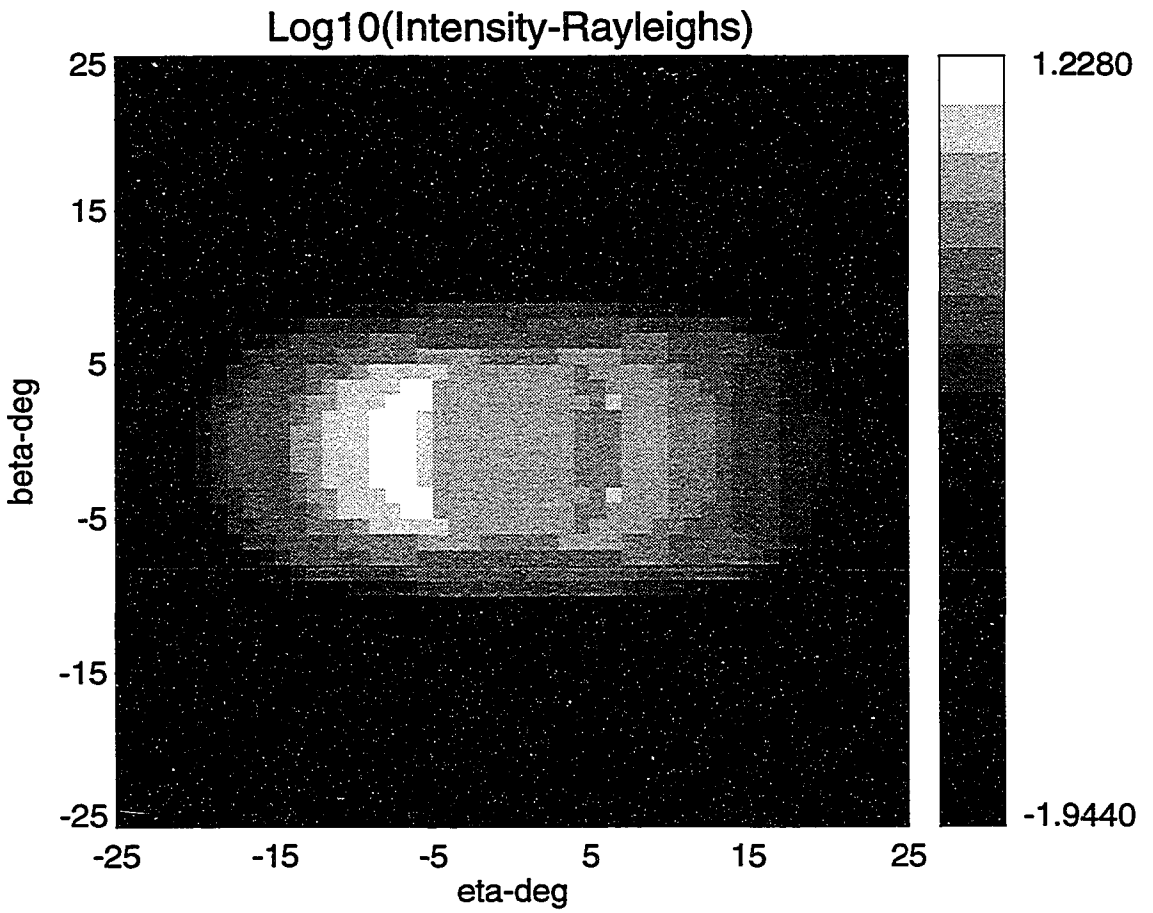

Figure 7.2 Simulated He^+ (30.4 nm) image using the densities in Fig. 7.1. The satellite is located at 9 R_e in the equatorial plane in the dusk sector and viewing towards the center of the Earth. The right side of the figure is in the day sector. Intensities are listed in log base 10 (Rayleighs).

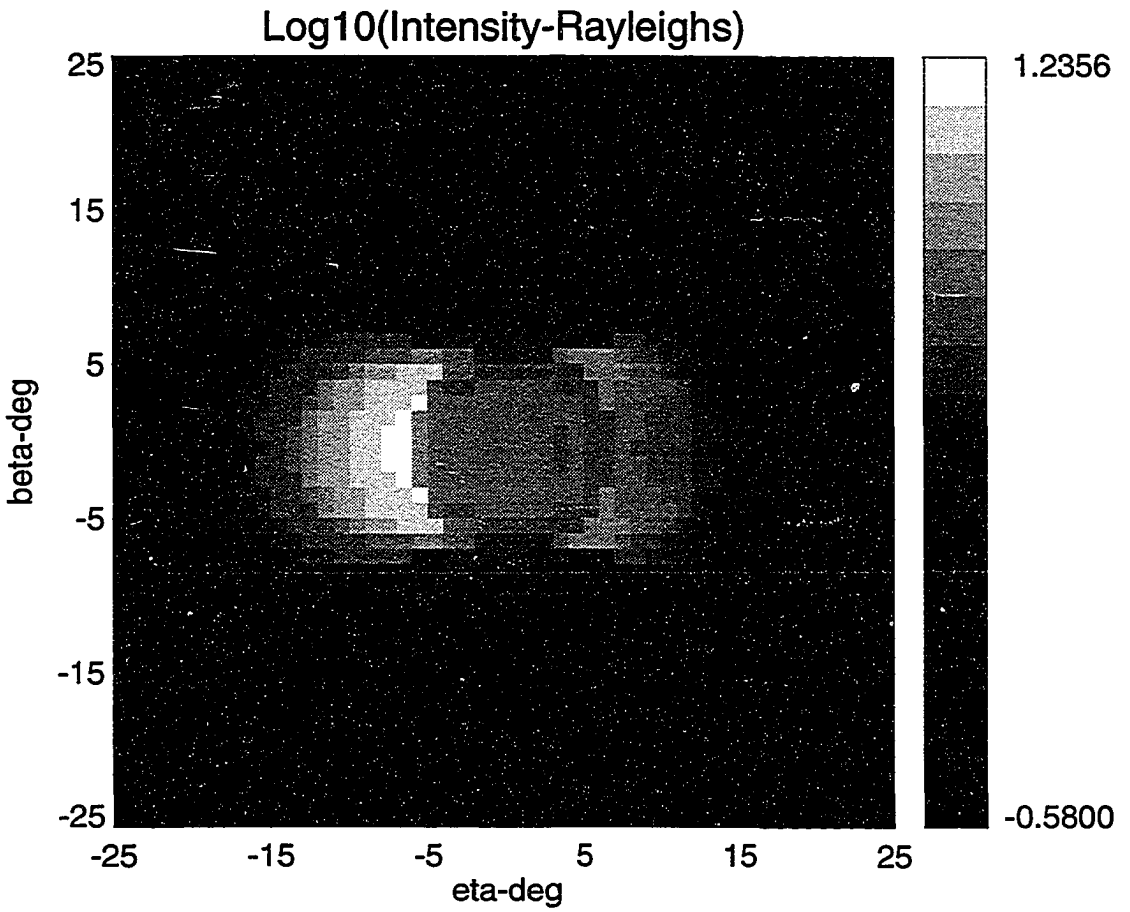

Figure 7.3 He^+ (30.4 nm) image obtained by minimization procedure. The satellite uses the same viewing geometry as that of Fig. 7.2. Intensities are listed in log base 10 (Rayleighs).

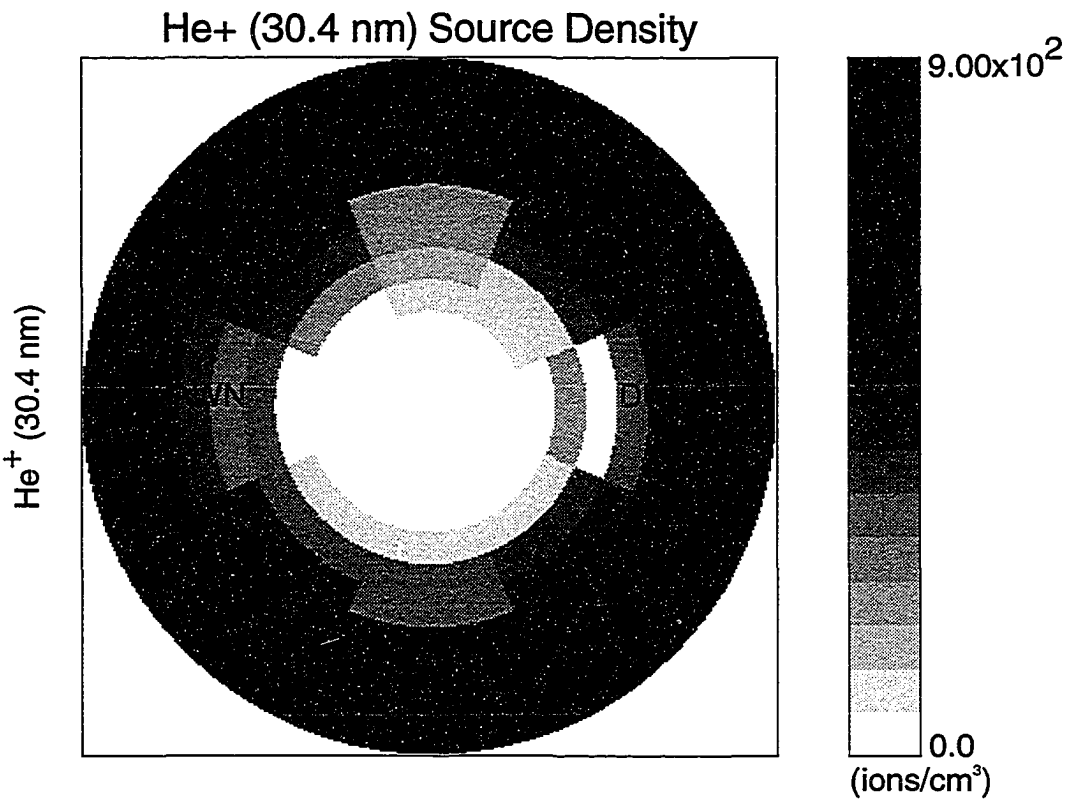

Figure 7.4 Extracted He^+ (30.4 nm) source distribution at 500 km. The bottom portion of the figure is in the noon sector.

Chapter 8 Conclusion

I am confident that the method of forward modelling to simulate magnetospheric images is very useful in estimating emission rates originating from the different component regions in the inner magnetosphere. The He^+ (30.4 nm) and O^+ (83.4 nm) emission line has received much attention because of the abundance of the He^+ and O^+ ion species in the ionosphere and in the plasmasphere. The large scattering rates of the ions make it favorable to image the ion populations in these wavelengths.

Since the cold ions are tied up to the magnetic field lines, the dipole nature of the near-Earth magnetic field may be seen in the images of He^+ 30.4 nm. Due to the heavy mass and smaller scale height of the O^+ ions, the O^+ ion densities decreases faster far away from the ionosphere than the He^+ ion densities and the dipole nature of the magnetic field may not be evident. Since the 83.4 nm emission line is optically thick, I expect an image at this wavelength to be a spherical glow.

The plasmasheet region contains very energetic O^+ ions which are believed to have originated in the ionosphere. Dynamic events like magnetic reconnection are believed to occur in the tail and large ion velocities have been observed in these regions. The large bulk motion of the ions along the Sun-Earth line may cause Doppler shifts of the O^+ absorption lines off the solar emission lines and I may see dim and bright regions in the tail. I note, however, that a simple Boltzmann velocity distribution was assumed and a more complex distribution may exist in the tail region. To see the gross features of the radiation belt and plasma sheet, a camera with an aperture area of 750 cm^2 with an exposure time of 1000 s is needed.

The possibility of detecting optical emissions from O^+ 83.4 nm and He^+ 30.4 nm ion outflows in the polar regions may be enhanced if a satellite is located at a distance of 9 R_e or greater in the equatorial plane and viewing towards the center of the Earth. Observations in 30.4 nm light may be favorable during disturbed times when the size of the plasmasphere is reduced. Doppler shifts and ionospheric glow may complicate the interpretation of the images of outflowing O^+ 83.4 nm ions. I believe, however, that if particle energization occurs in a small latitude range in the ionosphere dim regions in the polar cap may be evidence of Doppler shifts.

I have developed an inversion method that allows us to quantitatively extract density information from photometric He^+ 30.4 nm intensities obtained by low altitude orbiting rockets with a spin scan motion (internal view). By assuming the density profile to have a FLIP type shape everywhere inside the flux tubes I am able to determine source densities at 500 km in the ionosphere over a wide range of latitudes. The plasmapause may also be inferred from our analysis as well as the time development of the ion densities in the polar cap. More detailed analysis is required as to the accuracy and reliability of the extracted information.

I have extended the method of analysis for low altitude rockets to a satellite viewing externally at large distances. I have shown that it is possible to extract 3-D He^+ 30.4 nm ion distributions from 2-D images for a satellite viewing in one instant of time and one location. Although the method of image analysis is in its initial stage, the method is very promising in that the economic and technical difficulties posed by tomographic experiments may not be necessary.